

UNIVERSITY OF OKLAHOMA

GRADUATE COLLEGE

REACTION PATHWAYS AND CATALYST PHASE TRANSFORMATIONS
DURING SYNTHESIS OF NANOTUBES AND NANOWIRES BY THE VAPOR-
LIQUID-SOLID MECHANISM

A Dissertation

SUBMITTED TO THE GRADUATE FACULTY

in partial fulfillment of the requirements for the

degree of

Doctor of Philosophy

By

NATAPHAN SAKULCHAICHAROEN

Norman, Oklahoma

2006

UMI Number: 3205324



UMI Microform 3205324

Copyright 2006 by ProQuest Information and Learning Company.
All rights reserved. This microform edition is protected against
unauthorized copying under Title 17, United States Code.

ProQuest Information and Learning Company
300 North Zeeb Road
P.O. Box 1346
Ann Arbor, MI 48106-1346

REACTION PATHWAYS AND CATALYST PHASE TRANSFORMATIONS
DURING SYNTHESIS OF NANOTUBES AND NANOWIRES BY THE VAPOR-
LIQUID-SOLID MECHANISM

A DISSERTATION APPROVED FOR THE
SCHOOL OF CHEMICAL, BIOLOGICAL & MATERIALS ENGINEERING

BY

Daniel E. Resasco

Lance L. Lobban

Jeffrey H. Harwell

David W. Schmidtke

George B. Richter-Addo

© Copyright by NATAPHAN SAKULCHAICHAROEN 2006
All Rights Reserved.

ACKNOWLEDGMENTS

This work would not be completed without the influence of many people in my life. I thank everyone who encouraged me and supported me in many aspects of my life. Whatever mention I can make of them here can not match their true contributions and my deep appreciation.

First of all, I would like to acknowledge my thesis advisor, Dr. Daniel E. Resasco for his generous support, but most of all for his earnest guidance, inculcation and continued encouragement and friendship. It is with the deepest gratitude that I acknowledge his invaluable guidance as well as his advice.

I would like to thank everyone on the OU carbon nanotube group for their help and friendship, in particular to Drs. Walter Alvarez and Jose Herrera for their permanent encouragement and the guidance in the early stages of my Ph.D. work. I am very thankful also to Dr. Scott Russell, Greg Strout and Bill Chissoe from the Samuel Roberts Noble Electron Microscopy facility at OU for opening my eyes to the enthralling word of electronic microscopy. Their permanent help, advice and availability have been an important source of inspiration for the late stages of this project.

The experience with the entire carbon nanotube group at OU was wonderful and truly unforgettable. My progress and accomplishments are always associated with their assistance and ideas. I would like to thank in particular Leandro Balzano and Giulio Lolli, for their suggestions and help. Thanks are also due to the faculty at the University of Oklahoma for the knowledge that they have passed along during my studies in Norman, especially to the members of my doctoral committee, I appreciate their time dedicated to reviewing my thesis results.

Finally I would like to deeply thank my parents for their love, for raising me and giving me their care, but most of all for the many sacrifices they have made for my studies as well as so for the strong support and guidance they have provided all these years. I would like to thank also my brothers and my sister for being a constant source of love, motivation and joy through all my life. Last but definitely not least, I thank my husband Jose. His unconditional support, kindness, and love have completely changed my life in the last four years. He has made my life vibrant and fruitful. I truly thank him for everything he has done for me.

TABLE OF CONTENTS

CHAPTER 1 GROWTH OF SINGLE WALLED CARBON NANOTUBES

AND

SILICON NANOWIRES: AN INTRODUCTION TO THE VAPOR-LIQUID-SOLID (VLS) MECHANISM

1.1. GROWTH MECHANISM OF SILICON NANOWIRES	3
1.2. GROWTH MECHANISM OF CARBON NANOTUBES	10

CHAPTER 2 BACKGROUND AND INTRODUCTION TO THE STRUCTURE, SYNTHESIS AND CHARACTERIZATION OF CARBON NANOTUBES AND SILICON NANOWIRES

2.1. INTRODUCTION TO CARBON NANOTUBE STRUCTURE, SYNTHESIS AND CHARACTERIZATION	21
2.1.1 Synthesis of Single-walled carbon nanotubes	25

2.1.1.1. Arc discharge technique	25
2.1.1.2. Laser Ablation technique	27
2.1.1.3. Chemical vapor deposition	29
2.1.2 Structure characterization techniques	32
2.1.2.1. Electron microscopy	33
2.1.2.2. Raman spectroscopy	39
2.1.2.3. Optical Absorption Spectroscopy and Fluorescence	46
2.2. INTRODUCTION TO THE SYNTHESIS AND CHARACTERIZATION OF SILICON NANOWIRES	50
2.2.1. Synthesis of silicon nanowires	51
2.2.1.1. Laser ablation	51
2.2.1.2. Chemical Vapor Deposition (CVD)	54
2.2.1.3. Thermal evaporation	57
2.2.2. Structural characterization techniques	59
2.2.2.1. Electron microscopy	59
2.2.2.2. Raman Spectroscopy	62

CHAPTER 3

TEMPERATURE DEPENDENCE OF THE QUALITY OF SILICON NANOWIRES PRODUCED OVER A TITANIA- SUPPORTED GOLD CATALYST

3.1. INTRODUCTION	73
3.2. EXPERIMENTAL	75
3.3. RESULT AND DISCUSSION	77
3.4. CONCLUSIONS	86

CHAPTER 4

INFLUENCE OF CATALYST SUPPORT ON THE STRUCTURE OF SILICON NANOWIRES SYNTHESIZED BY DECOMPOSITION OF SILANE ON GOLD

4.1. INTRODUCTION	89
4.2. EXPERIMENTAL	91
4.3. RESULT AND DISCUSSION	93
4.4. CONCLUSIONS	108

CHAPTER 5

SYNTHESIS OF SINGLE-WALLED CARBON NANOTUBE BY CATALYTIC DECOMPOSITION OF ETHANOL

5.1. INTRODUCTION	111
5.2. EXPERIMENTAL	113
5.2.1. SWNT production	113
5.2.2. SWNT purification	115
5.3. RESULTS AND DISCUSSION	115
5.3.1. Effect of reaction temperature	115
5.3.2. Effect of carrier gas composition.	120
5.3.3. Effect of Fe/C ratio	122
5.3.4. Purification of SWNTs	125
5.4. CONCLUSIONS	130

CHAPTER 6
SYNTHESIS OF SINGLE-WALLED CARBON NANOTUBE ON
QUARTZ SUBSTRATES USING BIMETALLIC Co-Mo
CATALYSTS

6.1. INTRODUCTION	133
6.2. EXPERIMENTAL	135
6.2.1. Surface preparation	135

6.2.2. SWNT production	136
6.3. RESULT AND DISCUSSION	137
6.3.1. Production of SWNTs	137
6.3.2. Surface analysis of the quartz substrate	153
6.4. CONCLUSION	162

CHAPTER 7

MICROSCOPIC ANALYSIS OF SWNT GROWN ON Co-Mo CATALYSTS SUPPORTED ON A TEM GRID USING CO AND CH₄

7.1. INTRODUCTION	165
7.2. EXPERIMENTAL	167
7.2.1 Model catalyst study	167
7.2.2. Real catalyst study	168
7.3. RESULT AND DISCUSSION	169
7.3.1 Model catalyst study	169
7.3.2 CoMo/SiO ₂ powder catalyst	185
7.4. CONCLUSION	198

LIST OF TABLES

Table 4.1. XPS analysis of silicon nanowires obtained from various catalysts.	100
Table 4.2. The coordination parameters of Au sites obtained from curve fitting of EXAFS.	104
Table 5.1. Quality parameter ($G/(D+G)$) of SWNTs obtained using different carrier gases at 800 and 1000°C.	124
Table 6.1. Binding energies for CoMo impregnated quartz surface after subsequent treatments calcination (calcined), reduction and heat up to 850°C in He (reduced), and reaction with CO (reaction).	155
Table 6.2. XPS fitting results for the chemical state for Co and Mo on the quartz surface after subsequent treatments calcination (calcined), reduction and heat up to 850°C in He (reduced), and reaction with CO (reaction).	156
Table 7.1. Gaussian–Lorentzian fitting obtained on the optical absorption spectra of the carbon deposit obtained over CoMo (2:1)/SiO ₂ using CO and CH ₄ as feed at 750 and 850°C.	194

LIST OF FIGURES

- Figure 1.1.** Idealized drawing of VLS mechanism illustrated for the growth of a silicon crystal. Reprinted from Y. Wu and P. Yang, *J. Am. Chem. Soc.* 123, 3165 (2001) 2
- Figure 1.2.** (A) Laser ablation with energy $h\nu$ of $\text{Si}_{1-x}\text{Fe}_x$ target creates vapor of Si and Fe species. (B) The hot vapor condenses into Fe-Si metal alloy. (C) Nanowires growth begins after the liquid becomes supersaturated. (D) Growth terminates when the nanowire passes out of the hot reaction zone. Reprinted from A.M. Morales, C.M. Lieber, *Science* 279, 208 (1998) 4
- Figure 1.3.** Schematic growth mechanism of silicon crystal by VLS, (a) Liquid droplet on substrate and (b) silicon nanowire growth. Taken from R.S. Wagner, W.C. Ellis, *Appl. Phys. Lett.* 4, 89 (1964). 5
- Figure 1.4.** Phase diagram of the Au-Si system. 6
- Figure 1.5.** SEM images of (a) nucleation of multiple submicron and nanoscale silicon wires from a single gallium droplet and (b) silicon fibers ~900 nm thick, grown from of a liquid gallium pool. Adapted from M. K. Sunkara, a) S. Sharma, R. Miranda, G. Lian, E. C. Dickey, *Appl. Phys. Lett.* 79, 1546 (2001). 7
- Figure 1.6.** (a-e) Proposed growth mechanism for CSRs with stairlike inner structures and (f,g) SEM images of carrot-shaped rods (CSRs) growing in-groups on silicon wafer (f) and inner structure of individual CSR, respectively Adapted from Z. W. Pan, Z. R. Dai, C. Ma, Z.L. Wang., *J. AM. CHEM. SOC.* 124, 1817 (2002). 9
- Figure 1.7.** Model proposed by Baker et al. for the growth of catalytic carbon filament. Reprinted from R. T. K. Baker, M. A. Barber, P. S. Harris, F. S. Feates, R. J. Waite, *J. Catal.* 26, 51 (1996). 11
- Figure 1.8.** Graphic of a growth model for MWNTas proposed by Amelinckx et al. Reprinted from S. Amelinckx, X.B. Zhang, D. Bernaerts, X.F. Zhang, V. Ivanov, J.B. Nagy, *Science* 265, 635 (1994). 12

Figure 1.9. A schematic growth mechanism of a SWNT from a nanoparticle by CVD proposed by Li et al. Adapted from Y. Li, W. Kim, Y. Zhang, M. Rolandi, D. Wang, H. Dai, *J. Phys. Chem. B* 105, 11424 (2001). 13

Figure 1.10. Schematic of SWNT growth mechanism based on the VLS model for SWNT produced from floating catalyst method. Reprinted from F. Rohmund, L.K.L. Falk, E.E.B. Campbell, *AIP Conference Proceedings* 544, 234 (2000). 14

Figure 1.11. Schematic of the growth of SWNT based on the VLS model for SWNT produced by laser ablation. Reprinted from J. Gavillet, A. Loiseau, C. Journet, F. Willaime, F. Ducastelle, J.-C. Charlier, *Phys. Rev. Lett.* 87, 275504 (2001) 16

Figure 2.1. (a) Schematic of a portion of a graphene sheet rolled up to form a SWNT. (b) 2D graphene sheet illustrating lattice vectors a_1 and a_2 , and the roll-up vector $C_h = na_1 + ma_2$. The achiral, limiting cases of $(n, 0)$ and (n, n) armchair are indicated with thick, dashed lines, and the chiral θ angle is measured from the zigzag direction. The light, dashed parallel lines define the unrolled, infinite SWNT. The diagram has been constructed for $(n, m) = (4, 2)$. Reprinted from T. W. Odom, J.L. Huang, C. M. Lieber, *Ann. N.Y. Acad. Sci.* 960, 203 (2002) 23

Figure 2.2. Nanotubes are formed by rolling up a graphene sheet into a cylinder and capping each end with half of a fullerene molecule. Shown here is a $(5, 5)$ armchair nanotube (top), a $(9, 0)$ zigzag nanotube (middle) and a $(10, 5)$ chiral nanotube. The diameter of the nanotubes depends on the values of n and m . Reprinted from M. S. Dresselhaus, G. Dresselhaus, P. C. Eklund, *Science of Fullerenes and Carbon Nanotubes*, Academic Press, San Diego, pp. 756 (1996) 24

Figure 2.3. Schematic drawing of the apparatus for (a) arc discharge method (Reprinted from X. Zhao, et al., *Bull. Res. Inst. Meijo Univ.* 1, 7 (1996)) and (b) laser ablation method (Reprinted from A. Thess, R. Lee, P. Nikolaev, H. Dai, P. Petit, J. Robert, C. Xu, Y. H. Lee, S. G. Kim, A.G. Rinzler, D.T. Colbert, G. E. Scuseria, D. Tománek, J.E. Fischer, R. E. Smalley, *Science* 273, 483 (1996)) 27

Figure 2.4. High resolution images of SWNT (a) Scheme of the observation conditions with the electron beam perpendicular (1) or parallel (2) to the bundle axis; (b) Image of a SWNT bundle. Reprinted from Z. L. Wang, C. Hui, "Electron microscopy of nanotubes", Kluwer academic publishers (2003). 35

Figure 2.5. Selected area electron diffraction patterns of a SWNT bundles produced from CCVD : (a) Experimental pattern; (b) Kinematical simulation for a bundle mixing a total of 31 (16,0) and (11,5) nanotubes. Reprinted from Z. L. Wang, C. Hui, “Electron microscopy of nanotubes”, Kluwer academic publishers (2003).

36

Figure 2.6. SEM images of SWNT grown on flat substrate; (a) vertically aligned SWNT bundles grown on quartz surface (Reprinted from Y. Murakami, S. Chiashi, Y. Miyauchi, M. Hu, M.Ogura, T. Okubo, S. Maruyama, Chem. Phys. Lett. 385 298 (2004)); (b) the cross-network SWNTs on a SiO₂/Si surface fabricated by a two-step growth process (Reprinted from S. Huang, B. Maynor, X. Cai, J. Liu, Adv. Mater. 15, 1651 (2003)); (c) SWNT cylindrical pillars with 150-nm radius, 250-nm pitch, and 1- μ m height (Inset, SEM image of a root of a pillar, scale bar, 50 nm) (Reprinted from K. Hata, D. N. Futaba, K. Mizuno, T. Namai, M. Yumura, S. Iijima, Science 306, 1362 (2004)).

38

Figure 2.7. FT-Raman spectrum of a SWNT samples showing the characteristic first and second order bands as well as the G+RBM combination band. The insets reveal the typical detailed shapes of the RBM and the G-band. Reprinted from A. Kukovecz, Z. Konya, I. Kiricsi, Encyclopedia of Nanoscience and Nanotechnology, edited by H.S. Nalwa, Vol. 9, 923-946 (2004).

41

Figure 2.8. Radial breathing mode resonant Raman spectra of SWNTs grown at 750°C by CO disproportionation over CoMo catalyst. Reprinted from J. E. Herrera, L. Balzano, F. Pompeo and D. E Resasco, J. Nanosci. Nanotech., 3, 133 (2003).

43

Figure 2.9. (a,b) Profiles of the G-band spectra for three semiconducting (a) and three metallic (b) nanotubes. The frequencies for \square G and \square G are indicated in cm⁻¹ for each nanotube along with the corresponding linewidths in parentheses. (c) Dependence on reciprocal nanotube diameter 1/dt of \square G and \square G for both semiconducting nanotube (solid circles) and metallic nanotubes (open circles). Reprinted from A. Jorio, A.G. Souza Filho, G. Dresselhaus, M.S. Dresselhaus, A.K. Swan, M. S. Unlu, B. Goldberg, M.A. Pimenta, J.H. Hafner, C.M. Lieber, R. Saito, Phys. Rev. B, 65, 155412 (2002).

45

Figure 2.10. Schematic of density of electronic states for a single nanotube structure. Solid arrows depict the optical excitation and emission transitions of interest; dashed arrows denote non-radiative relaxation of the electron (in the conduction band) and hole (in the valence band) before emission. Reprinted from S. M. Bachilo, M. S. Strano, C. Kittrell, R.H. Hauge, R.E. Smalley, R. B.

48

Weisman, Science 298, 2361 (2002).

Figure 2.11. Absorption spectra of SWNT in SDS-D2O suspension. The top trace D is typical of tubes prepared in suspension without centrifugation. Trace C is from individual SDS micelle coated nanotubes after addition of PVP. Traces B and A are from samples of individual nanotubes separated and solubilized by SDS micelles. Reprinted from M. J. O'Connell, S. M. Bachilo, C. B. Huffman, V. C. Moore, M. S. Strano, E. H. Haroz, K. L. Rialon, P. J. Boul, W. H. Noon, C.r Kittrell, J. Ma, R. H. Hauge, R. B. Weisman, R. E. Smalley Science 297, 593 (2002). 49

Figure 2.12. Schematic of laser ablation method. The output from a pulsed laser (1) is focused (2) onto a target (3) located within a quartz tube; the reaction temperature is controlled by a tube furnace (4). A cold finger (5) is used to collect the product as it is carried in the gas flow that is introduced (6, left) through a flow controller and exits (6, right) into a pumping system. Reprinted from A.M. Morales, C.M. Lieber, Science 279, 208 (1998). 52

Figure 2.13. (a) TEM images of Si nanowires produced after laser ablating a Si_{0.9}Fe_{0.1} target. The dark spheres with a slightly larger diameter than the wires are solidified catalyst clusters; (b) Diffraction contrast TEM image of a Si nanowire. Reprinted from A.M. Morales, C.M. Lieber, Science 279, 208 (1998). 53

Figure 2.14. Au-Si binary phase diagram. Reprinted from J. HU, T. W. ODOM, C.M. LIEBER, Acc. Chem. Res. 32, 435 (1999). 56

Figure 2.15. TEM image showing two major morphologies of Si nanowires. Reprinted from N. Wang, Y.H. Tang, Y.F. Zhang, C.S. Lee, I. Bello, S.T. Lee, Chem. Phys. Lett. 299, 237 (1999). 58

Figure 2.16. SEM images; (a), (b) a typical SiNWs produced from thermal evaporation on Si substrate (Reprinted from H Pan, S Lim, C Poh, H Sun, XWu, Y Feng, J Lin, Nanotech. 16, 417 (2005)) and (c) other SiNWs morphology obtained from chemical vapor deposition of SiH₄ with molten Ga as catalyst (Z.Pan, S. Dai, D.B. Beach, D.H. Lowndes, Nano Lett. 3, 1279 (2003)). 60

Figure 2.17. (a) A typical TEM image showing general view of morphology of SiNWs (Reprinted from G.W. Zhou, Z. Zhang, Z.G. Bai, S.Q. Feng, D.P. Yu, Appl. Phys. Lett. 73, 677 (1998)) and (b) HRTEM image of SiNW with diameter of 13.2 nm. Reprinted from Y. Wu, Y. Cui, L. Huynh, C. J. Barrelet, D.C. Bell, C. M. Lieber, Nano Lett., 4,433 (2004). 61

Figure 2.18. Raman spectra of (a) crystalline silicon, (b) SiNW with 20 nm diameter, (c) SiNW with 13 nm diameter, and (d) nanowires of SiO₂. Reprinted from R.P. Wang, G.W. Zhou, Y.L. Liu, S.H. Pan, H.Z. Zhang, D.P. Yu, Z. Zhang, Phys. Rev. B, 61, 16827 (2000). 63

Figure 3.1. SEM micrograph of silicon nanowires produced at 500°C over a titania supported gold catalyst. 78

Figure 3.2. TEM micrograph of silicon nanowires produced at 500°C over a titania supported gold catalyst. 79

Figure 3.3. SEM images of different silicon containing products obtained at four different reactions temperatures: (a) 300°C, (b) 400°C, (c) 500°C and (d) 600°C 80

Figure 3.4. Silicon to titanium surface atomic ratio (diamonds) and Si⁰ to Si⁺⁴ surface atomic ratio (squares) as calculated from XPS analysis of the Si2p and Ti2p lines. 81

Figure 3.5. Upper panel: Raman spectra of the silicon nanowires produced at four different temperatures. The Raman spectra of silicon wafer and of the fresh Au/TiO₂ catalyst are also included for comparison. Lower panel: Raman spectra of the silicon nanowires obtained at 500°C using two different 633nm laser powers: 3.0 mW (solid line) and 0.3mW (thick solid line). 83

Figure 4.1. Raman spectra of silicon nanowires synthesized over gold supported on different supports (TiO₂, SiO₂, ZrO₂, and MgO) reduced at 200°C. Au/MgO prepared by impregnation were reduced at 200 and 500°C, denoted as MgO(R200) and MgO (R500), respectively. Au/MgO prepared by CVD method, denoted as MgO (CVD). The solid line shows the band at 520.5 cm⁻¹(bulk crystalline Si), and the dash line show the band at 470 cm⁻¹ (amorphous Si). The bands downshifted to 518 cm⁻¹ indicates the presence of SiNW. 94

Figure 4.2. SEM micrographs of silicon nanowires obtained from 1%Au supported on different supports; a) 1%Au/TiO ₂ , b) 1%Au/SiO ₂ , c) 1%Au/ZrO ₂ , d) 1%Au/MgO (IWI, reduced 200°C), e) 1%Au/MgO (IWI, reduced 500°C), and f) 1%Au/MgO (CVD).	96
Figure 4.3. Diameter distribution of silicon nanowires produced from 1%Au supported on TiO ₂ , SiO ₂ , and ZrO ₂ .	98
Figure 4.4. TEM micrographs of silicon nanowires obtained from 1%Au supported on different supports; a) 1%Au/TiO ₂ , b) 1%Au/SiO ₂ , c) 1%Au/ZrO ₂ , and d) 1%Au/MgO (CVD).	99
Figure 4.5. Au L ³ -edge X-ray absorption spectroscopic comparison of fresh Au supported on different supports (TiO ₂ , SiO ₂ , ZrO ₂ , and MgO) reduced at 200°C. Au/MgO prepared by impregnation were reduced at 200 and 500°C, denoted as MgO(R200) and MgO (R500), respectively. Au/MgO prepared by CVD method, denoted as MgO (CVD). A) Fourier transform of k ³ -weighted and B) XANES analysis.	103
Figure 4.6. TEM micrographs of fresh catalysts; a) 1%Au/TiO ₂ , b) 1%Au/SiO ₂ , c) 1%Au/ZrO ₂ , d) 1%Au/MgO (Reduced 200°C), and e) 1%Au/MgO (Reduced 500°C).	107
Figure 5.1. Schematic of SWNT reaction apparatus.	114
Figure 5.2. a) Raman spectra and b) G/(D+G) ratio of products obtained at different reaction temperature.	117
Figure 5.3. TEM images of products obtained at a) 800°C, b) 1000°C, and c) 1100°C	118
Figure 5.4. Raman spectra of products obtained at (A) 1000°C and (B) 800°C using different carrier gas mixture.	123
Figure 5.5. Raman spectra of SWNTs obtained from Fe/C ratio of a) 0.001 and b) 0.0005.	125

Figure 5.6. TEM images of SWNTs produced at 1000oC using solution with Fe/C ratio of (a) 0.0005 and (b) 0.001.	126
Figure 5.7. Raman spectra of as-prepared SWNTs compared with the sample after purification.	128
Figure 5.8. (a) and (b) TEM images of purified SWNTs at low and high magnification, respectively.	129
Figure 6.1. Raman spectra of products obtained on smooth quartz surfaces after reaction with CO and ethanol at 850°C (Laser excitation source of 632 nm).	138
Figure 6.2. (a) and (b) SEM images obtained on smooth quartz surfaces after reaction with CO (a) and ethanol (b). TEM images of product obtained on the smooth quartz surface after reaction with ethanol (c).	139
Figure 6.3. Raman spectra of products obtained over a) smooth quartz surface and b) scratched quartz surface after reaction with CO at 850°C.	141
Figure 6.4. SEM images obtained on smooth quartz surfaces (a and b) and scratched quartz surfaces (c and d) after reaction with CO at 850°C.	142
Figure 6.5. Raman spectra of products obtained on quartz surfaces after reaction with ethanol at 850°C using different carrier gases: a) smooth quartz surface with He as carrier gas, b) smooth quartz surface with H ₂ as carrier gas, and c) scratched quartz surface with H ₂ as carrier gas.	144
Figure 6.6. (Upper) Raman spectra of products obtained after reaction with ethanol at 850oC using mixtures of He and H ₂ gas as carrier with different He:H ₂ ratio: (a) pure H ₂ , (b) 1:1, (c) 1:2, (d) 1:3, and (e) 1:5. (Lower) Quality parameter (G/(D+G)) calculated from Raman spectra obtained using different laser energy.	148
Figure 6.7. Diameter distribution of SWNT products obtained after reaction with ethanol at 850°C using mixtures of He and H ₂ gas as carrier with different He:H ₂ ratios: (a) pure H ₂ , (b) 1:1, (c) 1:2, (d) 1:3, and (e) 1:5.	149

Figure 6.8. SEM images of the products obtained after reaction with ethanol at 850°C using a mixture of He and H₂ gas as carrier with different He:H₂ ratios: (a) pure H₂, (b) 1:1, (c) 1:2, and (d) 1:3. 151

Figure 6.9. Atomic percentages of Co and Mo of CoMo impregnated on quartz surface after calcination at 400°C (Calcined), reduction at 500°C and heat up to 850°C in He (Reduced), and reaction with CO at 850°C (Reaction) as obtained for XPS analysis. 160

Figure 6.10. Co/Mo and Co/Si ratio calculated from XPS analysis for CoMo impregnated on quartz surface after calcination at 400°C (Calcined), reduction at 500°C and heat up to 850°C in He (Reduced), and reaction with CO at 850°C (Reaction). 161

Figure 7.1. (a) Raman spectra of CoMo over silicon monoxide coated grid after two subsequent treatments; calcination at 500°C, reduction at 500°C and heating in He 850°C. Raman spectra of CoMoO₄ and MoO₂ are also shown. (b) SEM and (c) TEM images of CoMo over silicon monoxide coated grid after pretreatment to 850°C. 171

Figure 7.2. Raman spectra, SEM and TEM images obtained on a CoMo catalyst prepared over a silicon monoxide coated grid after reaction with CO for 1, 3, and 10 minutes. 173

Figure 7.3. TEM images of a metal particle of a CoMo 2:1 catalyst obtained over a silicon monoxide grid after expose to CO for 10 minutes at 850°C. 177

Figure 7.4. Raman spectra, SEM and TEM images obtained on a CoMo catalyst prepared over a silicon monoxide coated grid after reaction with CH₄ for 1, 3, and 10 minutes. 179

Figure 7.5. TEM images of (A) metal particles obtained on a CoMo 2:1 catalyst prepared over a silicon monoxide coated grid after reaction with CH₄ for 3 minutes and (B) the high magnification image of the circle area in (A). 181

Figure 7.6. Raman spectra of the products obtained over (a) CoMo (1:3)/SiO₂ powder catalyst using CO and CH₄ at 750°C and (b) CoMo (2:1)/SiO₂ powder catalyst using CO and CH₄ at 750°C and 850°C. 187

Figure 7.7. (a) contribution of the D band to the Raman spectra and (b) amount of carbon deposited from products obtained using CO and CH₄ as feed at 750 and 850°C. 189

Figure 7.8. TEM images of SWNTs obtained over CoMo (2:1)/SiO₂ powder catalysts using (a) CH₄ at 850°C, (b) CO at 850°C, (c) CH₄ at 750°C, and (d) CO at 750°C. 190

Figure 7.9. Optical absorption spectra of nanotubes produced various conditions; (a) CoMo (1:3)/SiO₂, CO 750°C, (b) CoMo (2:1)/SiO₂, CO 750°C, (c) CoMo (2:1)/SiO₂, CO 850°C, (d) CoMo (2:1)/SiO₂, CH₄ 750°C, and (e) CoMo (2:1)/SiO₂, CH₄ 850°C 192

Figure 7.10. XRD analysis of CoMo (1:3)/SiO₂ and CoMo (2:1)/SiO₂ powder catalyst after calcination and reduction in H₂ at 500°C 195

ABSTRACT

The discovery of carbon nanotubes and semiconductor nanowires has initiated an exploding research field in which enormous efforts have been invested due to their fundamental significance to the study of size- and dimensionality-dependent chemical and physical properties. Extensive research work is now focused on the study of the processes that occur during synthesis of these materials since they are key essentials needed to establish a method that provides large quantities of nanotubes and nanowires with well-determined and reproducible characteristics. A clear understanding of their formation mechanism is therefore a key issue for the development of further advances in this topic.

This thesis is focused on the study of the processes that take place on the catalytic particle during the growth of SWNT and SiNW using VSL processes over a cobalt molybdate and gold supported catalyst respectively. A series of analytical techniques have been employed to characterize the structure of the materials obtained and to appraise the physicochemical state of the catalytic particle. The state of Co and Mo has been investigated using laser Raman spectroscopy, X-ray photoelectron spectroscopy and Transmission electron microscopy. The chemical state of gold was studied using extended X-ray absorption fine structure spectroscopy, X-ray absorption near-edge spectroscopy, ultraviolet-visible diffuse reflectance spectroscopy and X-ray photoelectron spectroscopy. In a similar way, the SWNT and SiNW materials have been characterized using laser Raman spectroscopy, transmission electron microscopy, temperature programmed oxidation, scanning electron microscopy and optical absorption spectroscopy. The information obtained revealed that in for both SiNW and SWNT different synthesis conditions result in regimes in which different controlling rate-limiting steps determine the quantity and quality of the products obtained.

To get a deeper insight onto the kinetics of SWNT growth a detailed electron microscopy study was performed. By using a model system based on silica coated TEM grids as substrate, SWNT were grown under similar reaction condition as in the commercial CoMoCat® process. The observations from the model system showed that CO and CH₄ have different reactivity towards the cobalt molybdate catalytic particles species. Phase separation process of the pre-reduced cobalt molybdate species was observed when CO was used as feed. However, in the case of CH₄ a complex alloy seems to be formed on the pre-reduced cobalt molybdate before the growth of SWNTs starts, in this case a phase separation process was not observed. These phenomena were used to explain the differences in behavior of real powder catalysts under different reaction conditions reported on previous literature. Moreover it is demonstrated how this processes affect nanotube quality, carbon yield and the chiral distribution of nanotubes structures. Indeed the (n,m) population distribution of single-walled carbon nanotubes can be controlled by varying the gaseous feed composition and the reaction temperature. The clearly different distributions obtained when varying reaction conditions demonstrate that the (n,m) distribution is a result of differences in the growth kinetics, which in turn depends on the nanotube cap-metal cluster interaction.

CHAPTER 1

GROWTH OF SINGLE WALLED CARBON NANOTUBES AND SILICON NANOWIRES: AN INTRODUCTION TO THE VAPOR- LIQUID-SOLID (VLS) MECHANISM

The discovery of carbon nanotubes and semiconductor nanowires has initiated an exploding research field in which enormous efforts have been invested due to their fundamental significance to the study of size- and dimensionality-dependent chemical and physical properties (1-3). There are many synthetic mechanisms to produce Single walled carbon nanotubes (SWNT) and nanowires, among which vapor–liquid–solid (VLS) mechanism is the most extensively explored case where metal particles are employed as catalysts and generally an alloy droplet presents on the growth tip of each nanowire.

Indeed, the Vapor-Liquid-Solid (VLS) mechanism has been studied since 1960s on the basis of its innovation as a crystal growth phenomenon (4). Although the physics behind these phenomena was not clearly understood at that time many researchers used this mechanism to explain the growth of silicon or carbon whiskers. As aforementioned, the vapor liquid mechanism has been revived inside the framework of nanotube (5 - 7) and nanowire synthesis (4,8-19). The proposed growth mechanism

(Fig.1.1) involves the absorption of source material from the gas phase into a liquid droplet of catalyst. Upon supersaturation of the liquid alloy, crystal growth occurs by precipitation at the solid-liquid interface. This seed serves as a preferred site for further deposition of material at the interface of the liquid droplet, promoting the elongation of the seed into a nanowire or whisker, and suppressing further nucleation events on the same catalyst. Since the liquid droplet catalyzes the incorporation of material from the gas source to the growing crystal, the deposit grows anisotropically as a whisker whose diameter is dictated by the diameter of the liquid alloy droplet. In because of this concept in which vapor, liquid, and solid phases are involved, that this method is called the vapor-liquid-solid (VLS) mechanism for crystal growth (4,20,21). Recently electron microscopy studies have confirmed the presence of this three step model; real-time observations of Ge nanowire growth at high-temperature by situ transmission electron microscopy (22) clearly shows that there are three growth stages: formation of a Au-Ge alloy, nucleation of the Ge nanocrystal, and elongation of the Ge nanowire.

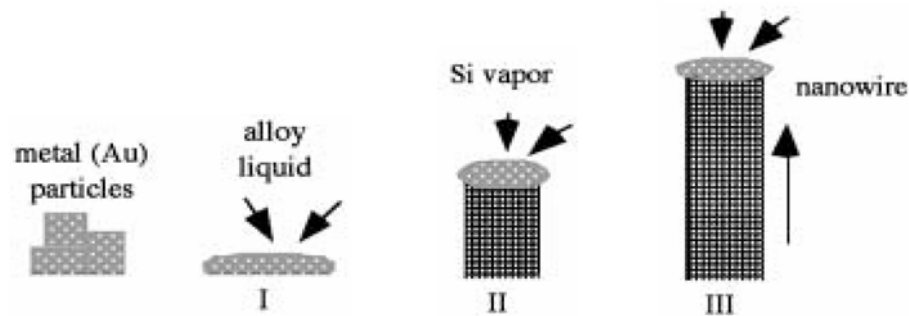


Figure 1.1 Idealized drawing of VLS mechanism illustrated for the growth of a silicon crystal (22).

An important feature in the VLS model is that it readily provides the intellectual underpinning needed for the prediction of good catalysts and synthesis conditions. First, equilibrium phase diagrams are used to choose a catalyst that can form a liquid alloy with the nanowire material of interest. The phase diagram is then used to choose a specific composition (catalyst: nanowire material) and synthesis temperature so that there is a coexistence of liquid alloy and solid nanowire material. By understanding these features optimal reaction conditions can be selected. For example, the Fe-Si phase diagram tells us that there is a broad area above 1200°C in the Si-rich region where $\text{FeSi}_x(\text{l})$ and $\text{Si}(\text{s})$ coexist. Therefore, Si nanowire synthesis can be achieved by laser ablation of a silicon rich target ($\text{Si}_{0.9}\text{Fe}_{0.1}$) at temperatures above 1200 °C (23).

There are copious examples on the literature on the application of the VLS mechanism to explain the growth of single walled carbon nanotubes (SWNT) and silicon nanowires (SiNW). A summary of various papers and reviews are discussed in the following sections and serve as an introduction for the present work.

1.1. GROWTH MECHANISM OF SILICON NANOWIRES

For the catalytic approach of silicon nanowire synthesis (i.e., laser ablation and chemical vapor deposition), the Vapor-Liquid-Solid (VLS) mechanism is the most accepted models used to explain the nanowire growth. Figure 1.2 shows the growth mechanism for silicon nanowires produced by laser ablation. In this particular case a Si_{1-x}

Fe_x target was laser-ablated to produce a vapor of Si and Fe that rapidly condense into Si-rich liquid nanocluster (Fig. 1.2B). When the liquid alloy becomes supersaturated the silicon phase precipitates and it crystallizes as nanowires (Fig 1.2C). The growth continues as long as the Fe-Si alloy remain in a liquid state and the Si reactant is available (5).

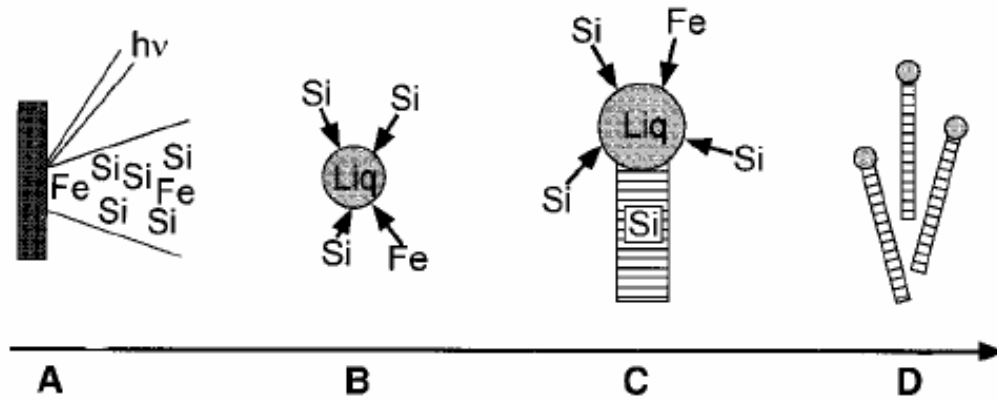


Figure 1.2 (A) Laser ablation with energy $h\nu$ of $\text{Si}_{1-x}\text{Fe}_x$ target creates vapor of Si and Fe species. (B) The hot vapor condenses into Fe-Si metal alloy. (C) Nanowires growth begins after the liquid becomes supersaturated. (D) Growth terminates when the nanowire passes out of the hot reaction zone (5).

For the case of chemical vapor deposition, the silicon containing feed is decomposed first to generate the reactant species in the vapor phase; this process is illustrated in Figure 1.3. Similarly, the Si species then form a liquid alloy with the metal catalyst, which in this particular case are Au nanoparticles. The Au-Si liquid alloy has been proposed to be the preferred site for Si deposition from the vapor, this deposition causes the liquid drop to become supersaturated with Si (4). The nanowire would grow

by precipitation of Si out of the droplet at the interface between solid Si and the liquid alloy. The growth continues until the growth conditions are changed (21). These phenomena can also be rationalized in terms of the phase diagram of the Au-Si system. As shown in Figure 1.4, as silicon is generated by decomposition of the silicon containing feed at temperature T_L , it is incorporated to the metallic gold particle until a Au-Si liquid alloy of composition C_1 is formed. As the supply of the silicon feed continues, the silicon concentration increase and the saturation point at C_2 is reached. A further increase in the silicon content of the liquid droplet results in supersaturation and silicon precipitation occurs. After precipitation the liquid composition will again become close to the equilibrium value (C_2) and the crystal growth will proceed following the same cycle (21).

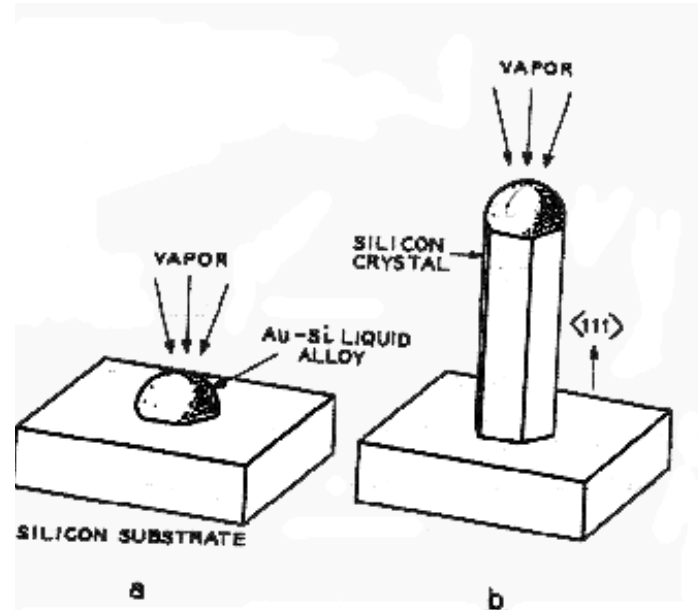


Figure 1.3 Schematic growth mechanism of silicon crystal by VLS, (a) Liquid droplet on substrate and (b) silicon nanowire growth (4).

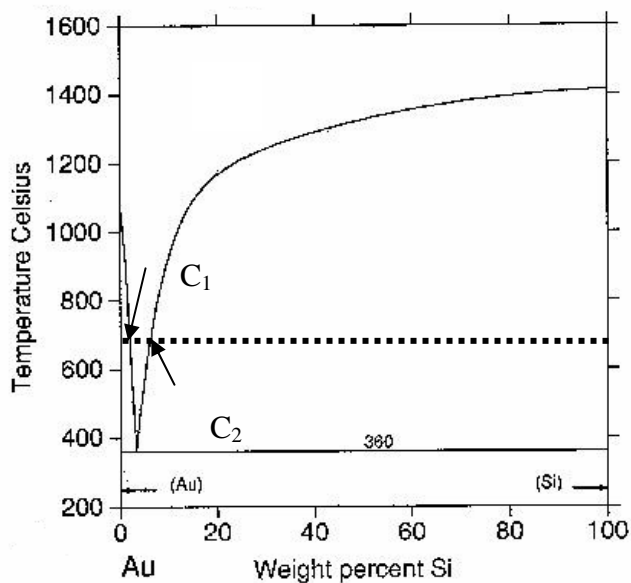


Figure 1.4 Phase diagram of the Au-Si system.

Sunkara *et al.* (24 - 27) reported a low-temperature non catalytic vapor-liquid-solid synthesis method. They synthesized silicon nanowires with uniform diameters distributed around 6 nm using gallium as the molten solvent, at temperatures less than 400°C in hydrogen plasma. Gallium forms a eutectic with silicon at extremely low temperature (29.8°C) and low concentration, which offers a wide temperature range for bulk synthesis of nanowires and also offering a potential method for bulk synthesis of silicon nanowires at temperatures significantly lower than 400°C. In this case, because of low miscibility and the high surface tension in the Ga-Si system, this system allows nanowire nucleation and growth from larger sized gallium droplets (Fig 1.5a), eliminating the need for nanometer sized liquid metal droplets to control the size of the

nanowire as in a typical VLS method. As a consequence, the size distribution of the resulting nanowires from an individual pool of gallium was uniform (Fig 1.5b). The diameter of these nanowires depends upon the concentration of Si at supersaturation in the Ga–Si liquid alloy, which then controls the crystallization rate and diameter distribution. However, the Si concentration at supersaturation in liquid gallium depends also on several variables such as substrate temperature, gas-phase composition, and plasma kinetics. These factors allow control of the size and size distribution of nanowires and eliminate the problems associated with the creation of nano-sized droplets.

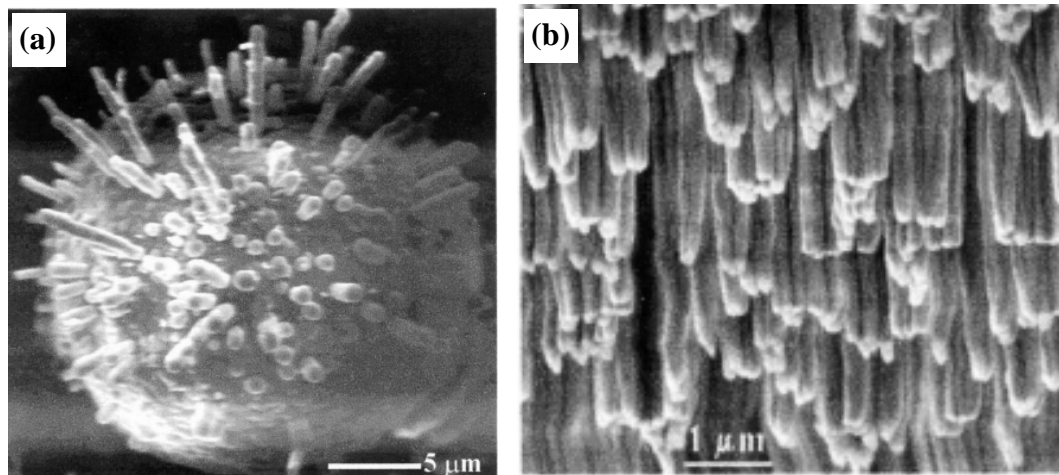


Figure 1.5 SEM images of (a) nucleation of multiple submicron and nanoscale silicon wires from a single gallium droplet and (b) silicon fibers ~900 nm thick, grown from of a liquid gallium pool (24).

Pan *et al.* (28) also reported gallium-catalyzed VLS growth of carrot-shaped rods (CSRs) of silicon over silicon wafers. The walls of these CSR are composed of highly aligned silica nanowires with diameters of 15-30 nm and length of 10-40 μm . In

this method, thermal decomposition of GaN powders was used to get the desirable Ga droplets with diameters of 5-50 μm . The proposed growth model for CSRs with stair-like inner structures is shown in Figure 1.6. First, the decomposition of GaN powders produces gallium vapor that rapidly condenses into liquid Ga clusters. These clusters then deposit onto the surface of the silicon wafer and grow into small gallium spheres as the upcoming Ga clusters are absorbed from the vapor (Fig. 1.6a). These hot liquid Ga spheres etch the silicon wafer to form a Ga-Si alloy. Silicon in the Ga-Si alloy evaporates into the gas to create a dense vapor of Si species around the silicon wafer region (Fig. 1.6b). At this stage, the vapor consists of Ga, O, and Si, and thus, the Ga sphere can also absorb Si species from the vapor. When the concentrations of Si and O in the gallium phase are high enough, silicon and oxygen react to form many SiO_2 nanoparticles on the surface of the lower hemisphere of the Ga sphere. These particles act as the nucleation sites, initiating the growth of the first batch (batch I) of the SiO_2 nanowires (Fig. 1.6c). The Ga sphere is then pushed away from the silicon wafer by the growing SiO_2 nanowires. From this stage, the gallium phase can only absorb Si species from the vapor since the gallium sphere is not in contact with the silicon wafer anymore. As this first batch of nanowires proceeds to grow, a second batch (batch II) of nanowires simultaneously nucleates and grows at nearly the same rate and direction above the first. As growth continues, the newly formed nanowires begin to exert a force on the batch below. When the force is great enough, the second batch of nanowires will lift the Ga sphere upward again, thereby detaching the first batch of nanowires from the Ga sphere and halting their growth (Fig. 1.6d). Since the Ga sphere is in the liquid state and the

nanowires connect to it though a thin oxide layer, the second batch of nanowires will then sink to the position the first batch initially occupied. A third batch (batch III) of nanowires then nucleates and grows above the second. The process of growth and detachment allows the formation of a tubular structure with a regular stair-like inner wall (Fig. 1.6e). For this case, the nanowires only grow from a band around the lower hemisphere surface of the Ga sphere.

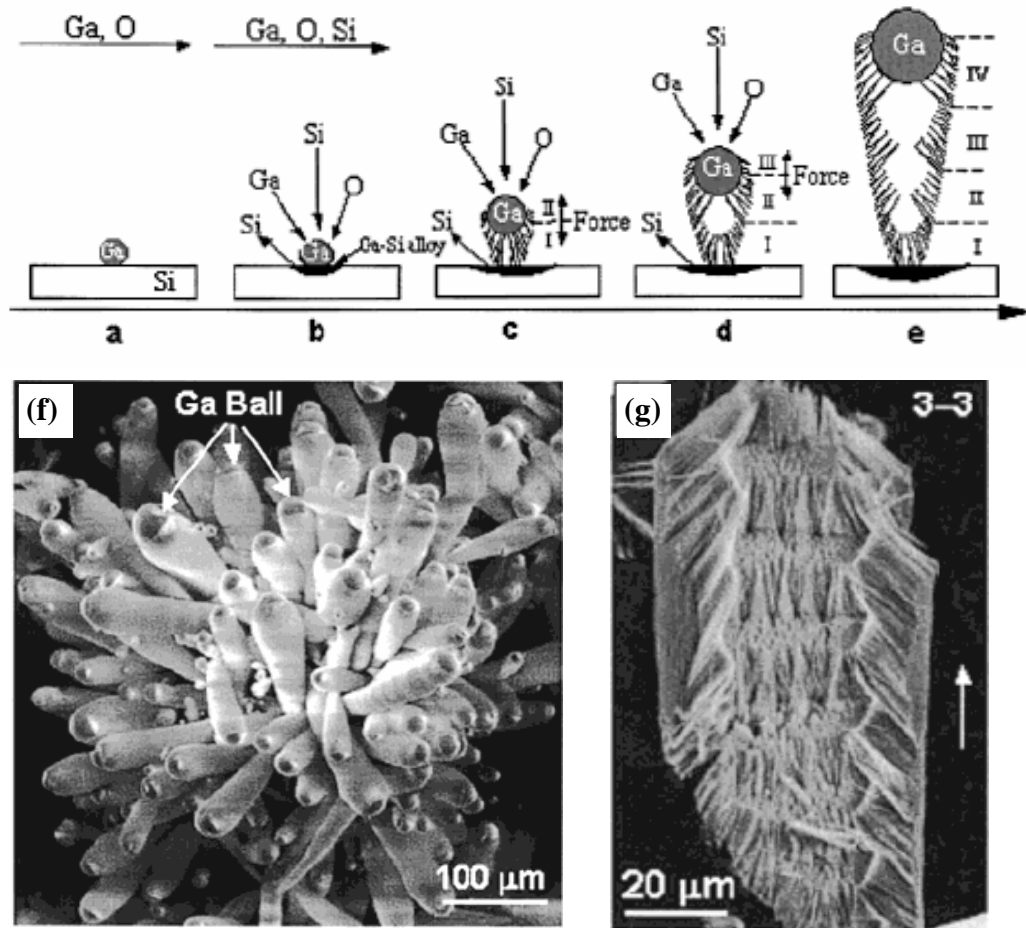


Figure 1.6 (a-e) Proposed growth mechanism for CSRs with stairlike inner structures and (f,g) SEM images of carrot-shaped rods (CSRs) growing in-groups on silicon wafer (f) and inner structure of individual CSR, respectively (28).

1.2. GROWTH MECHANISM OF CARBON NANOTUBES

Most of the detailed insights into the mechanism of filament growth has come from the skilful application of controlled atmosphere electron microscopy (CAEM) by Baker et al. since 1972 (29). This mechanism may be regarded as a realistic description even for the formation of carbon nanotubes. The proposed mechanism is illustrated in Figure 1.7. In short, it is suggested that the first step involves the decomposition of the hydrocarbon on the metal surfaces, producing hydrogen and carbon, which then dissolves in the metal. Upon the decomposition of hydrocarbon, a thermal gradient setups along the particle. The dissolved carbon then moves to the cooler part of the metal particle and leave the metal from there. The carbon moved from the metal initiates then the growth of carbon fibers and/or nanotubes.

Based on the interaction between metal particles and the support material, this proposed mechanism has been classified into two. When there is a weak interaction between the metal particles and the support the growing tube pushes the catalytic metal particles away from the support surface into the gas phase and as consequence carbon fibers with metal particles in their tips are formed. When the interaction between metal and support is strong, metal particles remain bonded to the surface and the filament grows from these metal islands. In both cases, there are free surfaces exposed to the gas phase which are not covered by carbon fibers or tubes. These two different menchanism are called “tip growth” and “base growth” depending on whether the filament pushes the

metal particle away from the support or not, these two mechanisms are frequently used to explain the growth process of carbon nanotubes. Moreover, Baker has proposed that during the growth process of the carbon filament, the metal must have liquid-like properties. This clearly indicates the similarities between this growth mechanism and the vapor-liquid-solid (VLS) mechanism for the growth of whiskers using catalysts.

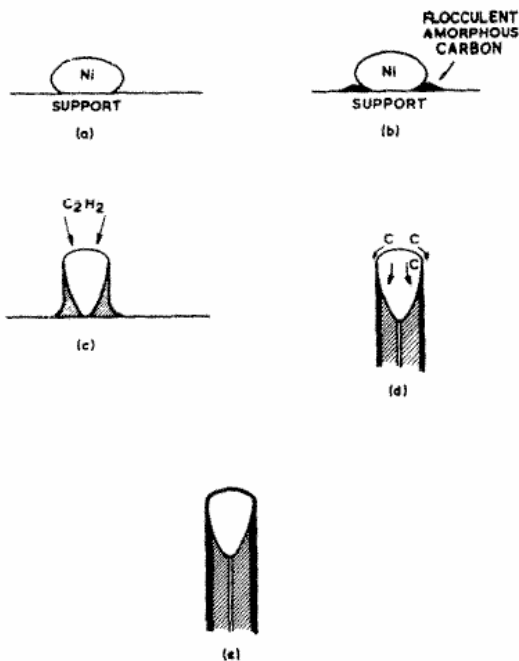


Figure 1.7 Model proposed by Baker et al. for the growth of catalytic carbon filament (29).

For nanotube growth similar mechanisms have been proposed, with the “tip-growth” mechanism well demonstrated for some multiwalled carbon nanotubes (MWNT) growth processes (30) while the “base-growth” mechanism has been proposed to explain

MWNT (31) and SWNTs (17) growth. Figure 1.8 shows one of the growth models for MWNT as described by Amelinckx *et al.* (30). In the first stage, the particle is lifted by the growing tubule, with carbon deposited at the annular contact with the particle and at the bottom contact with the support (Fig 1.8A-D). After the particle is captured within the tube, further growth may presumably continue by the extrusion through the base, while diffusion occurs along the graphite surface (Fig 1.8E-H).

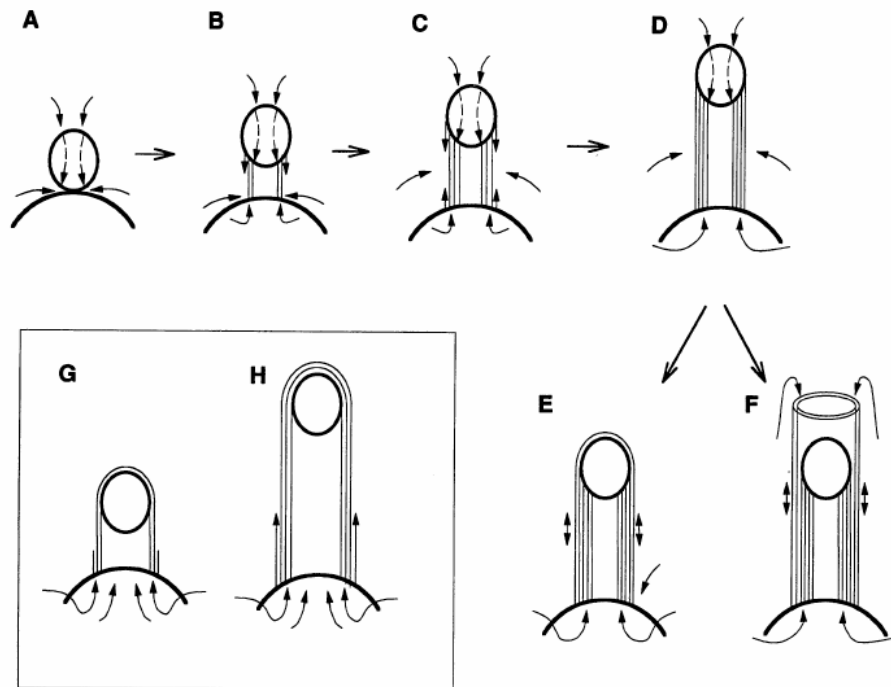


Figure 1.8 Graphic of a growth model for MWNTas proposed by Amelinckx *et al.* (30)

In a similar study, Li *et al.* (17) followed the growth of individual SWNT from a catalyst nanoparticle using TEM. They proposed that the process of SWNTs in their CVD process is well described by the base-growth model as shown in Figure 1.9.

This model is also similar to the model suggested by Baker et al. for filamentous carbon. At the early stages of the CVD reaction, carbon atoms catalytically decomposed from methane are absorbed into the metallic nanoparticle anchored on the support substrate, forming a carbon–metal solid-state solution in the particle. Once a super-saturation point

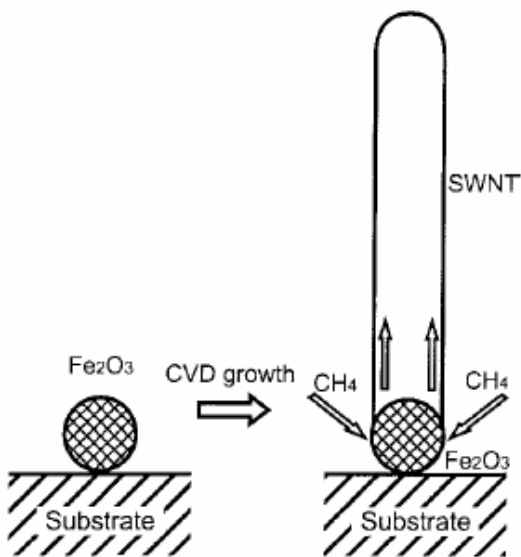


Figure 1.9 A schematic growth mechanism of a SWNT from a nanoparticle by CVD proposed by Li *et al.* (17).

is reached, carbon precipitates out from the particle surface. If the carbon supply to the nanoparticle continues, continued carbon precipitation occurs and leads to the growth of a single-walled nanotube. The growth terminates when the carbon supply to the nanoparticle becomes insufficient, leading to the formation of a nanotubes with finite length. The cause of carbon-supply shortage to a given nanoparticle during growth might be consequence of catalyst poisoning effects, which could inactivate the interface and cut

off the carbon supply to the particle. These poisoning effects may be due to amorphous-carbon deposition on the nanoparticle, or undesired changes in particle–support interactions during growth.

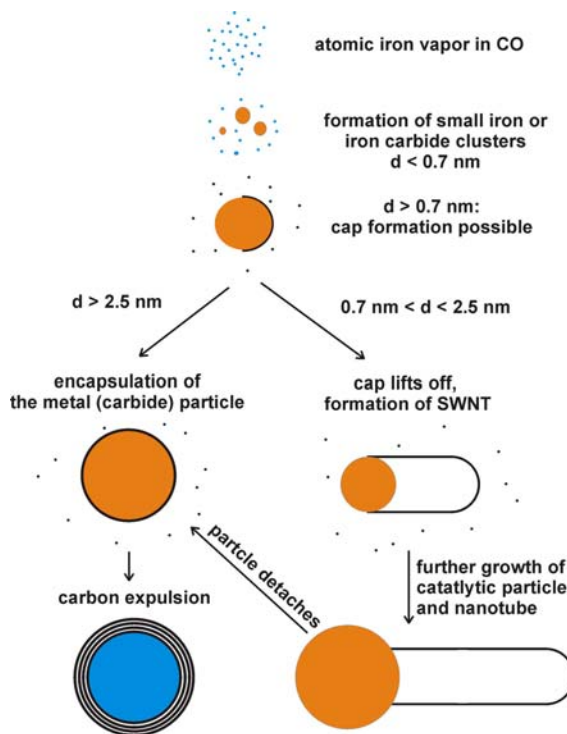


Figure 1.10 Schematic of SWNT growth mechanism based on the VLS model for SWNT produced from floating catalyst method (19).

An analogous growth mechanism for SWNT produced from a floating catalyst process is described in Figure 1.10. In this case iron nanoparticles catalyze the growth of SWNT in the gas phase using CO and $\text{Fe}(\text{CO})_5$ (19). The decomposition of $\text{Fe}(\text{CO})_5$ leads to the formation of small iron clusters, which provide the catalytic sites for the nanotube growth via the Boudouard reaction. It was proposed that after carbon forms and alloy

with the iron clusters the nucleation of a SWNT occurs if the particle size is in the 0.7-2.5 nm range. On the contrary, when the metal particle is larger than 2.5 nm, encapsulation of the metal alloy occurs. This proposed mechanism was suggested for SWNTs grown from individual metal particles.

Similarly, Gavillet *et al.* (6) have reported a similar growth mechanism of SWNT to explain the case in which carbon precipitates from particles larger than the tube diameter. However, in this case, the observations indicate that the whole bundle of SWNT was nucleated from a carbon-supersaturated catalyst particle. The schematics for this growth mechanism are illustrated in Figure 1.11. In this case the materials were produced either by laser ablation or arc discharge. The first step of the process is the formation of a liquid nanoparticle of metal supersaturated with carbon (Fig. 1.11a). These nanoparticles originate from plasma/vapor condensation in the moderate temperature zone of the arc discharge or laser ablation chamber. The supersaturation is generated by decomposition and absorption of carbonaceous structures on the surface of the nanoparticles (32,33). During the cooling, the carbon atoms are segregated at the surface because the solubility limit of carbon decreases. At this point, the carbon-metal alloy is either encapsulated by a graphene sheet (Figure 1.11b) or the precipitated carbon forms small caps of SWNT (Figure 1.11c) (17,34,35). After the nanotube caps nucleate, the growth continued via carbon incorporation into the metal alloy. The growth continues until the temperature is close to the eutectic temperature and as this temperature is reached the nanoparticles start to solidify. In some cases, the nanoparticles

can be embedded in amorphous carbon (Figure 1.11e) or in graphitic layers (Figure 1.11f) because of a limited carbon supply to the incipient nanotube structure.

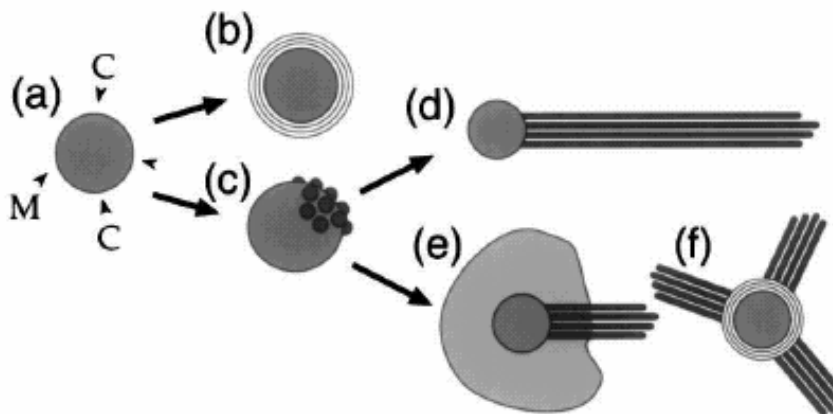


Figure 1.11 Schematic of the growth of SWNT based on the VLS model for SWNT produced by laser ablation (6).

Besides floating catalyst methods, laser ablation and arc discharge process, decomposition of carbon containing molecules over solid catalysts have been successfully used to grow SWNT as well. Among these, bimetallic catalyst systems are nowadays used for controlled SWNT synthesis. Resasco et al. (36-39) have proposed a growth model for SWNT over bimetallic Co-Mo catalysts supported on SiO_2 . Interestingly, the catalyst is only effective when both metals are simultaneously present and a low Co:Mo ratio is used. To explain this observation the authors claimed that cobalt is stabilized by molybdenum in an oxidized form in a chemical environment similar to the one of cobalt in CoMoO_4 , this interaction being stable even at high temperatures. Only when CO is in contact with the catalyst, the CoMoO_4 species are converted to an unstable CoMo carbide; Co is no longer stabilized in this new matrix and

starts migrating towards the surface where it gets reduced in the form of very small Co metallic clusters which trigger SWNT growth. A similar explanation was proposed by Murakami *et al.* (40) for the growth of vertically aligned SWNT on quartz surface using a Co-Mo bimetallic catalyst as well. Based on XPS observations, they proposed that nanoparticles oxide species composed of CoO, MoO₃, and CoMoO_x are present on the catalyst before reaction. Under reaction condition, the strong interactions between Co and CoMoO_x underlayers help preventing these well-dispersed nano-sized catalyst particles against agglomeration, leading to the formation of metallic cobalt nanoparticles which would catalyze SWNT growth

A similar concept was also used by Pierre *et al.* (41,42) as well; in this case pristine metal nanoparticles are formed in situ at a temperature high enough for them to catalyze the decomposition of CH₄ and the subsequent formation of SWNTs and DWNTs (double walled carbon nanotubes). In this method, Mg_{0.90}Fe_xCo_yO (x+y =1) solid solutions were synthesized by the ureic combustion route. The presence of Co²⁺ ions hinders the dissolution of iron in the MgO lattice and favors the formation of MgFe₂O₄-like particles in the oxide powder, which tends to alloy with cobalt upon reduction forming iron-rich α -Fe/Co particles with a size and composition (around Fe_{0.50}Co_{0.50}) adequate for nanotube formation.

From all the proposed growth mechanisms mentioned above, it is obvious that the size of the metal particles plays a vital role in the production of carbon nanotubes.

Catalyst with well dispersed and stable nano-sized metal particles are clearly needed in the production of SWNTs by the CVD method; moreover these nano-sized metal particles determine the diameter of SWNTs. On the other hand, in the case of arc-discharge and laser-ablation techniques, the diameter of SWNTs does not essentially depend on the size of the metal particles since the bundle of SWNTs seems to emerge from metal particles larger than the tube diameter.

REFERENCES

- 1 S. Iijima, Nature 354, 56 (1991)
- 2 J. Hu, T.W. Odom, C.M. Lieber, Acc. Chem. Res. 32, 435 (1999)
- 3 S.M. Prokes, K. Wang, Mater. Res. Soc. Bull. 24, 13 (1999)
- 4 R.S. Wagner, W.C. Ellis, Appl. Phys. Lett. 4, 89 (1964)
- 5 A.M. Morales, C.M. Lieber, Science 279, 208 (1998)
- 6 J. Gavillet, A. Loiseau, C. Journet, F. Willaime, F. Ducastelle, J.-C. Charlier, Phys. Rev. Lett. 87, 275504 (2001)
- 7 M. Yudasaka, Y. Kasuya, M. Takizawa, S. Bandow, K. Takahashi, F. Kokai, S. Iijima, AIP Conference Proceedings 544, 217 (2000)
- 8 Y. Zhang, Q. Zhang, N. Wang, Y. Yan, H. Zhou, J. Zhu, J. Cryst. Growth 226, 185 (2001)
- 9 J. Westwater, D.P. Gosain, S. Tomiya, S. Usui, J. Vac. Sci. Technol. B 15, 554 (1997)
- 10 J. Westwater, D.P. Gosain, S. Usui, Phys. Stat. Sol. 165, 37 (1998)
- 11 N. Ozaki, Y. Ohno, S. Takeda, Appl. Phys. Lett., 73, 3700 (1998).

- 12 Y. Cui, L.J. Lauhon, M.S. Gudiksen, J. Wang, C.M. Lieber, *Appl. Phys. Lett.* 78, 2214 (2001)
- 13 Z.Q. Liu, S.S. Xie, W.Y. Zhou, L.F. Sun, Y.B. Li, D.S. Tang, X.P. Zou, C.Y. Wang, G. Wang, *J. Cryst. Growth* 224, 230 (2001)
- 14 J. Niu, J. Sha, X. Ma, J. Xu, D. Yang, *Chem. Phys. Lett.* 367, 528 (2003)
- 15 Z.Q. Liu, W.Y. Zhou, L.F. Sun, D.S. Tang, X.P. Zou, Y.B. Li, C.Y. Wang, G.Wang, S.S. Xie, *Chem. Phys. Lett.* 341, 523 (2001)
- 16 H. Dai, A.G. Rinzler, P. Nikolaev, A.Thess, D.T. Colbert, R.E. Smalley, *Chem. Phys. Lett.* 26, 471 (1996)
- 17 Y. Li, W. Kim, Y. Zhang, M. Rolandi, D. Wang, H. Dai, *J. Phys. Chem. B* 105, 11424 (2001)
- 18 H. Kanzow, A. Ding, *Phys. Rev. B* 60, 11180 (1999)
- 19 F. Rohmund, L.K.L. Falk, E.E.B. Campbell, *AIP Conference Proceedings* 544, 234 (2000)
- 20 R.S. Wagner, W.C. Ellis, *Trans. Met. Soc. AIME*, 233, 1053 (1965)
- 21 R. S. Wagner, in *Whisker Technology*, edited by A. P. Levitt (Wiley-Interscience, New York, 1970), pp. 47-119.
- 22 Y. Wu and P. Yang, *J. Am. Chem. Soc.* 123, 3165 (2001)
- 23 J. Hu, T. W. Odom, C. M. Lieber, *Acc. Chem. Res.*, 32, 435 (1999)
- 24 M. K. Sunkara,a) S. Sharma, R. Miranda, G. Lian, E. C. Dickey, *Appl. Phys. Lett.* 79,1546 (2001)
- 25 S. Sharma, M.K. Sunkara, G.Lian, *Proc. 2002 Annual AIChE Meeting at Indianapolis*, 16 (2002)
- 26 S. Sharma, M.K. Sunkara, G. Lian, E.C. Dickey, *Mat. Res. Soc. Symp. Proc.* 703, 123 (2002)
- 27 S. Sharma, M.K. Sunkara, *Nanotechnology* 15, 130 (2004)

- 28 Z. W. Pan, Z. R. Dai, C. Ma, Z.L. Wang., J. AM. CHEM. SOC. 124, 1817 (2002)
- 29 R. T. K. Baker, M. A. Barber, P. S. Harris, F. S. Feates, R. J. Waite, J. Catal. 26, 51 (1996)
- 30 S. Amelinckx, X.B. Zhang, D. Bernaerts, X.F. Zhang, V. Ivanov, J.B. Nagy, Science 265, 635 (1994)
- 31 S. Fan, M. G. Chapline, N. R. Franklin, T. W. Tomblor, A. M. Cassell, H. Dai, Science, 283, 512 (1999)
- 32 H.M. Cheng, F. Li, G. Su, H.Y. Pan, L.L. He, X. Sun, M.S. Dresselhaus, Appl. Phys. Lett. 72, 3282 (1998)
- 33 J.F. Colomer, G. Bister, I. Willems, Z. Konya, A. Fonseca, J.B. Nagy, G. Van Tendeloo, Chem. Commun. 14, 1343 (1999), Chem. Phys. Lett. 317, 83 (1990)
- 34 X. Fan, R. Buczko, A.A. Puretzky, D.B. Geohegan, J.Y. Howe, S.T. Pantelides, S.J. Pennycook, Phys. Rev. Lett. 90, 145501 (2003)
- 35 S. Maruyama, Y. Murakami, Y. Shibuta, Y. Miyauchi, S. Chiashi, J. Nanosci. Nanotechno. 4, 360 (2004)
- 36 D.E. Resasco, W. E. Alvarez, F. Pompeo, L. Balzano, J.E. Herrera, B. Kitiyanan, A. Borgna, J. Nanopart. Res. 4, 131 (2002)
- 37 B. Kitiyanan, W.E. Alvarez, J.H. Harwell, D.E. Resasco, Chem. Phys. Lett. 317, 497 (2000).
- 38 J.E. Herrera, L. Balzano, A. Borgna, W. E. Alvarez, D.E. Resasco, J. Catal. 204, 129 (2001).
- 39 W.E. Alvarez, B. Kitiyanan, A. Borgna, D.E. Resasco, Carbon 39, 547 (2001)
- 40 Y. Murakami, Y. Miyauchi, S. Chiashi, S. Maruyama, J. Catal. 225, 230 (2004).
- 41 A. Peigney, C. Laurent, F. Dobigeon, A. Rousset, J. Mater. Res., 12, 613 (1997)
- 42 P. Coquay, A. Peigney, E. De Grave, E. Flahaut, R. E. Vandenberghe, C. Laurent, J. Phys. Chem. B., 109, 17813 (2005).

CHAPTER 2

BACKGROUND AND INTRODUCTION TO THE STRUCTURE, SYNTHESIS AND CHARACTERIZATION OF CARBON NANOTUBES AND SILICON NANOWIRES

2.1. INTRODUCTION TO CARBON NANOTUBE STRUCTURE, SYNTHESIS AND CHARACTERIZATION.

A carbon nanotube (CNT) is a hollow tube formed by the roll up of graphite sheet (s) into a cylinder. It can be classified as a single-wall carbon nanotube (SWNT) or a multiwall carbon nanotube (MWNT) depending on the number of graphite sheets that compose the nanotube wall. MWNT were first discovered by the electron microscopist Sumio Iijima in 1991 (1). The distance between the atomic graphitic sheets of the walls in the MWNT is ~ 0.34 nm, which is similar to the interplanar spacing in graphite. The diameter of the MWNT can range from a few to tens of nanometers, and its length from micrometers to millimeters (2). SWNT were later discovered in 1993 simultaneously by Iijima and Ichihashi (3) and Bethune *et al.* (4). In the case of SWNT, the typical diameter is in the order of a nanometer, while its length can reach several microns.

The structure of carbon nanotubes have been confirmed using high-resolution microscopy techniques. These experiments have demonstrated that nanotubes are cylindrical structures based on the hexagonal lattice of carbon atoms that forms crystalline graphite. A schematic representation of SWNT structure is shown in Figure 2.1. The diameter and helicity of a SWNT are identified by the roll-up vector (chiral vector) $\mathbf{C}_h = n\mathbf{a}_1 + m\mathbf{a}_2 \equiv (n, m)$, which connects crystallographically equivalent sites on this sheet. \mathbf{a}_1 and \mathbf{a}_2 are the graphene lattice vectors, and n and m are integers. Using these so called chirality vectors, three different types of nanotubes structures can be defined armchair, zigzag and chiral nanotubes; depending on how the two-dimensional graphene sheet is "rolled up". Armchair nanotubes are formed when $n = m$ and the chiral angle is 30° . Zigzag nanotubes are formed when either n or m are zero and the chiral angle is 0° . All other nanotubes, with chiral angles values between 0° and 30° , are known as chiral. As shown in Figure 2.2. The diameter of a SWNT is given by :

$$d = (n^2 + m^2 + nm)^{1/2} 0.0783 \text{ nm} \quad (1)$$

A remarkable consequence of the different values the roll up vector can take is that SWNTs can be either electrically metallic or show semiconducting behavior depending on the values the (m, n) components. In fact, the most interesting properties of SWNT relate to their electronic band structure. The armchair tubes are always metallic whereas the zigzag and chiral can be either metallic or semiconducting. Electronic-band structure calculations predict that the (n, m) indices determine whether a SWNT will be a

metal or a semiconductor. SWNTs are metallic if their (n, m) indices satisfy the condition in which $(n - m)/3$ is an integer; otherwise, the SWNTs are semiconductor (5-8). Based solely on geometry, one-third of the nanotubes will be metallic and two-thirds semiconductor.

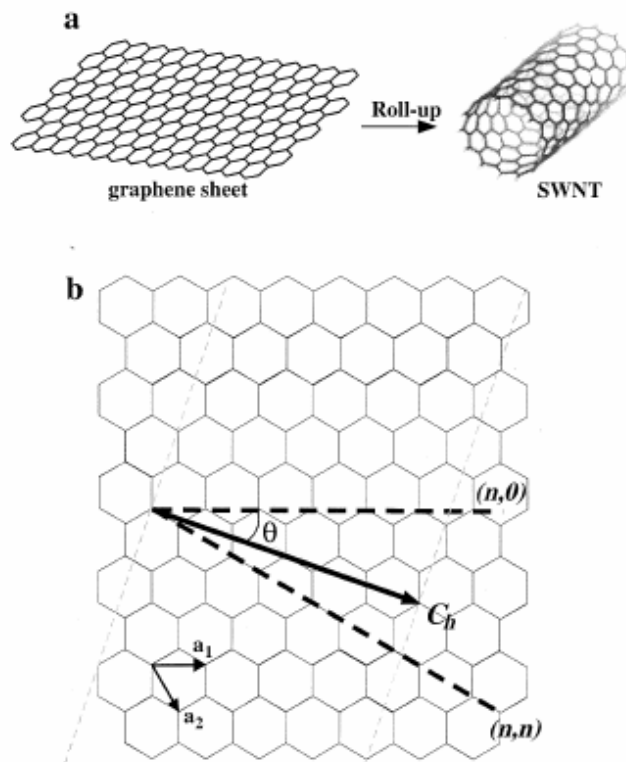


Figure 2.1 (a) Schematic of a portion of a graphene sheet rolled up to form a SWNT. (b) 2D graphene sheet illustrating lattice vectors a_1 and a_2 , and the roll-up vector $C_h = na_1 + ma_2$. The achiral, limiting cases of $(n, 0)$ and (n, n) armchair are indicated with thick, dashed lines, and the chiral θ angle is measured from the zigzag direction. The light, dashed parallel lines define the unrolled, infinite SWNT. The diagram has been constructed for $(n, m) = (4, 2)$ (8).

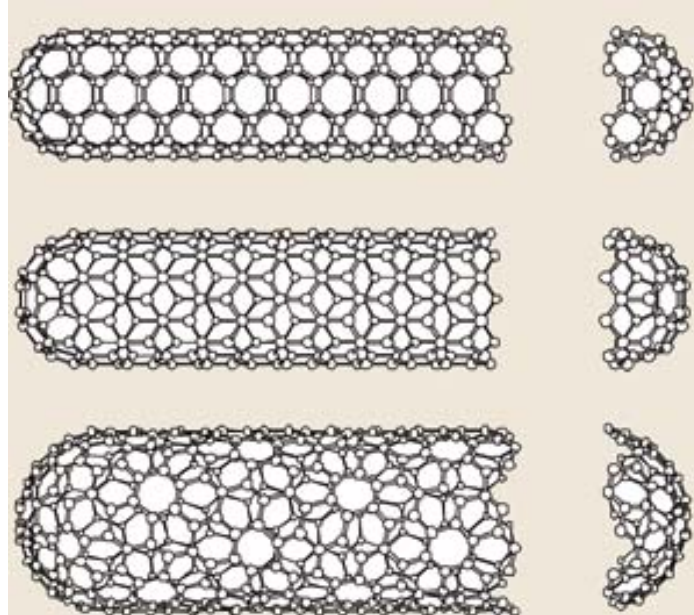


Figure 2.2 Nanotubes are formed by rolling up a graphene sheet into a cylinder and capping each end with half of a fullerene molecule. Shown here is a (5, 5) armchair nanotube (top), a (9, 0) zigzag nanotube (middle) and a (10, 5) chiral nanotube. The diameter of the nanotubes depends on the values of n and m (9).

At the same time, nanotubes are expected to be very strong and have high elastic moduli, just as the carbon fibres commonly used in aerospace applications; however, single-wall nanotubes are remarkably flexible. They can be twisted, flattened and bent into small circles or around sharp bends without breaking, and severe distortions to the cross-section of nanotubes do not cause them to break. Therefore, they are promising candidates as components or strong fibers with light weight and high electrical conductivity. Based on these properties, carbon nanotubes offer exciting possibilities for nanometer-scale electronic applications, such as field effect transistors (FETs), diodes or memories (10-14). It has also been suggested that carbon nanotubes could be used in

displays or for the tips of electron probes, such as nanotube based chemical force microscopy tips (15) as well as nanotweezers (16).

2.1.1 Synthesis of Single-walled carbon nanotubes

2.1.1.1 Arc discharge technique

The arc-discharge method has been used for a long time for the production of fullerenes. In this technique, carbon atoms are evaporated by plasma of an inert gas such as He that is ignited by high currents passed through opposing carbon anode and cathode. A schematic of the apparatus is shown in Figure 2.3a. Arc discharge can produce both an SWNT and an MWNT. It was found that addition of metals such as cobalt to the graphite electrodes resulted in the formation of extremely fine tubes with single-layer walls (SWNT). Unlike the arc discharge for SWNT synthesis, there is no need for mixing catalytic metal in the anode if MWNT is the desired product (3). In a typical arc discharge apparatus, the arc is generated between two graphite rods, which are mounted in a stainless steel vacuum chamber equipped with a vacuum line and a gas inlet. One of the graphite electrodes (cathode) is fixed and is connected to a negative potential. The other electrode (anode) is moved from outside the chamber in a linear motion feed through to adjust the gap between the electrodes. In a standard operation, a given background pressure is stabilized within the cell by adjusting the incoming flow of an inert gas such as helium and the pumping speed. A voltage-stabilized DC power supply

is normally used, and discharge is typically carried out at a voltage of 20 V. The current depends on the diameter of the rods, their separation, and the gas pressure. It is usually in the range of 50-100 A. During the discharge, plasma is formed generating temperatures of the order of 3700°C. The temperature is particularly high on the anode surface and this electrode is rapidly consumed by vaporization.

The quality and yield of the nanotubes are dependant on the arc discharge process parameters such as inert gas and pressure (17-20), plasma stability (18) and the geometry and distance between the electrodes (21). A large scale production method has been developed by Ebbensen and Ajayan (17) by optimizing the process parameters. By using water-cooled copper as a cathode, tens of micrometer length tubes of high quality could be obtained (21). However, the product is full of impurities such as fullerenes, carbonaceous nanoparticles, and catalyst. Typically after purification, only 1% of the initial deposit remains as final product. Journet *et al.* (22) reported a novel technology leading to yields of nanotube production as high as 70-90%. Their method was similar to the original technique, but with slightly different reactor geometry and different catalysts (nickel/yttrium mixture instead of cobalt).

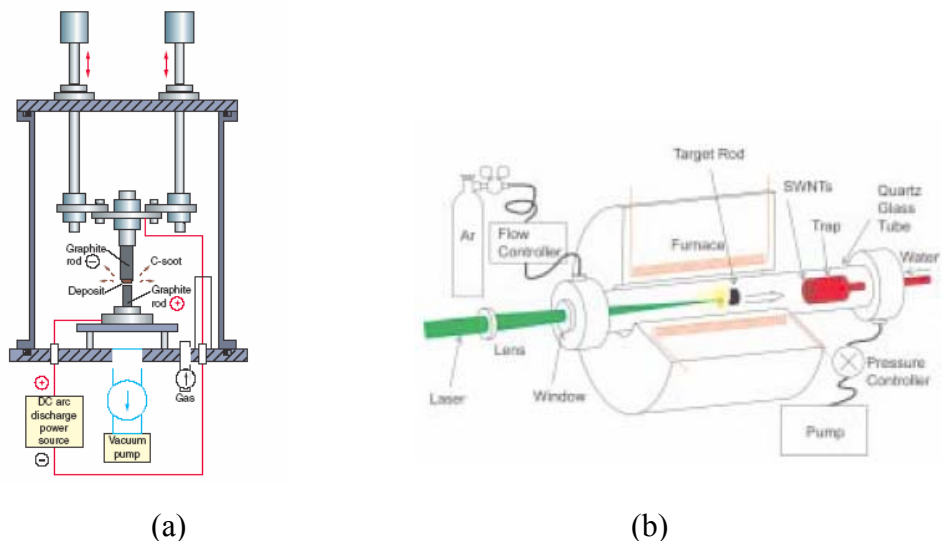


Figure 2.3 Schematic drawing of the apparatus for (a) arc discharge method (23) and (b) laser ablation method (24).

2.1.1.2. Laser Ablation technique

It was not until 1995 that Smalley and colleagues at Rice University showed that SWNT can be efficiently produced by laser ablation of a graphite rod (25). In the following year, that same group produced what was considered at the time the best SWNT material; over 70% of the volume of material was nanotubes bundled together into ropes (24). In a typical laser ablation experiment, the Nd:YAG laser pulse is focused on a graphite target containing 1-2 at% catalyst metal (24, 26, 27). A schematic of the apparatus is shown in Figure 2.3b. The target rod is placed in a furnace, kept in inert atmosphere and the system is heated to 800-1400°C. A flow of inert gas is passed through the chamber to carry the nanotubes “downstream”, SWNTs condense from the

laser vaporization plume and are deposited on a collector outside the furnace zone. It was found that the structure of the carbon species produced with this method strongly depends on the background argon pressure (28). When the pressure is lower than 100 Torr no SWNTs are produced. Apparently, the Ar pressure plays an important role in the heat transfer phenomena and assists in the metal evaporation. The texture of the target was also found to have an effect on the quantity of SWNT, for example, twice as much SWNTs were produced when carbon targets contained Ni and Co nitrates instead of Ni-Co metals or oxides. This effect was the result of a better dispersion and smaller particle size of the metals when nitrates were used (29). Dai *et al.* (30) concluded that a better control over the growth and quality of nanotubes can be achieved by the application of this direct vaporization method.

It has been proposed that the laser ablation method can be modified to make a quasi-continuous production mode. Indeed, Eklund *et al.* have recently developed a modification of the pulsed laser vaporization technique that, according to the authors, should result in large-scale production of high-quality SWNT (31). In this method, ultrafast ablation was achieved by using a high power free-electron laser. The modified setup includes a T-shaped quartz growth chamber placed inside a furnace to keep the chamber at 1000°C. The laser radiation enters from a sidearm that protrudes out the furnace near the center of the hot zone and strikes the carbon target, which is mounted on a rotating / translating rod. A jet of preheated argon deflects the ablation plume away from the incident laser beam, continuously sweeping the target region. The SWNT soot is

then collected from a water-cooled copper coldfinger at the end of the quartz nanotube. A special feature of this method was the use of the free-electron laser (FEL) operated at a peak laser flux that is about 1000 times greater than the flux used in typical Nd:YAG based systems, but each FEL pulse is only 1/200,000 as long as the typical 10 ns Nd:YAG pulse.

2.1.1.3. Chemical vapor deposition

The catalytic decomposition of carbon-containing compounds on appropriate metal catalysts is another method of producing SWNT. Indeed, chemical vapor deposition (CVD) has become a key production technology for solid-state materials via chemical reactions of the incoming source gases at an appropriate temperature. CVD has the advantage of offering a nanotubes synthesis route in large-scale, which is very important for commercial endeavor. Moreover, it has been shown that chemical vapor deposition on catalytically patterned surfaces offers unique advantages in the growth of self-organized nanotubes at specific locations with desired orientations (32, 33, 34).

In the CVD method, the main process parameters are the hydrocarbon source, catalyst, and reaction temperature. The synthesis temperature for MWNT is typically in the range of 600-900°C and 700-1100°C for SWNT. However, there are several reports showing that SWNT can be produced at reaction temperature as low as 650°C (35, 36), which is much lower than the temperature employed in the arc discharge and laser

methods. A variety of carbon-containing molecules have been used such as CO, CH₄, ethylene, acetylene, ethanol, or benzene. The catalyst materials are typically transition metals such as Ni, Fe, Co, and their alloys.

The way SWNT are generated from this method is one of the most intriguing questions. It has been demonstrated that the diameter of the carbon nanotube is determined by the size of the metal cluster responsible for its growth (33,37,38). Therefore, it is important to tailor the catalytic precursors in such a way that the catalyst particles retain a small size during SWNT growth. For instance, Resasco *et al.* (39-42) have designed CoMo bimetallic system in which small metallic Co particles are produced only under reaction conditions. A similar approach has been undertaken by Haller *et al.* using Co and a Co-MCM-41 catalysts in which prior to exposure to CO, the reduced cobalt species strongly interacting with the silica framework do not nucleate into larger clusters in the presence of He or H₂, preserving near atomic cobalt dispersion (43, 44).

An alternative to the catalytic decomposition of carbon-containing molecules over solid catalyst has been the so-called “floating catalyst” method. Sen *et al.* (45) prepared carbon nanotubes by decomposition of ferrocene, cobaltocene, and nickelocene under reductive conditions. In this case, the precursor provides both the carbon and the metal to catalyze the synthesis reaction. Similarly, in other methods benzene or hexane has been added to ferrocene improving the yield (46). A variation of the floating catalyst method resulted in the commercial process known as HiPCo that produces 10 g/day of

high-purity carbon single-walled nanotubes (47). In this process, SWNT are grown at high-pressure (30–50 atm) and high-temperature (900–1100°C) under flowing CO. The catalyst is iron in the form of small clusters that are generated in situ as continuously added iron pentacarbonyl decomposes in the reactor.

As mentioned above the great advantage of the CVD method is also the growth of self-organized nanotubes at specific locations with desired orientations. Recently, surface CVD growth of SWNTs has attracted much attention (48-53). Direct CVD growth on flat substrates is a relatively inexpensive method to create isolated, low-defect density SWNTs, whereas nanotubes fabricated by laser ablation or arc discharge are initially synthesized as bundles and have to be purified and suspended in solution before deposition onto a surface for device fabrication. These postsynthetic treatments may introduce defects and alter the electronic properties of SWNTs due to the highly oxidative chemicals and ultrasonication processes used for purification and dispersion. Huang *et al.* (54, 55) have directly grown millimeter-long, well-aligned SWNTs in large areas on flat substrate using monodispersed Fe/Mo nanoparticles as catalysts and CO as feeding gas. The lengths of the SWNTs can be more than 2 mm. The orientation of nanotubes is directly controlled by the direction of gas flow in the CVD system without the use of any external force like electric and magnetic fields. They can easily fabricate 2D nanotube networks with controlled geometry by using a two-step process.

Recently, vertically aligned SWNT growth has been reported by several authors. Murakami *et al.* (56) reported for the first time a reproducible technique for synthesizing a film of vertically aligned SWNT on a quartz surface, using the so called alcohol-CVD technique. On their method, a bimetallic Co–Mo catalyst was supported on a quartz substrate by dip-coating the substrate in an acetate solution. Ethanol was used as carbon source under Ar/H₂ environment at 800°C with a background pressure on the CVD chamber below 2×10^{-2} Torr. Uniformly vertical alignment of SWNTs film with 1.5 μm was reported. Hata *et al.* (57) have also shown the growth of vertically aligned SWNT up to 2.5 millimeters in height by ethylene CVD by using Ar or He with H₂ that contained a small and controlled amount of water vapor.

2.1.2 Structure characterization techniques used in this dissertation

A first step in a systematic approach towards improved SWNT synthesis study and tailoring of their electronic and mechanical properties is feedback from reliable characterization techniques since as-prepared SWNTs are normally obtained as a mixture of various helicity nanotubes, containing impurities such as metal catalyst, and other carbon species. Several methods have been applied to obtain this information. The techniques comprise local probes such as transmission electron microscopy (TEM), electron diffraction, scanning electron microscopy (SEM), and scanning tunneling microscopy (STM), combined with tunneling spectroscopy and bulk-sensitive probes such as Raman scattering, optical absorption spectroscopy and fluorescence. Also

temperature-programmed oxidation (TPO) is employed to identify the amount of SWNT obtained after reaction on CVD processes. In the subsequent section some of these methods will be introduced and the kind of information that can be obtained from them will be discussed.

2.1.2.1. Electron microscopy

Electron microscopy has been used to reveal the diameter and helicity of SWNT materials, making it possible to determine their atomic structure. The two most common types of electron microscopes available commercially are the transmission (TEM) and scanning electron microscope (SEM). In the SEM, the specimen is scanned with a focused beam of electrons which produce "secondary" electrons as the beam hits the specimen. These secondary electrons are detected and plotted as function of the position of the primary electron beam, producing a three-dimensional image of the surface of the specimen. Specimens in the TEM are examined by passing the electron beam through them, revealing more information of the internal structure of specimens. Depending on the sample thickness, a fraction of the electrons passes through it without suffering significant energy loss. Since the attenuation of the electrons depends on the density and thickness of the sample, the transmitted electrons form a two-dimensional (2D) projection of the sample. Electrons can also be diffracted by particles if these are favorably oriented toward the electron beam; the crystallographic information that can be obtained from these diffracted electrons is the basis for electron diffraction.

Among the various analytical techniques, high-resolution transmission electron microscopy (HRTEM) has played a key role in the discovery and characterization of carbon nanotubes. TEM is a powerful technique that is indispensable for characterizing nanomaterials. When a nanotube is observed in projection, the side walls give rise to high image contrast governed by the electron imaging principles. This fortunate situation makes the examination of tubule diameter and tubule morphology (such as bending, flattening, etc.) a quite straightforward task.

Single-walled nanotubes are rarely observed as individual entities. During synthesis, they gather on a hexagonal lattice to form bundles of tubes (“ropes”) held together by Van der Waals forces. In this case, observation is possible with the electron beam perpendicular to its axis (situation 1) or parallel to its axis (situation 2) as shown in Figure 2.4. While nanotube diameter can be directly obtained from the transmitted electron images electron diffraction (ED) is a powerful technique for the direct determination of the helicity. The diffraction pattern of a bundle of SWNT consists of intense spots along a line perpendicular to the tube axis, called the equatorial line, and a distribution of non-equatorial $hk.0$ nodes. When the tube axis is normal to the incident electron beam, the hexagonal structure of the graphene layer causes a hexagonal arrangement of 1010 and 1120 reflections as shown in Figure 2.5. The orientation of this pattern depends on the helicity of the tube. The (n,m) indices can be computed from diffraction patterns based on the kinematical diffraction theory (58-60) and the value of

chiral angle can be measured directly in the pattern from the relation positions of the spots around the first (1010) spots or second (1120 spots) diffraction circles.

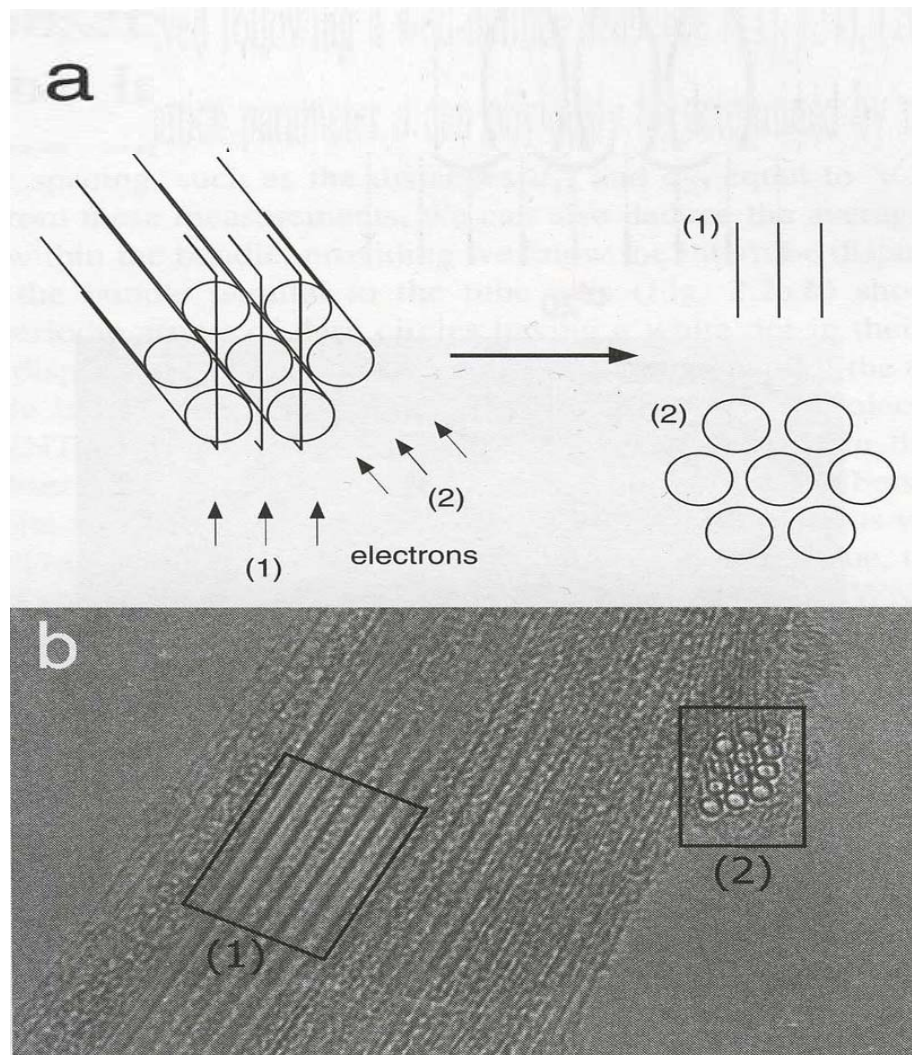


Figure 2.4 High resolution images of SWNT (a) Scheme of the observation conditions with the electron beam perpendicular (1) or parallel (2) to the bundle axis; (b) Image of a SWNT bundle (60)

An example of electron diffraction pattern is displayed on Figure 2.5. In this case, the inner circle contains three hexagons of weak and elongated spots. One of them corresponds to a zigzag structure ($\alpha = 0^\circ$). The two other sets of hexagons correspond to a chiral structure with a chiral angle of 16° . The simulated diffraction pattern shown in Figure 2.5b was computed at normal incidence for an assembly of 31 nanotubes, in a bundle mixing (16,0) tubes and (11,5) tubes. Another possibility leading to a similar result is to mix (15,0) tubes with (12,5) tubes (60).

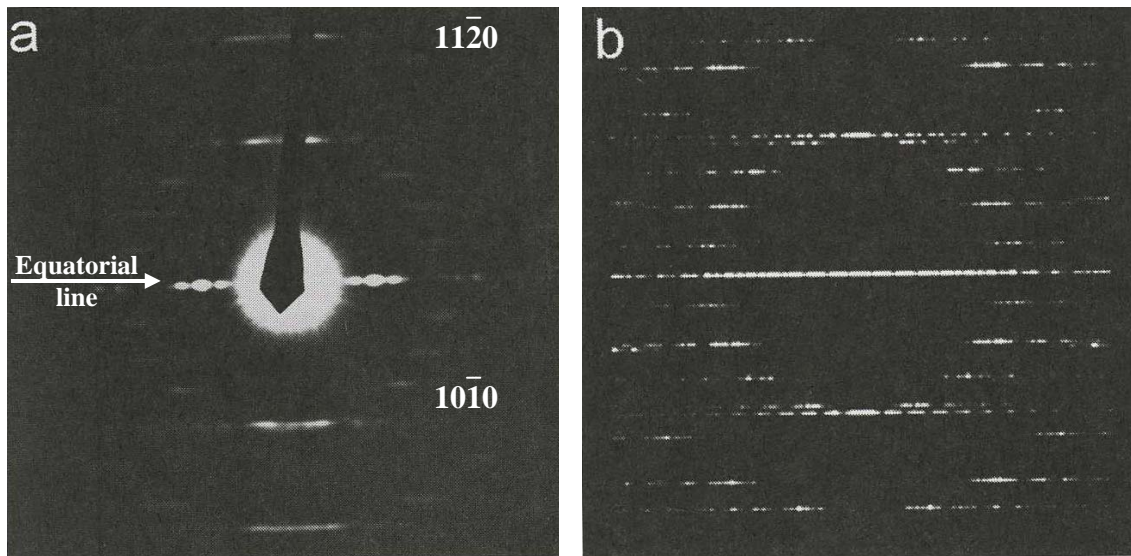


Figure 2.5 Selected area electron diffraction patterns of a SWNT bundles produced from CCVD : (a) Experimental pattern; (b) Kinematical simulation for a bundle mixing a total of 31 (16,0) and (11,5) nanotubes (60).

In contrast to transmission electron microscopy, scanning electron microscopy is to a certain extent a limited tool to characterize SWNT, regardless of the high magnifications that can be achieved with SEM instruments. The main problem with the

application of SEM to SWNT characterization analysis is that it cannot differentiate between SWNT and MWNT. This is mostly due to the tendency of SWNT to adhere strongly to each other, forming bundles or ropes of 5-20 nm in diameter. In contrast to TEM, SEM cannot resolve the internal structure of these SWNT bundles. However, the technique constitutes a good way to check bulk yields as well as the alignment of nanotubes.

SEM can yield valuable information regarding the purity of a sample as well as an insight on the degree of aggregation of raw and purified SWNT materials. More importantly, since now SWNTs are also direct grown on flat substrates, SEM has become a valuable tool for alignment appraisal since it can evaluate the length and also the density of these materials (Fig 2.6a). For instance, Figure 2.6 shows the results of one of such studies where vertically aligned SWNTs are grown from lithographically patterned catalyst islands into well-defined vertical-standing organized structures. Figure 2.6b also shows a nice example on how SEM can be used to characterize SWNT materials, in this case SWNTs were grown on a horizontally fashion on a flat substrate. It is clear then how SEM has become a crucial technique used in SWNTs characterization.

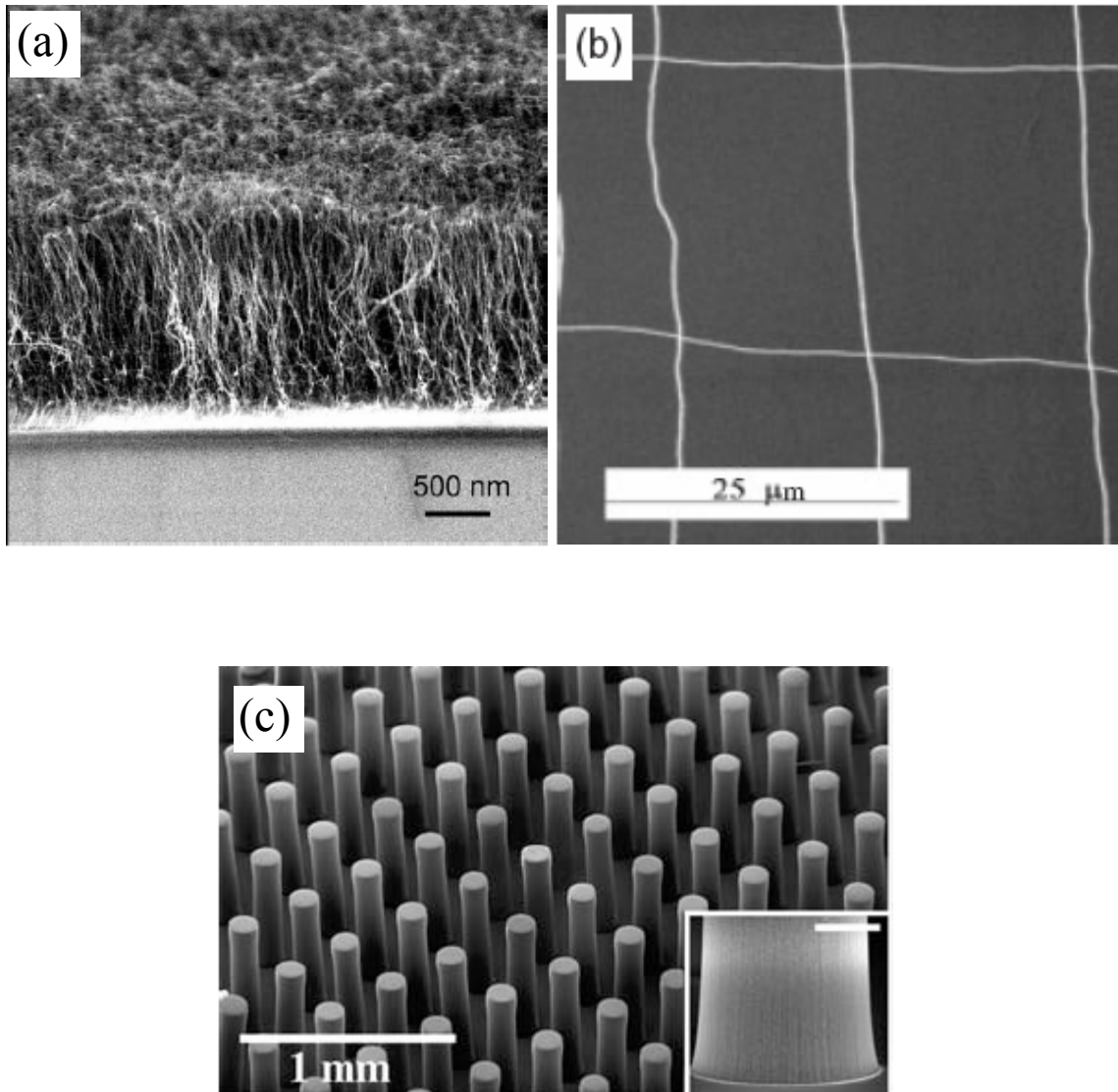


Figure 2.6 SEM images of SWNT grown on flat substrate; (a) vertically aligned SWNT bundles grown on quartz surface (56); (b) the cross-network SWNTs on a SiO₂/Si surface fabricated by a two-step growth process (55); (c) SWNT cylindrical pillars with 150-μm radius, 250-μm pitch, and 1-mm height (Inset, SEM image of a root of a pillar, scale bar, 50 μm) (57).

2.1.2.2. Raman spectroscopy

Raman spectroscopy is a very powerful SWNT characterization technique used to get information on their vibration and electronic structure. Raman spectroscopy is based on the inelastic scattering of visible light by matter. When light interacts with a substance it may be absorbed by the substance, transmitted, or scattered. The light may be scattered in an elastic or inelastic fashion. Elastic scattering is the most common phenomenon and occurs without loss of photon energy. By contrast, a very small fraction of the incoming light experiences inelastic scattering, in which the scattered wave has a different frequency than that of the incoming wave. This frequency difference is called the Raman shift. If, upon collision with a molecule the photon loses some of its energy, the resulting radiation has a positive Raman shift (Stokes radiation). In contrast, when the incoming photons gain energy the resulting radiation has higher frequencies (anti-Stokes radiation) and negative Raman shift is observed. Both the Stokes and anti-Stokes radiation are composed of discrete bands related to molecular vibrations of the substance.

A limitation of Raman spectroscopy is the extremely low crosssections associated with the process (almost 1 photon is inelastically scattered for every 10^6 photons that interact with the sample). Thus, a very intense light source has to be used to get a measurable signal. Moreover, since a very precise measure of frequency of the incoming light is needed to calculate the Raman shift, the use of a monochromatic

excitation light is necessary. A laser light then becomes the logical choice for excitation light source to perform Raman spectroscopy.

Sometimes, the low efficiency of the Raman scattering process can be improved through the so-called resonant Raman effect. This resonant effect occurs when the photon energy of the exciting or scattered light beam matches the energy of an allowed optical electronic transition of a chromophoric group within the sample (61, 62). In the particular case of SWNT the resonant Raman effect is very strong due to the sharp spikes present in the one-dimensional electronic density of states. The energy difference between the spikes falls in the visible and near –infrared range (63-68) and as consequence , when the excitation laser energy is close to that of an allowed optical transition between singularities in the one-dimensional density of states of SWNT the Raman intensity is greatly enhanced (69-71).

In Figure 2.7, the Fourier transform (FT)-Raman spectrum of an arc discharge derived SWNT sample is illustrated. The spectrum has three main first order components: the so-called radial breathing mode (RBM) at around 180 cm^{-1} , the D-band at 1330 cm^{-1} , and the G-band between 1560 and 1600 cm^{-1} . Typical second order and combination bands are also depicted.

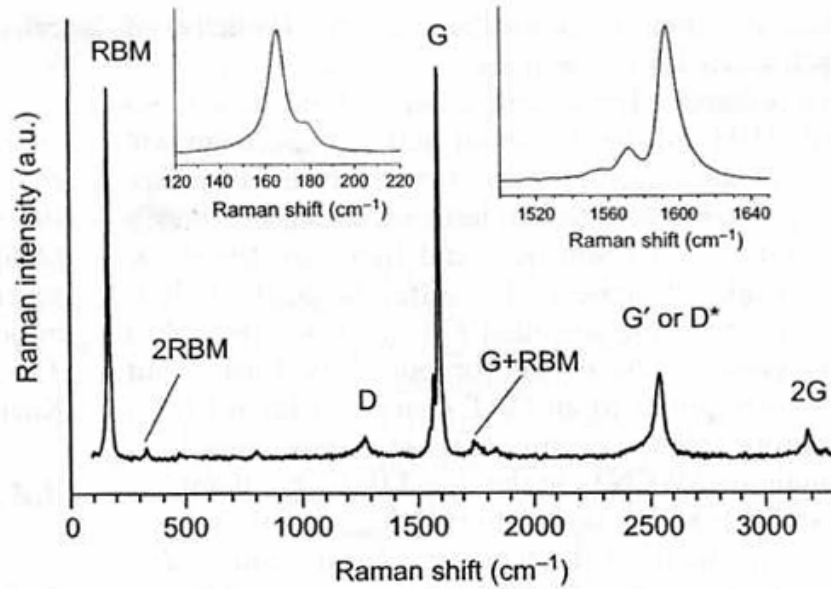


Figure 2.7 FT-Raman spectrum of a SWNT samples showing the characteristic first and second order bands as well as the G+RBM combination band. The insets reveal the typical detailed shapes of the RBM and the G-band (72).

The radial breathing mode is a low frequency (below 300 cm^{-1}) A_1 mode corresponding to the total symmetric in-phase motion of all carbon atoms in the SWNT perpendicular to the tube axis. These bands have been proposed to be independent of chirality (73). Bandow et al. calculated the RBM frequencies of all types of SWNT and found that all frequencies fall on a common line according to the expression (74):

$$\bar{\gamma} = \frac{223.75}{d}$$

where $\bar{\gamma}$ is in units of cm^{-1} and d is the nanotube diameter in nm.

However, a slight correction has been made to the original formula since intertube coupling needs to be considered when the nanotubes are present in a bundle. This correction was achieved by using a Lennard- Jones potential to account for van der Waals interactions among the nanotubes in a bundle (75, 76). A significant upshift of the RBM has indeed been found for nanotubes in bundles with respect to isolated nanotubes. The calculated data were best fitted by the following non- linear phenomenologic relation between the RBM frequency and the nanotube diameter:

$$\bar{\gamma} = \frac{238}{d^{0.93}}$$

where $\bar{\gamma}$ is in units of cm^{-1} and d is the nanotube diameter in nm.

A remarkable feature of the RBM is that its position varies with the energy of the excitation laser even when measuring the very same SWNT sample (77,78). As mentioned above, the information obtained by Raman spectroscopy is the result of the resonant Raman Effect which is particularly strong in SWNT. Therefore, the nanotubes that contribute most strongly to the Raman scattering for a given excitation wavelength are those which are in resonant with the incident or scattered light. Consequently, the spectral shape and position of the Raman RBM do not directly reflect the true diameter distribution in the SWNT sample, but rather the subset of nanotubes that are in resonance with the incident or scattered photon. Figure 2.8 shows an example of this effect, on a set of samples produced by catalytic disproportionation of CO over a supported CoMo catalyst at 750°C (79). The RBM bands show a strong dependence on the laser energy,

which confirms the relation among the energy separation on densities of states singularities with the nanotube diameter.

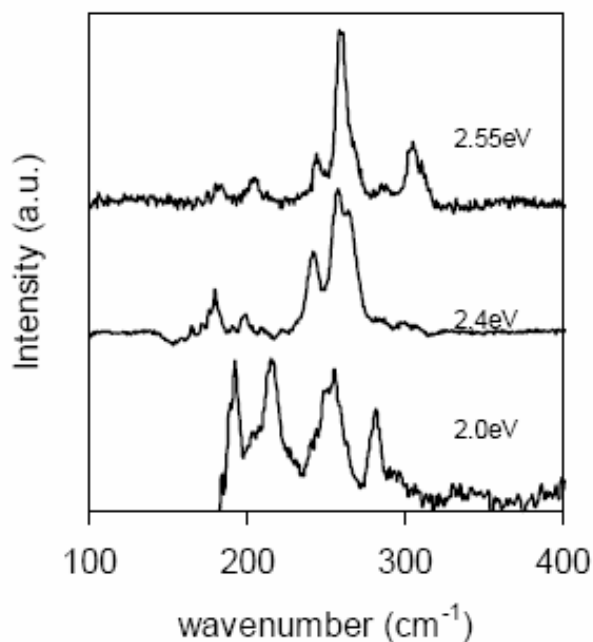


Figure 2.8 Radial breathing mode resonant Raman spectra of SWNTs grown at 750°C by CO disproportionation over CoMo catalyst (79).

Besides the radial breathing mode band, the Raman spectra of SWNTs also comprise a disorder-induced Raman band (D band), which is a feature common to all sp^2 hybridized disordered carbon materials. This so-called D-band is a weak to medium intensity peak observed between 1250 and 1450 cm^{-1} . The position of the D-band is not particularly sensitive to the diameter distribution of the sample. This band exhibits a strongly linear dispersive behavior as a function of laser excitation energy ($1.0 < E_{laser} < 4.5$ eV) (80,81). The D-band is usually regarded as an overall indicator of defects: sp^3

carbon atoms, holes in the SWNT walls, attached functional groups, and in fact, non-nanotube graphitic domains may all contribute to the D-band (72). The D-band has been related not just to defects on SWNT but also to the presence of other forms of disordered carbon such as carbon nanoparticles and amorphous carbon (82). And therefore its relative intensity has been used as a semi-quantitative indicator of the presence of undesired forms of carbon (i.e., microcrystalline graphite, amorphous carbon, MWNT, carbon nanofibers).

The most intense lines of the SWNT Raman spectrum are found between 1500 and 1605 cm^{-1} in the so-called G-band region which corresponds to the tangential C-C stretching vibrations. The band consists of non- or weakly diameter dispersive phonons of A_1 , E_1 , and E_2 symmetries. The G-band is an intrinsic feature of carbon nanotubes that is closely related to vibrations in all sp^2 carbon materials, and the position of the G-band frequency in SWNTs is not affected by the energy of the laser beam.

The most useful features of the G-band are the characteristic differences between the G-band lineshapes for metallic and semiconducting nanotubes as shown in Figure 2.9. Isolated semiconducting nanotubes (Fig. 2.9a) characteristically show two dominant Lorentzian features with 6-15 cm^{-1} linewidths at room temperature (83), the lower frequency component associated with vibrations along the circumferential direction

(ω_G^-), and the higher frequency component (ω_G^+) attributed to vibrations along the direction of the nanotube axis.

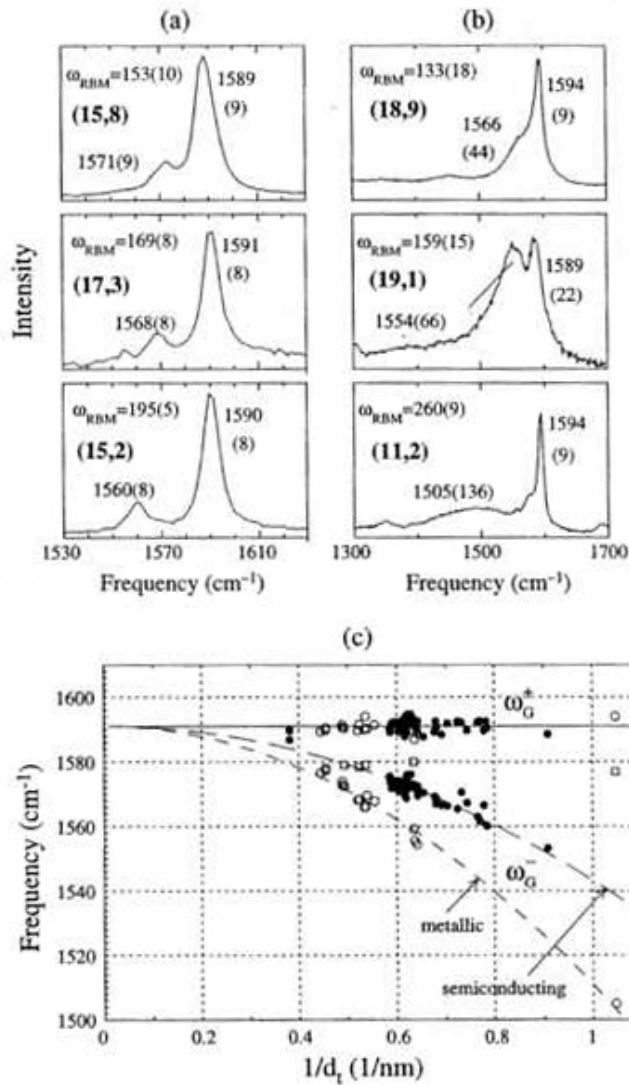


Figure 2.9 (a,b) Profiles of the G-band spectra for three semiconducting (a) and three metallic (b) nanotubes. The frequencies for ω_G^+ and ω_G^- are indicated in cm⁻¹ for each nanotube along with the corresponding linewidths in parentheses. (c) Dependence on reciprocal nanotube diameter $1/d_t$ of ω_G^+ and ω_G^- for both semiconducting nanotube (solid circles) and metallic nanotubes (open circles) (84).

The Raman spectra for metallic nanotubes (Fig. 2.9b) also have two dominant components with similar origins, but in this case, the upper frequency ω_G^+ component has a Lorentzian lineshape that is almost as narrow as that for the semiconducting nanotubes, but the lower frequency ω_G^- component is very broad Breit-Wigner-Fano line, with a strong coupling to a continuum, identified with surface plasmons (85). The G-band linewidths for the semiconducting nanotubes at the single nanotube level do not vary much with diameter, with the smallest observed FWHM intensity linewidth for the circumferential ω_G^- component for metallic nanotubes, however, increases very substantially with decreasing d_t , reflecting the increased Breit-Wigner-Fano coupling (83). The dependence on reciprocal nanotube diameter $1/d_t$ of ω_G^+ and ω_G^- for both semiconducting nanotubes and metallic nanotubes is shown in Figure 2.9c.

2.1.2.3. Optical Absorption Spectroscopy and Fluorescence

Another way to probe the electronic properties of SWNT is through their optical absorption spectra. Using Raman spectroscopy, metallic and semiconductor SWNTs can be observed. But due to the resonance effect, obtaining a full analysis to identify all of the different structures in the sample would require a large set of spectra using different laser wavelengths. However, Raman spectroscopy also has limitations, because investigators have not yet find a way to quantify the amount present of different nanotube structures in the sample by means of Raman spectra. With optical spectroscopy

or fluorescence, an analysis of the composition and semiquantitative distributions of tube diameter and chiral angle of bulk SWNT samples can be obtained. The technique is based on the well known phenomenon of light absorption or emission after excitation by a chromophore group present in the sample. In the case of SWNTs when the light sent to the sample matches the energy of an allowed electronic transition between Van Hove singularities, light in the visible and near infrared range can be absorbed. The observed absorption peaks are identified with interband transitions $E_{ii}(d_i)$ between the i th van Hove singularity in the valence band (occupied states) to the i th singularity in the conduction band (empty states). Figure 2.10 shows the qualitative pattern of sharp van Hove peaks, which arise from quasi-one-dimensionality, predicted for electronic state densities of semiconducting SWNTs. Moreover, in the case of semiconducting nanotubes light absorption at photon energy E_{22} could be followed by fluorescence emission near E_{11} as shown Fig. 2.10. The values of E_{11} and E_{22} will vary with tube structure (86,87).

Since SWNTs tend to aggregate in bundles that are bound by van der Waals attraction, these tube-tube perturbations cause optical spectra of bundles to be excessively broadened and blurred, preventing detailed spectral analysis. Indeed, fluorescence was originally reported on SWNT samples dissolved in organic solvents and integrated in polymer matrices. In those earlier observations, the fluorescence was explained either in terms of electronic structures associated with defects in the nanotubes or in terms of the presence of functional groups that were attached to the SWNT during the functionalization processes (88, 89).

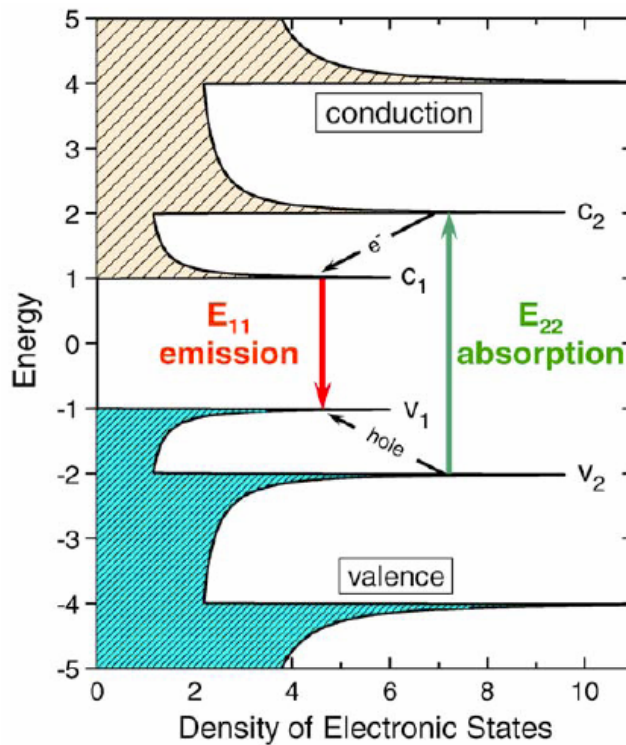


Figure 2.10 Schematic of density of electronic states for a single nanotube structure. Solid arrows depict the optical excitation and emission transitions of interest; dashed arrows denote non-radiative relaxation of the electron (in the conduction band) and hole (in the valence band) before emission (86).

However the absence of fine structure in the emission spectra did not allow linking the observed emission spectra to the intrinsic electronic structure of SWNT. A breakthrough in SWNT characterization was made by O’Connell et al. (90) in 2002, who observed fluorescence from SWNT samples consisting of individual nanotubes suspended in aqueous solutions of sodium dodecyl sulfate. In this suspension, the samples did not undergo any chemical modification. In contrast to the earlier studies, the fluorescence spectra displayed a well-defined fine structure.

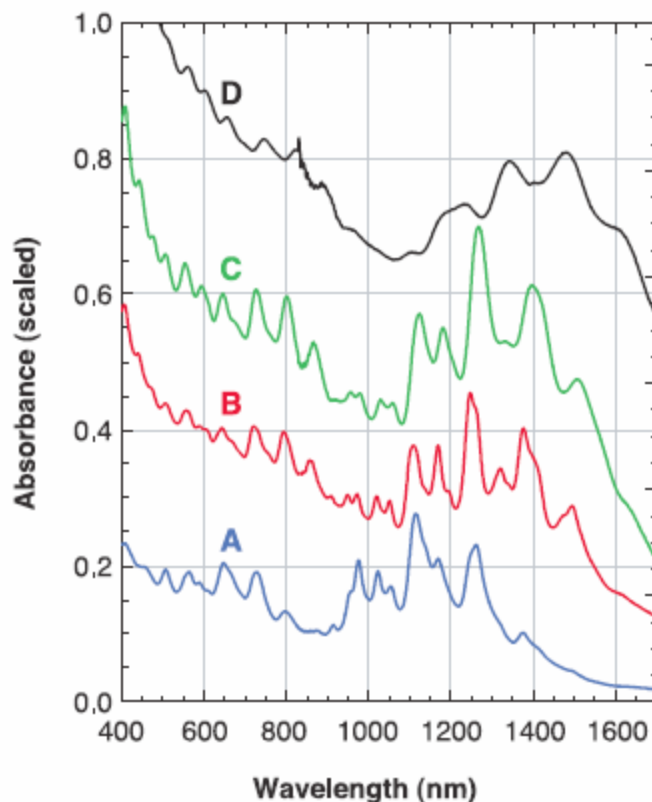


Figure 2.11 Absorption spectra of SWNT in SDS-D₂O suspension. The top trace D is typical of tubes prepared in suspension without centrifugation. Trace C is from individual SDS micelle coated nanotubes after addition of PVP. Traces B and A are from samples of individual nanotubes separated and solubilized by SDS micelles (90).

It became clear then that SWNT need to be individually suspended in water by common surfactants or polymers, to get a well resolved absorption or emission spectra. Among the various surfactants investigated, sodium dodecyl sulfate (SDS) (90) and sodium dodecylbenzene sulfonate (NaDDBS) (91,92) are nowadays the most commonly used. For instance, Figure 2.11 shows typical optical absorption spectra of a SWNT suspension. As is seen in traces A, B, and C, the electronic absorption spectrum

of decanted supernatant samples shows more pronounced structure than the sample of trace D, which was prepared without achieving a good surfactant dispersion,. Indeed the broadened and red-shifted absorption features present on spectrum D show that most nanotubes in the sample are still aggregated in bundles.

2.2. INTRODUCTION TO THE SYNTHESIS AND CHARACTERIZATION OF SILICON NANOWIRES

Semiconductor nanowires have recently aroused great interest both from a fundamental quantum physics point of view but also from an application perspective for their use as sensitive detectors. The first reports on the synthesis of semiconductor whiskers of Si, Ge or GaN appeared over 30 years ago; however in recent years, the development of new techniques allow much better control of size and structure of low-dimensional materials and the fabrication of nanowires. Semiconductor nanowires are especially attractive building blocks since these materials can be synthesized in single-crystalline form with precisely controlled structures, diameters and lengths, chemical compositions and doping/electronic properties. If the nanowire is grown from a semiconductor, its electrical properties can be altered by adding small amounts of a second substance, called a dopant. Adding boron to a silicon nanowire, for example, increases the number of ‘holes’ within the network of electrons available for conduction, whereas adding phosphorus creates additional free electrons (93).

Among the nanowires from different materials, silicon nanowires (SiNWs) have attracted much attention because silicon is the most important semiconductor material as of now. Silicon nanowires differ significantly from bulk silicon and may find applications in the new emerging field of nanoelectronic. Among many researchers, Dr. Charles M. Lieber's research group has developed many applications in nanoelectronic and biological and chemical nanosensors using silicon nanowires. For instance, they have used Boron-doped silicon nanowires (SiNWs) to create highly sensitive, real-time electrically based sensors for biological and chemical species (94). Recently, they reported two-terminal silicon nanowire electronic devices that function as ultrasensitive and selective detectors of DNA (95). Also SiNWs can be used to configure field effect transistors (FET) by depositing the nanomaterial on an insulating substrate surface, making source and drain contacts to the nanowire ends, and then configuring either a bottom or top gate electrode. This basic approach has open the door to hybrid electronic systems consisting of nanoscale building blocks integrated with more complex planar silicon circuitry (96).

2.2.1 Synthesis of silicon nanowires

2.2.1.1 Laser ablation

As in the case of carbon nanotubes, SiNW can be produced using a variety of methods. The schematic for a laser ablation apparatus for SiNW synthesis is shown in

Figure 2.12. In this method, a pulsed frequency-doubled Nd–yttrium-aluminum-garnet laser (wavelength, 532 nm) is used to ablate targets that contain the element desired in the nanowire and the metal catalyst component. The target, for example $\text{Si}_{1-x}\text{Fe}_x$, is located within a quartz furnace tube in which the temperature, pressure, and residence time can be varied. The growth of the Si nanowires occurred only for temperatures greater than 1150°C when a Fe catalyst is used (97). Another approach to laser ablation synthesis is to use a pure transition ablation target instead of a Si-containing one, to produce metal nanoclusters which catalyse the growth. In this case, the Si source is a silicon-containing feed (i.e. SiH_4) that is flow on the system.

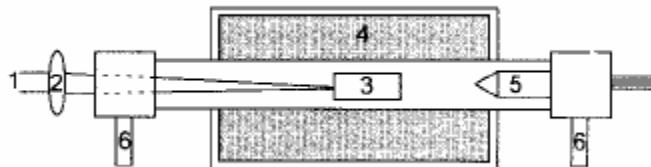


Figure 2.12 Schematic of laser ablation method. The output from a pulsed laser (1) is focused (2) onto a target (3) located within a quartz tube; the reaction temperature is controlled by a tube furnace (4). A cold finger (5) is used to collect the product as it is carried in the gas flow that is introduced (6, left) through a flow controller and exits (6, right) into a pumping system (97).

Figure 2.13 shows typical SiNW structures grown using laser ablation of a $\text{Si}_{0.9}\text{Fe}_{0.1}$ target at 1200°C . The transmission electron microscope (TEM) image (Fig. 2.13A) shows primarily wirelike structures with remarkably uniform diameters on the order of 10 nm with lengths >1 mm and often as large as 30 mm. The TEM images also

show that virtually all of the nanowires terminate at one end in nanoclusters with diameters 1.5 to 2 times that seem to connect different nanowires. Higher resolution TEM images recorded on individual nanowires (Fig. 2.13B) provide further insight into the structure of these materials. A diffraction contrast image (inset) shows that the nanowires consist of a very uniform diameter crystalline core, which surrounded by an amorphous coating (97).

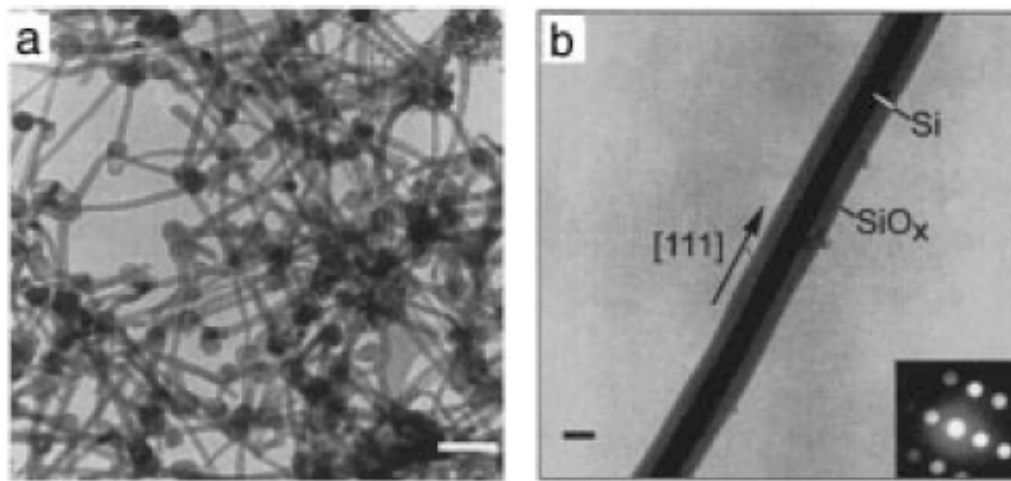


Figure 2.13 (a) TEM images of Si nanowires produced after laser ablating a $\text{Si}_{0.9}\text{Fe}_{0.1}$ target. The dark spheres with a slightly larger diameter than the wires are solidified catalyst clusters; (b) Diffraction contrast TEM image of a Si nanowire (97).

Cui et al (93) illustrated that single crystal and even n-type and p-type SiNWs can be produced via this approach. SiNWs can be doped with boron (p-type) by incorporating B_2H_6 in the reactant flow or doped with phosphorus (n-type) using a Au-P target (99.5:0.5 wt %) additional red phosphorus (99%) at the reactant gas inlet. Moreover, some kind of diameter control can be achieved when laser ablation is

performed in different ambient gases (98). SiNWs with the diameter distributions around 13.2 and 9.5 nm have been obtained respectively in He and Ar (5% H_2). Laser ablation of Si containing targets in N_2 has shown SiNW products with the smallest diameter (around 6 nm), mixed in with some spherical particles with diameter ranging from about 9 nm to several hundred nm.

Silicon nanowires with high yield, uniform diameter distribution, and high purity can be grown by laser ablation at high temperatures (99-100). In this particular case study the target was made by mixing silicon powder with nano-sized Ni and Co powder. The target was ablated at a temperature of 1200°C by using an excimer laser with a wavelength of 248 nm at pressure of about 500 Torr Ar. Wang et al. (101) have reported as well the synthesis of SiNWs with uniform diameter by laser ablation of highly pure Si powder targets mixed with SiO_2 . Bulk quantities of SiNWs were obtained by mixing 30-70% of SiO_2 into the Si powder target. They claimed that in this case SiO_2 acted as a special catalyst and greatly enhanced the one-dimensional growth of SiNWs.

2.2.1.2 Chemical Vapor Deposition (CVD)

Decomposition of Si containing feed over adequate metal catalysts is the most widely used route to synthesis of silicon nanowires. Among the catalyst used, gold has been generally used in this process because the Au-Si systems shows an eutectic Si-rich region with Si as the primary solid phase at very low temperatures (~360°C) as

shown later in Figure 2.14. Therefore, the process can take place at temperatures lower than those by laser ablation or thermal evaporation, which normally perform at temperatures above 1000°C. Besides gold, other metals such nickel and iron have also been used as catalysts in the CVD method. For instance Zhang et al. (102) used a thin Ni film to obtain silicon nanowires. In that particular case, the optimum reaction temperature was 900°C, which is close to the eutectic temperature of the Si/Ni system (966°C). In the case of iron, Liu et al. used a porous Fe/SiO₂ catalyst prepared by sol gel process (103) and reported that very straight silicon nanowires could be produced at 500°C. The silicon sources that are usually used for the CVD process are silane (SiH₄) and silicon tetrachloride (SiCl₄). Westwater et al. (104, 105) have reported that the use of silane as Si source to prepare silicon nanowires via CVD yields much thinner nanowires than the ones produced from SiCl₄. Furthermore, silane is easily decomposed at lower temperature than SiCl₄ so the synthesis reaction can be carried out at relatively low temperatures (102, 104, 105).

Sunkara et al. (106) has reported the method to synthesize SiNWs with uniform diameters distributed around 6 nm using gallium at temperatures less than 400°C in hydrogen plasma. Similarly, Pan et al. (107) illustrated the synthesis of silicon oxide nanowires using molten Ga as catalyst over an alumina substrate. In this case silicon oxide nanowires assemblies with fishbonelike, gourdlike, spindlelike, badmintonlike, and octopuslike morphologies were obtained by CVD of silane at 1150°C. The morphology,

distribution, and density of products vary gradually with their positions on the alumina substrate.

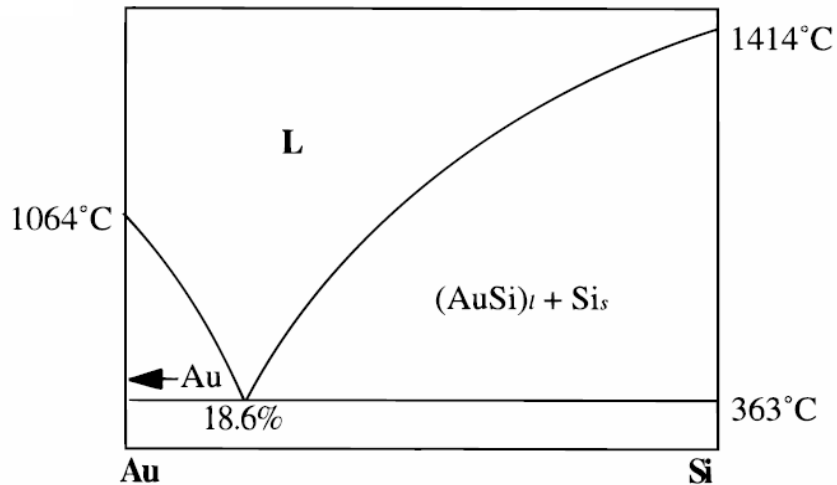


Figure 2.14 Au-Si binary phase diagram (108).

Similar to the growth of carbon nanotubes, the size of the metal catalysts normally determine the diameter of the nanowires, therefore, SiNWs with a narrow size distribution could be obtained by exploiting well-defined catalysts. Cui *et al.* (109) reported the production of controlled diameter SiNWs by using well-defined Au nanoclusters and SiH₄. Moreover, by arranging these catalytic nanoparticles in a template ordered SiNW arrays can be obtained. An important advantage of this approach is that the nanostructures prepared in this way can be diameter-controllable and well defined. Along this line, Zhang *et al.* have synthesized SiNW first by electrochemically depositing Au catalyst into nanoporous membranes and then growing SiNWs by pyrolysis of silane.

The nanowire diameter and length are dependent on the pore diameter and the growth time of the nanowire formed within the template (110,111).

2.2.1.3. Thermal evaporation

Silicon nanowire can be produced in bulk quantities by thermal evaporation. In this method, a powder mixture is placed in quartz tube inside a furnace at temperatures above 1100°C. As in the case of laser ablation, an inert carrier gas is generally kept flowing during the thermal evaporation process. Silicon nanowires are formed directly on the inside wall of the quartz tube or can be collected using other substrates such as silicon wafer, alumina, or zeolite at the exit port of the carrier gas.

Different powder mixtures have been used to synthesize SiNWs by thermal evaporation methods. Pure SiO powder or a mixture of highly pure Si powder and SiO₂ are used. The product then obtained has two major forms of SiNWs as shown in Figure 2.15. SiNWs with uniform diameters and smooth surfaces are one major component, while the other kind (Si nanoparticles) coexists with the nanowires. Notice the absence of metal particles when the product obtained by thermal evaporation is compared to the one obtained by laser ablation (Figure 2.13a) are compared. The arrow in Fig. 2.15 points at an oxide linked chain of Si nanoparticles. Most SiNWs are extremely long (>10 μm) and randomly oriented (112,113). It has been also reported that the presence of SiO₂ in the powder targets significantly enhances SiNWs yield. Typically, products obtained by

using a powder target composed of 50% SiO₂ and 50% Si have shown to lead to yields over 30 times greater than the amount generated when metal containing targets are used.

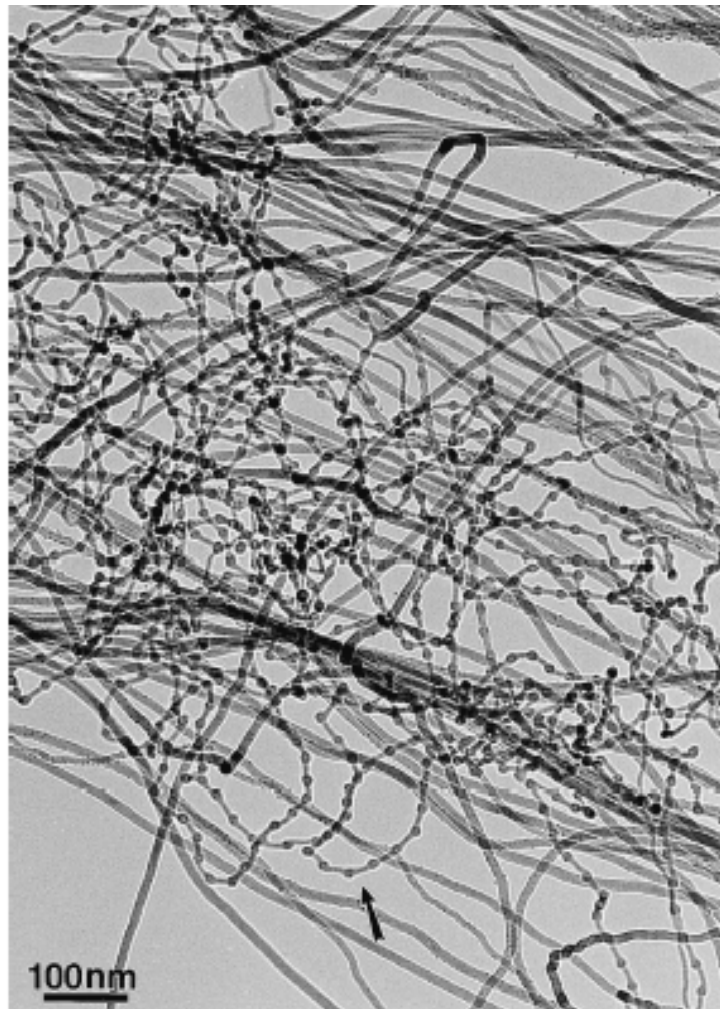


Figure 2.15 TEM image showing two major morphologies of Si nanowires (113).

2.2.2. Structural characterization techniques

2.2.2.1. Electron microscopy

As for the case of characterization of carbon nanotubes, SEM and TEM are powerful tools for SiNW structural characterization and provide valuable information on the structural arrangement, spatial distribution, yield, and geometrical features of the nanowires. Examples of SEM micrographs shown in Figure 2.16 clearly indicate how structural features at the 10 nm to 10 μm length scales can be probed (114) by using electron microscopy. SEM images of the representative morphology of SiNWs obtained from thermal evaporation method at high temperature (1100°C) are shown in Figure 2.16a and b. In Figure 2.16(a), dense nanowires can be observed. The sample consists of SiNWs with diameters ranging from 10 to 100 nm and length up to a few hundred micrometres. The SiNWs are tangled together above the Si substrate, and most of the SiNWs are smoothly curved with straight sections along the nanowires, as shown in Fig. 2.16(b). The SEM observation of SiNWs roots remaining on the substrate proves that the nanowires were grown directly from the substrate. Figure 2.16c shows how different morphologies of SiNWs obtained from CVD of SiH_4 at 1150°C with molten Ga as the catalyst (107) can be studied using SEM. Moreover by combining electron microscopy imaging with energy dispersive X-ray analysis (EDS) the authors found that nanowires have a chemical composition in the form of SiO_x with a Si/O atomic ratio of ~ 1.5 .

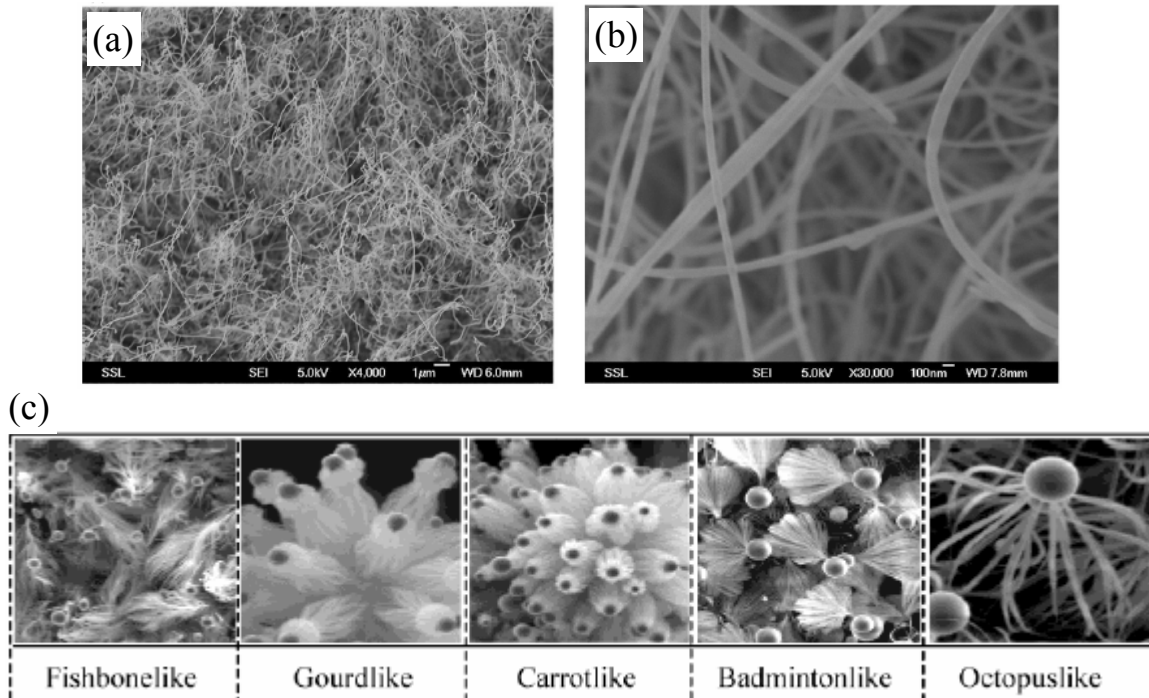


Figure 2.16 SEM images; (a), (b) a typical SiNWs produced from thermal evaporation on Si substrate (114) and (c) other SiNWs morphology obtained from chemical vapor deposition of SiH₄ with molten Ga as catalyst (107).

TEM and high resolution transmission electron microscopy (HRTEM) are powerful imaging tools to study nanowires at the atomic scale as well, and they often provide more detailed geometrical features than SEM images. TEM studies can also yield information regarding the crystal structure, crystal quality, grain size, and crystal orientation along the the nanowires axis. Figure 2.17a is a typical TEM image micrograph showing the morphology of high pure SiNWs with uniform distribution of diameters. The crystal quality of nanowires can be revealed from HRTEM images with atomic resolution, along with selected area electron diffraction (SAED) patterns. For

example, Figure 2.17b show microstructure details of a straight SiNW, indicating single crystallinity and showing [112] lattice planes, thus indicating the growth direction of the nanowires (115), this information is supplemented by the corresponding electron diffraction pattern (upper right).

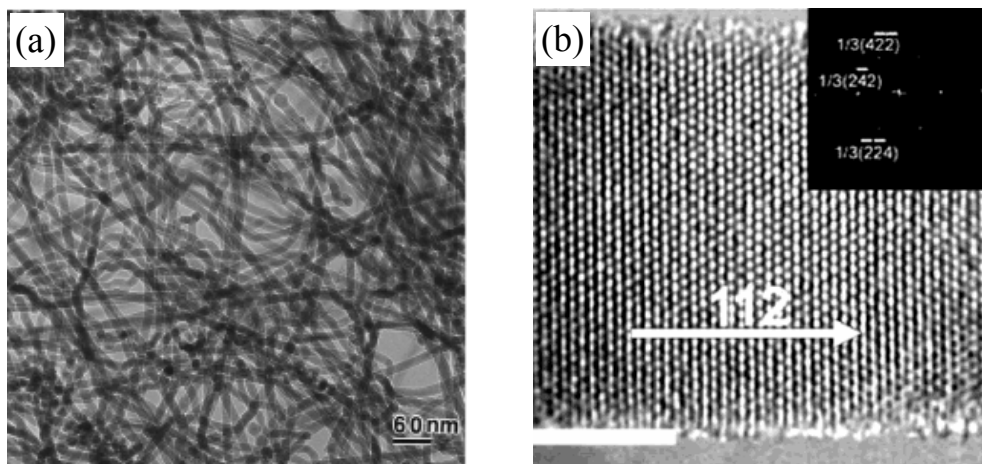


Figure 2.17 (a) A typical TEM image showing general view of morphology of SiNWs (116) and (b) HRTEM image of SiNW with diameter of 13.2 nm (115).

The work by Zhou *et al.* offers another example on useful HRTEM can be for SiNW characterization (116). In this study the microstructures of SiNWs synthesized by oven-laser ablation are evaluated. Based on HRTEM observations, the authors propose that the different morphologies of the SiNWs can be consistently explained on the basis of the role of planar defects during SiNWs formation. Wu *et al.* (115) have also employed HRTEM to follow the controlled growth of molecular-scale silicon nanowires. They demonstrated that the SiNWs grown with silane reactant in hydrogen have single

crystal structures with little or no visible amorphous oxide down to diameters as small as 3 nm. Structural characterization of a large number of samples showed that the smallest-diameter nanowires grow primarily along the [110] direction, whereas larger nanowires grow along the [111] direction. The [110] growth of smallest nanowire does not seem to arise from the formation of a liquid/solid (110) interface, but from (111) plane which forms during initial nucleation.

2.2.2.2. Raman Spectroscopy

Raman scattering is a valuable technique to characterize the lattice microstructure and the crystal symmetry of nanocrystalline materials. As for the case of carbon nanotubes, the Raman spectra of silicon nanowires provide useful information on the nanostructure of these materials. Raman spectra of silicon nanowires, single-crystal silicon (c-Si) and completely oxidized silicon nanowires are shown in Figure 2.18 (100,117). A Raman peak at 520 cm^{-1} with the full width at half maximum (FWHM) of 2.8 cm^{-1} can be seen in the Raman spectrum of c-Si (Fig. 2.18a). This Raman band is associated to the scattering of the first-order optical phonon of c-Si. In addition, there are two broad peak at ~ 300 and 970 cm^{-1} , which are originated by the scattering of two transverse acoustic (2TA) phonons and two transverse optical (2TO) phonons, respectively. In contrast, the Raman spectrum of SiO_2 nanowires (Fig. 2.18d) contains a very broad and asymmetrical peak at $\sim 460\text{ cm}^{-1}$ with a sharp peak at 490 cm^{-1} . A redshift of the phonon frequency has been consistently observed in the Raman spectra of SiNWs

and has been related to the compressive stress from the oxide skin at the wire surface (118). The Raman spectra also show prominent features at ~ 504 and 511 cm^{-1} for SiNWs with diameter distribution of 13 ± 3 and 15-60 nm, respectively (Fig. 2c and 2b). In both cases the Raman peaks are downshifted and broaden respect to that of bulk silicon. Moreover the intensity of the red shift seems to be related to the diameter of the nanowire.

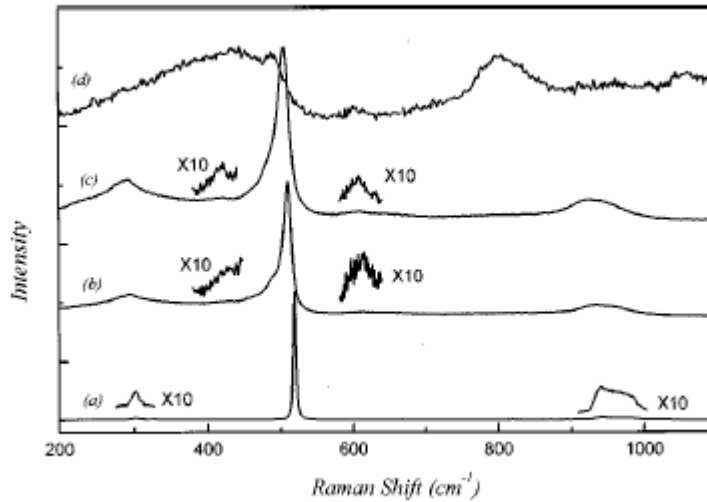


Figure 2.18 Raman spectra of (a) crystalline silicon, (b) SiNW with 20 nm diameter, (c) SiNW with 13 nm diameter, and (d) nanowires of SiO_2 (117).

Whereas it is well-known that effects of sample heating caused by laser radiation and compressive stress give rise to a frequency shifts of Raman peaks, the cause for the frequency shift of the Raman bands of SiNW is the confinement of the phonon along the nanowire the cause. In an ideal crystal, the correlation length is infinite, the phonon eigenstates are plane waves and therefore, the usual $k = 0$ momentum selection

rule of the first-order Raman spectrum can be satisfied. As the crystallite is reduced to the nanoscaled, the crystal momentum conservation rules are relaxed, allowing phonons with wave vector $|k| = |k'| \pm 2\pi/L$ to participate in the first-order Raman scattering. Here k' is the wave vector of the incident light and L is the size of the crystal. As a result, redshift, broadening, and asymmetry of the first-order optical phonon are observed (117, 119).

REFERENCES

- 1 S. Iijima, Nature 354, 56 (1991)
- 2 D. Kim, Encyclopedia of nanoscience and Nanotechnology, edited by H.S. Nalwa, V.5, p. 879-894 (2004)
- 3 S. Iijima, T. Ichihashi, Nature, 363, 603 (1993)
- 4 D.S. Bethune, C.H. Kiang, M.S. de Vries, G. Gorman, R. Savoy, J. Vasquez, R. Beyers, Nature, 363, 605 (1993)
- 5 N. Hamada, S. Sawada, A. Oshiyama, Phys. Rev. Lett. 68, 1579 (1992)
- 6 J.W. Mintmire, B.I. Dunlap, C.T. White, Phys. Rev. Lett. 68, 631 (1992)
- 7 R. Saito, M. Fujita, G. Dresselhaus, M.S. Dresselhaus, Appl. Phys. Lett. 60, 2204 (1992)
- 8 T. W. Odom, J.L. Huang, C. M. Lieber, Ann. N.Y. Acad. Sci. 960, 203 (2002)
- 9 M. S. Dresselhaus, G. Dresselhaus, P. C. Eklund, Science of Fullerenes and Carbon Nanotubes, Academic Press, San Diego, pp. 756 (1996)
- 10 S.J. Tans , A.R.M. Verschueren, C. Dekker, Nature 393, 49 (1998)

- 11 T. Rueckes, K. Kim, E. Joselevich, G.Y. Tseng, C.L. Cheung, C.M. Lieber, *Science* 289, 94 (2000)
- 12 M. Freitag, M. Radosavljevic, Y. Zhou, A.T. Johnson, W.F. Smith, *Appl. Phys. Lett.* 79, 3326 (2001)
- 13 S.J. Wind, J. Appenzeller, R. Martel, V. Derycke, Ph. Avouris, *Appl. Phys. Lett.* 80, 3817 (2002)
- 14 M.A.El. Khakani, J. H. Yi, *Nanotechnology* 15, S534 (2004)
- 15 S.S. Wong, E. Joselevich, A.T. Woolley, C.L. Cheung, C.M. Lieber, *Nature* 394, 52 (1998)
- 16 P. Kim, C.M. Lieber, *Science* 286, 2148 (1999)
- 17 T.W. Ebbensen, P.M. Ajayan, *Nature* 358, 220 (1992)
- 18 H. Zhang, X. Xue, D. Wang, Y. He, S. Peng, *Mater. Chem.phys.* 58, 1 (1999)
- 19 Y. Ando, X. Zhao, H. Kataura, Y.Achiba, K. Kaneto, M. Tsuruta, S. Uemura, S. Iijima, *Diamond Rel. Mater.* 9, 847 (2000)
- 20 M. Cadek, R. Murphy, B. McCarthy, A. Drury, B.Lahr, R.C. Barklie, M. in het Panhuis, J.N.Coleman, W.J. Blau, *Carbon* 40, 923 (2002)
- 21 D.T. Colbert, J. Zhang, S. M. McClure, P. Nikolaev, Z. Chen, J.H. Hafner, D.W. Owens, P.G. Kotula, C.B. Carter, J.H. Weaver, A.G. Rinzler, R.E. Smalley, *Science* 266, 1218 (1994)
- 22 C. Journet, W. K. Maser, P.Bernier, A. Loiseau, M.L. delaChapelle, S. Lefrant, P. Deniard, R.Lee, and J.E. Fischer, *Nature* 388, 756 (1997)
- 23 X. Zhao, et al., *Bull. Res. Inst. Meijo Univ.* 1, 7 (1996)
- 24 A. Thess, R. Lee, P. Nikolaev, H. Dai, P. Petit, J. Robert, C. Xu, Y. H. Lee, S. G. Kim, A.G. Rinzler, D.T. Colbert, G. E. Scuseria, D. Tománek, J.E. Fischer, R. E. Smalley, *Science* 273, 483 (1996)
- 25 T. Guo, P. Nikolaev, A. Thess, D.T. Colbert, R.E. Smalley, *Chem. Phys. Lett.* 243, 49 (1995)

- 26 S. Iijima, T. Wakabayashi, and Y. Achiba, *J. Phys. Chem.* 100, 5839 (1996)
- 27 T. Wakabayashi, D. Kasuya, H. Shiromaru, S. Suzuki, K. Kikuchi, Y. Achiba, *Z. Phys. D* 40, 414 (1997)
- 28 M. Yudasak, T. Komatsu, T. Ichihashi, Y. Achiba, S. Iijima, *J. Phys. Chem. B* 102, 4892 (1998)
- 29 M. Yudasaka, M. Zhang, S. Iijima, *Chem. Phys. Lett.* 323, 549 (2000)
- 30 H.J. Dai, A. G. Rinzler, P. Nikolaev, A. Thess, D.T. Colbert, and R. E. Smalley, *Chem. Phys. Lett.* 260, 471 (1996)
- 31 P. C. Eklund, B. K. Pradhan, U. J. Kim, and Q. Xiong, J. E. Fischer, A. D. Friedman, B. C. Holloway, K. Jordan, M. W. Smith, *Nano Lett.* 2, 561 (2002)
- 32 H. Dai, *Phys. World* 13, 43 (2000)
- 33 H. Dai, J. Kong, C. Zhou, N. Franklin, T. Tombler, A. Cassell, S. Fan, M. Chapline, *J. Phys. Chem. B*, 103, 11246 (1999)
- 34 S. Huang, B. Maynor, X. Cai, J. Liu, *Adv. Mater.*, 15, 1651 (2003)
- 35 A. R. Harutyunyan, B. K. Pradhan, U. J. Kim, G. Chen, P. C. Eklund, *Nano Lett.* 2, 525 (2002)
- 36 Y. Murakami, Y. Miyauchi, S. Chiashi, S. Maruyama, *Chem. Phys. Lett.* 377, 49 (2003)
- 37 C.L. Cheung, A. Kurtz, H. Park, C.M. Lieber, *J. Phys. Chem. B*, 106, 2429 (2002)
- 38 O. Jost, A.A. Gorbunov, J. Moller, W. Pompe, A. Graff, R. Friedlein, X. Liu, M.S. Golden, J. Fink, *Chem. Phys. Lett.* 339, 297 (2001)
- 39 D.E. Resasco, W. E. Alvarez, F. Pompeo, L. Balzano, J.E. Herrera, B. Kitiyanan, A. Borgna, *J. Nanopart. Res.* 4, 131 (2002)
- 40 B. Kitiyanan, W.E. Alvarez, J.H. Harwell, D.E. Resasco, *Chem. Phys. Lett.* 317, 497 (2000)

- 41 J.E. Herrera, L. Balzano, A. Borgna, W. E. Alvarez, D.E. Resasco, J. Catal. 204, 129 (2001)
- 42 W.E. Alvarez, B. Kitiyanan, A. Borgna, D.E. Resasco, Carbon 39, 547 (2001)
- 43 D. Ciuparu, Y. Chen, S. Lim, Y. Yang, G.L. Haller, L. Pfefferle, J. Phys. Chem. B 108, 15565 (2004)
- 44 D. Ciuparu, Y. Chen, S. Lim, G.L. Haller, L. Pfefferle, J. Phys. Chem. B, 108, 10196 (2004)
- 45 R. Sen, A. Govindaraj, C. N. R. Rao, Chem. Phys. Lett. 267 276 (1997)
- 46 R. Sen, A. Govindaraj and C. N. R. Rao, Chem. Mater. 9, 2078 (1997)
- 47 M. J. Bronikowski, P. A. Willis, D. T. Colbert, K. A. Smith and R. E. Smalley, J. Vac. Sci. Technol. A 19, 1800 (2001)
- 48 A.M. Cassell, N.R. Franklin, T.W. Tomblor, E.M. Chan, J. Han, H.J. Dai, Am. Chem. Soc. 121, 7975 (1999)
- 49 V. Derycke, R. Martel, M. Radosvljevic, F.M.R. Ross, P. Avouris, Nano Lett. 2, 1043 (2002)
- 50 N.R. Franklin, Y.M. Li, R.J. Chen, A. Javey, H.J. Dai, Appl. Phys. Lett. 79, 4571 (2001)
- 51 E. Joselevich, C.M. Lieber, Nano Lett. 2, 1137 (2002)
- 52 B. Zheng, C. Lu, G. Gu, A. Makarovski, G. Finkelstein, J. Liu, Nano Lett. 2, 895 (2002)
- 53 S. Huang, X. Cai, C. Du, and J. Liu, J. Phys. Chem. B 107, 13251 (2003)
- 54 S. Huang, X. Cai, J. Liu, J. Am. Chem. Soc. 125, 5636 (2003)
- 55 S. Huang, B. Maynor, X. Cai, J. Liu, Adv. Mater. 15, 1651 (2003)
- 56 Y. Murakami, S. Chiashi, Y. Miyauchi, M. Hu, M.Ogura, T. Okubo, S. Maruyama, Chem. Phys. Lett. 385 298 (2004)

- 57 K. Hata, D. N. Futaba, K. Mizuno, T. Namai, M. Yumura, S. Iijima, *Science* 306, 1362 (2004)
- 58 S. Amelinckx, A. Lucas, P. Lambin, *Rep. Prog. Phys.* 62, 1471 (1999)
- 59 L.C. Quin, *J. Mater. Res.* 9, 2450 (1994)
- 60 Z. L. Wang, C. Hui, “Electron microscopy of nanotubes”, Kluwer academic publishers (2003)
- 61 S. A. Asher, *Anal. Chem.* 65, 59A (1993)
- 62 S. A. Asher, *Anal. Chem.* 65, 201A (1993)
- 63 A. Kasuya, M. Sugano, T. Maeda, Y. Saito, K. Tohji, H. Takahashi, Y. Sasaki, M. Fukushima, Y. Nishina and C. Horie, *Phys. Rev. B* 57, 4999 (1998)
- 64 M. S. Dresselhaus, G. F. Dresselhaus and R Saito, *Solid State Commun.* 84, 201 (1992)
- 65 E. Richter, and K. R. Subbaswamy, *Phys. Rev. Lett.* 79, 2738 (1997)
- 66 M. A Pimenta, A. Marucci, S.A. Empedocles, M. G, Bawendi, E. B. Hanlon, A. M. Rao, P. C. Eklund, R. E. Smalley, G. Dresselhaus and M. S. Dresselhaus, *Phys. Rev. B* 58, R16016 (1998)
- 67 C. T. White and T. N. Todorov, *Nature* 393, 240 (1998)
- 68 D. Östling, D. Tománek, A. Rosén, *Phys. Rev. B* 55, 13980 (1997)
- 69 H. Kataura, Y. Kumazawa, Y. Maniwa, I. Umez, S. Suzuki, Y. Ohtsuka, Y. Achiba, *Synth. Met.* 103, 2555 (1999)
- 70 P. Corio, S. D. M. Brown, A. Marucci, M. A. Pimenta, K. Kneipp, G. Dresselhaus, M. S. Dresselhaus, *Phys. Rev. B* 61, 13202 (2000)
- 71 S. Reich and C. Thomsen, *Phys. Rev. B*, 62, 4273 (2000)
- 72 A. Kukovecz, Z. Konya, I. Kiricsi, *Encyclopedia of Nanoscience and Nanotechnology*, edited by H.S. Nalwa, Vol. 9, 923-946 (2004)

- 73 R. Saito, T. Takeya, T. Kimura, G. Dresselhaus and M. S. Dresselhaus, Phys. Rev. B 57, 4145 (1998)
- 74 S. Bandow, S. Asaka, Y. Saito, A. M. Rao, L. Grigorian, E. Richter, P. C. Eklund. Phys. Rev. Lett. 80, 3779 (1998)
- 75 A. M. Rao, E. Richter, S. Bandow, B. Chase, P. C. Eklund, K. A. Williams, S. Fang, K. Subbaswamy, M. Menon, A. Thess, R. E. Smalley, G. Dresselhaus, M. S. Dresselhaus Science 187, 275 (1997)
- 76 A. M. Rao, J. Chen, E. Richter, U. Schlecht, P. C. Eklund, R. C. Haddon, U. D. Venkateswaran, Y.-K. Kwon, D. Tomanek, Phys. Rev. Lett., 86, 3895 (2001)
- 77 Z. H. Yu., L.E. Brus, J. Phys. Chem. B, 105, 6831 (2001)
- 78 M. Milnwe, J. Kuri, M. Hulman, H. Kuzmany, Phys. Rev. Lett., 84, 1324 (2001)
- 79 J. E. Herrera, L. Balzano, F. Pompeo and D. E Resasco, J. Nanosci. Nanotech., 3, 133 (2003)
- 80 F. Tuinstra, J.L. Koenig, J. Phys. Chem., 53, 1126 (1970)
- 81 R.P. Vidano, D.B. Fishbach, L.J. Willis, T.M. Loehr, Solid State Commun., 39, 341 (1981)
- 82 H. Jantoljak, U. Kuhlmann, C. Thomsen, S. Curran, S. Roth, W. Maser, C. Journet, P. Bernier, Mol. Cryst. Liq. Cryst. Sci. Technol., Sect. C 10, 145 (1998)
- 83 A. Jorio, C. Fantini, M.S.S. Dantas, M.A. Pimenta, A.G. Souza Filho, Ge. G. Samsonidze, V.W. Brar, G. Dresselhaus, M.S. Dressaelhaus, A.K. Swan, M.S. Unlu, B.B. Goldberg, R.Saito, Phys. Rev. B, 66, 115411 (2002)
- 84 A. Jorio, A.G. Souza Filho, G. Dresselhaus, M.S. Dresselhaus, A.K. Swan, M. S. Unlu, B. Goldberg, M.A. Pimenta, J.H. Hafner, C.M. Lieber, R. Saito, Phys. Rev. B, 65, 155412 (2002)
- 85 S.D.M. Brown, A. Jorio, P. Corio, M.S. Dresselhaus, G. Dresselhaus, R. Saito, K. Kneipp, Phys. Rev. B 63, 155414 (2001)
- 86 S. M. Bachilo, M. S. Strano, C. Kittrell, R.H. Hauge, R.E. Smalley, R. B. Weisman, Science 298, 2361 (2002)

- 87 T. W. Odom, J.-L. Huang, P. Kim, C. M. Lieber, *J. Phys. Chem. B* 104, 2794 (2000)
88. Y.-P. Sun, B. Zhou, K. Henbest, K. Fu, W. Huang, Y. Lin, S. Taylor and D. L. Carroll, *Chem. Phys. Lett.* 351, 349 (2002)
89. J. E. Riggs, Z. Guo, D. L. Carroll and Y.-P. Sun, *J. Am. Chem. Soc.* 122, 5879 (2000)
90. M. J. O'Connell, S. M. Bachilo, C. B. Huffman, V. C. Moore, M. S. Strano, E. H. Haroz, K. L. Rialon, P. J. Boul, W. H. Noon, C.r Kittrell, J. Ma, R. H. Hauge, R. B. Weisman, R. E. Smalley *Science* 297, 593 (2002)
- 91 M.F. Islam, E. RojasD.M. Bergey, A.T. Johnson, A.G. Yodh, A. G. *Nano Lett.* 3, 268 (2003)
- 92 O. Matarredona, H. Rhoads, Z. Li, J.H. Harwell, L. Balzano, D. E. Resasco, *J. Phys. Chem. B* 107, 13357 (2003)
- 93 Y. Cui, X. Duan, J. Hu, C.M. Lieber, *J. Phys. Chem. B* 104, 5213 (2000)
- 94 Y. Cui, Q. Wei, H. Park, C.M. Lieber, *Science* 293, 1289 (2001)
- 95 J. Hahm, C.M. Lieber, *Nano Lett.*, 4, 51 (2004)
- 96 Y. Cui, Z. Zhong, D. Wang, W. U. Wang, C.M. Lieber, *Nano Lett.*3, 149 (2003)
- 97 A.M. Morales, C.M. Lieber, *Science* 279, 208 (1998)
- 98 Y. F. Zhang, Y.H. Tang, H.Y. Peng, N.Wang, C.S. Lee, I. Bello, S.T. Lee, *Appl. Phys. Lett.* 75, 1842 (1999)
- 99 D.P. Yu, C.S. Lee, I. Bello, X.S. Sun, Y.H. Tang, G.W. Zhou, Z.G. Bai, Z. Zhang, S.Q. Feng, *Solid State Commun.* 105, 403 (1998)
- 100 K. Sattler, "Silicon Nanowires", *Encyclopedia of Nanoscience and Nanotechnology*, Edited by H.S. Nalwa, Vol. 9, 815-835 (2004)
- 101 N. Wang, Y.F Zhang, Y.H. Tang, C.S. Lee, S.T. Lee, *Appl. Phys. Lett.* 73, 3902 (1998)

- 102 Y. Zhang, Q. Zhang, N. Wang, Y. Yan, H. Zhou, J. Zhu, *J. Cryst. Growth* 226, 185 (2001)
- 103 Z.Q. Liu, S.S. Xie, W.Y. Zhou, L.F. Sun, Y.B. Li, D.S. Tang, X.P. Zou, C.Y. Wang, G. Wang, *J. Cryst. Growth* 224, 230 (2001)
- 104 J. Westwater, D.P. Gosain, S. Tomiya, S. Usui, *J. Vac. Sci. Technol. B* 15, 554 (1997)
- 105 J. Westwater, D.P. Gosain, S. Usui, *Phys. Stat. Sol.* 165, 37 (1998)
- 106 M. K. Sunkara, S. Sharma, Miranda, G. Lian, E. C. Dickey, *Appl. Phys. Lett.* Vol. 79, 1546 (2001)
- 107 Z.Pan, S. Dai, D.B. Beach, D.H. Lowndes, *Nano Lett.* 3, 1279 (2003)
- 108 J. HU, T. W. ODOM, C.M. LIEBER, *Acc. Chem. Res.* 32, 435 (1999)
- 109 Y. Cui, L. J. Lauhon, M. S. Gudiksen, J.Wang, C. M. Lieber, *Appl. Phys. Lett.* 78, 2214 (2001)
- 110 X. -Y. Zhang, L. -D Zhang, G.-W Meng, G. -H Li, N.-Y Jin-Phillipp, F. Phillipp, *Adv. Mater.*13, 1238 (2001)
- 111 K.-K Lew, C. Reuther, A.H. Carim, J.M. Redwing, *J. Vac. Sci. Technol. B* 20, 389 (2002)
- 112 N. Wang, Y.H. Tang, Y.F. Zhang, C.S. Lee, S.T. Lee, *Phys. Rev. B* 58, R16024 (1998)
- 113 N. Wang, Y.H. Tang, Y.F. Zhang, C.S. Lee, I. Bello, S.T. Lee, *Chem. Phys. Lett.* 299, 237 (1999)
- 114 H Pan, S Lim, C Poh, H Sun, XWu, Y Feng, J Lin, *Nanotech.* 16, 417 (2005)
- 115 Y. Wu, Y. Cui, L. Huynh, C. J. Barrelet, D.C. Bell, C. M. Lieber, *Nano Lett.*, 4,433 (2004)
- 116 G.W. Zhou, Z. Zhang, Z.G. Bai, S.Q. Feng, D.P. Yu, *Appl. Phys. Lett.* 73, 677 (1998)

- 117 R.P. Wang, G.W. Zhou, Y.L. Liu, S.H. Pan, H.Z. Zhang, D.P. Yu, Z. Zhang, Phys. Rev. B, 61, 16827 (**2000**)
- 118 D. Papadimitriou, A.G. Nassiopoulos, J. Appl. Phys. 84, 1059 (**1998**)
- 119 H. Richter, Z.P. Wang, L.Ley, Solid State Commun. 39, 625 (**1981**)

CHAPTER 3

TEMPERATURE DEPENDENCE OF THE QUALITY OF SILICON NANOWIRES PRODUCED OVER A TITANIA-SUPPORTED GOLD CATALYST

3.1. INTRODUCTION

Silicon nanowires (SiNWs) have been widely studied because of their unique growth behavior, their electrical and mechanical properties, as well as their potential applications in nanoelectronic devices and circuits (1-3). Several synthesis methods have been reported in the literature including laser ablation (1, 4-5), chemical vapor deposition (3,6-13), and thermal evaporation (14-17). Among these synthesis methods, the most widely used has been chemical vapor deposition (CVD), whose production mechanism has been explained in terms of a vapor-liquid-solid (VLS) growth model. In this mechanism, the role of the metal catalyst is to form a liquid alloy droplet of relatively low solidification temperature (6). Gold has been generally used in this process because the Au-Si alloy has a low eutectic temperature in which a silicon-rich eutectic alloyed is formed. Therefore, the process can take place at temperatures lower than those by laser ablation or thermal evaporation. Besides gold, other metals such nickel and iron have been used as catalysts in the CVD method. For instance Zhang et al. (3) used a thin Ni

film to obtain silicon nanowires. In that particular case, the optimum reaction temperature was 900°C which is close to the eutectic temperature of the Si/Ni system (966°C). In the case of iron, Liu et al. used a porous Fe/SiO₂ catalyst prepared by a sol gel process (11) and reported that very straight silicon nanowires could be produced at 500°C. The silicon sources that are usually used for the CVD process are silane (SiH₄) and silicon tetrachloride (SiCl₄). Westwater et al. (7,8) have reported that the use of silane as Si source to prepare silicon nanowires via CVD yields much thinner nanowires than the ones produced from SiCl₄ (3,6). Furthermore, silane is easily decomposed at lower temperature than SiCl₄ so the synthesis reaction can be carried out at relatively low temperatures (3,7,8).

For a long time, gold has been considered a catalytically inactive metal. However, recent studies (18, 19) have shown that its reactivity can be drastically altered when it is in the form of very small clusters and supported on a suitable substrate. Highly dispersed Au supported on titania, alumina, or other supports exhibits a very high activity for several reactions. One of the supports used that have resulted in the greatest activity enhancement has been titania, TiO₂ (20-22). In the production of Si nanowires, we may expect that the decomposition of the silane precursor can be accelerated by the presence of a catalytic surface. Therefore, it is important to investigate the production of Si nanowires on a catalyst such as Au/TiO₂, which has shown enhanced catalytic activity.

Most CVD nanowire growth procedures reported in the literature have focused on flat substrates, over which catalytic particles have been deposited. The present contribution reports the growth of silicon nanowires by silane CVD on Au-containing porous TiO₂ powders of high-surface area. In this report, the catalyst was prepared by the incipient wetness impregnation technique, which is perhaps the simplest method for catalysts preparation. The growth temperature has been varied from 300 to 600°C in order to find the optimum conditions for SiNWs growth. The product was characterized by TEM and SEM electron microscopy combined with Raman, and X-ray photoelectron spectroscopy (XPS). The fresh catalyst and product synthesized at 600°C were also characterized by EXAFS.

3.2. EXPERIMENTAL

Silicon nanowires were prepared by chemical vapor deposition of silane on a 1 wt % Au/TiO₂ catalyst, synthesized by incipient wetness impregnation of AuCl₃ onto calcined TiO₂ (surface area 50m²/g). After impregnation, the catalyst was dried at 120°C and then reduced in hydrogen flow at 200°C for 2 hours. The catalyst was then placed into a quartz reaction cell, preheated at 200°C in vacuum (pressure lower than 10⁻³ Torr) for 1 hour and then further heated to the reaction temperature. When the temperature was stabilized, the silane was fed into the reaction cell and kept for 30 minutes. The approximate pressure inside the reactor was about 400 Torr.

Before the silane decomposition reaction, the color of the catalyst was a light purple. After the reaction, the sample treated at 500°C displayed a yellowish green. By contrast, those reacted at 300, 400, and 600°C were dark blue, almost black.

The products were examined by scanning electron microscopy on a SEM, JEOL JSM-880 and by transmission electron microscopy on a TEM, JEOL JEM-2000FX. Raman spectra of the Si deposits were obtained using a Jovin Yvon-Horiba LabRam 800 equipped with a CCD detector with a laser excitation source of 632nm (He-Ne laser). X-ray photoelectron spectroscopy (XPS) was conducted on a Physical Electronics PHI 5800 ESCA system equipped with monochromatic Al K_{α} X-ray source to quantify the surface composition and the oxidation state of the silicon product. The binding energies were corrected by reference to the C(1s) line at 284.5 eV. The fitting of the XPS spectra and the quantification of the surface atomic ratios were obtained with Gauss-Lorentz peaks, using the MultiPak software from Physical Electronics.

X-ray absorption characterization of fresh and spent catalysts was conducted at the National Synchrotron Light Source at Brookhaven National Laboratory, using beam line X-18B equipped with a Si (1 1 1) crystal monochromator. The X-ray ring at the NSLS has an energy of 2.5 GeV and ring current of 80–220 mA. The EXAFS experiments were conducted in a stainless steel sample cell at liquid nitrogen temperature.

3.3. RESULT AND DISCUSSION

Within the range of reaction temperatures investigated, the sample obtained at 500°C produced the highest density of Si nanowires with the best structure. The SEM observations shown in Figure 3.1 illustrate the type of Si structures obtained in this sample. It can be observed that large quantities of SiNWs are formed over the Au/TiO₂ catalyst at 500°C. The SEM micrographs also show that these nanowires have a very high aspect ratio, with lengths ranging from 10 to 40 micrometers and diameters in the range 8-35 nm. The TEM analysis of this sample further demonstrated the high uniformity of the nanowires along their axis. As seen in Figure 3.2, almost the full body of the nanowire is well-crystallized silicon while a very thin amorphous layer (thinner than about 3 nm) covers the surface. In the inset, the electron diffraction pattern is included. This perfect pattern indicates that the nanowire is essentially a Si single crystal. As shown below, a small amount of silicon oxide was detected by XPS. This oxide may be the thin amorphous layer that cover the surface of the nanowires.

To compare the structure of the Si deposits produced at different temperatures, we analyzed the various products by SEM. As illustrated in Figure 3.3, striking differences are observed as a function of the reaction temperature. In contrast with the high density of well-structured nanowires obtained at 500°C, very low densities were observed at either lower (400°C) or higher temperatures (600°C). No SiNW were observed after reaction at 300°C.

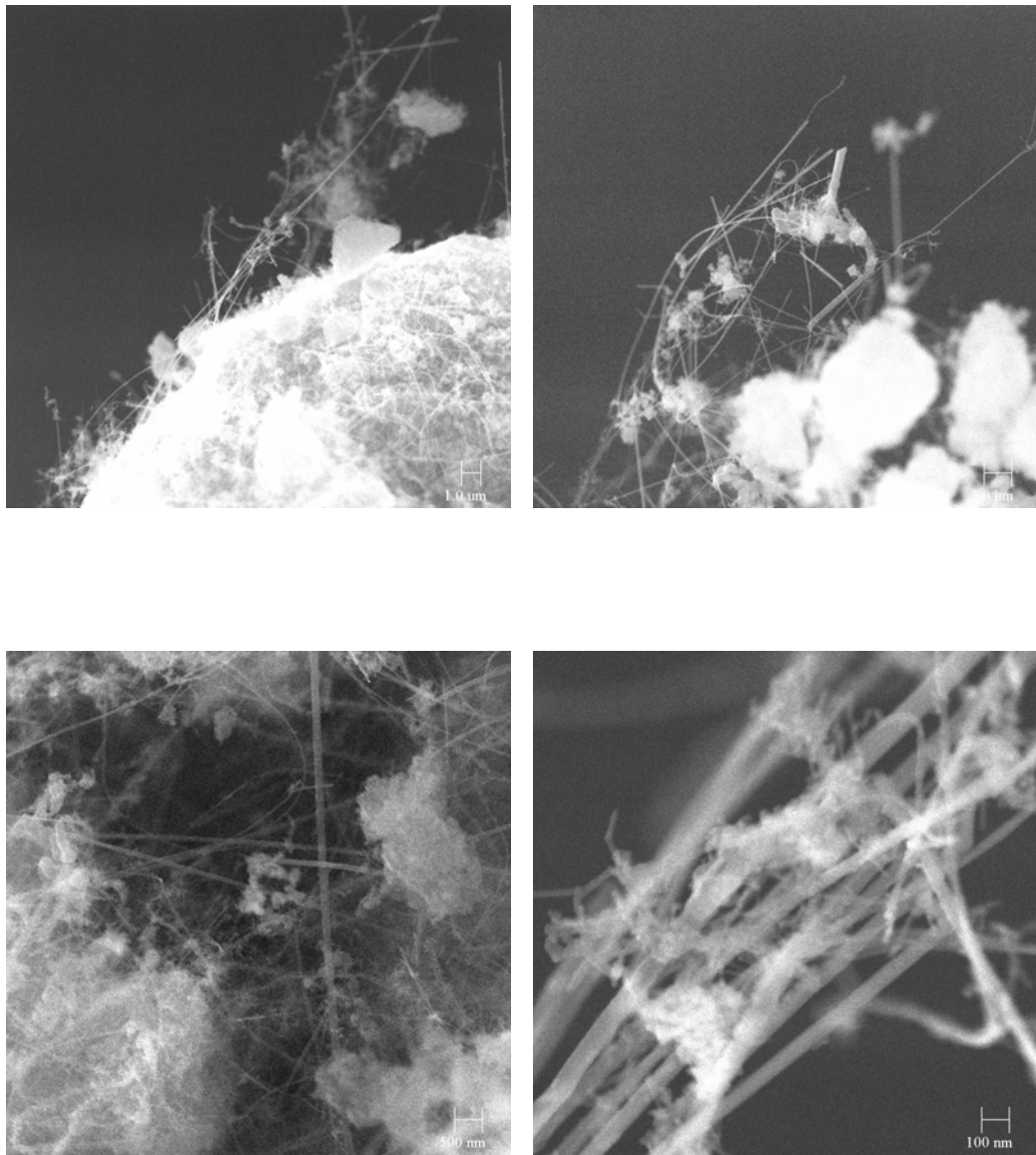


Figure 3.1 SEM micrograph of silicon nanowires produced at 500°C over a titania supported gold catalyst.

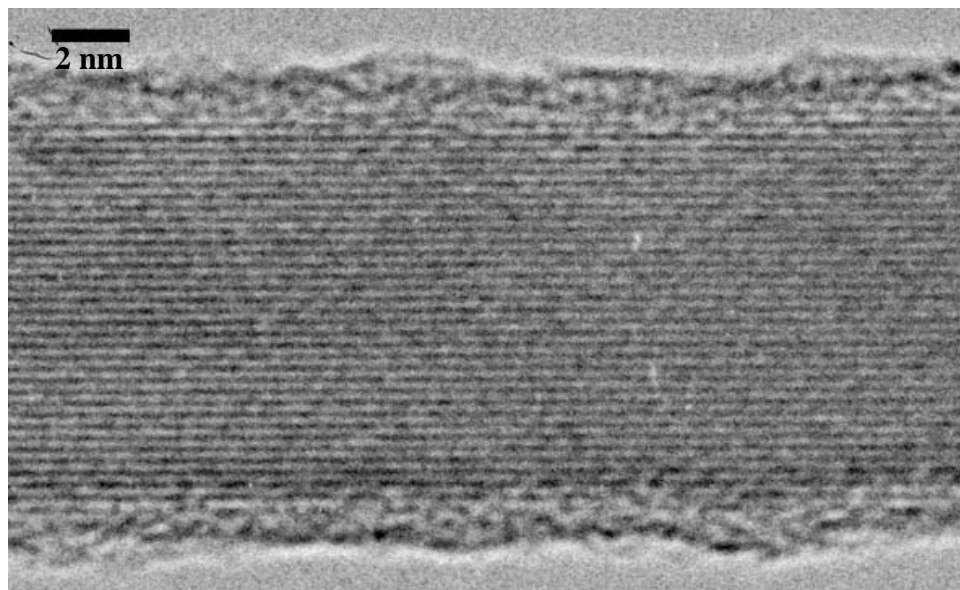
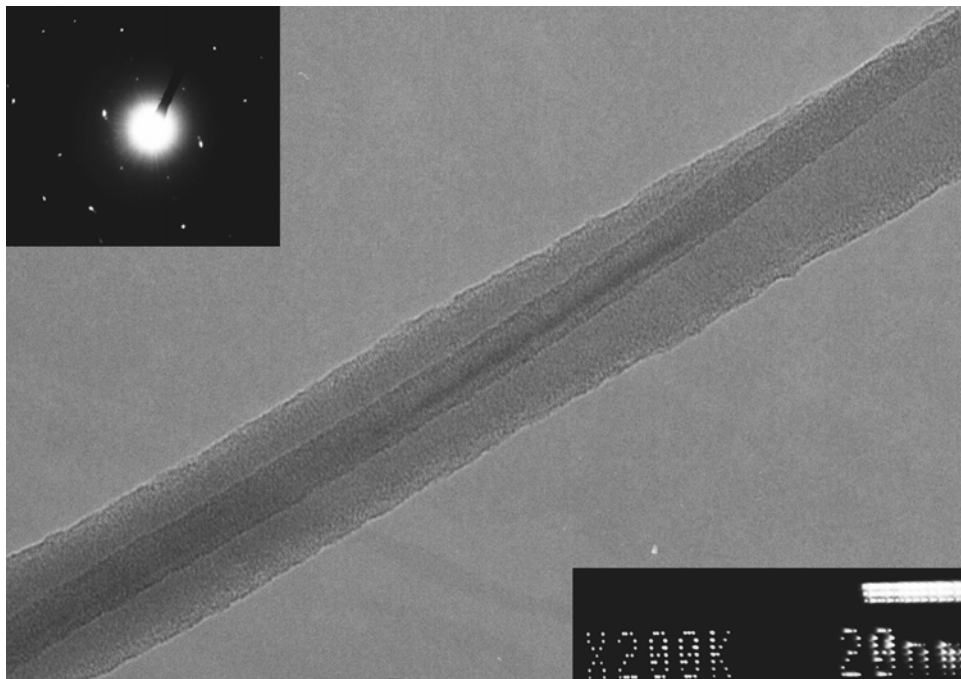


Figure 3.2 TEM micrograph of silicon nanowires produced at 500°C over a titania supported gold catalyst.

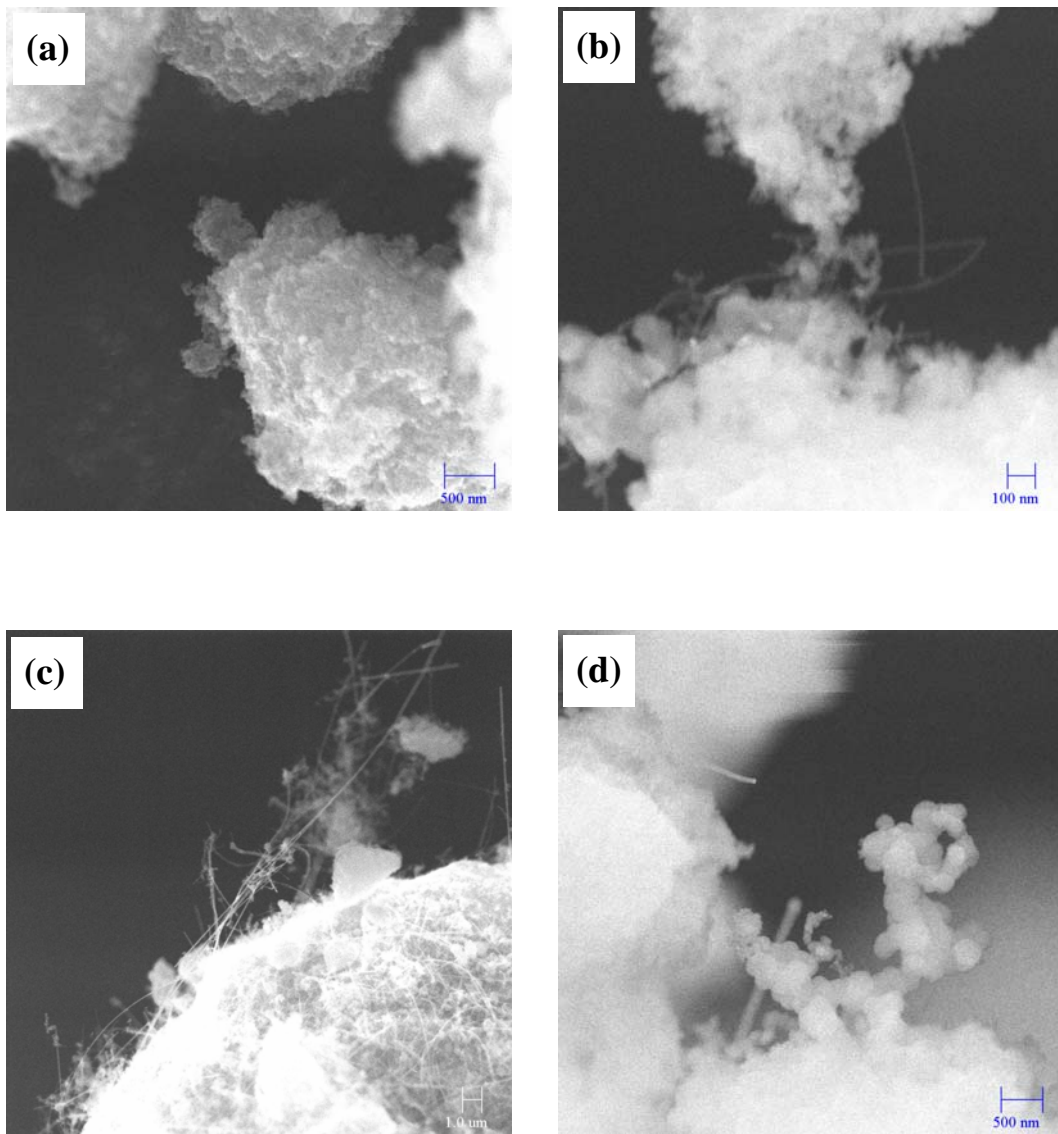


Figure 3.3 SEM images of different silicon containing products obtained at four different reactions temperatures: (a) 300°C, (b) 400°C, (c) 500°C and (d) 600°C.

To obtain a more quantitative comparison of the density of SiNW left on the catalyst surface after reaction at different temperatures, the samples were analyzed by X-ray photoelectron spectroscopy (XPS). The XPS intensity ratio of Si (2p) to Ti ($2p_{3/2} + 2p_{1/2}$) can be taken as a relative measure of the Si nanowire density. The results shown in Figure 3.4 are in perfect agreement with the SEM observations.

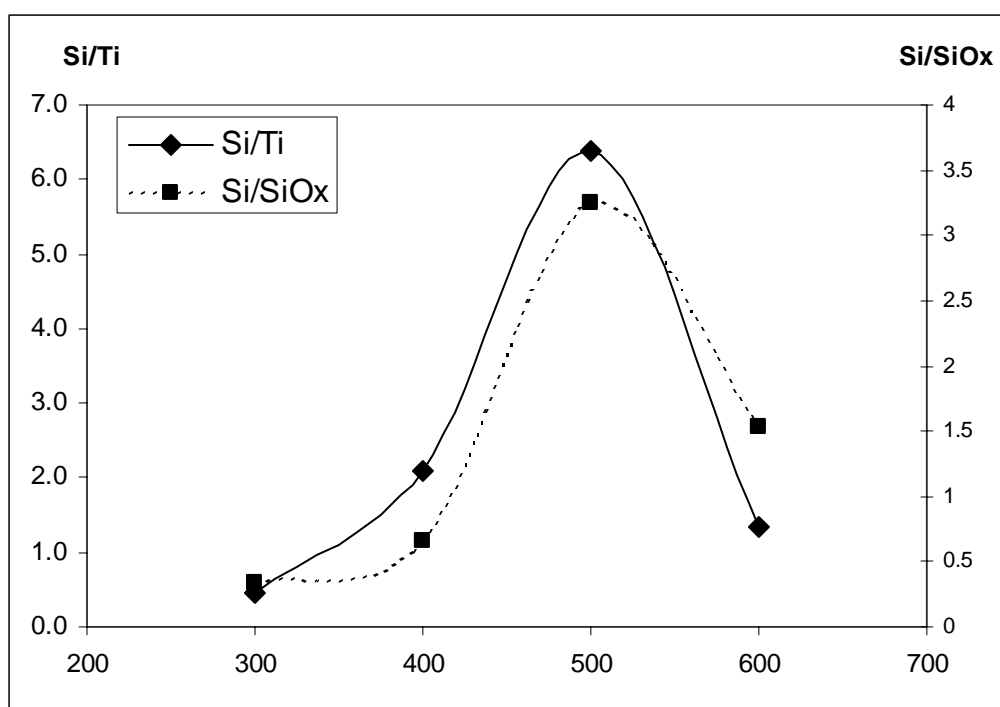


Figure 3.4 Silicon to titanium surface atomic ratio (diamonds) and Si^0 to Si^{+4} surface atomic ratio (squares) as calculated from XPS analysis of the Si2p and Ti2p lines.

The maximum Si/Ti ratio was obtained on the sample prepared at 500°C, with much lower values for those prepared at either lower or higher temperatures. At the same time, to evaluate the degree of Si oxidation on the four samples after exposure to air at

ambient temperature, the ratio of metallic Si to oxidized Si was obtained from the XPS spectra. This ratio was calculated by fitting the Si signal using two different Gaussian components, one corresponding to Si⁰ (E_B= 99 eV) and the other one to Si⁺⁴ (E_B= 103 eV). Again, in agreement with the TEM observations, the sample produced at 500°C showed a much lower degree of oxidation than the other samples. The high Si/Si⁺⁴ ratio on the sample obtained at this temperature reveals that the SiNWs are composed mostly of silicon with a small contribution from silicon oxide. At 300, 400, and 600°C the Si/Si⁺⁴ ratio greatly decreases. It may be expected that, under these non-optimal conditions, more amorphous Si deposits are formed, which are therefore more prone to oxidation. It is also interesting to notice that the Si/Si⁺⁴ ratio for the product obtained at 600°C is slightly higher than those obtained below 500°C.

Raman spectroscopy was employed to further characterize the different products obtained in this study. Figure 3.5 shows the Raman spectra for the samples obtained at the four different temperatures. Since both, the bare catalyst and the product may generate Raman bands, the spectra of a reference silicon wafer and that of the fresh catalyst are included in the figure. The spectrum for the fresh catalyst reveals the presence of broad bands at 400, 516 and 639 cm⁻¹, while the Silicon wafer shows a sharp and symmetric peak at 520.5 cm⁻¹. Therefore, the band at 518 cm⁻¹ observed on the product obtained at 500°C can be ascribed to Si deposits. The observed downshift is indeed significant, reproducible, and has been previously observed. A downshift respect

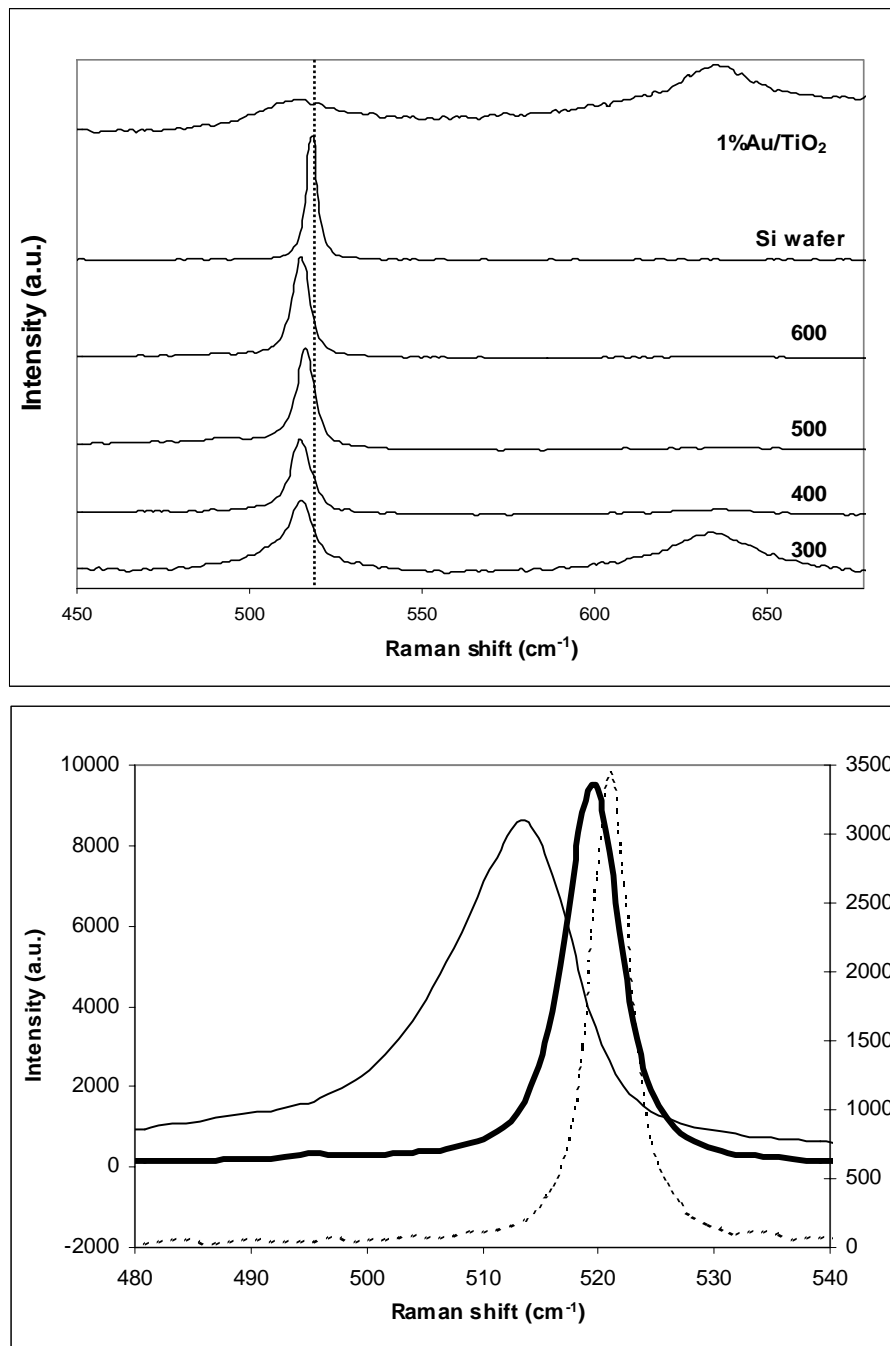


Figure 3.5 Upper panel: Raman spectra of the silicon nanowires produced at four different temperatures. The Raman spectra of silicon wafer and of the fresh Au/TiO₂ catalyst are also included for comparison. Lower panel: Raman spectra of the silicon nanowires obtained at 500°C using two different 633nm laser powers: 3.0 mW (solid line) and 0.3mW (thick solid line).

to the Si wafer has been consistently observed and attributed to the quantum confinement of the SiNW structure (15, 12, 11, 23, 24).

It is very interesting to note that the band at 518 cm^{-1} was only observed on the product generated at 500°C . The materials produced under other reaction temperatures (300°C , 400°C , and 600°C) had the Si band located at 516 cm^{-1} . In agreement with the observations from the other techniques, the material obtained at 300°C gave a very weak Si signal, and overlapped with the spectra of the fresh catalyst, indicating a low yield of metallic Si. Another interesting variation in the Raman was observed when the power of the laser energy was varied, while keeping the excitation wavelength constant. It was found that the Raman band (Figure 3.5b) obtained using a high laser power (3.0 mW) was more asymmetric and broader than that obtained with a lower laser power (0.3mW). When the laser power was increased, the position of the 518 cm^{-1} band was shifted to 513 cm^{-1} . This phenomenon has been previously reported and it has been ascribed to nanowire heating by the laser beam. The change in the symmetry of the peak has been explained in terms of a Fano interference between scattering from the $k=0$ optic phonon and laser-induced electronic continuum electron scattering in the conduction band (24). Therefore, both band shift by heating and the asymmetry of the band are fingerprints of Si nanowires.

To explain the strong dependence of the Si nanowire yield and reaction temperature reported in this work, one needs to consider the plausible growth mechanism.

The eutectic of a Si-Au mixture is determined by the composition of X%Si Y%Au and temperature of 363°C. It is expected that at least a fraction of the supported gold will be in the molten state under most of the reaction conditions employed in this work. Therefore, the so-called vapor-liquid-solid VLS model could be evoked again to describe the SiNW growth process. According to the VLS model the growth of crystalline Si nanowire should take place in a sequence of steps that includes the catalytic decomposition of the SiH₄ over Au, followed by dissolution of Si into the molten silicon-gold solution and precipitation at the other end of the droplet in the form of crystalline Si. Depending on the reaction conditions any of these steps could be the rate-limiting. Since chemical reactions typically require a high energy of activation, one may expect a sharp (i.e. exponential) variation with temperature for the rate of silane decomposition. Conversely, the rate of diffusion is typically a less pronounced variation with temperature (i.e. square root). At low temperatures, the rate of decomposition may become very low and consequently limiting step of the overall growth rate. Under those conditions, the rate of SiNW growth would be low, but as the temperature increases, the growth would quickly increase until the rate of decomposition and diffusion become comparable. At even higher temperatures, the rate of decomposition becomes much higher than the rate of diffusion. As a result, Si may accumulate in high concentrations at the Au surface, causing the encapsulation of the particle with little growth of SiNW. At the same time, when the temperatures are exceedingly high, sintering of the Au nanoclusters may occur, which would also limit the nanowire growth and promote encapsulation. EXAFS was used to characterize the catalyst, both as a fresh catalyst and after reaction at 600°C. It

was observed that the magnitude of the Fourier Transform for the Au–Au bonds, corresponding to the spent sample was 15% higher than that of the fresh catalyst, indicating that the spent catalyst has Au particles larger than those in the fresh catalyst, which shows that some sintering of the Au clusters occurs under reaction at high temperature.

3.4. CONCLUSIONS

The production of silicon nanowires via chemical vapor deposition of silane over gold supported on TiO₂ catalyst has been investigated at varying temperatures. It was found that the optimum reaction temperature is 500°C. Silicon nanowires produced at this temperature have a well-crystallized silicon core with a very thin amorphous silicon dioxide outer layer. The length of the nanowires is in the range of 10 to 40 micrometers. At lower temperatures, nanowires are produced in lower yields and with lower quality than those obtained at the optimum temperature (500°C). Similarly, at temperatures higher than the optimum, lower yields and quality were obtained. The appearance of an optimum temperature is due to a change in rate limiting step in the growth process.

ACKNOWLEDGEMENTS

This research was conducted with financial support from the Department of Energy, Office of Basic Energy Sciences (grant No. DE-FG03-02ER15345). We also acknowledge Dr. Zhongrui Li and Dr. Guoda Lian for helping in the analysis of EXAFS and TEM, respectively.

REFERENCES

- 1 A.M. Morales, C.M. Lieber, *Science* 279, 208 (1998)
- 2 A. P. Alivisatos, *Science* 271, 933 (1996)
- 3 Y. Zhang, Q. Zhang, N. Wang, Y. Yan, H. Zhou, J. Zhu, *J. Cryst. Growth* 226, 185 (2001)
- 4 N. Wang, Y.H. Tang, Y.F. Zhang, C.S. Lee, S.T. Lee, *Phys. Rev. B* 58, R16024 (1998)
- 5 Y.F. Zhang, Y.H. Tang, N. Wang, C.S. Lee, I. Bello, S.T. Lee, *J. Cryst. Growth* 197, 136 (1999)
- 6 R.S. Wagner, W.C. Ellis, *Appl. Phys. Lett.* 4, 89 (1964)
- 7 J. Westwater, D.P. Gosain, S. Tomiya, S. Usui, *J. Vac. Sci. Technol. B* 15, 554 (1997)
- 8 J. Westwater, D.P. Gosain, S. Usui, *Phys. Stat. Sol.* 165, 37 (1998)
- 9 N. Ozaki, Y. Ohno, S. Takeda, *Appl. Phys. Lett.*, 73, 3700 (1998)
- 10 Y. Cui, L.J. Lauhon, M.S. Gudiksen, J. Wang, C.M. Lieber, *Appl. Phys. Lett.* 78, 2214 (2001)

- 11 Z.Q. Liu, S.S. Xie, W.Y. Zhou, L.F. Sun, Y.B. Li, D.S. Tang, X.P. Zou, C.Y. Wang, G. Wang, *J. Cryst. Growth* 224, 230 (2001)
- 12 J. Niu, J. Sha, X. Ma, J. Xu, D. Yang, *Chem. Phys. Lett.* 367, 528 (2003)
- 13 Z.Q. Liu, W.Y. Zhou, L.F. Sun, D.S. Tang, X.P. Zou, Y.B. Li, C.Y. Wang, G.Wang, S.S. Xie, *Chem. Phys. Lett.* 341, 523 (2001)
- 14 H.Y. Peng, Z.W.Pan, L. Xu, X.H. Fan, N. Wang, C.S. Lee, S.T. Lee, *Adv. Mat.* 13, 317 (2001)
- 15 D.P. Yu, Z.G. Bai, Y. Ding, Q.L. Hang, H.Z. Zhang, J.J. Wang, Y.H. Zou, W. Qian, G.G. Xiong, H.T. Zhou, S. Q. Feng, *Appl. Phys. Lett.* 72, 3458 (1998)
- 16 X.H. Fan, L. Xu, C.P. Li, Y.F. Zheng, C.S. Lee, S.T. Lee, *Chem. Phys. Lett.* 334, 229 (2001)
- 17 C.P. Li, X.H. Sun, N.B. Wong, C.S. Lee, S.T. Lee, B. K. Teo, *Chem. Phys. Lett.* 365, 22 (2002)
- 18 Haruta, M., *Catal. Today* 36, 153 (1997)
- 19 Bond, G. C., and Thompson, D. T., *Catal. Rev. Sci. Eng.* 41, 319 (1999)
- 20 C. Mohr, H. Hofmeister and P. Claus , *J. Catal.* 213, 86 (2003)
- 21 X-F. Lai and D. W. Goodman, *J. Mol. Catal. A*, 162, 33 (2000)
- 22 T. Akita, M. Okumura, K. Tanaka, and M. Haruta, *Journal of Catalysis* 212, 119 (2002)
- 23 J. Qi, J.M. White, A.M. Belcher, Y. Masumoto, *Chem. Phys. Lett.*, 372, 763 (2003)
- 24 R. Gupta, Q. Xiong, C.K. Adu, U. J. Kim, P.C. Eklund, *Nano Lett.*, 3, 627 (2003)

CHAPTER 4

INFLUENCE OF CATALYST SUPPORT ON THE STRUCTURE OF SILICON NANOWIRES SYNTHESIZED BY DECOMPOSITION OF SILANE ON GOLD

4.1 INTRODUCTION

Silicon nanowires (SiNWs) can be synthesized by several methods; the most widely used is chemical vapor deposition (CVD) of Si-containing compounds on Au nanoparticles that act as a catalyst. The model used to explain the growth mechanism for this method is called Vapor-Liquid-Solid mechanism (VLS) (1-8). In the VLS mechanism, the role of the metal particle is to catalyze the decomposition of the gaseous molecules and to form an alloy of relatively low melting temperature to allow for the formation of a liquid droplet through which the growing species can diffuse (1). Gold has been widely used in this process because the Au-Si alloy exhibits a eutectic at relatively low temperatures, easy to achieve under laboratory conditions (9-11).

The VLS model consists of three main steps, (i) catalytic decomposition of the Si-containing molecule, preceded by adsorption on the Au surface; (ii) diffusion of the Si

deposited over the Au surface through the liquid Au-Si alloy; and (iii) nucleation and growth of the Si nanowire after supersaturation of the liquid Au-Si alloy has been reached (12, 13). It has been proposed that the rate-limiting step for the growth process is the catalytic decomposition of the Si containing molecule on the Au surface rather than the diffusion step. For example, Lew and Redwing (12) have noted that the activation energy of 22 kcal/mol experimentally observed for the growth of Si nanowires on Au in the temperature range 400-500°C is much higher than that expected for Si diffusion in liquid metal (1-4 kcal/mol) and more consistent with a catalytic decomposition reaction.

Being a noble metal with fully occupied d-orbitals, gold has been generally considered unsuitable as a catalyst for any reaction. In fact, Au is notably unreactive for most reactions and has poor adsorption abilities (14). However, at the nanoscale level Au has been found to be a remarkably active catalyst. Recent studies (15,16) have shown that the reactivity of Au can be enhanced when it is dispersed in the form of very small clusters and supported on a suitable substrate. Specifically, the catalytic properties of Au depend on three major factors, which are the support, the preparation method, and the size of the Au clusters (17,18). On suitable metal oxide supports, Au was found to be active for several reactions, for instance Au supported on reducible metal oxides (TiO_2 , $\alpha\text{-Fe}_2\text{O}_3$, Co_3O_4) or hydroxides of alkaline earth metal ($\text{Be}(\text{OH})_2$, $\text{Mg}(\text{OH})_2$) is very active for low temperature oxidation of CO (19), while Au supported on activated carbon, TiO_2 , SiO_2 or ZrO_2 have shown unusual activity for hydrochlorination of acetylene,(20,21) and for hydrogenation of acrolein,(22,23) respectively. Additionally,

compared to platinum, Au nanoparticles are far more active for the low-temperature oxidation of certain compounds, such as CO (15).

All these studies clearly indicate how the support affects the catalytic activity of Au species in the case of solid Au particles. Therefore, it is interesting to investigate the effect of different supports on the catalytic activity of Au in the context of Si nanowires growth by chemical vapor deposition of silane in which Au is in the liquid state. In this contribution we have investigated the catalytic activity of Au supported on different metal oxides powders (TiO_2 , SiO_2 , ZrO_2 , and MgO). High-surface-area supported catalysts could have an impact if large-scale production of Si nanowires is attempted. This type of catalysts are currently used in large-scale manufacture of materials based on fluidized-bed reactor technology. The product obtained by chemical vapor deposition of silane has been characterized by transmission electron microscopy (TEM) and scanning electron microscopy (SEM) combined with Raman, and X-ray photoelectron (XPS) spectroscopies, while the fresh catalysts have been characterized using TEM and X-ray absorption spectroscopy (EXAFS, XANES).

4.2 EXPERIMENTAL

The catalysts used in this work were prepared by incipient wetness impregnation of AuCl_3 on selected supports, which are TiO_2 , SiO_2 , ZrO_2 , and MgO . The ZrO_2 support was prepared by calcination of $\text{Zr}(\text{OH})_4$ in air at 800°C . The TiO_2 was P25

from Degussa ($50 \text{ m}^2/\text{g}$), it was calcined in air at 550°C before impregnation. The SiO_2 (silica gel, $500 \text{ m}^2/\text{g}$) and MgO were obtained from Aldrich. The AuCl_3 was dissolved in distilled water and impregnated on the solid support to give a total loading of 1 wt.% of Au. After impregnation, the catalysts were dried at 120°C and then reduced under hydrogen flow at 200°C for 2 hours. A second pretreatment at 500°C in H_2 was used also for the MgO supported catalyst. Because of the nature of the MgO support (see below), an alternative catalyst preparation method based on chemical vapor deposition (CVD) was used. In this method the MgO support was heated under vacuum at 300°C for 3 hours. The pretreatment was performed in a packed bed reactor with an on/off valve at each end of the reactor, which allowed for a quick isolation of the sample after treatment. Pretreated MgO was then mixed with the appropriate amount of solid gold acetate necessary to achieve a total loading of 1.0 wt.% gold. The mixture was then reloaded on the reactor and slowly heated to 200°C to decompose the acetate. This sample will be denoted as 1% Au/MgO (CVD) to differentiate it from the sample obtained using conventional incipient wetness impregnation, which will be labeled 1% Au/MgO (IWI). Before reaction, the corresponding catalyst was placed in a quartz reactor and heated in vacuum for 2 hour, then heated to the reaction temperature. To effect the growth of Silicon nanowires silane vapor was decomposed at 500°C for 30 minutes at a total pressure of about 150 Torr.

The silicon products were examined by scanning electron microscopy, JEOL JSM-880 and by transmission electron microscopy, JEOL-2000FX. Raman spectra of the

Si deposits were obtained using a Jovin Yvon-Horiba LabRam 800 equipped with a CCD detector with a laser excitation source of 632nm (He-Ne laser). X-ray photoelectron spectroscopy (XPS) was conducted on a Physical Electronics PHI 5800 ESCA system equipped with monochromatic Al K_{α} X-ray source to quantify the surface composition and the oxidation state of the silicon product. The binding energies were corrected by reference to the C(1s) line at 284.5 eV. The fitting of the XPS spectra and the quantification of the surface atomic ratios were obtained with Gauss-Lorentz peaks, using the MultiPak software from Physical Electronics. Before reaction, the fresh catalysts were characterized by Transmission Electron microscopy and X-ray absorption. The X-ray absorption spectra were obtained at the National Synchrotron Light Source at Brookhaven National Laboratory, using beam line X-18B equipped with a Si (111) crystal monochromator. NSLS runs at dedicated mode with an energy of 2.5 GeV and ring current of 80-220 mA. The XAFS experiments were conducted in a stainless steel sample cell at liquid nitrogen temperature.

4.3. RESULT AND DISCUSSIONS

After chemical vapor deposition of silane over the Au catalysts, the products were characterized by Raman spectroscopy to determine the presence of silicon nanowires. As shown in Figure 4.1 the products obtained over the 1%Au/TiO₂, 1%Au/SiO₂, 1%Au/ZrO₂, and 1%Au/MgO (CVD) catalysts show a Raman band at about 515-518 cm⁻¹. This band is downshifted with respect to the Raman band observed for a

Si wafer (bulk crystalline Si, 520.5 cm^{-1}). This shift is due to a quantum confinement effect of nanowire structures (24).

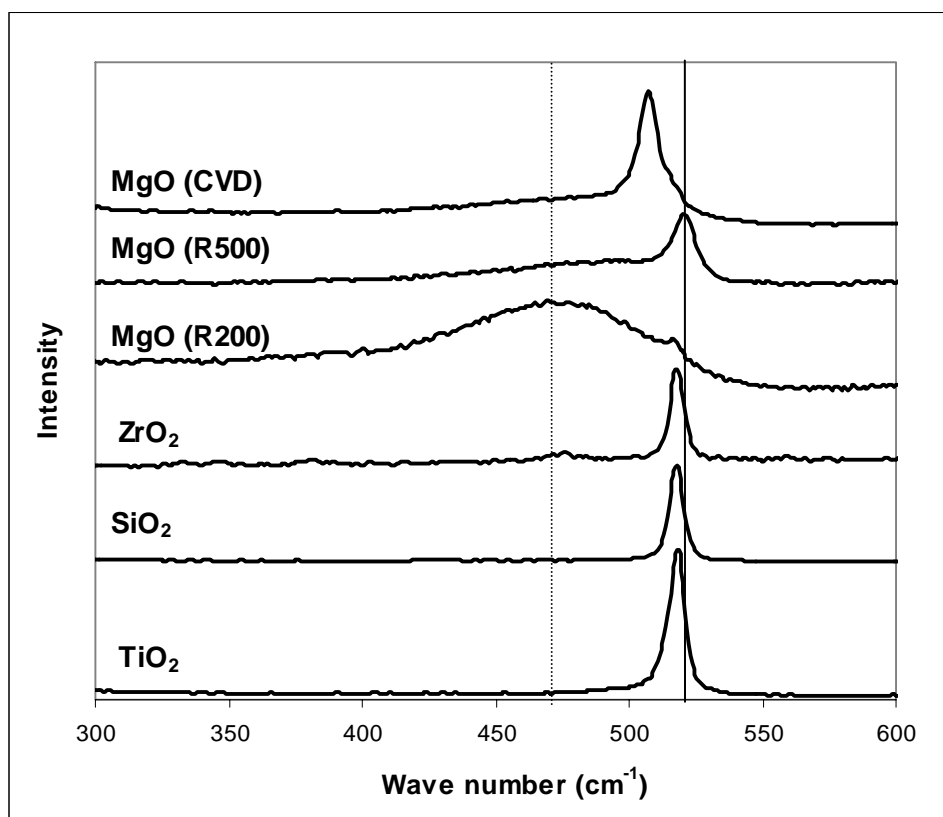


Figure 4.1 Raman spectra of silicon nanowires synthesized over gold supported on different supports (TiO₂, SiO₂, ZrO₂, and MgO) reduced at 200°C. Au/MgO prepared by impregnation were reduced at 200 and 500°C, denoted as MgO(R200) and MgO (R500), respectively. Au/MgO prepared by CVD method, denoted as MgO (CVD). The solid line shows the band at 520.5 cm^{-1} (bulk crystalline Si), and the dash line show the band at 470 cm^{-1} (amorphous Si). The bands downshifted to 518 cm^{-1} indicates the presence of SiNW.

In the case of the product obtained over the 1%Au/MgO (IWI) catalyst reduced at 200°C, there is a broad band appearing at 475 cm^{-1} , which is characteristic of

amorphous silicon (25), however no band is observed in the region of crystalline silicon. This could imply that either no silicon nanowires have been formed on the catalyst or that the yield of the nanowires is very low. The sample obtained over a 1%Au/MgO (IWI) catalyst reduced at a higher temperature, shows a Raman band at 520.5 cm^{-1} , while a small broad band at 475 cm^{-1} is still observed. The downshift due to quantum confinement effect was not observed in this case. This result indicates that, as in the case of the 1%Au/MgO (IWI) catalyst, a very low yield of nanowires was obtained even after reduction at high temperature. It is also important to mention that the product obtained over the 1%Au/ZrO₂ and 1%Au/MgO (CVD) catalysts show a very small and broad band at 475 cm^{-1} , which indicates that the product contains some amount of amorphous silicon in addition to silicon nanowires (band at 518 cm^{-1}).

Figure 4.2 shows the SEM micrographs of the silicon nanowires produced over each catalyst. The products obtained from 1%Au/TiO₂ and 1%Au/SiO₂ show very high yield of silicon nanowires, while the product obtained from 1%Au/ZrO₂ has lower yield. In the case of 1%Au/MgO (CVD) catalyst, the yield of nanowires is higher than the product obtained over the ZrO₂-supported catalyst but not as high as the ones obtained over the TiO₂ and SiO₂ supports. However, a lot of small particles can be observed on product obtained over 1%Au/MgO (CVD) catalyst as indicated with the arrows in Figure 2f. As discussed above, Raman spectra of product produced over this catalyst shows the presence of a broad band at 475 cm^{-1} , which is the characteristic of amorphous silicon. Therefore, it is plausible that these particles are amorphous silicon

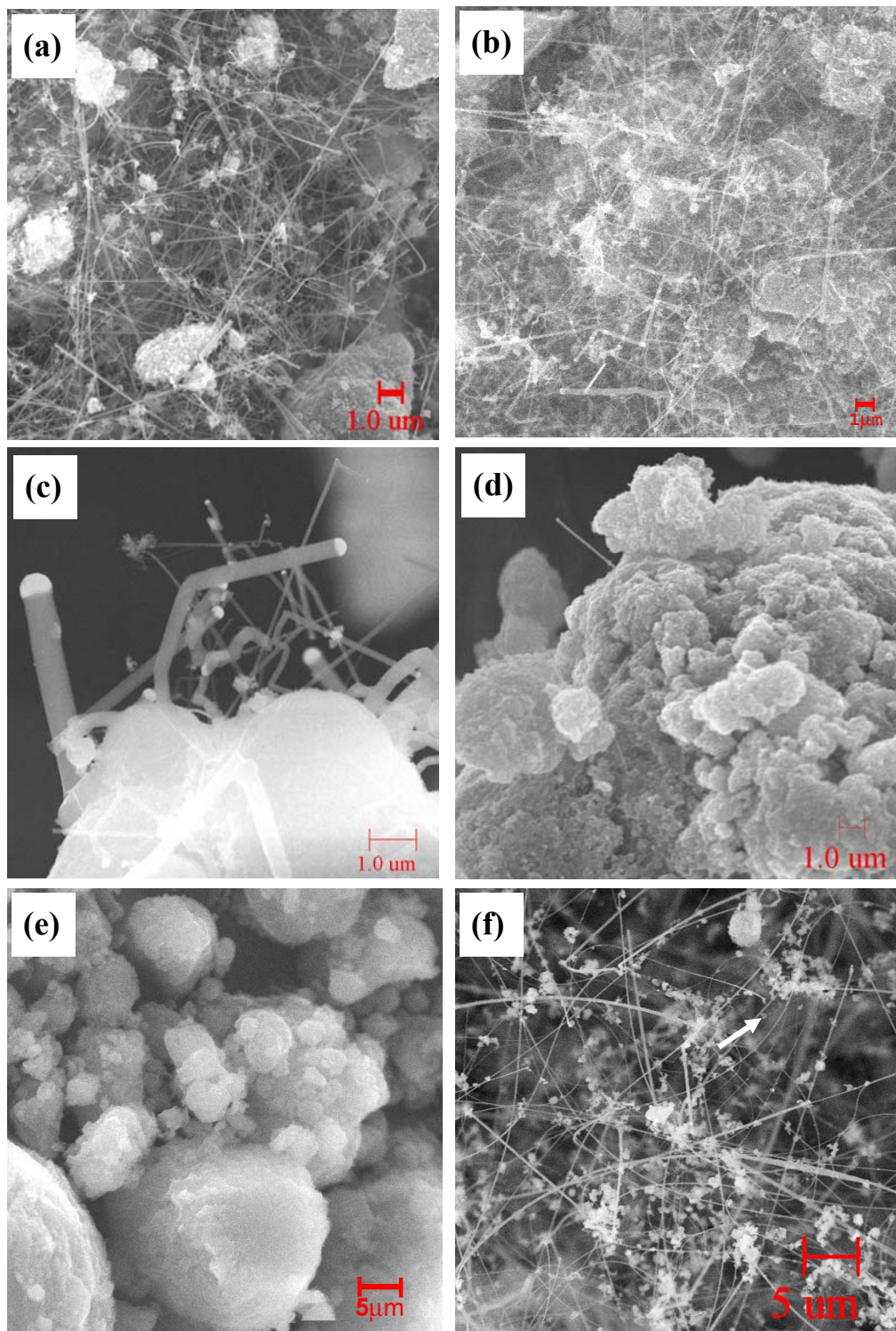


Figure 4.2 SEM micrographs of silicon nanowires obtained from 1%Au supported on different supports; a) 1%Au/TiO₂, b) 1%Au/SiO₂, c) 1%Au/ZrO₂, d) 1%Au/MgO (IWI, reduced 200°C), e) 1%Au/MgO (IWI, reduced 500°C), and f) 1%Au/MgO (CVD).

formed during the decomposition of silane. In contrast, the SEM micrographs indicate that only a few nanowires are obtained over the 1%Au/MgO (IWI) catalyst. These results perfectly agree with the Raman spectra. The difference in behavior between these two different catalyst preparation methods is discussed below.

Interesting differences on the quality of the SiNW can be observed from a detailed analysis of the SEM micrographs. Clearly, the morphology of nanowires obtained over the 1%Au/ZrO₂ catalyst is quite different from that of the nanowires obtained over the other catalysts (1%Au/TiO₂, 1%Au/SiO₂, and 1%Au/MgO (CVD)). The nanowires obtained over the ZrO₂-supported catalyst have larger diameter and shorter length, while the Au particles are clearly seen at the tip of the nanowires. Moreover, some of these appear kinked or bent. In contrast, in the product obtained using the Au/TiO₂, Au/SiO₂, and Au/MgO (CVD) catalyst, the nanowires are several tens micrometers long, very straight, and with smaller diameter. These results are better described in Figure 4.3, which presents the diameter distribution obtained from a detailed analysis of several SEM and TEM micrographs. The total count of nanowires was more than 100 for TiO₂ and SiO₂-supported catalysts, but only 50 for the case of ZrO₂ due to the lower yield obtained on this support. It can be seen that the product obtained from 1%Au/TiO₂ has the narrowest diameter distribution with an average diameter of nanowires of 8-15 nm. The nanowires synthesized on the SiO₂-supported gold have similar average diameter to those from TiO₂ support but a broader distribution. In contrast, the nanowires obtained on the ZrO₂ supported catalyst have a very large average

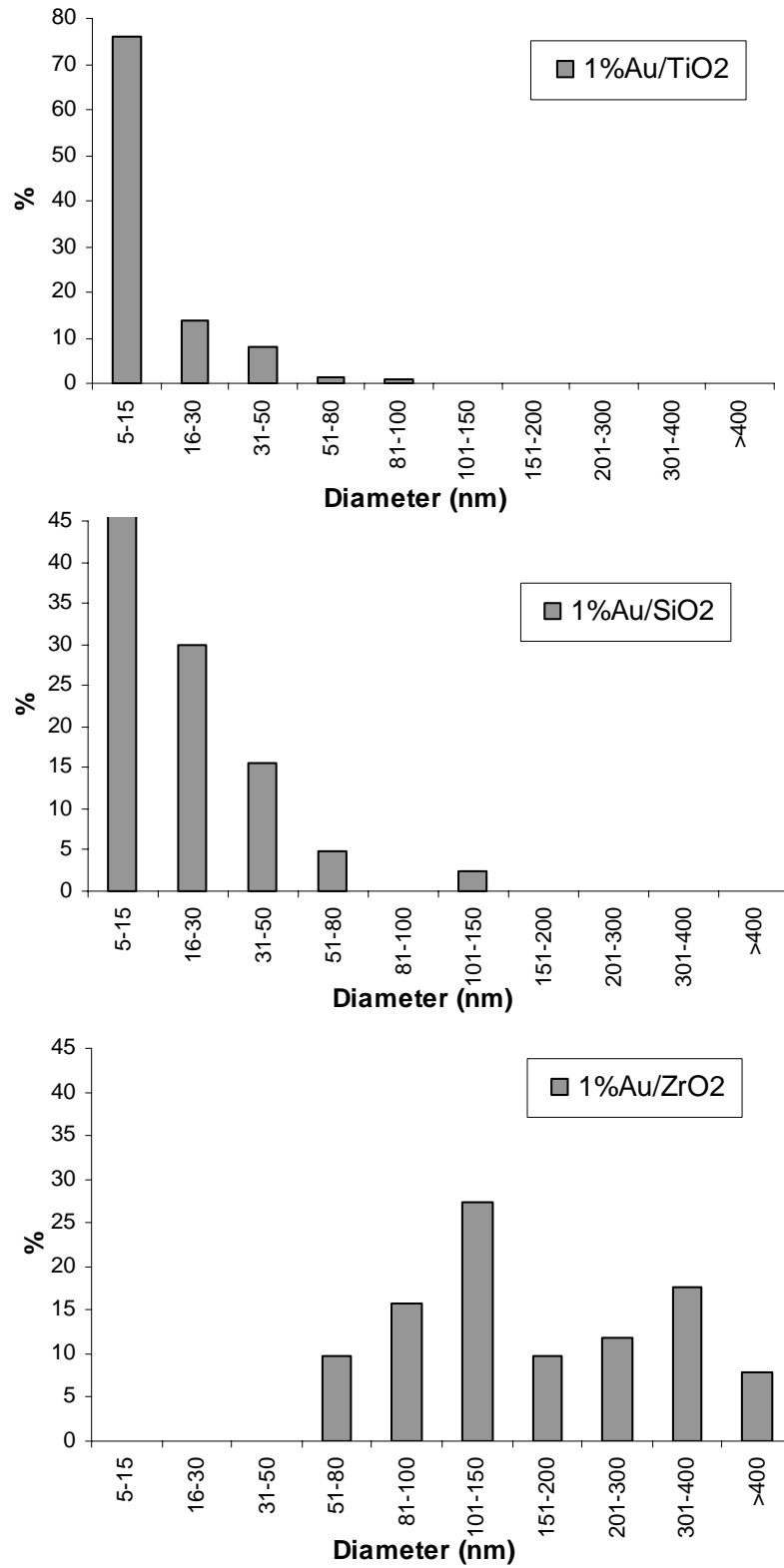


Figure 4.3 Diameter distribution of silicon nanowires produced from 1%Au supported on TiO₂, SiO₂, and ZrO₂.

diameter and the broadest diameter distribution, ranging from 50 to more than 400 nm.

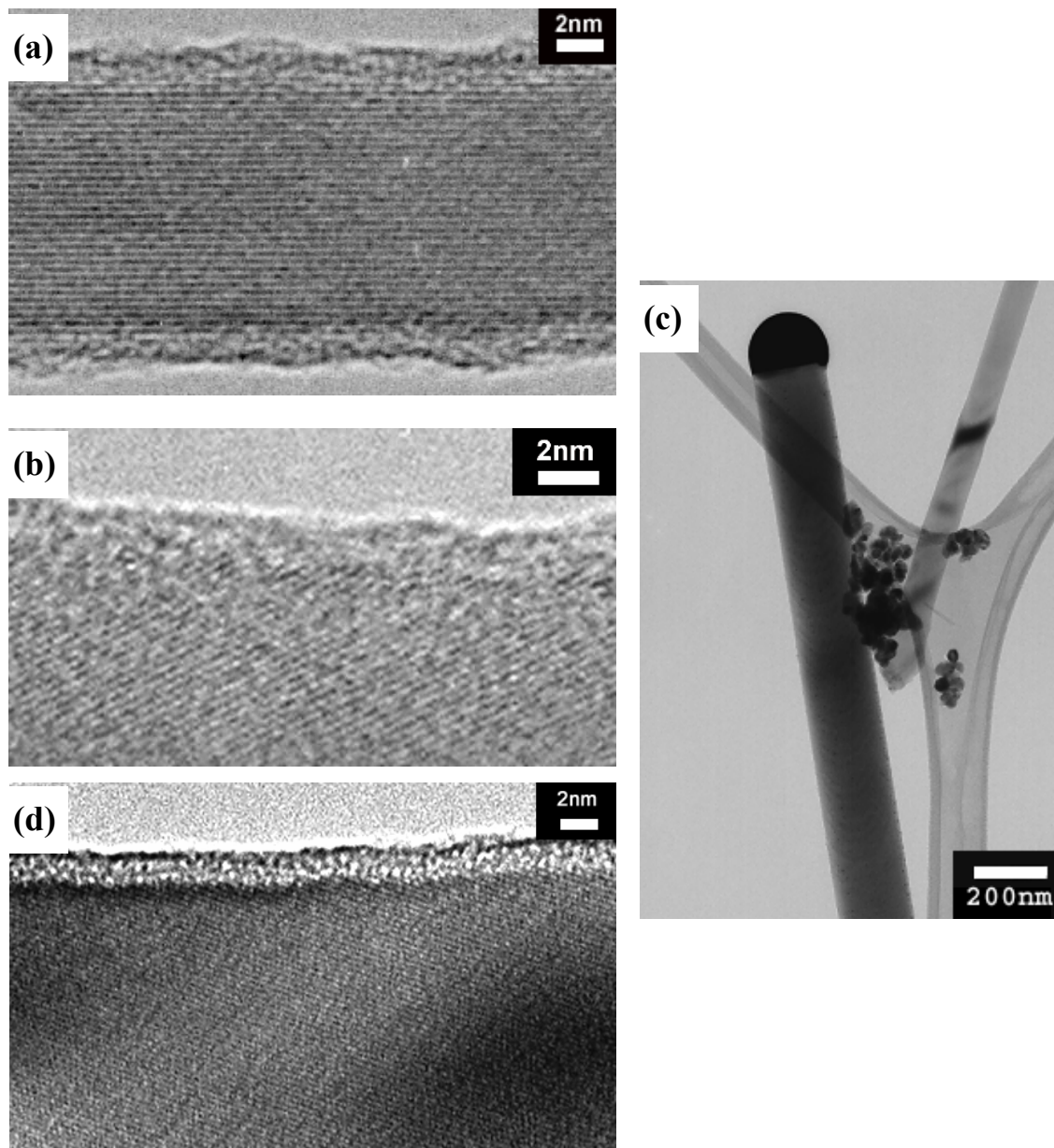


Figure 4.4 TEM micrographs of silicon nanowires obtained from 1%Au supported on different supports; a) 1%Au/TiO₂, b) 1%Au/SiO₂, c) 1%Au/ZrO₂, and d) 1%Au/MgO (CVD).

The microstructure of the silicon nanowires was investigated by TEM as shown in Figure 4.4. For 1%Au/TiO₂, 1%Au/SiO₂, and 1%Au/MgO (CVD) catalysts, it is obvious that the nanowires consist of a well-structured crystalline silicon core and a very thin layer of amorphous silicon oxide sheath. In the case of the ZrO₂ support, the silicon crystalline core and silicon oxide amorphous layer cannot be clearly differentiated. However, XPS data shown in Table 4.1 shows that the Si⁰/Si⁴⁺ ratio for the product obtained on the ZrO₂ support is much lower than the one obtained on the TiO₂ and MgO (CVD) supports.

Table 4.1 XPS analysis of silicon nanowires obtained from various catalysts.

Catalysts	Reduction Temperature (°C)	Si⁰/Si⁴⁺	Si/Metal support (Si/Ti and Si/Zr)
1%Au/TiO ₂	200	3.243	6.38
1%Au/ZrO ₂	200	0.672	1.22
1%Au/MgO	200	0.627	-
1%Au/MgO	500	1.759	-
1%Au/MgO (CVD)	-	1.06	-

As mentioned above, the nanowires from the ZrO₂ support have much larger diameters than those produced on TiO₂, SiO₂, and MgO (CVD) supports. Although the relative thickness of the amorphous oxide layer and silicon crystalline core may not be much different than those on TiO₂, SiO₂, and MgO (CVD) supports, the absolute thickness of the amorphous oxide layer may be larger. XPS is a surface-sensitive technique, that is, the observed signal corresponds to the electrons coming from less than a few nanometers from the surface, i.e. Si⁴⁺ species. As a result, the nanowires produced on the ZrO₂ support may show a lower value of the Si⁰/Si⁴⁺ ratio. These results also match the Raman spectra of this sample shown in Figure 4.1. Indeed, the product obtained over the ZrO₂-supported catalyst shows a peak at 475cm⁻¹ indicating the presence of amorphous silicon.

For the product obtained over the MgO-supported (IWI) catalyst reduced at 200°C and 500°C the XPS data also agree well with the Raman results (Figure 4.1). The product obtained over the MgO-supported (IWI) catalyst reduced at 200°C showed the presence of amorphous silicon (Raman band at 475 cm⁻¹). This material is, in turn, easily oxidized in air. Consequently, the resulting Si⁰/Si⁴⁺ ratio is lower than unity, indicating a large amount of silicon oxide. On the other hand, the product obtained over the MgO-supported (IWI) catalyst reduced at 500°C has a relatively high Si⁰/Si⁴⁺ ratio; this observation is consistent with the previous Raman result, which indicates the presence of crystalline silicon (Raman band at 520cm⁻¹). It is also noteworthy that the Si⁰/Si⁴⁺ ratio

of the product obtained from 1%Au/MgO (IWI) reduced at 500°C is higher than the one produced from 1%Au/MgO (CVD) catalyst. This result can be explained based on the previous SEM observations, which shows the presence of small particles of amorphous silicon on the product obtained from 1%Au/MgO (CVD) catalysts, resulting in a lower value of the $\text{Si}^0/\text{Si}^{4+}$ ratio. The atomic ratio of Si/Ti or Si/Zr obtained by XPS is also shown in Table 4.1. This ratio could be taken as a measurement of the yields of silicon nanowires. It can be seen that the yield of silicon nanowires obtained on the TiO_2 support is higher than that synthesized on the ZrO_2 support. This difference is in agreement with the SEM results shown in Figure 4.2. In the case of 1%Au/MgO, the peak of Au ($4f_{7/2}+4f_{5/2}$) overlaps with the Mg (2p) and hence the yield could not be determined by XPS.

To understand the differences observed in the performance of the different supports the fresh catalysts were characterized by EXAFS and XANES. By a proper data handling, these techniques can provide an estimate of the cluster size (EXAFS) and identify the chemical state (XANES) of gold before reaction. The magnitude of the Fourier Transform for k^3 -weighted Au L_3 -edge EXAFS function for each catalyst and the corresponding coordination numbers are shown in Figure 4.5A and Table 4.2, respectively. Table 4.2 also includes other structural parameters that result from the fitting routine (bond length, Debye Waller factor, and energy shift). The normalized radial distribution (Figure 4.5A) clearly show the presence of significant Au-Au coordination on the freshly reduced catalysts supported on TiO_2 , SiO_2 , and MgO (CVD).

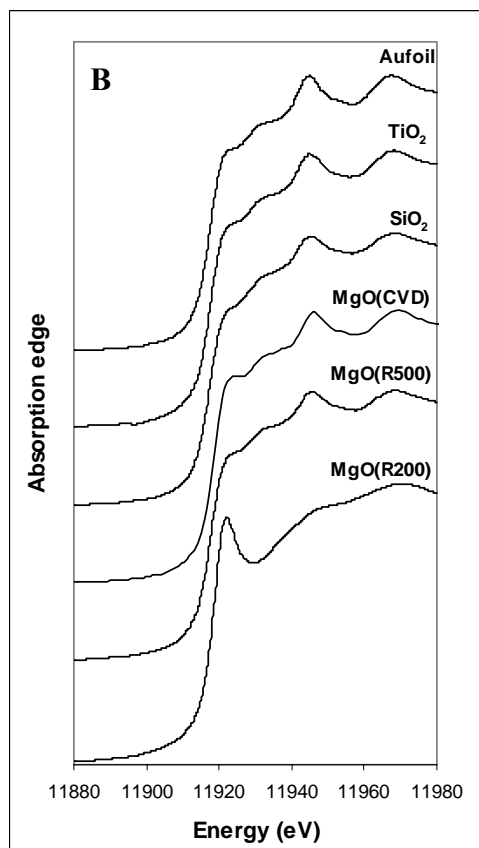
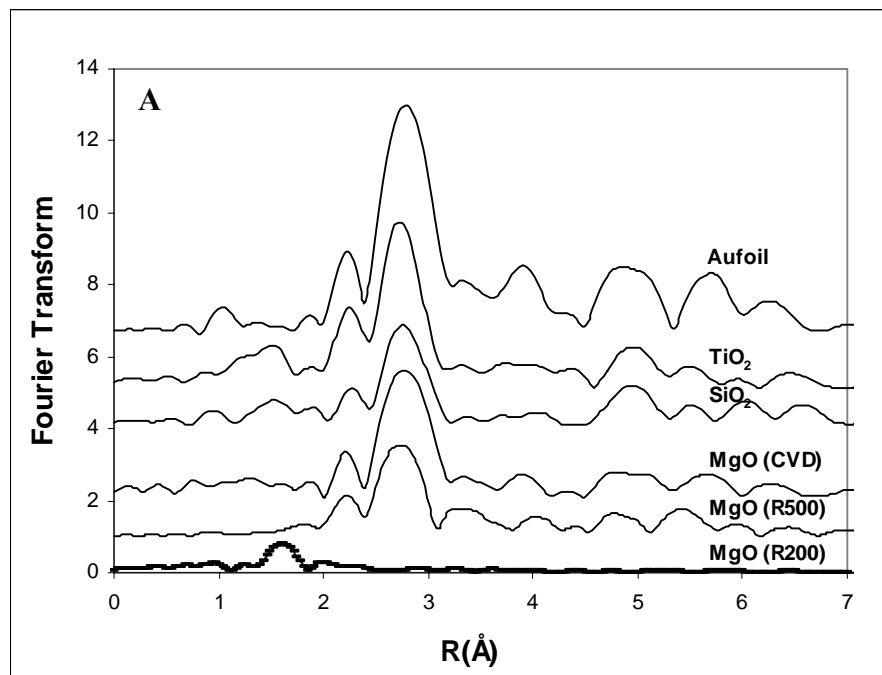


Figure 4.5 Au L^3 -edge X-ray absorption spectroscopic comparison of fresh Au supported on different supports (TiO_2 , SiO_2 , ZrO_2 , and MgO) reduced at $200^\circ C$. Au/MgO prepared by impregnation were reduced at 200 and $500^\circ C$, denoted as MgO(R200) and MgO (R500), respectively. Au/MgO prepared by CVD method, denoted as MgO (CVD). A) Fourier transform of k^3 -weighted and B) XANES analysis.

Table 4.2. The coordination parameters of Au sites obtained from curve fitting of EXAFS ^(b).

Catalysts	Reduction Temperature (°C)	Shell	N	R(Å)	σ^2 (Å ²)	ΔE_0 (eV)
Au/TiO ₂	200	Au-Au	9.63	2.87	0.0041	3.08
Au/SiO ₂	200	Au-Au	7.92	2.86	0.0049	6.63
Au/MgO	200	Au-O	1.37	1.97	0.0026	9.85
Au/MgO	500	Au-Au	7.86	2.84	0.0048	2.92
Au/MgO (CVD)	-	Au-Au	9.07	2.87	0.0048	6.93

[a] The errors of data and fits are roughly estimated from the change of the residual factors to be 15% for N, 0.25% for R, 10% for σ^2 and 4 eV for ΔE_0 . No ambiguities of the theoretical standards are included.

[b] Shell indicates the type of ligands for each shell of the fit. N is the coordination number, R is the metal-scatterer distance. σ^2 is a mean square deviation in R. ΔE_0 is the shift in E_0 for the theoretical scattering functions.

By contrast, when supported on MgO (IWI), gold tends to exhibit Au-O bonds and a high state of dispersion. From a detailed analysis of the coordination numbers of Au over the different supports, the size of the Au particles can be predicted. It is smaller on SiO₂ than on TiO₂ and MgO (CVD). Similarly, the Au particles on MgO support, prepared by impregnation, appear as highly dispersed even after reduction at high temperature. The intensity of the white line observed in the XANES spectra shown in Figure 4.5B clearly illustrates that the Au species present in the fresh Au/MgO (IWI) catalyst reduced at 200°C is not in the metallic form, but rather as an oxide. This would explain the unusually low activity of this sample. That is, the 1%Au/MgO (IWI) catalyst reduced at 200°C does not produce silicon nanowires under conditions at which the other

catalysts clearly do. Since according to the Vapor-Liquid-Solid mechanism it is required that the Au particle form an alloy with the Si species decomposed from silane, if no metallic Au species are present in the system the Au-Si alloy cannot be formed; which explains the low activity of the Au/MgO (IWI) catalyst. Moreover, if gold is in the oxide form, the catalytic decomposition of SiH_4 (rate-limiting step) might be slower, thus resulting in diminished growth rate and very low yield of Si nanowires.

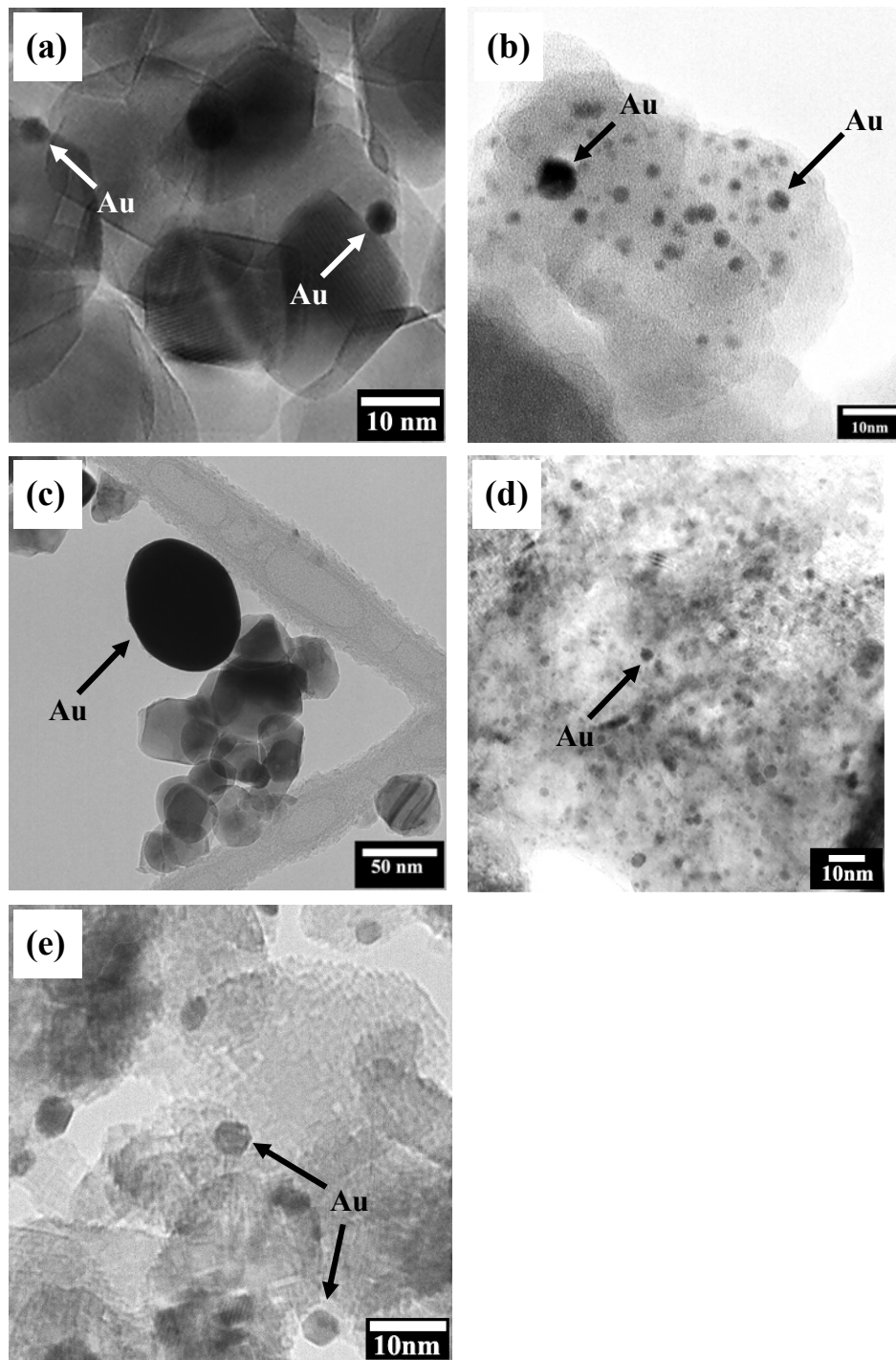
The difference on activity observed on the MgO-supported obtained from three different preparation methods cannot be explained solely in light of the EXAFS results. While on the sample reduced at 200°C gold is oxidic, on the Au/MgO (CVD) and Au/MgO (IWI) reduced at 500°C Au it is in metallic form; however, a high yield of high quality silicon nanowires are just observed in the case of the CVD-prepared catalyst. It is clear then that the differences in activity cannot be attributed solely to the Au oxidation state, but on the support-metal interaction itself. Zdrzil (26) has reported the effect of preparation method on the morphology of MgO-supported catalysts. He found that during the aqueous impregnation technique, MgO can react with H_2O to form $\text{Mg}(\text{OH})_2$. Although MgO is formed again during subsequent calcination, it might cover the metallic particles, avoiding the contact between them and the gas phase. Based on this explanation it is possible that the Au particles supported on MgO prepared by incipient wetness impregnation might be embedded into MgO substrate during the catalyst preparation and therefore not being exposed to the surface. As a consequence, under reaction conditions, the Au/MgO prepared by impregnation method shows lower activity

than the one prepared by CVD method, which has most of the Au particles exposed to the gas phase.

It is a well-known fact that at the nanoscale level Au may be an active catalytic metal while it is inactive at a larger scale, i.e. gold particles of nanometric size are active for low-temperature oxidation while larger particles are not. From TEM analysis of the fresh catalysts shown in Figure 4.6, it is obvious that the size of Au particles on ZrO₂ support is larger than that of TiO₂ and SiO₂ supports. This might be the cause for the lower activity of the ZrO₂-supported catalyst.

Another prediction of the VLS mechanism is that the diameter of the nanowires should be similar to the size of the metallic Au particles. As shown in Figure 4.5A, the size of Au particle supported on SiO₂ is smaller than those observed for the TiO₂ support; however the silicon nanowires produced from these two supports have similar average diameters. The silicon nanowires observed on the SiO₂ support exhibited a broader diameter distribution. Although the EXAFS analysis indicates that the average diameter of Au particles is smaller for the SiO₂ support than for the TiO₂ support, we need to emphasize that EXAFS provides an average of particle sizes. By contrast, the TEM micrographs obtained on the fresh catalysts show that the Au particles supported on SiO₂ exhibit a wide range of particle sizes. The plausible explanation can be the agglomeration of Au particles under reaction conditions. In this case the metal support interaction would play a central role. It is well known that Au particles supported on TiO₂

Figure 4.6. TEM micrographs of fresh catalysts; a) 1%Au/TiO₂, b) 1%Au/SiO₂, c) 1%Au/ZrO₂, d) 1%Au/MgO (Reduced 200°C), and e) 1%Au/MgO (Reduced 500°C).



are more effectively stabilized than those supported on SiO₂ and ZrO₂ (27). This would in turn result in a higher mobility of Au particles supported on SiO₂ and ZrO₂ than on TiO₂. As a result, silicon nanowires obtained from 1%Au/SiO₂ and 1%Au/ZrO₂ should have broader diameter distribution than the one obtained over 1%Au/TiO₂. In the case of the ZrO₂ support, the Au particles observed from TEM are quite large, which then resulted in larger silicon nanowires, as expected from the VLS mechanism.

4.4. CONCLUSIONS

The synthesis of silicon nanowires by chemical vapor deposition of silane has been studied over Au supported on different supports at 500°C and at about 150 Torr. Gold supported on TiO₂ and SiO₂ gives a high yield of high quality silicon nanowires. These nanowires consist of well-crystallized silicon core and very thin layer of amorphous silicon oxide. Gold supported on ZrO₂ gives silicon nanowires of larger diameter and with a wider diameter distribution. The material obtained using this particular support indicates the presence of some amounts of amorphous silicon. In case of MgO-supported catalysts, 1%Au/MgO prepared by CVD method gives a high yield of high quality SiNW but not as high as TiO₂ and SiO₂ support. On the other hand, 1%Au/MgO prepared by incipient wetness impregnation show very few nanowires in both 1%Au/MgO reduced at 200°C and 500°C due to the presence of Au oxide and the morphology of the Au particles on the support, respectively.

ACKNOWLEDGMENT

This research was conducted with financial support from the Department of Energy, Office of Basic Energy Sciences (grant No. DE-FG03-02ER15345). Technical support from the personnel at NSLS, Brookhaven National Lab, for the EXAFS experiments is gratefully acknowledged. Partial support from the National Science Foundation under Grant No. EPS-0132534 is also acknowledged.

REFERENCES

- 1 R.S.Wagner, W.C. Ellis, Appl. Phys. Lett. 4, 89 **(1964)**
- 2 J. Westwater, D.P. Gosain, S. Tomiya, S. Usui, J. Vac. Sci. Technol. B 15, 554 **(1997)**
- 3 J. Westwater, D.P. Gosain, S. Usui, Phys. Stat. Sol. 165, 37 **(1998)**
- 4 N. Ozaki, Y. Ohno, S. Takeda, Appl. Phys. Lett. 73, 3700 **(1998)**
- 5 Y. Cui, L.J. Lauhon, M.S. Gudiksen, J. Wang, C.M. Lieber, Appl. Phys. Lett. 78, 2214 **(2001)**
- 6 Z.Q. Liu, W.Y. Zhou, L.F. Sun, D.S. Tang, X.P. Zou, Y.B. Li, C.Y. Wang, G. Wang, S.S. Xie, Chem. Phys. Lett. 341, 523 **(2001)**
- 7 J. Niu, J. Sha, X. Ma, J. Xu, D. Yang, Chem. Phys. Lett. 367, 528 **(2003)**
- 8 A.H. Carim, K.K. Lew, J.M. Redwing, Adv. Mater. 13, 1489 **(2001)**
- 9 R. S Wagner, Whisker Technology, Wiley-Interscience: New York **(1970)**
- 10 Y. Wu, P. J. Yang, Am. Chem. Soc. 123, 3165 **(2001)**

- 11 H.Wang, G. S. Fischman, *J. Appl. Phys.* 76, 1557 (1994)
- 12 K.-K. Lew, J.M. Redwing, *J. Cryst. Growth* 254, 14 (2003)
- 13 S. Hofmann, C. Ducati, R.J. Neill, S. Piscanec, A.C. Ferrari, J. Geng, R.E. Duni-Borkowski, J.J. Robertson, *J. J. Appl. Phys.* 94, 6005 (2003)
- 14 G.C. Bond, *Catal. Today* 72, 5 (2002)
- 15 M. Haruta, *Catal. Today* 36, 153 (1997)
- 16 G. C. Bond, D. T. Thompson, *Catal. Rev. Sci. Eng.* 41, 319 (1999)
- 17 M. Valden, X. Lai, D.W. Goodman *Science* 281, 1647 (1998)
- 18 M. Haruta, *Chemical Record* 3, 75 (2003)
- 19 M. Haruta, S. Tsubota, T. Kobayashi, H. Kageyama, M.J. Genet, B.J. Delmon, *Catal.* 144, 175 (1993)
- 20 D. Thompson, *Gold Bull.* 31, 111 (1998)
- 21 G.J. Hutchings, *Gold Bull.* 29, 123 (1996)
- 22 C. Mohr, P. Claus, *Science Progress* 84, 311 (2001)
- 23 Schimpf, S.; Lucas, M.; Mohr, C.; Rodemerck, U.; Brucker, A.; Radnik, J.; Hofmeister, H.; Claus, P. *Catal. Today* 72, 63 (2002)
- 24 R. P. Wang, G.W. Zhou, Y.L. Liu, S.H. Pan, H.Z. Zhang, Z. Zhang, *Phys. Rev. B* 61, 16827 (2000)
- 25 H.Z. Richter, P. Wang, L. Ley, *Solid State Commun.* 39, 625 (1981)
- 26 M. Zdrzil, *Catal. Today* 86, 151 (2003)
- 27 Grunwaldt, J-D; Maciejewski, M.; Becker, O. S.; Fabrizioli, P.; Baiker, A. J. *Catal.* 186, 458 (1999)

CHAPTER 5

SYNTHESIS OF SINGLE-WALLED CARBON NANOTUBE BY CATALYTIC DECOMPOSITION OF ETHANOL

5.1. INTRODUCTION

In chapter 2, we have mentioned that among the SWNTs synthesis methods available the catalytic chemical vapor deposition (CVD) method is the most appropriate for large-scale production of these materials. The floating catalyst approach is one of the interesting methods. The advantage of this method is that there is no support materials used in the catalyst because the metal catalyst particles are produced in-situ; therefore, no purification step to remove the catalyst support is needed, which helps decreasing the amount of defects in SWNT generated during purification processes.

In fact, production of long nanotube strands, up to several centimeters in length, consisting of aligned SWNTs has been reported using mixture of n-hexane, ferrocene and thiophene (1,2). This mixture was also used to co-synthesize of SWNTs and carbon fibers (CFs) under different reaction conditions (3). Benzene has been used as well to produce the rope-like bundles of SWNTs using ferrocene as catalyst source, and thiophene as promoter (4). In this particular case, the authors claimed that with the

addition of different amounts of thiophene, either SWNTs (0.5-5 wt.% addition) or MWNTs (higher than 5 wt.% addition) can be obtained.

Using the floating catalyst method, continuous gas phase techniques have been developed using coalesced iron catalyst particles using either metallocene (5,6) or iron pentacarbonyl ($\text{Fe}(\text{CO})_5$) (7) supplied to the reactor together with a carbon source gas. For example, the so-called HiPco process (8,9,10) using the disproportionation reaction of high-pressure and high-temperature CO with $\text{Fe}(\text{CO})_5$ as a catalyst seed is producing nowadays almost amorphous-free commercial SWNTs. Double-walled carbon nanotubes (DWNTs) produced by the floating catalyst method have been reported as well (11). Indeed, aligned DWNTs long ropes with a narrow diameter distribution have been grown using CH_4 as hydrocarbon source (12).

In this chapter, we explored the synthesis of SWNT using the floating catalyst method, but using ethanol as carbon source and ferrocene as catalyst. The election of such feedstock was based on reports by Maruyama and coworkers indicating the synthesis of high purity single-walled carbon nanotubes over Fe/Co catalysts supported on zeolite (13, 14) and Co/Mo mixtures deposited on Si wafers and quartz substrates (15, 16). The products we obtained using the ethanol/ferrocene system were characterized mainly by Raman spectroscopy and transmission electron microscopy.

5.2. EXPERIMENTAL

5.2.1. SWNT production

Ethanol (C_2H_5OH) was used as carbon feedstock. Ferrocene ($C_{10}H_{10}Fe$) was dissolved into ethanol to obtain Fe/C molar ratio of 0.001. Using a mixture of H_2 (200 sccm) and He (50 sccm) as carriers the liquid mixture was injected to a preheating zone ($180^\circ C$) a rate of 0.5 ml/min using a syringe pump. After vaporization of the liquid mixture in the preheating zone the vapor passed through a reaction chamber held at reaction temperature. The film of SWNT was collected at the cold part of the reactor. The total reaction time was 30 minutes. The reaction temperature was varied from 700-1100 $^\circ C$ in order to find the optimum conditions. The reactor schematics are illustrated in Figure 5.1. Experiments changing the carrier gas composition were also performed (total flow rate held at 250 sccm) in order to study the effect of the carrier gas composition in the synthesis of SWNT at 800 and 1000 $^\circ C$. In some experiments a lower Fe/C molar ratio (0.0005) was used as well.

All the products were characterized by Raman spectroscopy (Jovin Yvon-Horiba LabRam 800 equipped with a CCD detector with a laser excitation source of 632nm, He-Ne laser), transmission electron microscopy on a TEM, JEOL-2000FX and temperature programmed oxidation. TPO measurements were carried out by passing a continuous flow ($0.25\text{ cm}^3\text{ s}^{-1}$) of 2% O_2/He (Airgas 99.99%) over the samples as the

temperature was increased linearly at $10^{\circ}\text{C s}^{-1}$ to 900°C . CO_2 and CO formed were quantitatively converted to methane in a methanator by mixing the effluent with $0.83 \text{ cm}^3 \text{ s}^{-1} \text{ H}_2$ and passing over a 15% $\text{Ni}/\text{Al}_2\text{O}_3$ catalyst held at 673 K . CH_4 formation rates were measured by a flame ionization detector (SRI model 110), calibrated with $100 \mu\text{l}$ pulses of CO_2 , and by combustion of known amounts of graphite.

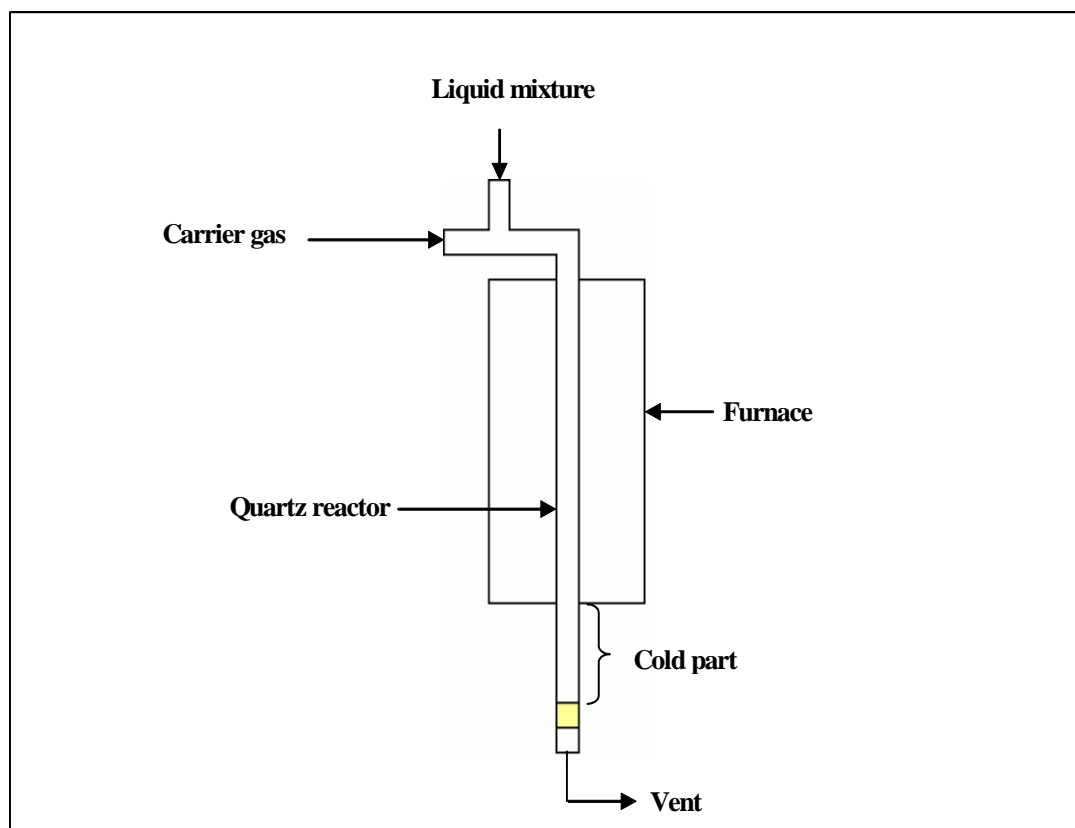


Figure 5.1 Schematic of SWNT reaction apparatus.

5.2.2. SWNT purification

After reaction the obtained material was purified. The purification procedure started with the oxidation of the as-prepared SWNT film, collected from the cold part of the reactor, in wet air at a flow rate of 50 sccm at 225°C for 10 hr in order to get rid of amorphous carbon. Subsequently, the film was sonicated in concentrated HCl for 1 hr, the suspension was then filtered and washed with deionized water and finally dried at 100°C for 2-3 hr. The purified sample was then characterized using Raman spectroscopy and TEM.

5.3 RESULT AND DISCUSSION

5.3.1. Effect of reaction temperature

The effect of the reaction temperature on the quality and yield of the SWNT was studied by varying the temperature from 700°C to 1100°C. Figure 5.2a shows the Raman spectra of the products obtained from five different samples produced at different reaction temperatures. It is observed that in the case of the materials grown at temperatures between 800-1000°C, the G band displays a very high intensity while the intensity of the D band is very low. Also, the radial breathing mode bands of SWNT are clearly observed and show a relatively high intensity indicating the presence of high quality SWNTs in the product. A contrasting behavior is observed in the case of the

materials grown at 700°C and 1100°C. In these two cases the intensity of the D band is quite high, whereas radial breathing mode bands are not observed. Figure 5.2b illustrates the values obtained for a quality parameter calculated from the Raman spectra, as $[G/(D+G)]$; where, D and G are the integrated areas of the D (disorder) and G Raman bands, respectively. This term is a good indication of the quality of the SWNT sample, since it qualitatively measures the amount of ordered SWNT compared to defects and other disordered sp^3 carbon species. As we have reported before a $(G/(D+G))$ parameter approaching unity is representative of a high-quality product. (17). The values obtained for this quality parameter clearly indicate that the sample produced 1000°C exhibits the highest $(G/(D+G))$ quality, while the samples obtained at lower temperatures show much lower values, which obviously point to the presence of undesirable forms of carbon. As we approach 1000°C, which seems to be the optimal reaction temperature, the $(G/(D+G))$ parameter increases; however, when the reaction temperature increases to 1100°C the selectivity dramatically decreases once again. The TEM micrographs obtained for the product synthesized at 800,1000, and 1100°C are shown in Figure 5.3 and match perfectly with the Raman observations. At 800°C, small amount of SWNT are observed together with residual iron particles which some are encapsulated by graphite. Whereas big bundles of SWNTs are observed in the sample produced at 1000°C. Finally, for the case of the product obtained at 1100°C, the TEM images clearly show that it is composed of carbon nanofibers, amorphous carbon and metal particles encapsulated with carbon.

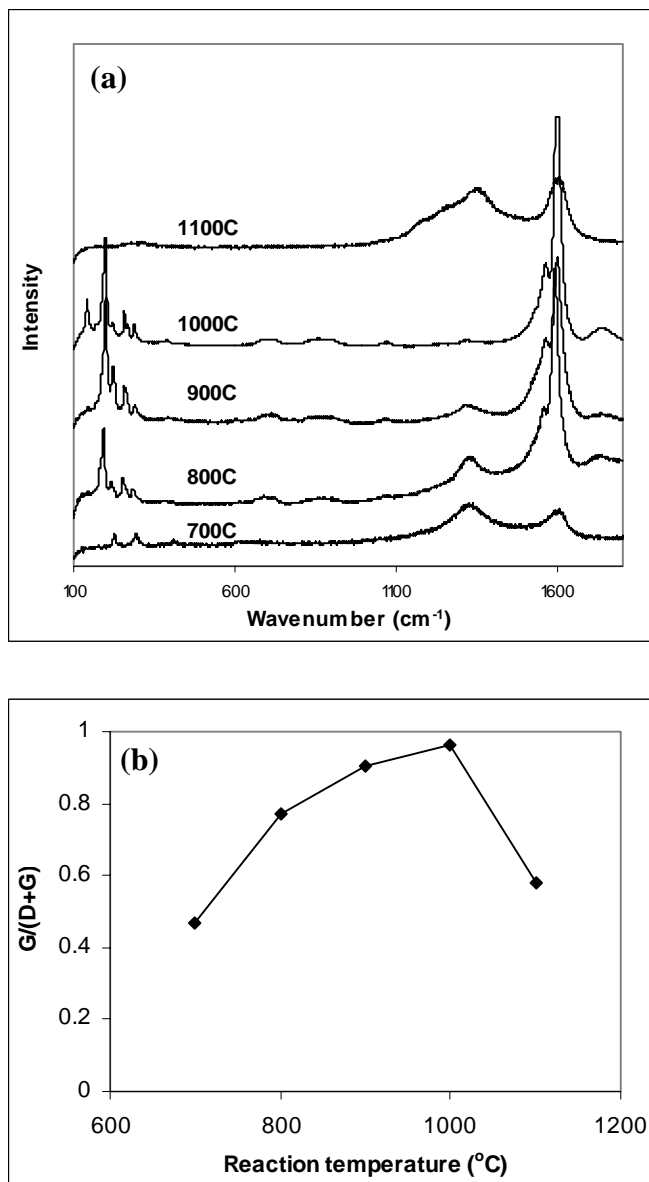


Figure 5.2 a) Raman spectra and b) G/(D+G) ratio of products obtained at different reaction temperature.

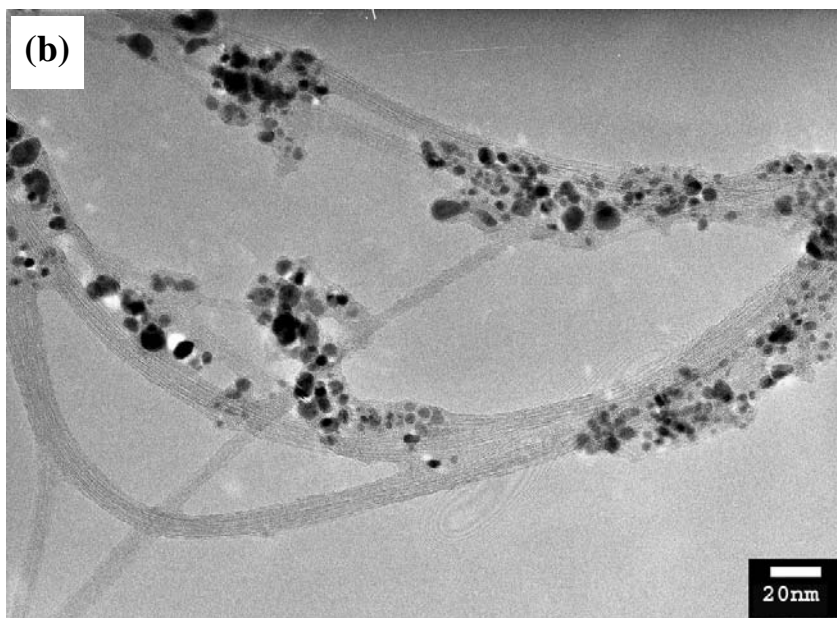
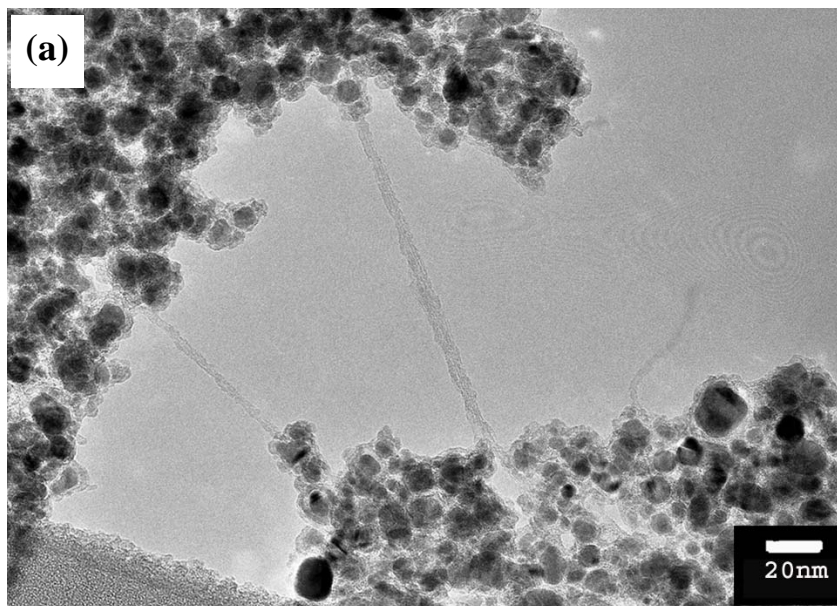


Figure 5.3 TEM images of products obtained at a) 800°C, b) 1000°C, and c) 1100°C

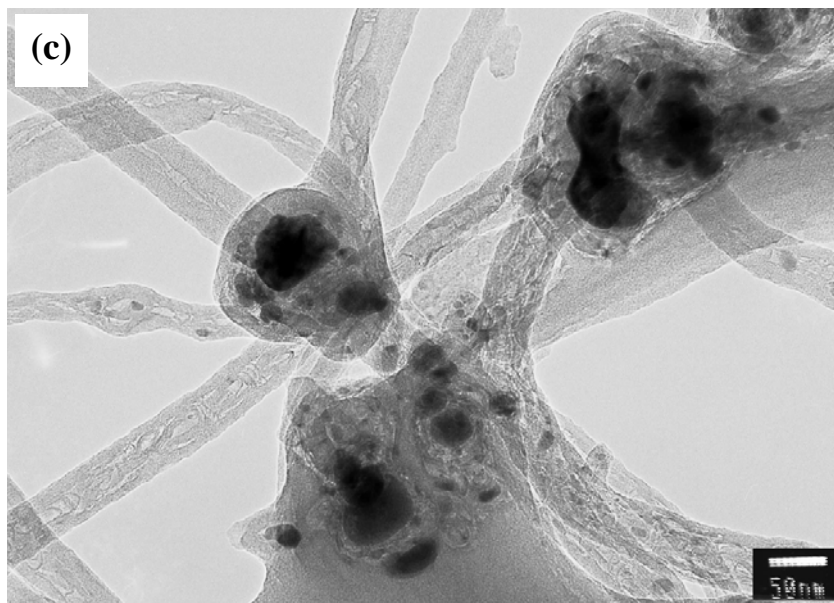


Figure 5.3 (cont'd) TEM images of products obtained at a) 800°C, b) 1000°C, and c) 1100°C

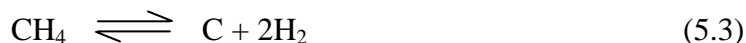
The production of SWNTs from this method could be explained by the mechanism proposed in Figure 1.10. When the liquid mixture of ethanol and ferrocene is vaporized into the reactor zone, thermal decomposition of the mixture occurs, leading to the formation of iron clusters and carbon. Iron and carbon then form a metal alloy; once the alloy is formed diffusion of more carbon into the alloy occurs, which results in carbon supersaturation. The supersaturation is then followed by the formation of a nanotube cap, which precedes SWNT growth (18,19,20). In fact, Kanzow *et al.* ⁽²¹⁾ has proposed that the growth of SWNTs depends on the kinetic energy of the system and the work of adhesion between the graphitic sheet and the metal particle. If the kinetic energy is greater than the work of adhesion in such a way that it is enough to provide the energy for

bending the graphitic sheet, nucleation of SWNT occurs. If not, the formation of MWNTs or encapsulation of metal particle takes place instead. This could be used to explain the reason for which the optimum reaction temperature is 1000°C. At lower temperatures, the kinetic energy of the system may not be enough to overcome the work of adhesion. However, at temperatures above 1000°C the rate of thermal decomposition of the reactant is very fast, resulting in the rapid segregation of a graphitic sheet which would finally lead to encapsulation of the metal particle. Additionally, at this temperature the rate of agglomeration of the iron particles is faster (e.g. Figure 5.3c, large metal particles are observed). These large particles result in the formation of carbon nanofibers since the system has high kinetic energy together with a high carbon supply.

5.3.2. Effect of carrier gas composition.

As observed in the previous session, the optimum temperature for production of SWNT by pyrolysis of ethanol is 1000°C. The carrier gas used in that case was a mixture of H₂ (200 sccm) and He (50 sccm). In this session, the effect of carrier gas composition is studied at two different reaction temperatures: 800°C and 1000°C. Figure 5.4A shows the Raman spectra of each product obtained using different carrier gas compositions at 1000°C. It can be seen that intensity of G band is very high while that of D band is very low for the products obtained at each gas composition, indicating that there is not much effect on the quality of SWNT produced at this temperature when the gas composition is changed. On the other hand, at 800°C even though the characteristic

bands corresponding to SWNT were observed (high G and low D band intensity, together with breathing mode), the effects of carrier gas composition are noticeable. As described in Fig. 5.4B and Table 5.1, when the relative amount of He increases in the He/H₂ mixture introduced into the system the quality parameter (G/(D+G)) decreased. This can be explained based on the growth mechanism showed in Figure 1.10 as well. As described in section 5.3.1, the cap formation is a critical step in SWNT growth. At the optimum temperature (1000°C), the cap formation is favored by the high kinetic energy of the system; however, we expect that the cap formation and therefore SWNT nucleation is slower at 800°C because of the lower kinetic energy of the system. Therefore, at 800°C even though carbon atoms do segregate from the metal particle nucleation does not take place resulting in metal encapsulation. At this reaction conditions, it is likely that ethanol undergoes decomposition, leading to the formation of CH₄, H₂, and CO or dehydration to give C₂H₄ and H₂O as shown in equation (5.1) and (5.2), respectively (22-25). CH₄, C₂H₄, and CO can continue to decompose providing carbon supply to the metal particle as illustrated in Eq. (5.3), (5.4), and (5.5), respectively.



As mention above, at 800°C and when H₂ was used as carrier gas the quality parameter ($G/(D+G)$) is higher than in the case of a pure He flow. As described in the equations above, H₂ is byproduct of carbon deposition in all three cases (ethanol, CH₄, and C₂H₄ decomposition). Therefore when H₂ is used as carrier gas, a shift on the reaction to the reactant side is observed. Moreover a decrease on the *fugacity* of carbonaceous species on a metal surface (26,27) is also expected. In this case, as H₂ is introduced to the system, it can react with the carbon atoms that are deposited over the metal surface. This phenomenon helps slowing down the formation of a graphitic sheet, leading to a lower rate of metal encapsulation, resulting in higher quality parameter ($G/(G+D)$). As a matter of fact, the effect of hydrogen on the morphology of carbon deposits has been previously studied in the context of vapor-grown carbon fiber synthesis. In those studies it was proposed that the presence of a critical level of H₂ on a CO containing feed serves to keep “clean” the active sites responsible for the decomposition of the carbon bearing gas during the early stages of the reaction, leading to the deposition of ordered forms of carbon over the catalyst (28-31).

5.3.3. Effect of Fe/C ratio

As observed from the TEM micrographs shown in Fig. 5.3a and b, a large amount of metal particles are observed at both reaction temperatures. In previous experiments, the Fe/C ratio used was 0.001; this ratio was decreased to 0.0005 to attempt to reduce the amount of metal particles in the product.

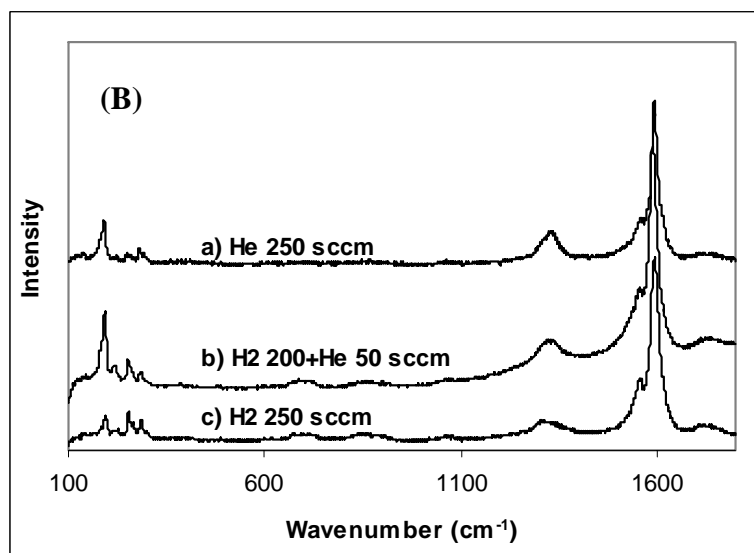
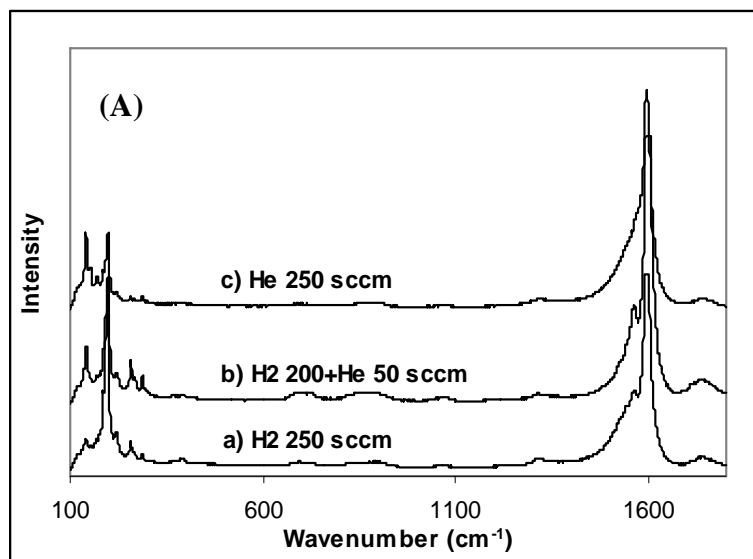


Figure 5.4 Raman spectra of products obtained at (A) 1000°C and (B) 800°C using different carrier gas mixture

Table 5.1. Quality parameter (G/(D+G)) of SWNTs obtained using different carrier gases at 800 and 1000°C.

Flow rate (sccm)		G/(D+G)	
H ₂	He	800 (°C)	1000 (°C)
250	0	0.911	0.958
200	50	0.773	0.964
0	250	0.778	0.964

This experiment was conducted at 1000°C using He at a flow rate of 250 sccm as carrier gas. The Raman spectra of the two products are shown in Figure 5.5. Both Raman spectra show high quality SWNTs. Nevertheless, temperature programmed oxidation (TPO) showed that the carbon amount obtained from the solution mixture of ethanol and ferrocene with Fe/C ratio of 0.001 is about 50 wt. %, which is remarkably higher than that amount of product obtained using the solution with Fe/C ratio of 0.0005, which yielded a carbon amount of about 15 wt.%. It is likely that in the case of a lower amount of Fe, the total rate ethanol decomposition decreases, leading to a lower amount of carbon deposition. However, even though the Fe/C ratio was decreased by half, large amount of metal particles were still observed under the electron microscope, as demonstrated in Figure 5.6.

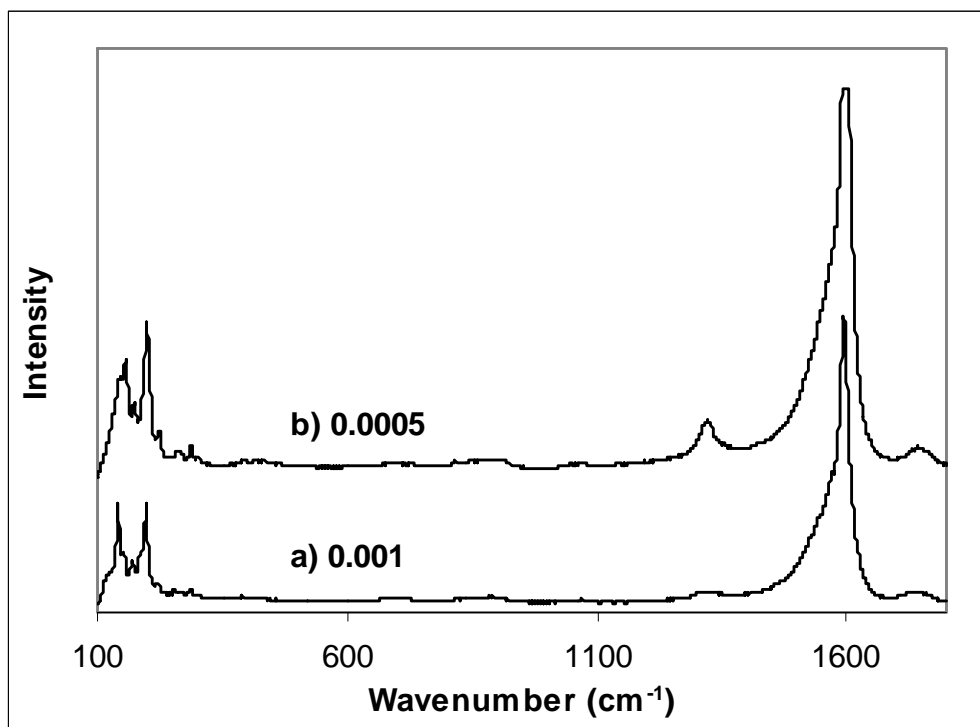


Figure 5.5 Raman spectra of SWNTs obtained from Fe/C ratio of a) 0.001 and b) 0.0005

5.3.4. Purification of SWNTs

As mentioned in the previous section, the SWNT materials obtained showed a large amount of metallic impurities. To remove these impurities the raw SWNTs obtained at 1000°C using a solution mixture with a Fe/C ratio of 0.001 and He as carrier gas were purified using the following protocol.

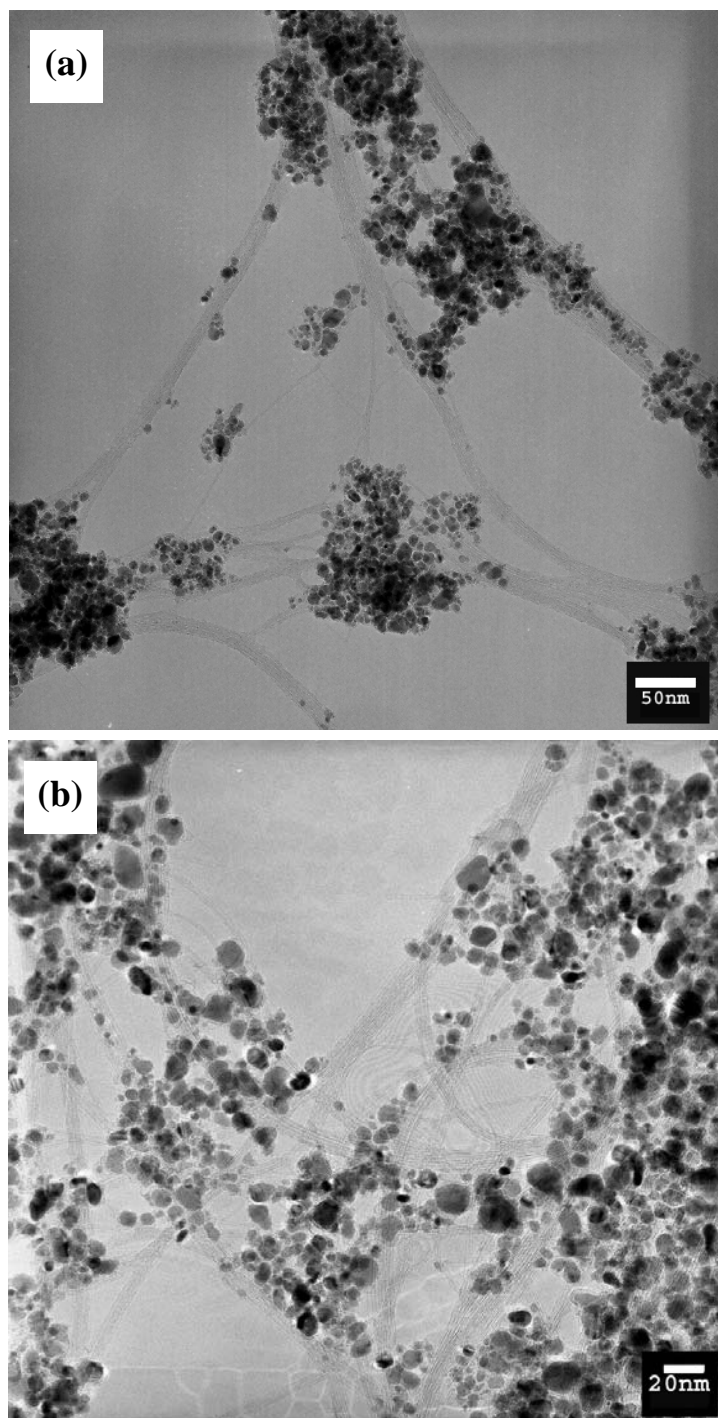


Figure 5.6 TEM images of SWNTs produced at 1000°C using solution with Fe/C ratio of (a) 0.0005 and (b) 0.001.

The amorphous carbon was oxidized first using wet air at 225°C, then the materials were treated with HCl to remove the iron particles. The Raman spectra of the purified sample and as-prepared SWNTs are shown in Figure 5.7. When compared to the as-prepare SWNTs, the purified sample shows a higher intensity of the D band, which as mentioned above, is the signature of disorder carbon in the sample. This increase in D band intensity might originate from damage in SWNT walls resulting from the purification process. TEM was used as well to investigate the quality of the purified sample. From a detailed analysis of low magnification TEM micrographs (Fig. 5.8a) it is clear that there are still a number of metal particles present in the purified samples but clearly a lower amount when compared to the as-prepared materials (Fig. 5.6b.) On the other hand, the high magnification image shown in Figure 5.8b shows a big bundle of SWNTs together with the graphitic rings and some amorphous carbon. These graphitic rings are the ones formed during the encapsulation of the metal particles during synthesis, while the amorphous carbon might have been generated from the SWNTs damaged during the purification process. The TEM results are in perfectly agreement with the Raman spectra shown in Figure 5.7, showing again an increase on the amount of amorphous carbon after the purification step.

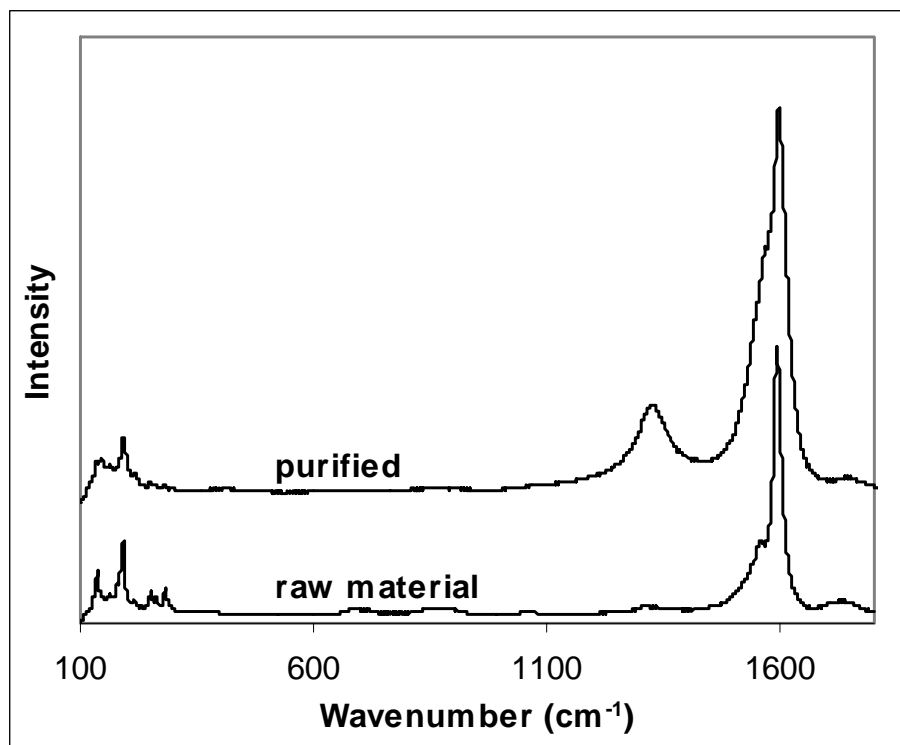


Figure 5.7 Raman spectra of as-prepared SWNTs compared with the sample after purification.

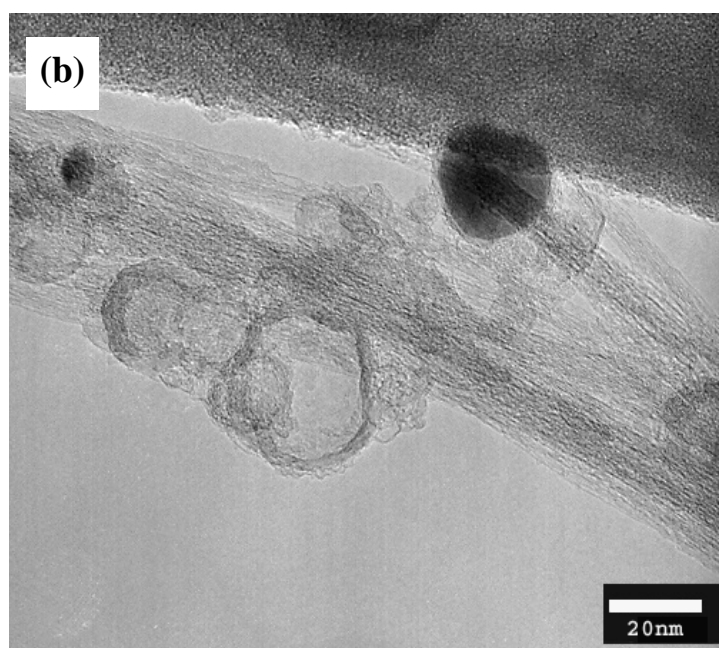
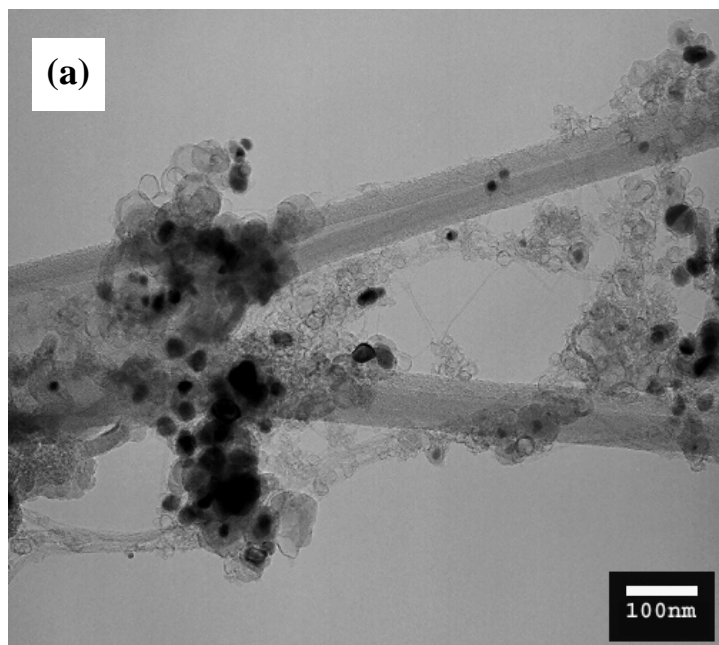


Figure 5.8 (a) and (b) TEM images of purified SWNTs at low and high magnification, respectively.

5.4 CONCLUSIONS

SWNTs were produced using the floating catalyst method using a mixture of ethanol and ferrocene. Under our reaction conditions the optimum reaction temperature for SWNT synthesis seems to be 1000°C. The quality of SWNTs is not changed with the carrier gas composition is varied at this temperature; however, at 800°C, the quality of SWNTs can be improved by increasing the amount of H₂ in the carrier gas. The reason for the effect of the carrier gas composition at 800°C on SWNT quality was explained based on the VLS growth mechanism. The yield of SWNTs depends on the Fe/C ratio used in the precursor solution; when this ratio decrease, the amount of carbon obtained decreased but the quality of product does not change. In addition, substantial removal of remaining iron catalyst form the raw SWNT material was achieved by oxidation in wet air and HCl dissolution. The quality of SWNTs slightly decreases after purification process, mainly by formation of amorphous carbon.

REFERENCES

- 1 H.W. Zhu, C.L. Xu, D.H. Wu, B.Q. Wei, R. Vajtai, P.M. Ajayan, *Science* 296, 884 (2002)
- 2 H.W. Zhu, B. Jiang, C.Xu, D. Wu, *Chem. Commun.*, 1858 (2002)
- 3 H. Zhu, X. Li, C.Xu, D. Wu, *Mater. Res. Bull.* 37, 177 (2002)
- 4 H.M. Cheng, F.Li, G.Su, H.Y. Pan, L.L. He, X. Sun, M.S. Dresselhaus, *Appl. Phys. Lett.* 72, 3282 (1998)

- 5 H.M. Cheng, F. Li, X. Sun, S.D.M. Brown, M.A. Pimenta, A. Marucci, G. Dresselhaus, M.S. Dresselhaus, *Chem. Phys. Lett.* 289, 602 (1998)
- 6 L. Ci, S. Xie, D. Tang, X. Yan, Y. Li, Z. Liu, X. Zou, W. Zhou, G. Wang, *Chem. Phys. Lett.* 349, 191 (2001)
- 7 B.C. Satishkumar, A. Govindaraj, R. Sen, C.N.R. Rao, *Chem. Phys. Lett.* 293, 47 (1998)
- 8 P. Nikolaev, M.J. Bronikowski, R.K. Bradley, F. Rohmund, D.T. Colbert, K.A. Smith, R.E. Smalley, *Chem. Phys. Lett.* 313, 91 (1999)
- 9 M.J. Bronikowski, P.A. Willis, D.T. Colbert, K.A. Smith, R.E. Smalley, *J. Vac. Sci. Technol. A* 19, 1800 (2001)
- 10 W. Zhou, Y.H. Ooi, R. Russo, P. Papanek, D.E. Luzzi, J.E. Fisher, M.J. Bronikowski, P.A. Willis, R.E. Smalley, *Chem. Phys. Lett.* 350, 6 (2001)
- 11 J. Wei, L. Ci, B. Jiang, Y. Li, X. Zhang, H. Zhu, C. Xu, D. Wu, *J. Mater. Chem.* 13, 1340 (2003)
- 12 W. Ren, H.M. Cheng, *J. Phys. Chem B* 109, 7169 (2005)
- 13 S. Maruyama, R. Kojima, Y. Miyauchi, S. Chiashi, M. Kohno, *Chem. Phys. Lett.* 360, 229 (2002)
- 14 Y. Murakami, Y. Miyauchi, S. Chiashi, S. Maruyama, *Chem. Phys. Lett.* 374, 53 (2003)
- 15 Y. Murakami, Y. Miyauchi, S. Chiashi, S. Maruyama, *Chem. Phys. Lett.* 377, 49 (2003) ; *Jpn. J. Appl. Phys.* 43, 1221 (2004)
- 16 Y. Murakami, S. Chiashi, Y. Miyauchi, M. Hu, M. Ogura, T. Okubo, S. Maruyama, *Chem. Phys. Lett.* 385, 298 (2004)
- 17 J.E. Herrera, D.E. Resasco, *Chem. Phys. Lett.* 376, 302 (2003)
- 18 X. Fan, R. Buczko, A.A. Puretzky, D.B. Geohegan, J.Y. Howe, S.T. Pantelides, S.J. Pennycook, *Phys. Rev. Lett.* 90, 145501 (2003)
- 19 S. Maruyama, Y. Murakami, Y. Shibuta, Y. Miyauchi, S. Chiashi, *J. Nanosci. Nanotechnol.* 4, 360 (2004)

- 20 D. E. Resasco, W. E. Alvarez, F. Pompeo, L. Balzano, J. E. Herrera, B. Kitiyanan, A. Borgna, *J. Nanopart. Res.* 4, 131 **(2002)**
- 21 H. Kanzow, A. Ding, *Phys. Rev. B* 60, 11180 **(1999)**
- 22 J. M. Davidson, C.M. McGregor, *Ind. Eng. Chem. Res.* 40, 108 **(2001)**
- 23 J. Llorca, R. Ramirez de la Piscina, J. Sales, N. Homs, *Chem. Commun.* 641 **(2001)**
- 24 Y.Cong, V. van Spaendonk, R.I. Masel, *Surf. Sci.* 385, 246 **(1997)**
- 25 R.I. Masel, W.T. Lee, *J. Catal.* 165, 80 **(1977)**
26. M. Ishioka, T. Okada, K. Matsubara, *Carbon* 30, 859 **(1992)**
27. M. Ishioka, T. Okada, K. Matsubara, M. Endo, *Carbon*, 30, 865 **(1992)**
- 28 . A. Jr Sacco, F. W. A. H.Geurts, G. A.Jablonski, S. Lee, R. A Gately, *J. Catal.* 119, 322 **(1989)**
29. G. A. Jablonski, F. W. A. H. Geurts, A. Jr. Sacco, *Carbon* 30, 99 **(1992)**
30. G. A. Jablonski, F. W. A. H. Geurts, A. Jr. Sacco, R. R. Biederman, *Carbon* 30, 87 **(1992)**
- 31 . R. T. K. Baker, *Catal. Rev. Sci. Eng.* 19, 161 **(1979)**

CHAPTER 6

SYNTHESIS OF SINGLE-WALLED CARBON NANOTUBE ON QUARTZ SUBSTRATES USING BIMETALLIC Co-Mo CATALYSTS

6.1 INTRODUCTION

Single-walled carbon nanotubes are widely considered as ideal candidates for interconnections and active components in nanoscale electronic devices, such as quantum wires (1), field-effect transistors (2, 3) and field emitters (4). Most of the SWNT-based devices used materials synthesized by either laser ablation or the arc discharge method. Recently, surface CVD growth of SWNTs has attracted much attention (5-10) as an alternative route for fabrication of such devices. Indeed, it has been demonstrated that the direct CVD growth of SWNT over flat substrates is a relatively inexpensive method which can be tuned to create isolated, low-defect SWNTs (10), whereas nanotubes fabricated by laser ablation or arc discharge are initially synthesized as bundles and have to be purified and suspended in solution before deposition onto a surface for device fabrication. These post-synthetic treatments may introduce defects and alter the electronic properties of SWNTs due to the highly oxidative chemicals and ultra sonication processes

used for purification and dispersion. Huang *et al.* have directly grown millimeter-long, well-aligned SWNTs in large areas on a flat substrate using monodispersed Fe/Mo nanoparticles as catalysts and CO as feeding gas. The lengths of the SWNTs reported were more than 2 mm. Moreover, they reported that the orientation of nanotubes is directly controlled by the direction of gas flow in the CVD system without the use of any external force like an electric or magnetic field (11,12). Kim *et al.* (13) have used a mixture of methane and ethylene as the feed gas in the SWNT synthesis on flat substrates using well-controlled isolated catalytic Fe₂O₃ nanoparticles. Reports on the growth of vertically aligned single-walled carbon nanotubes on silicon and quartz substrates using ethanol (14), ethylene (15), and methane (16) have recently appeared in the literature

Our group has reported several times the good performance of a CoMo bimetallic catalyst formulation supported on SiO₂ used in the production of SWNTs using CO as feed gas (17- 20). In the present chapter we report an attempt to impregnate this bimetallic CoMo catalyst over a flat quartz substrate using the liquid based dip-coat method reported by Murakami *et al.* (21). SWNTs were then directly synthesized on the substrate using CO and ethanol as carbon containing molecule. The results indicate the suitability of this catalyst for SWNT synthesis over flat substrates.

6.2 EXPERIMENTAL

6.2.1. Surface preparation

A metal acetate solution containing both Co and Mo was first prepared by dissolving molybdenum acetate $(\text{CH}_3\text{COO})_2\text{Mo}$ and cobalt acetate tetrahydrate $(\text{CH}_3\text{COO})_2\text{Co}\cdot 4\text{H}_2\text{O}$ in ethanol to achieve a 0.01 wt% concentration of each metallic species. To obtain total dissolution, the mixture was sonicated for 2 hr. Fused quartz plates with a thickness of 1 mm were used as substrate. Two different kinds of quartz substrates were used; (i) as purchased, denoted as “smooth surface” and (ii) after a gently scratch of the surface using a solid abrasive to roughen the surface on both sides of the substrate, this substrate is denoted as “scratched surface”. The substrate was cut into stripes of about $5 \times 10 \text{ mm}^2$, in order to remove any metallic impurity the strips were soaked in 3% H_2O_2 solution at 50°C for 15 minutes and carefully rinsed with deionized water. The substrate piece was then submerged into the metallic acetate solution described above for 10 min. The surface of the substrate was rapidly dried above the liquid contact level as soon as it was removed from the solution. All these processes were run in an exhaust hood to avoid surface contamination by dust particles. Right after drying the samples were placed on a closed Pyrex petri dish and placed in a furnace maintained at 400°C for 5 min in air to decompose acetates or any other organic residues and to form the mixed oxide of Co-Mo bimetallic catalyst.

The surface was characterized by X-ray photoelectron spectroscopy (XPS), Physical Electronics PHI 5800 ESCA system, equipped with monochromatic Al K_{α} X-ray source. The binding energies were corrected by reference to the C(1s) line at 284.5 eV. The fitting of the XPS spectra and the quantification of the surface atomic ratios were obtained with Gauss-Lorentz peaks, using the MultiPak software from Physical Electronics.

6.2.2. SWNT production

The substrate was put into a reactor where they were reduced at 500°C in H₂ flow (100 sccm) for 30 minutes and heated up to reaction temperature (850°C) in He using a flow rate of 100 sccm and a heating ramp of 10°C/min; after reaching 850°C CO (50 sccm) or ethanol were fed to the reactor for 1 hr. In the case of ethanol, He, H₂, or a mixture of these two gases was used as carrier gas with He to H₂ ratio of 1:1, 1:2, 1:3, and 1:5 keeping the overall flow rate constant at 150sccm. Before reaching the reactor this gas mixture was passed through an ethanol bubbler kept at room temperature.

The synthesized SWNTs were characterized by Raman spectroscopy using a Jovin Yvon-Horiba LabRam 800 equipped with a CCD detector with a laser excitation source of 632nm (He-Ne laser), 514, and 488nm (Ar laser). Scanning electron microscopy (JEOL 880) and transmission electron microscopy (JEOL 2000FX) were also used for SWNTs analysis.

6.3 RESULT AND DISCUSSION

6.3.1. Production of SWNTs

First, the smooth surface impregnated with Co-Mo bimetallic catalyst was used to undergo the reaction with CO and ethanol at 850°C, in this study He was used as carrier gas when ethanol was used as feed. After reaction, the substrate was still transparent in the case of CO; however, it looks dark when ethanol was used. Raman spectra of the surface after reaction with CO and ethanol at 850°C are shown in Figure 6.1. It is noticeable that SWNTs were observed only when CO was used as carbon containing molecule as a sharp peak of G band and radial breathing mode were detected with low intensity of D band. However, in the case of ethanol, the D band and G band intensity are comparable with no characteristic breathing mode at low frequency. This can imply that there are no SWNTs generated when ethanol was used as feed. The surface was then investigated using scanning electron microscopy, the micrographs are illustrated in Figure 6.2a and b. From SEM images, the low density of tube-like materials was detected after the surface was reacted with CO (Fig. 6.2a). On the contrary, very high density of these tube-like materials was observed in the case of ethanol as feed. As monitored by Raman spectroscopy, the tube-liked materials in the case of CO are believed to be SWNTs, while the ones observed on the surface after reaction with ethanol are either MWNTs or carbon filaments. This observation was confirmed by transmission electron microscopy (TEM) as the image in Figure 6.2c shows. It is clear that the

materials obtained from ethanol decomposition using He as carrier gas are mostly MWNTs. Unfortunately, because of low density of materials obtained after reaction with CO, TEM analysis could not be performed on this sample.

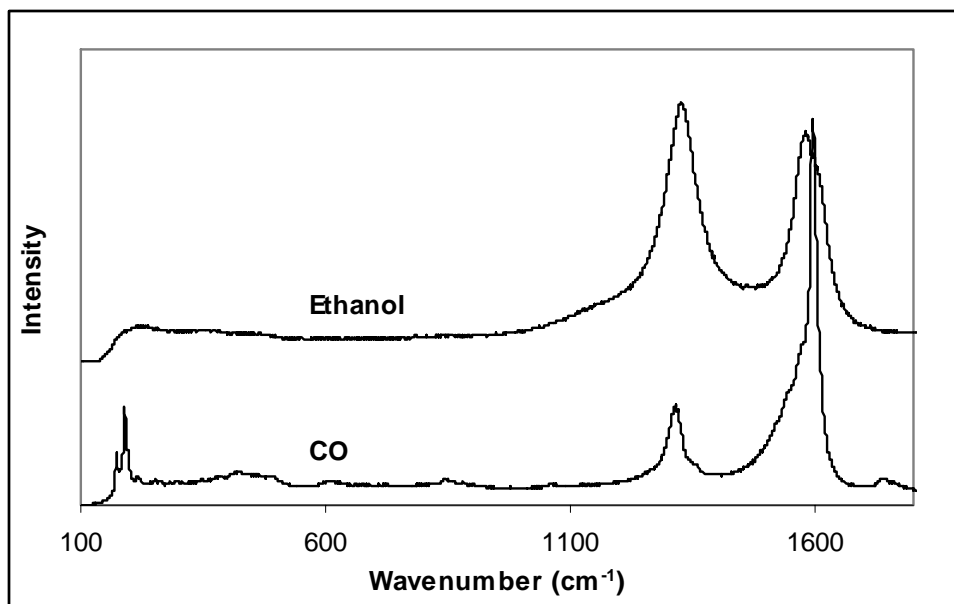


Figure 6.1 Raman spectra of products obtained on smooth quartz surfaces after reaction with CO and ethanol at 850°C (Laser excitation source of 632 nm).

Interestingly, in the case of CO used as feed, although the Raman spectra is better than when ethanol was used as feed, we detected by doing SEM analysis in different regions of the substrate, that the distribution of SWNTs on the surface was not homogenous.

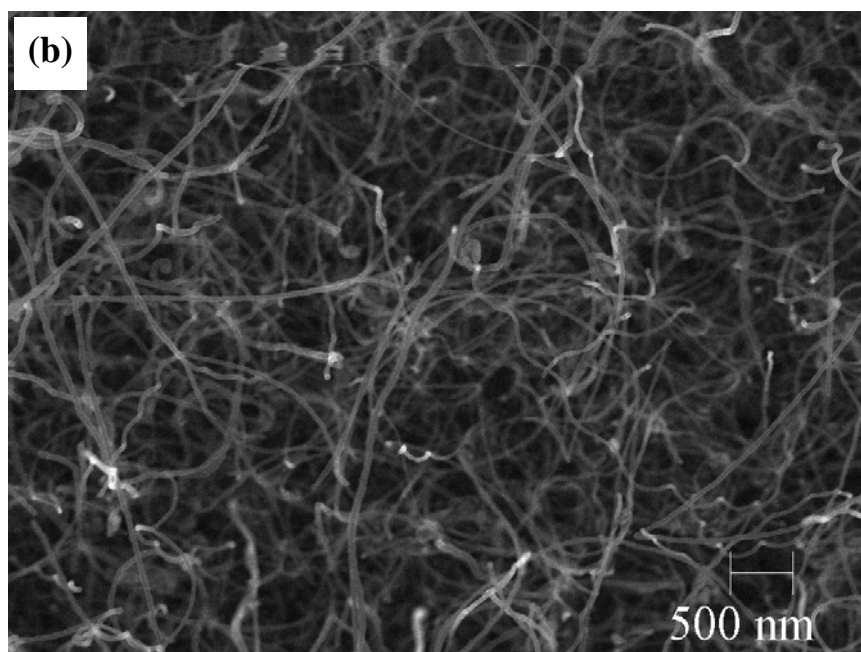
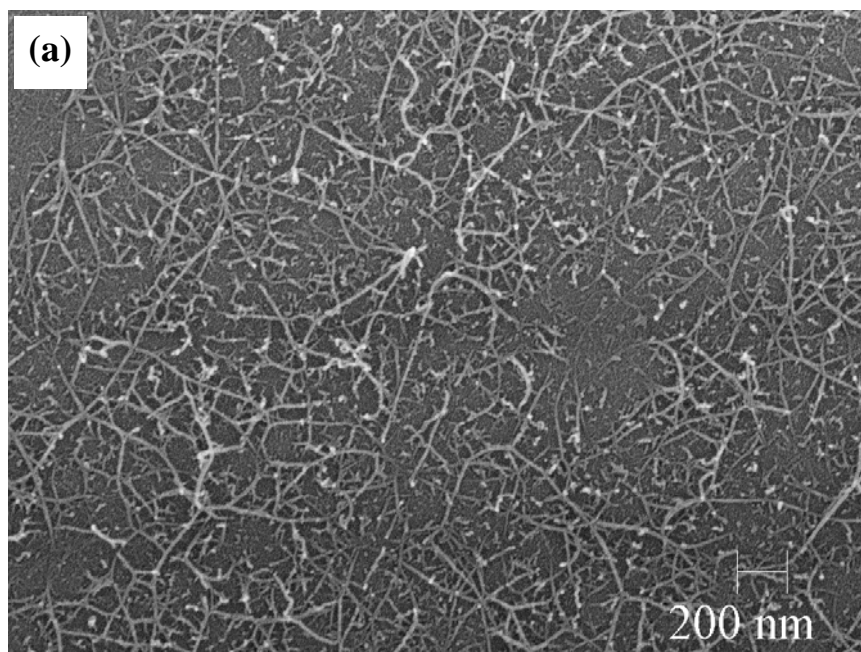


Figure 6.2 (a) and (b) SEM images obtained on smooth quartz surfaces after reaction with CO (a) and ethanol (b). TEM images of product obtained on the smooth quartz surface after reaction with ethanol (c).

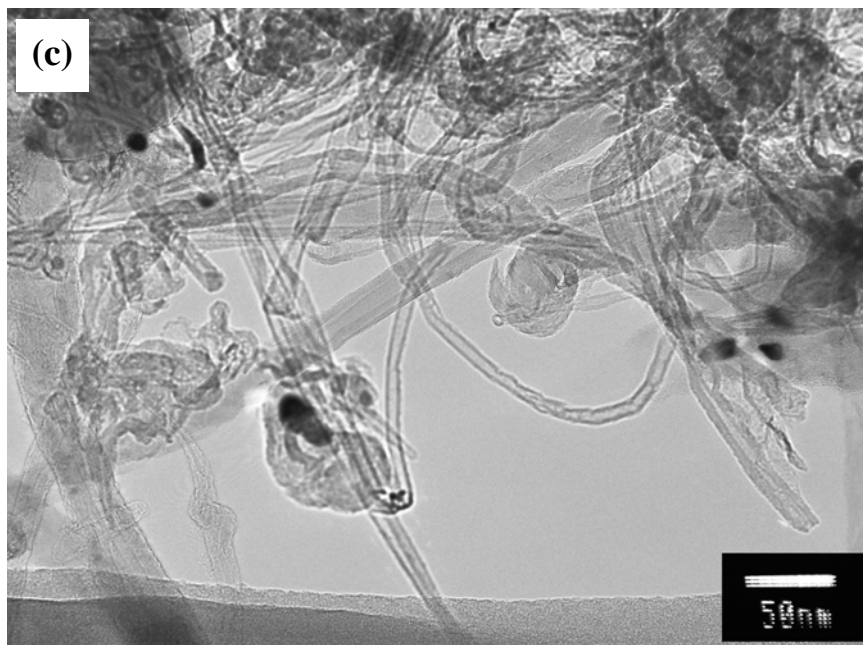


Figure 6.2 (cont'd) (a) and (b) SEM images obtained on smooth quartz surfaces after reaction with CO (a) and ethanol (b). TEM images of product obtained on the smooth quartz surface after reaction with ethanol (c).

In addition, it was brought to our attention that the materials obtained near the edge of the quartz stripes (coarse edges) showed Raman spectra of SWNT with lower D band intensity, indicating a product of better quality in this case. Therefore we attempted a roughening of the quartz surface before impregnation of the cobalt and molybdenum acetates onto the substrate. These new “scratched” substrates also went through the same process as the smooth substrate (calcinations, reduction, and reaction with CO at 850°C). The Raman spectra of the SWNT materials obtained on this “scratched” surfaces are shown in Figure 6.3. It clear that in the case of the Raman spectra obtained for the products synthesized over the scratched surface (Fig.6.3b), the D band intensity is lower

than in the case of product obtained on CoMo impregnated on the smooth quartz substrate (Fig. 6.3a). This indicates that the amount of amorphous or disorder carbon in the case of CoMo impregnated on smooth surface is larger than in the case of scratched surface.

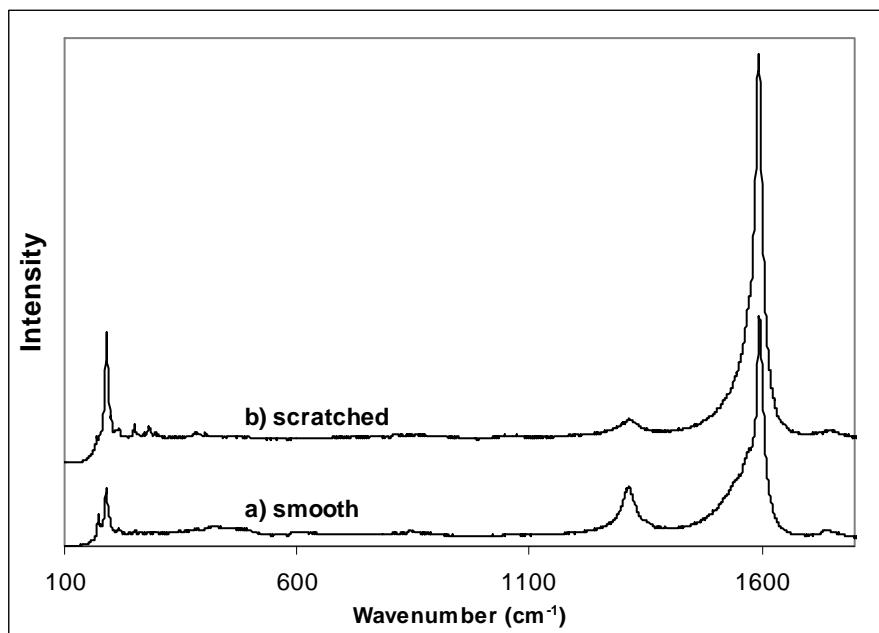


Figure 6.3 Raman spectra of products obtained over a) smooth quartz surface and b) scratched quartz surface after reaction with CO at 850°C.

To corroborate the Raman observations electron microscopy was performed on these two different samples. SEM images of these two surfaces are compared in Figure 6.4.

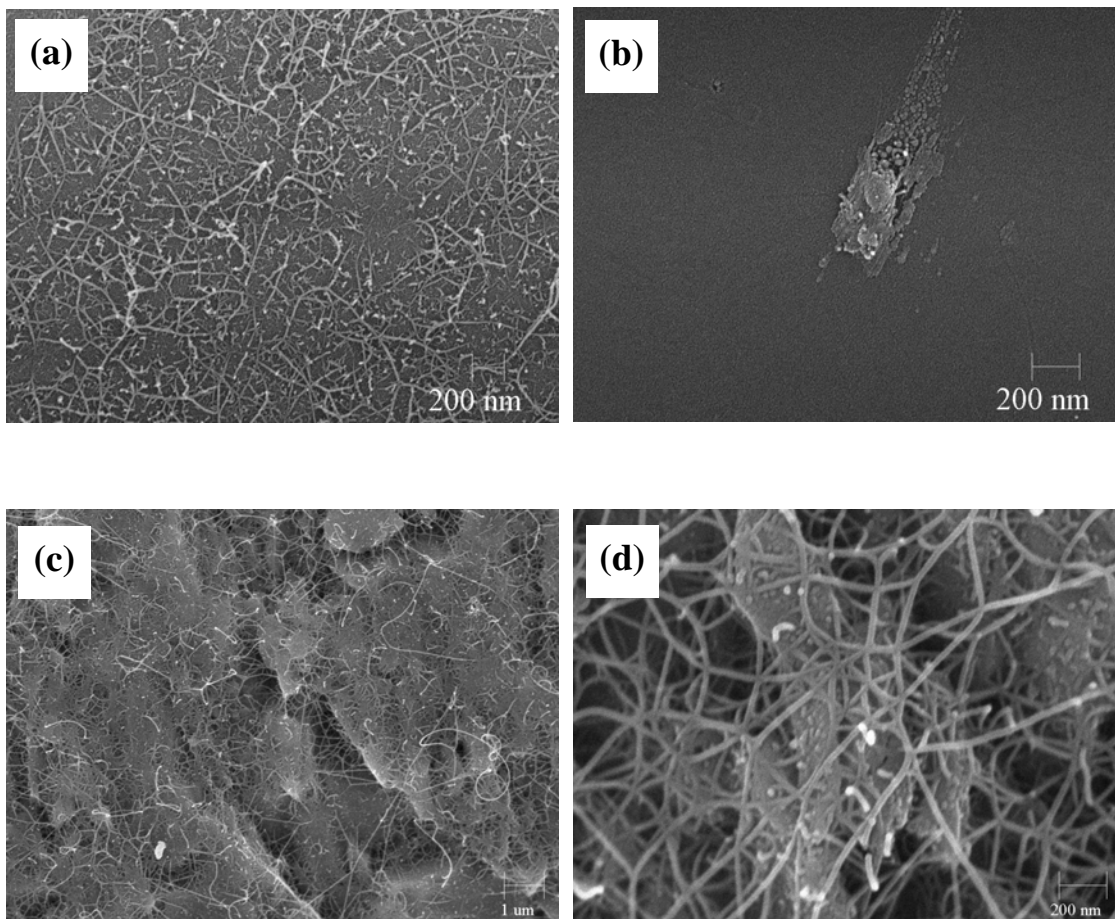


Figure 6.4 SEM images obtained on smooth quartz surfaces (a and b) and scratched quartz surfaces (c and d) after reaction with CO at 850°C.

As mentioned above, in the case of smooth surface SEM analysis indicated heterogeneity on the product distribution. By observing this substrate using SEM (Fig. 6.4a and b) it is clear that the yield of SWNT is not the same in all areas. A contrasting behavior is observed in the case of the materials obtained over the scratched surface. In this particular case, the product distribution is improved as shown in the SEM image of this substrate obtained at low magnification (Fig.6.4c). With higher magnification, high

density of SWNTs entangle on the surface is observed. This difference between smooth and scratched surface was rationalized in terms of the catalyst distribution as discussed below.

As illustrated by Raman spectroscopy and SEM above (Figure 6.1 and Figure 6.2), when ethanol is used as feed, MWNTs were synthesized. However, in these experiments, He was used as carrier gas. In the previous chapter we demonstrated that the effect of varying the carrier gas composition is critical in production of SWNTs using the floating catalyst method with ethanol as feed. Indeed, when H₂ was employed as carrier gas at 800°C, the quality of the material obtained increased (Table 5.1). Based on this observation we attempted to improve the quality of the material obtained using ethanol decomposition over the flat quartz surface by changing the carrier gas from He to H₂. We performed this study on the smooth quartz surface. Raman spectra of the carbonaceous deposits obtained on the smooth surface using He and H₂ as carrier gases after ethanol decomposition are shown in Figure 6.5. The Raman spectra of the product obtained over the scratched surface using H₂ is also show. It can be seen that the relative intensity of the D band compared to the G band decreases when H₂ was used as carrier gas. Also the radial breathing mode which is the characteristic band of SWNTs is clearly visible when H₂ is used a carrier gas indicating the presence of SWNTs. The reason for the improving on product quality might be rationalized in the same way proposed earlier in section 5.3.2 That is it is possible that when H₂ was used as carrier gas, the reaction equilibrium of the possible chemical reactions is shifted toward the reactants, resulting in

a slower reaction rate, otherwise it might due to the so-called “cleaning effect”. As H_2 is introduced to the system, it can react with the carbon atoms that are deposited over the metal surface. This phenomenon helps slowing down the formation of a graphitic sheet, leading to a lower rate of metal encapsulation, resulting in higher quality parameter ($G/(G+D)$).

We attempted to further improve the product quality by using the scratched surface under the same conditions (i.e. H_2 carrier gas, ethanol as carbon source). The product quality on this surface shown to be further enhanced as the decrease on the D band intensity indicates in Figure 6.5c.

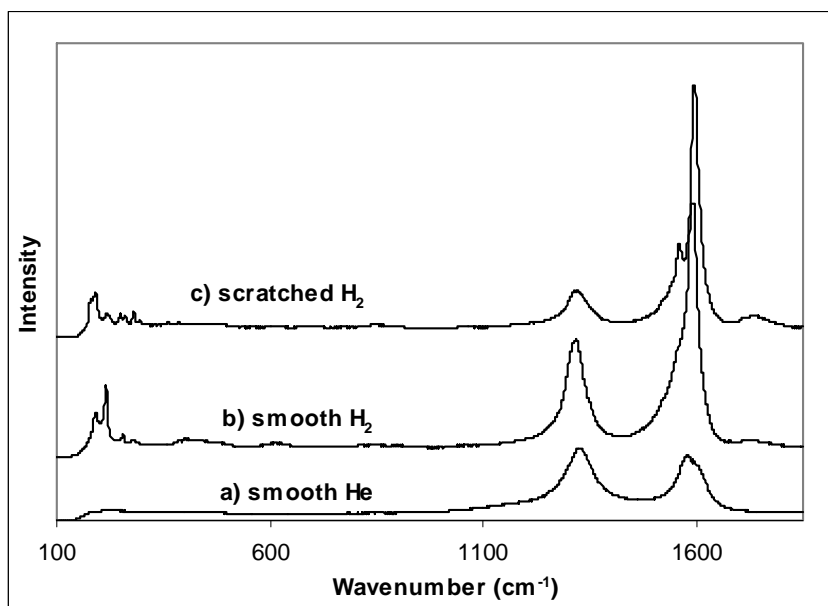


Figure 6.5 Raman spectra of products obtained on quartz surfaces after reaction with ethanol at 850°C using different carrier gases: a) smooth quartz surface with He as carrier gas, b) smooth quartz surface with H_2 as carrier gas, and c) scratched quartz surface with H_2 as carrier gas.

We also studied the effect of different ratios of He and H₂ on the quality and morphology of the SWNT materials obtained over a CoMo impregnated scratched quartz surface. The molar ratio of He to H₂ used in these series of experiment were 1:1, 1:2, 1:3, and 1:5. The Raman spectra and quality parameter (G/(D+G)) of the products obtained over the substrate treated using these different molar ratios of He to H₂ are shown in Figure 6.6. As the amount of He introduced into the system increases the intensity of the D band shows a systematic decrease. Indeed, the value of the quality parameter (G/(D+G)) increases from 0.7 (in case of pure H₂) to 0.9 when about 20% of He (He to H₂ ratio 1:5) is introduced in the system. The (G/(D+G)) value remains constant at about 0.9 even at about 35% of He in the carrier gas (He to H₂ ratio 1:2). Then it drops to 0.8 when 50% of He was mixed with H₂ (He to H₂ ratio 1:1). Therefore, the quality of product obtained on the surface can be improved by mixing small amount of He in H₂ stream as the carrier gas (He to H₂ ratio 1:2, 1:3, and 1:5). However, if a lot of He is added to the system (He to H₂ ratio 1:1), the quality of product began to decrease and product of a similar quality to that obtained using the smooth quartz surface with pure He, i. e. MWNTs.

To evaluate the effect of the carrier composition on the morphology of the material obtained we performed a detailed Raman analysis of the material using three different excitation lines. By using this kind of analysis it is possible to obtain an accurate description of the SWNT diameter distribution by probing the different energy gaps between singularities in the valence and conduction bands of the electronic density of

states of SWNTs through the resonant Raman effect. Indeed, calculations linking these singularities with nanotube diameters have been conducted by Kataura *et al.* (²²) and their results are reproduced in Figure 6.7 and used to evaluate our experimental data. In this Figure, the calculated results for each possible nanotube structure (Kataura's plot) is used as a background; with the solid and open circles representing nanotubes with metallic and semiconducting character, respectively. The diameter distribution of the SWNTs obtained over our quartz surface using different He:H₂ ratios are shown in Figure 6.7. As mentioned above, three different laser excitation energies were used to identify the tube diameters obtained on each He to H₂ ratio. Superimposed over the so-called Kataura's plot, the Raman data obtained in the present work for each observed nanotube diameter, as inferred from the frequency of the radial breathing mode bands (see section 2.1.2.2), are indicated with solid circles. The different colors red, green, and blue indicate results obtained using laser lines with 2.0, 2.4, or 2.55 eV energies respectively. It can be seen that the different He to H₂ ratio used shows a very broad diameter distribution, and a clear trend in diameter change at different He:H₂ ratios cannot be observed, indeed all the materials seem to yield SWNT with diameters ranging from 0.7 to 1.8 nm. This result seems to point out that although under our reaction condition the gas composition changes the quality of the product obtained it does not have an impact on the nanotube diameter.

SEM images obtained on the surfaces after reaction with ethanol using mixtures of He and H₂ with ratios 1:1, 1:2, and 1:3 are shown together with that one

obtained on the material synthesized using pure H₂ as carrier gas in Figure 6.8. The most important observation is that when He is added to the system, the amount of short nanotubes decreases dramatically. As we can see from Figure 6.8a, when pure H₂ is used as carrier gas, a large number of short nanotubes is observed. With using a 1:1 He to H₂ ratio the amount of short nanotubes obtained decreases, as the ratio change to 1:2 and 1:3, only few short nanotubes are detected and the material becomes abundant in nanotubes of longer length. This observation is in agreement with Raman spectra that show the decreases in D band intensity with a decrease in the He to H₂ ratio, since shorter length of SWNTs have commonly a larger density of defects than longer nanotubes.

As mentioned in section 5.3.2, H₂ can help reducing the amount of carbon supplied to the catalyst by shifting the reaction equilibrium of the possible chemical reactions toward the reactants, resulting in a slower reaction rate, and to clean the catalyst surface as well, by reacting with the carbon atoms that are deposited over the metal surface, which helps slowing down the formation of a graphitic sheet, leading to a lower rate of metal encapsulation. These two effects might play an important role in the case of ethanol decomposition over the flat quartz surfaces. On the other hand, as observed above, the quality of the products obtained using a mixture of He and H₂ gases is further improved as the amount of He in the carrier increases as the calculated values of the quality parameter ($G/(D+G)$) calculated from the Raman spectra indicate (Figure 6.6).

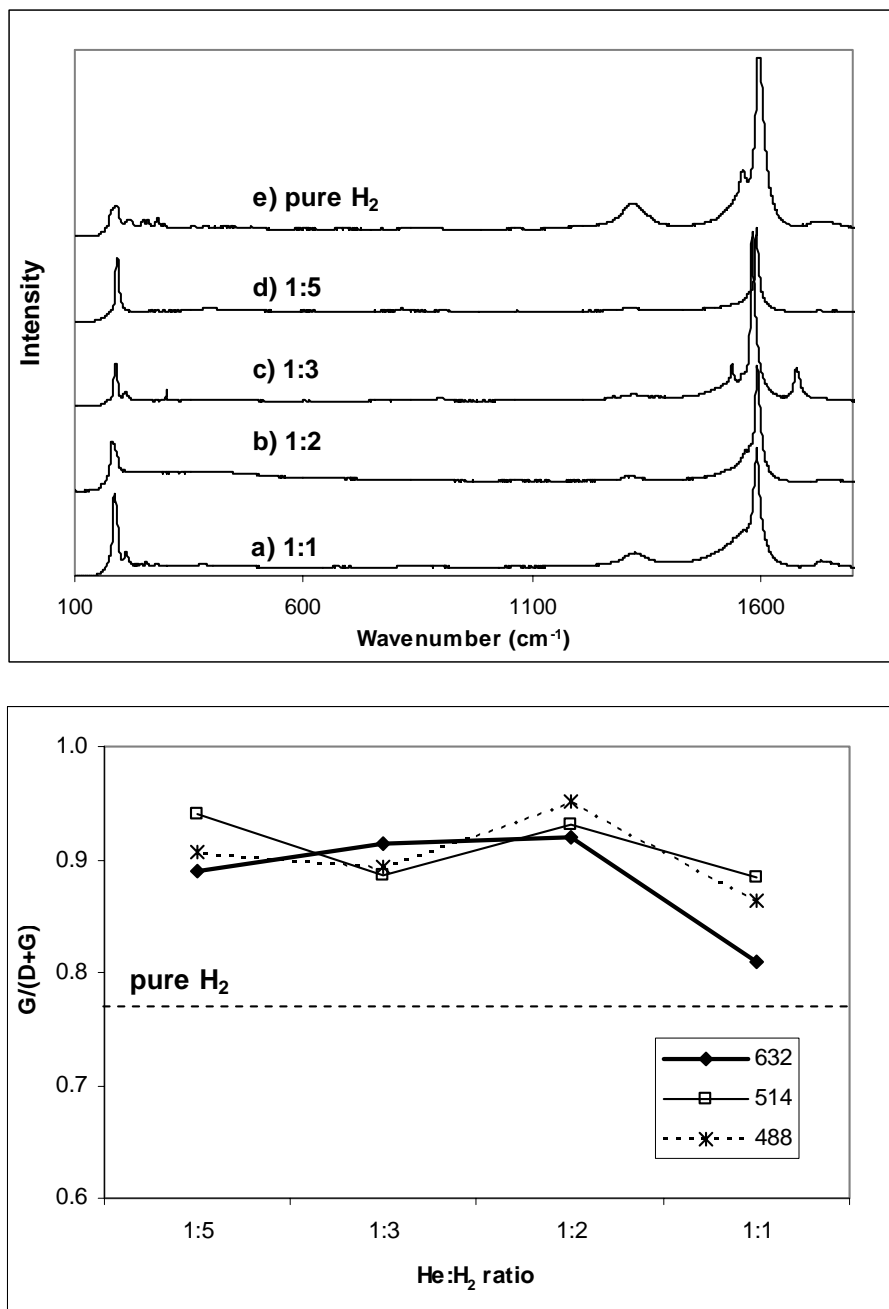


Figure 6.6 (Upper) Raman spectra of products obtained after reaction with ethanol at 850oC using mixtures of He and H₂ gas as carrier with different He:H₂ ratio: (a) pure H₂, (b) 1:1, (c) 1:2, (d) 1:3, and (e) 1:5. (Lower) Quality parameter (G/(D+G)) calculated from Raman spectra obtained using different laser energy.

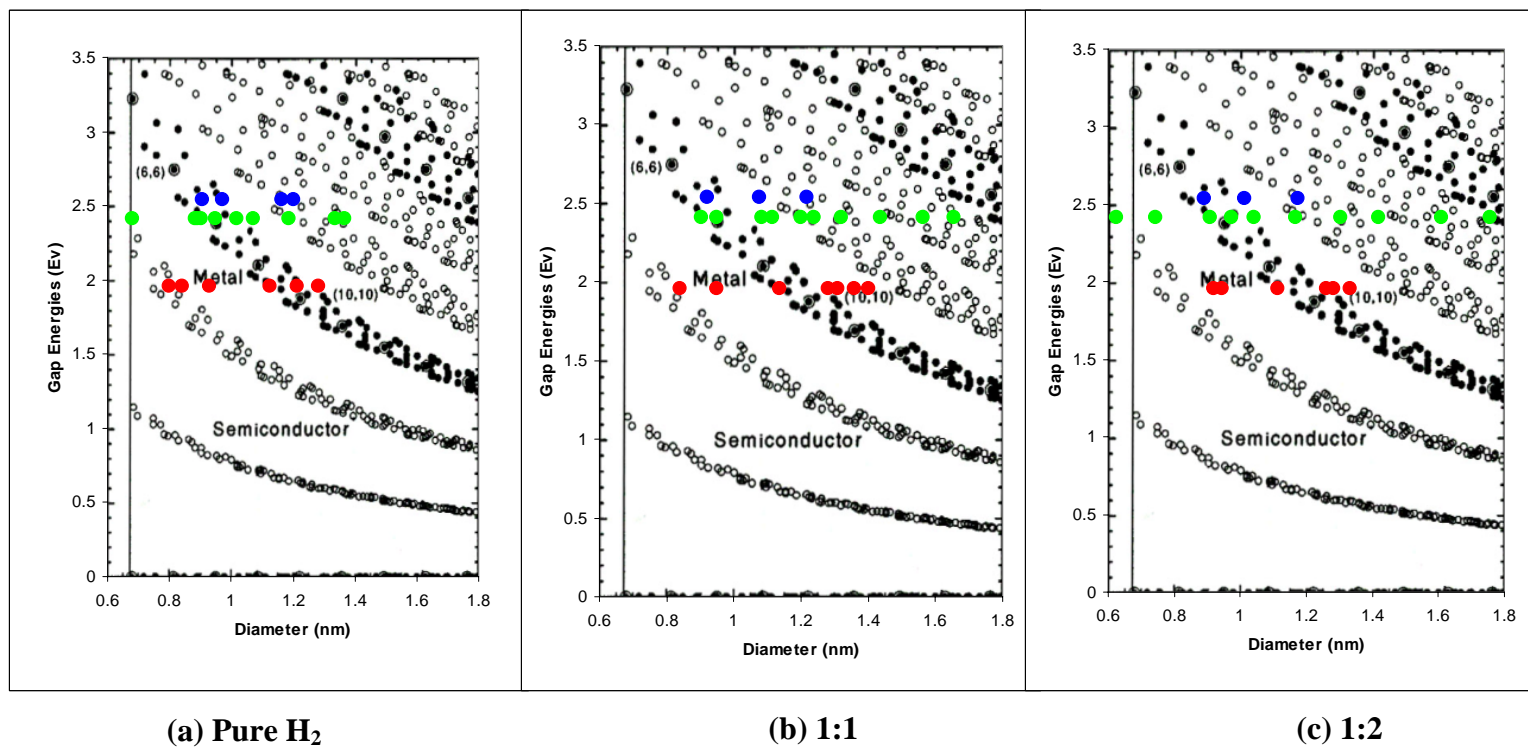
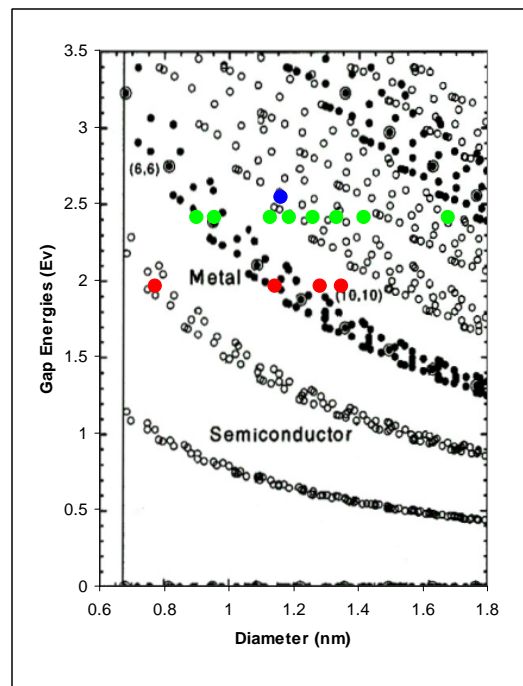
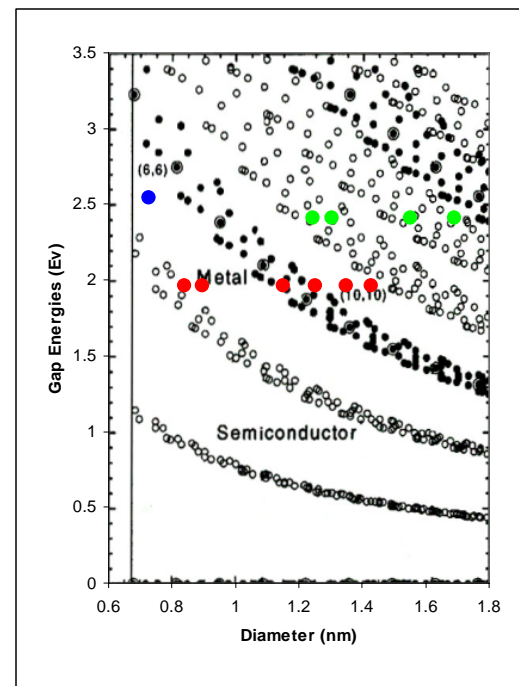


Figure 6.7 Diameter distribution of SWNT products obtained after reaction with ethanol at 850°C using mixtures of He and H₂ gas as carrier with different He:H₂ ratios: (a) pure H₂, (b) 1:1, (c) 1:2, (d) 1:3, and (e) 1:5.



(d) 1:3



(e) 1:5

Figure 6.7 (cont'd) Diameter distribution of SWNT products obtained after reaction with ethanol at 850°C using mixtures of He and H₂ gas as carrier with different He:H₂ ratios: (a) pure H₂, (b) 1:1, (c) 1:2, (d) 1:3, and (e) 1:5.

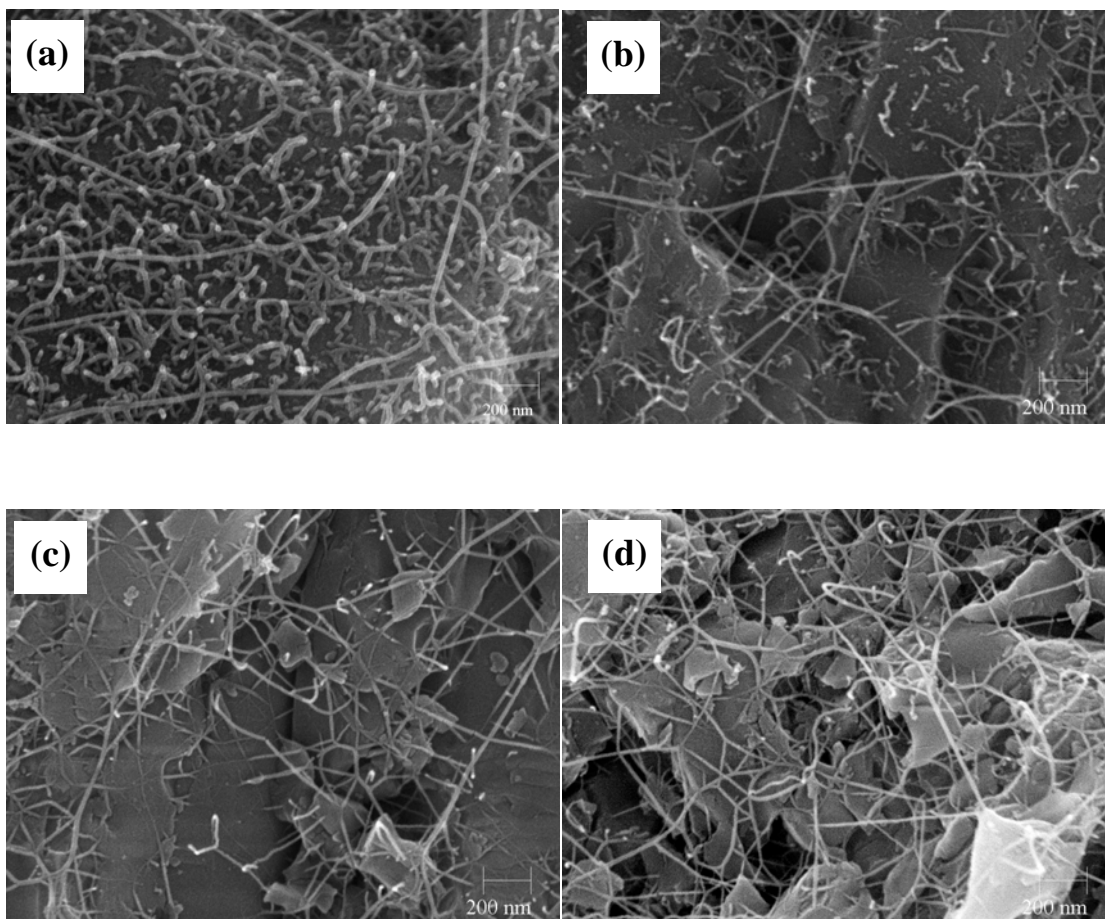


Figure 6.8 SEM images of the products obtained after reaction with ethanol at 850°C using a mixture of He and H₂ gas as carrier with different He:H₂ ratios: (a) pure H₂, (b) 1:1, (c) 1:2, and (d) 1:3.

We can rationalize this behavior in terms of the competition between the rate of carbon supply to the metal particle and the rate of metal agglomeration. In the case of pure H₂ as carrier gas, the amount of carbon supply from ethanol decomposition decreases and as consequence the reaction rate of carbon decomposition decreases; moreover hydrogen might also remove already deposited carbon from the metal surface

by a gasification mechanism (formation of methane or another light hydrocarbons). These two effects prevent metal encapsulation by graphite and also the formation of MWNT or carbon nanofibers, which are observed when pure He was used as carrier gas. However, since the substrate used in these series of experiments has an extremely low surface area compared to catalyst supports commonly used, the distance between different metal particles in this substrate might be smaller. As a consequence at the high temperatures used here the rate of metal agglomeration should be higher than in case of porous supports, particularly when H₂ is present. This leads to a higher amount of large metal particles and therefore formation of MWNT, carbon nanofibers, or metal encapsulation is observed. In the case of a small amount of He added to dilute the H₂ stream, it is possible that the rate of metal agglomeration slows down leading to a decrease on the formation of MWNT or metal encapsulation. Moreover, when a small amount of He is introduced, the rate of ethanol decomposition increases, resulting in a higher rate of carbon supply to the nanoparticle which in turn leads to a higher amount of long SWNTs in contrast to the product observed when H₂ alone was used as carrier gas (short SWNTs). However, as the amount of He further increases the rate of carbon supply increases accordingly, resulting again in higher rate of MWNTs formation and the decrease in product quality.

6.3.2. Surface analysis of the quartz substrate

In section 6.3.1 we showed that the surface morphology (whether smooth or scratched) plays a crucial role on the quality and homogeneity of product obtained over the quartz substrate. The surface that was roughened before impregnation with CoMo yields SWNTs of higher quality than those obtained over the smooth quartz surface as shown by Raman spectra in both CO and ethanol cases. To understand the catalyst morphology XPS analysis of the impregnated CoMo surface was performed after calcination in air at 400°C, reduction in H₂ at 500°C, heating up to 850°C in He, and reaction with CO at 850°C. The binding energies of the Co 2p_{3/2} and Mo 3d_{5/2} levels obtained for both smooth and scratched quartz surfaces are shown in Table 6.1. From a detailed analysis of the data in Table 6.1, it is clear that smooth and scratched quartz exhibit similar chemical states after calcination, reduction, and reaction. After calcinations in air at 400°C, the main peak in the spectra corresponding to the Co 2p_{3/2} level shows a maximum at about 781 eV, which has been previously attributed to Co²⁺ in CoMoO₄ species (780.5-781.4 eV) (19, 23-26). After reduction and reaction with CO, the spectra shows an additional peak centered at about 778 eV, which corresponds to metallic Co (777.8-778.5 eV) (19, 24-27). In the case of the Mo 3d_{5/2} level, it can be observed that after calcination the surface is mainly composed of a single doublet, with the main peak centered at 232 eV, which is attributed to Mo⁶⁺ in MoO₃ (232.2–233.0 eV) [19, 25-30] and/or nonstoichiometric Co molybdates, CoMoO_x (232.1–232.3 eV for stoichiometric Co molybdate where x = 4) [19, 24, 25]. After reduction in H₂ and

heating up to 850°C in He, there are two additional bands that appear in the Mo spectra , one at about 228 and the other one at 231 eV, which correspond to Mo⁴⁺ in MoO₂ and to an intermediate state such as Mo⁵⁺, respectively (19)

The fraction of the different chemical states of Co and Mo were obtained from the fitting of the XPS spectra using asymmetric curves. The results are shown in Table 6.2. Several interesting observations can be drawn from a detailed analysis of the results illustrated in Table 6.2. First, it is clear that the change in the chemical state of Co with different treatments is more dramatic for the smooth than for the scratched quartz surface. Indeed, the peak centered at 781 eV, which corresponds to Co²⁺ species decreases to about 27% of the overall Co content, together with the appearance of about 73% of metallic Co after reduction. Moreover, after reaction with CO the amount of Co in metallic state increases to 87% of the overall Co content. For the case of the scratched quartz surface, the amount of oxidized cobalt is around 36% respect to 64% of metallic Co after reduction, and after reaction with CO, the Co²⁺ contribution to the XPS spectra decreases to about 25%. From these values it is possible to conclude that the reduction of Co during the pretreatment and reaction stages is easier when CoMo is impregnated on the smooth quartz surface.

Table 6.1 Binding energies for CoMo impregnated quartz surface after subsequent treatments calcination (calcined), reduction and heat up to 850°C in He (reduced), and reaction with CO (reaction).

Catalysts	Co 2p_{3/2} peak		Mo 3d_{5/2} peak	
	position (eV)		position (eV)	
	Smooth	Scratched	Smooth	Scratched
Calcined	781.83	781.57	232.36	232.31
Reduced	778.37	779.01	228.03	227.79
	781.62	781.66	231.02	231.04
			232.58	232.40
Reaction	778.92	778.80	228.39	228.54
	781.83	781.59	231.60	231.37

Our previous work (19) has clearly established that in the case of SWNT production using CoMo (1:3)/SiO₂ as catalyst, after calcination Co and Mo are in the form of CoMoO₄ species. EXAFS and XANES analysis of the real powder catalyst showed that even under the H₂ environment at high temperature Co and Mo species are still in the oxidized state, forming a Co-Mo suboxide instead of stoichiometric CoMoO₄ species. When CO is in contact with the catalyst, these pre-reduced cobalt molybdate species are converted to an unstable CoMo carbide; Co is no longer stabilized in this new

matrix and starts migrating towards the surface where it gets reduced to form very small Co metallic clusters which trigger SWNT growth.

Table 6.2 XPS fitting results for the chemical state for Co and Mo on the quartz surface after subsequent treatments calcination (calcined), reduction and heat up to 850°C in He (reduced), and reaction with CO (reaction).

	Composition (%)					
	Scratched surface			Smooth surface		
	Calcined	Reduced	Reaction	Calcined	Reduced	Reaction
Co²⁺ (781 eV)	100	36.09	25.18	100	27.43	13.23
Co⁰ (778 eV)	0	63.91	74.82	0	72.57	86.77
Mo⁶⁺ (232 eV)	100	11.82	0	100	6.62	0
Mo⁵⁺ (231 eV)	0	29.68	31.98	0	37.72	18.29
Mo⁴⁺ (228 eV)	0	58.50	68.02	0	55.66	81.71

From the XPS results obtained on the CoMo impregnated on the quartz substrate shown above, we can also state that after calcination Co and Mo are forming CoMoO_4 species. However, after reduction at high temperature some of these CoMoO_4 species get reduced, yielding metallic Co and Co^{2+} that might still be interacting with Mo in the form of a cobalt molybdate suboxide. This difference from the CoMo/SiO₂ real catalyst is possibly arising from the low surface area of the quartz substrate compared to that of silica gel used as support in the case of CoMo/SiO₂ catalyst and also to the fact that in the case of the flat surface samples the molar ratio of Co to Mo is about 1.6. Therefore, there is excess amount of Co that does not interact with Mo; these Co can be reduced easier than the ones that interact with Mo (19), yielding metallic cobalt after pretreatment in hydrogen.

The Co and Mo atomic percentage obtained based on the XPS results on the scratched and smooth surfaces after each treatment is shown in Figure 6.9. It can be seen that the amount of Co and Mo on smooth quartz surface is higher for almost an order of magnitude than those in the case of the scratched quartz surface. Both smooth and scratched quartz surfaces exhibit similar trends after treatment with H₂ at 500°C heating up to 850°C in He and reaction with CO at 850°C. However, the quantity of Co and Mo detected by XPS on the smooth surface after calcination is much higher than on the scratched surface. After the reduction in H₂ at 500°C and heating to 850°C in He, the amount of Co and Mo significantly drop from 12% to 4% (atomic %) in the case of the smooth quartz surface, while these same quantities slightly decrease in the case of

scratched quartz surface from about 2% to 1%. After reaction with CO at 850°C, the concentration of Co and Mo on the surfaces dimly changes compared to the large variation observed when the calcined samples are reduced in H₂. In order to obtain a better description of the surface composition at each stage we also calculated Co to Mo and Co to Si atomic ratios; the results are shown in Figure 6.10. In the case of Co/Mo ratio, a similar trend is observed on both smooth and scratched surfaces, that is an increase in the Co/Mo ratio at each stage (Figure 6.10). These changes probably arise from the exposure of Co atoms onto the surface after treatments with H₂ and CO. The Co/Si ratio obtained on the smooth quartz surface after calcinations is very high compared to the value obtained for the scratched quartz surface. This same value then drops dramatically after treatment in H₂ at 500°C and decreases slightly after reaction with CO. This trend is the same as the one observed in each treatment step for the % of atomic Co (Figure 6.9.) Therefore, it is possible that the change in this ratio is mostly effected by a variation of the amount of Co on the surface indicating that the dispersion of Co on the smooth quartz surface decreases significantly after treatment in H₂. In the case of scratched quartz surface, the values for atomic %Co and Co/Si atomic ratio are not affected as dramatically by the treatment step. These two different behaviours can be explained if one assumes that in the case of the smooth quartz surface, the cobalt molybdate species are forming a thin layer over the silica after calcination; then after treatment in H₂ at high temperature, reduction of the metal oxide species takes place, some metallic cobalt nucleation takes place and the initial thin film of cobalt molybdate dewets the silica surface. As a consequence the relative amount of cobalt on the surface

detected by XPS decreases. However, in the case of scratched quartz surface, because the roughness of the surface might yield a higher surface area, the amount of cobalt molybdate might not be enough to form a thin film to cover the entire quartz surface, leading to a relatively low concentration of cobalt on the surface observed by XPS. Therefore, after treatment in H₂ at high temperature, even though dewetting of the film might occur, the change is not as dramatic because in this case the silica surface is already exposed before treatment.

To summarize, from XPS results, we can conclude that in both smooth and scratched quartz substrate the Co and Mo species are in the form of CoMoO₄ after calcination in air at 400°C. This cobalt molybdate species are reduced at high temperature in the presence of H₂ to give metallic Co together with some of Co-Mo suboxide species. Then after reaction with CO at 850°C the amount of metallic Co increases. However, on the case of the smooth quartz surface, the formation of metallic Co is faster than in the case of the scratched quartz surface as XPS shows higher fraction of metallic Co compare to Co²⁺. As a result, metal agglomeration take place, leading to the rapidly decrease in the dispersion of Co on the smooth quartz surface, which then result in lower quality of SWNT obtained on this surface as observed in Figure 6.3. For the case of the scratched quartz surface, the roughness of the surface might give a higher surface area which helps preventing metal agglomeration, resulting in the improvement of SWNT quality.

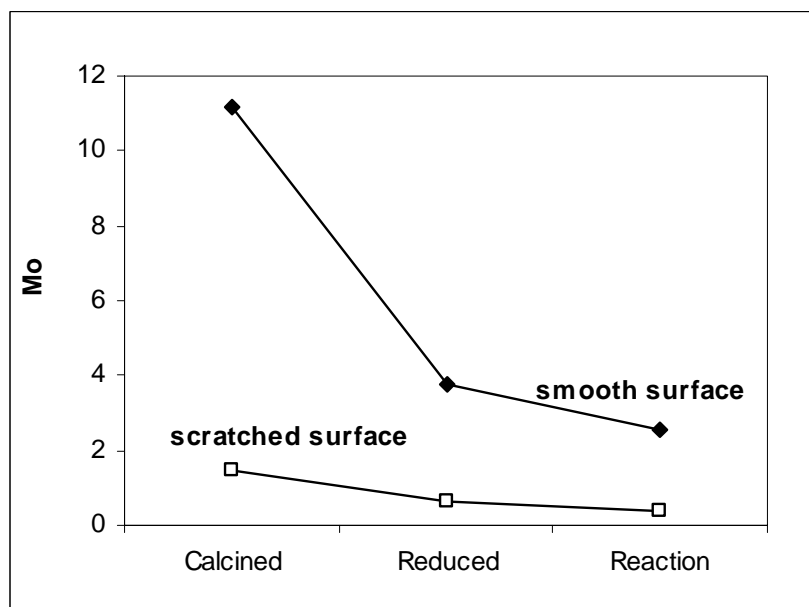
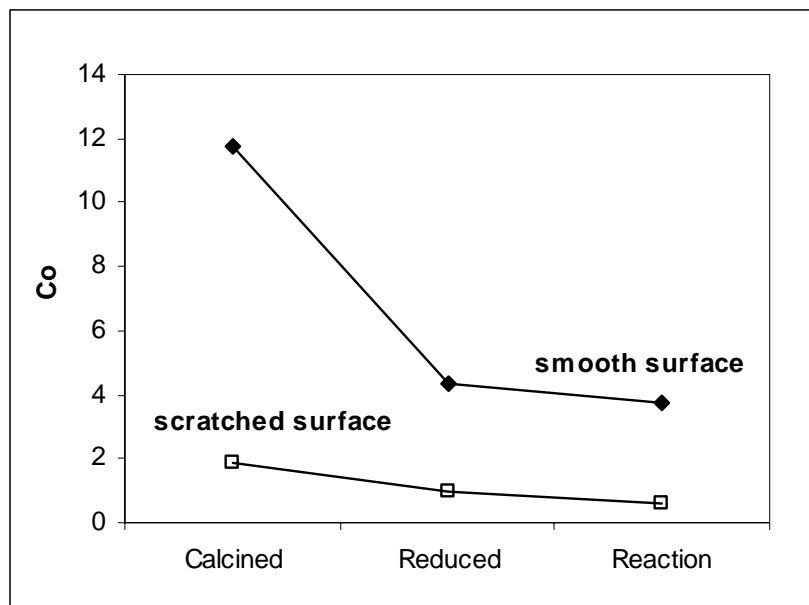


Figure 6.9 Atomic percentages of Co and Mo of CoMo impregnated on quartz surface after calcination at 400°C (Calcined), reduction at 500°C and heat up to 850°C in He (Reduced), and reaction with CO at 850°C (Reaction) as obtained for XPS analysis.

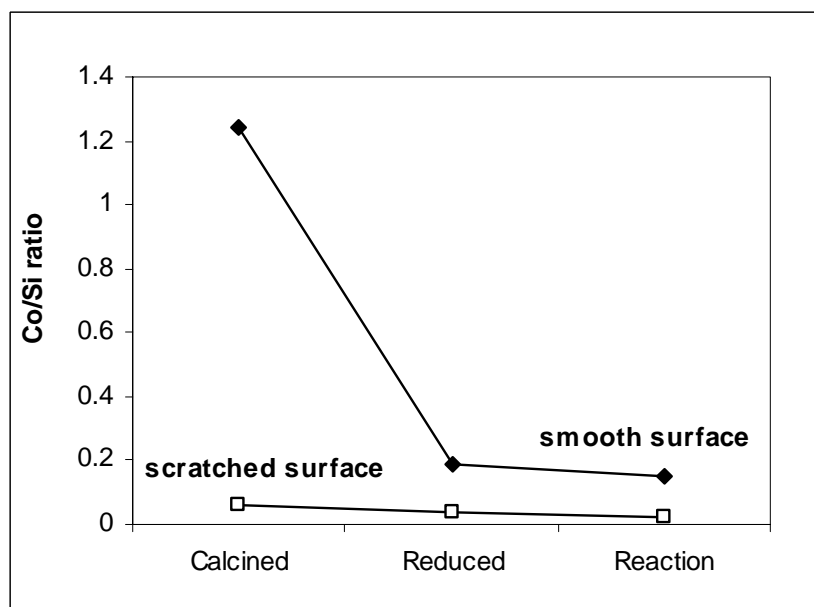
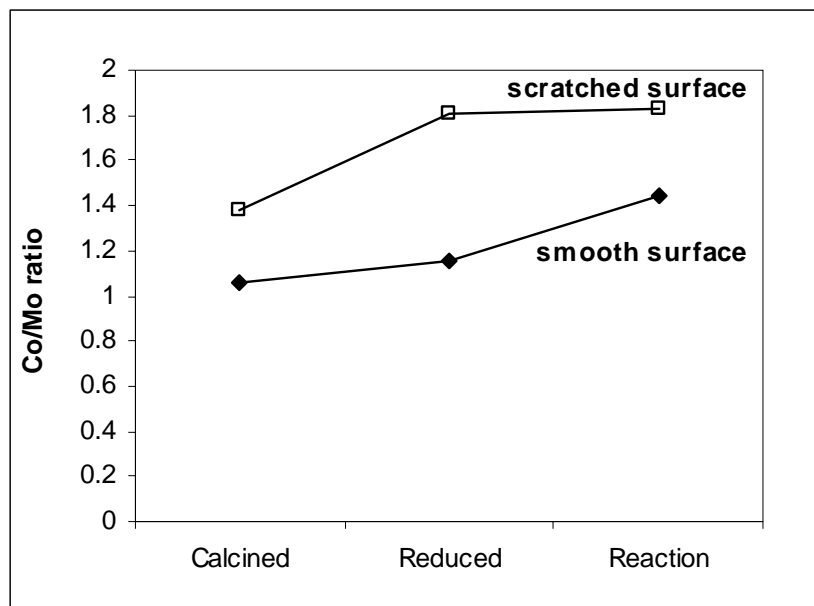


Figure 6.10 Co/Mo and Co/Si ratio calculated from XPS analysis for CoMo impregnated on quartz surface after calcination at 400°C (Calcined), reduction at 500°C and heat up to 850°C in He (Reduced), and reaction with CO at 850°C (Reaction).

6.4. CONCLUSIONS

In this chapter, we have showed that SWNT can be synthesized over flat quartz substrates impregnated with CoMo bimetallic catalysts by using CO or ethanol as carbon feedstock. The surface structure of the quartz substrate plays a critical role on the quality of the SWNTs obtained. The surface roughened before catalyst impregnation yields SWNT of higher quality. The reason for this observation has been attributed to the lower rate of metal agglomeration on the surface compared to that one observed on the smooth quartz surface. In the case of ethanol used as carbon containing molecule, the carrier gas composition also has a significant impact on the quality of SWNTs. When He was used as carrier gas, MWNTs are obtained instead of SWNTs. However, when H₂ was employed, SWNTs were obtained. The quality of the product improves when He was added to the H₂ stream up to about 35%. This phenomenon has been rationalized in terms of a balance between the rate of carbon supply and rate of metal agglomeration.

REFERENCES

- 1 S. J. Tans, M.H. Devoret, H. Dai, A. Thess, R.E. Smalley, L.J. Geerligs, C. Dekker, *Nature* 386, 474 (1997)
- 2 S.J. Tans, A.R.M. Verschueren, C. Dekker, *Nature* 393, 49(1998)
- 3 C. Zhou, J. Kong, H. Dai, *Appl. Phys. Lett.* 76, 1597 (2000)
- 4 J. M. Bonard, J.P. Salvetat, T. Stockli, L. Forro, A. Chatelain, *Appl. Phys. A* 69, 245 (1999)

- 5 A.M. Cassell, N.R. Franklin, T.W. Tomblor, E.M. Chan, J. Han, H.J. Dai, Am. Chem. Soc. 121, 7975 (1999)
- 6 V. Derycke, R. Martel, M. Radosvljevic, F.M.R. Ross, P. Avouris, Nano Lett. 2, 1043 (2002)
- 7 N.R. Franklin, Y.M. Li, R.J. Chen, A. Javey, H.J. Dai, Appl. Phys. Lett. 79, 4571 (2001)
- 8 E. Joselevich, C.M. Lieber, Nano Lett. 2, 1137 (2002)
- 9 B. Zheng, C. Lu, G. Gu, A. Makarovski, G. Finkelstein, J. Liu, Nano Lett. 2, 895 (2002)
- 10 S. Huang, X. Cai, C. Du, and J. Liu, J. Phys. Chem. B 107, 13251 (2003)
- 11 S. Huang, X. Cai, J. Liu, J. Am. Chem. Soc. 125, 5636 (2003)
- 12 S. Huang, B. Maynor, X. Cai, J. Liu, Adv. Mater. 15, 1651 (2003)
- 13 W. Kim, H. C. Choi, M. Shim, Y. Li, D. Wang, H. Dai, Nano Lett. 2, 703 (2002)
- 14 Y. Murakami, S. Chiashi, Y. Miyauchi, M.H. Hu, M. Ogura, T.Okubo, S. Maruyama, Chem. Phys. Lett. 385, 298 (2004)
- 15 K. Hata, D.N. Futaba, K. Mizuno, T. Namai, M. Yumura, S. Iijima, Science 306, 1362 (2004)
- 16 G. Zhang, D. Mann, L. Zhang, A. Javey, Y. Li, E. Yenilmez, Q. Wang, J. P. McVittie, Y. Nishi, J. Gibbons, H. Dai, PNAS , 102, 16141 (2005).
- 17 D.E. Resasco, W. E. Alvarez, F. Pompeo, L. Balzano, J.E. Herrera, B. Kitiyanan, A. Borgna, J. Nanopart. Res. 4, 131 (2002)
- 18 B. Kitiyanan, W.E. Alvarez, J.H. Harwell, D.E. Resasco, Chem. Phys. Lett. 317, 497 (2000).
- 19 J.E. Herrera, L. Balzano, A. Borgna, W. E. Alvarez, D.E. Resasco, J. Catal. 204, 129 (2001).
- 20 W.E. Alvarez, B. Kitiyanan, A. Borgna, D.E. Resasco, Carbon 39, 547 (2001)

- 21 Y. Murakami, Y. Miyauchi, S. Chiashi, S. Maruyama, Chem. Phys. Lett. 377, 49 (2003)
- 22 H. Kataura, Y. Kumazawa, Y. Maniwa, I. Umezu, S. Suzuki, Y. Ohtsuka, Y. Achiba, Synth. Met. 103, 2555 (1999)
- 23 M. Hu, Y. Murakami, M. Ogura, S. Maruyama, T. Okubo, J. Catal. 225, 230 (2004)
- 24 M. Probst, M. Vob, R. Denecke, L. Viscido, J.M. Heras, D. Borgmann, H.-P. Steinruck, J. Electron Spectrosc. Relat. Phenom. 114, 539 (2001)
- 25 V.L. Parola, G. Deganello, C.R. Tewell, A.M. Venezia, Appl. Catal.A 235, 171 (2002)
- 26 R. Kleyna, H. Mex, M. Vos, D. Borgmann, L. Viscido, J.M. Heras, Surf. Sci. 433, 723 (1999)
- 27 R. Riva, H. Miessner, R. Vitali, G.D. Piero, Appl. Catal. A 196,111 (2000)
- 28 B.R. Quincy, M. Houalla, A. Proctor, D.M. Hercules, J. Phys. Chem. 94, 1520 (1990)
- 29 F. Solymosi, J. Cserenyi, A. Szoke, T. Bansagi, A. Oszko, J. Catal. 165, 150 (1997)
- 30 G. Chen, T.E. Ford, C.R. Clayton, J. Colloid Interface Sci. 204, 237 (1998)

CHAPTER 7

MICROSCOPIC ANALYSIS OF SWNT GROWN ON Co-Mo CATALYSTS SUPPORTED ON A TEM GRID USING CO AND CH₄

7.1. INTRODUCTION

The chemical vapor deposition (CVD) method is a technique widely used for the synthesis of SWNTs. Many researchers consider chemical vapor deposition (CVD) as the only viable approach to large-scale production. As a result, research is underway to optimize the CVD growth, i.e., to investigate the effect of catalyst composition, variation of supporting/substrate materials, synthesis temperature and hydrocarbon gases. Various carbon-containing molecules are used as feed, such as CH₄, C₂H₄, C₂H₂, CO, or C₂H₅OH (1-8). Our group has focused on the disproportionation of CO over bimetallic CoMo catalysts, which exhibited a high selectivity towards the production of SWNT at relatively low temperatures (9, 10).

Significant efforts are currently focused on trying to understand the mechanistic details of the SWNT growth. Understanding the growth mechanisms could lead to higher controllability in the SWNT production. There are two main proposed growth mechanisms, which are base-growth and tip-growth mechanism. The “tip-

growth” mechanism is well demonstrated for certain multiwalled carbon nanotubes (MWNTs) (11) and “base-growth” for both MWNTs (12) and SWNTs (13). In case of SWNTs grown from CVD on the powder catalyst, it is very difficult to image the origin of the SWNTs by TEM because the metal particles are usually small and also disturbed by the catalyst support. Direct observation of SWNT growth from the thin substrate containing isolated metal particle was first made by Li *et al.* (13, 14). In that work, discrete catalytic nanoparticles were placed on ultrathin alumina membrane. It has been found that under certain operating conditions the catalyst nanoparticle remains on the supporting substrate, whereas the nanotube grows away from the particle with a closed-end. This observation has led the authors to propose their result as a clear evidence for base growth model. Gavillet *et al.* in a series of transmission electron microscopy studies (15-17) have proposed a similar growth mechanism for SWNTs obtained from arc discharge or laser ablation. This mechanism, which adopts the concepts of the vapor-liquid-solid (VLS) model (18), is called root-growth mechanism in which the bundle of SWNTs nucleates from a catalyst nanoparticle that is supersaturated with carbon. Similar models have been reported by Alvarez *et al.* for SWNTs produced by the solar method (19).

In the present contribution, electron microscopy was used to investigate the growth mechanism of SWNT over a bimetallic Co-Mo catalyst. A model system based on a silicon dioxide TEM grid impregnated with a CoMo catalyst was used as catalyst and treated under similar reaction condition as in the powder catalyst and the

observations obtained from this model system were used to explain the differences in behavior of this Co-Mo bimetallic in powder catalyst under different reaction conditions..

7.2. EXPERIMENTAL

7.2.1 Model catalyst study

Lacey silicon monoxide membranes TEM grids were obtained from Ted pella Inc. The grid was first calcined at 500°C for 5 minutes in order to generate a silica surface on the membrane. A solution containing Co and Mo was prepared by dissolving cobalt (II) acetate tetrahydrate and molybdenum (II) acetate dimer in ethanol. The solution was then dropped on the calcined grids and further calcined at 400°C for 5 minutes to decompose the acetate and form Co-Mo metallic oxide species. The grid was then put into a reactor where they were reduced at 500°C in H₂ flow and heated up to reaction temperature (850°C) in He, after reaching 850°C CO or CH₄ were fed to the reactor. Different reaction times were used, ranging from 1 to 10 minutes.

After reaction, the TEM grid was directly characterized by Raman spectroscopy using a Jovin Yvon-Horiba LabRam 800 equipped with a CCD detector with a laser excitation source of 632nm (He-Ne laser). Transmission electron microscopy (JEOL 2000FX and JEOL 2010) and scanning electron microscopy (JEOL 880) were used to investigate the morphology of the catalyst and SWNT obtained after reaction.

7.2.2. Real catalyst study

Bimetallic CoMo supported on high surface area SiO₂ powder was prepared by incipient wetness impregnation. The bimetallic samples, prepared by coimpregnation of aqueous ammonium heptamolybdate and Co nitrate solutions on the support, had Co:Mo molar ratios of 1:3 and 2:1. After impregnation, the solids were dried overnight at 120°C and then calcined in air at 500°C for 2 hr. 50 mg of catalysts were placed in a horizontal quartz reactor of 0.5 inch diameter, heated in H₂ up to 500 °C and then in He to reaction temperature (i.e. 750°C or 850°C). Subsequently, the carbon-containing gas (either CO or CH₄) was introduced at a flow rate of 50 cm³/min for 10 min.

The products were examined by Raman while the amount of carbon deposited was determined by temperature programmed oxidation (TPO) as described in our previous work (20). In short, a continuous flow of 5% O₂ in He is passed over the product containing the carbon deposits while the temperature is linearly increased at a heating rate of 10°C/min. The evolution of CO₂ produced by the oxidation of the carbon species is monitored using flame ionization detector. Quantification of the evolved CO was calibrated with 100 µl pulse of CO.

Optical absorption spectra were measured using a Bruker Equinox 55 FTNIR. 5-10 mg of as-prepared materials was dispersed in 2 ml of 10 CMC (0.48wt. %) sodium dodecylbenzene sulfonate (NaDDBS) using dynamic ultrasonic agitation in a horn sonic

dismembrator (Model 500, Fisher Scientific) running at 10% power output for 1.5 hr. The suspension was then centrifuged (Sorvall SS-3, Du pont Instruments) at 15000 rpm for 30 minutes. The resulting supernatant was then used for the optical absorption measurement. Transmission electron microscope (TEM, JEOL 2000FX) was also used to monitor the SWNTs in these as-prepared materials.

7.3. RESULT AND DISCUSSION

7.3.1 Model catalyst study

Electron microscopy and Raman spectroscopy were used to characterize the model Co-Mo catalysts directly prepared over a silicon monoxide coated copper TEM grid. The use of this model system has allowed us to get a deeper insight at the fundamental level of the bimetallic Co-Mo system. This approach was undertaken in order to obtain direct observations of the transformations undergone by the catalyst under the different precursor gas during different growth times, as well as to assess the onset of the nanotube growth. Although the catalyst formulation (Co/Mo ratio, support composition) and reaction conditions attempt to mimic those of the high-surface area support, the resulting particle size and types of nanotube produced were not the same, and as described below, the particle size plays an important role. Nevertheless, the observed behavior is expected to be qualitatively the same as that in the real process.

Figure 7.1 shows the Raman spectra together with SEM and TEM images obtained for a silicon monoxide coated grid impregnated with Co-Mo after calcination in air at 500°C. The Raman spectra obtained for analytical references of CoMoO₄, and MoO₂ are also include for a direct comparison. It is clear that after calcination the catalyst shows the presence of CoMoO₄ species. After pretreatment in H₂ and before reaction, the cobalt molybdate bands become distorted; this change in the spectrum might be related to the loss of crystallinity of cobalt molybdate species upon thermal treatment in H₂. The observed spectral changes also indicate the formation of free molybdenum (IV) oxide species. As shown in Figure 7.1, the Raman spectrum of the MoO₂ reference shows a sharp peak at ~830 cm⁻¹ indicating that the shoulder observed at this position on the spectra of the catalyst pretreated at 850°C might be related to the segregation of free molybdenum species from the cobalt molybdate phase. Therefore, it seems that although a direct Co-Mo interaction existed on the calcined catalyst, prior to reaction there is a mixture of the original cobalt molybdate species together with a new MoO₂ phase generated during thermal treatment. Figure 7.1 also shows SEM and TEM images obtained for these catalyst particles after treatment at 850°C, the images show that some crystalline structure is still present before nanotube growth.

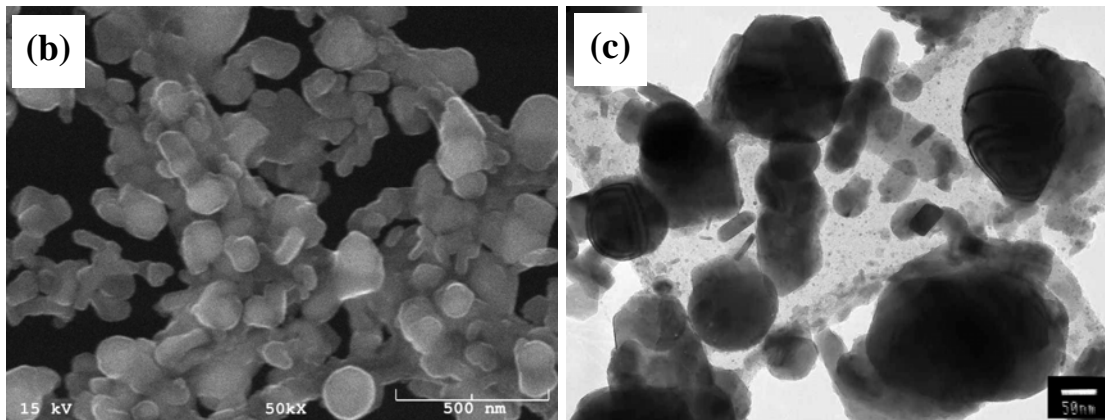
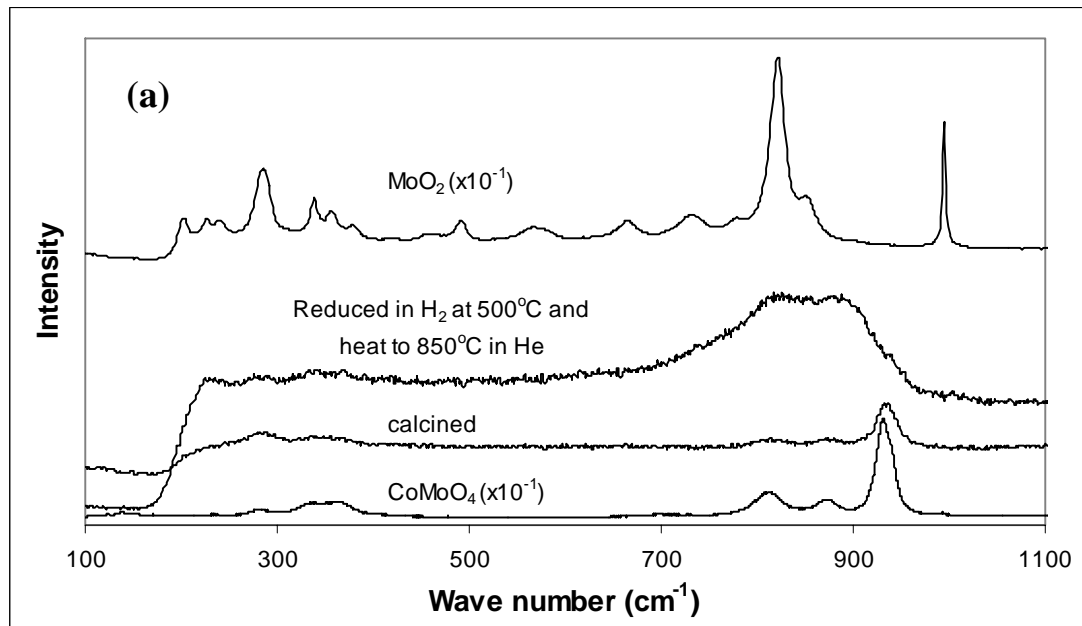


Figure 7.1 (a) Raman spectra of CoMo over silicon monoxide coated grid after two subsequent treatments; calcination at 500°C, reduction at 500°C and heating in He 850°C. Raman spectra of CoMoO_4 and MoO_2 are also shown. (b) SEM and (c) TEM images of CoMo over silicon monoxide coated grid after pretreatment to 850°C.

Figure 7.2 shows the Raman spectra and electron microscopy images obtained on the same materials after contact with CO at different times. For CO exposures of 1 minute, the spectrum looks similar to that obtained on the material right before contact with CO (see Fig. 7.1). However, the intensity of the peak at $\sim 830\text{ cm}^{-1}$ decreases, and as a result the peak at about 900 cm^{-1} appears more pronounced. This change implies that the MoO_2 species generated during pretreatment disappear upon introduction of CO. After exposure to CO for 3 minutes, the bands corresponding to Mo=O species completely disappear while two small bands become apparent at $\sim 1580\text{ cm}^{-1}$ and $\sim 1340\text{ cm}^{-1}$. These two bands indicate the formation of carbonaceous species on the catalyst surface. Indeed, the band at $\sim 1580\text{ cm}^{-1}$ (G band) is attributed to the in-plane stretching mode of ordered crystalline graphitic structures while the band at 1340 cm^{-1} (D band) has been related to the vibration of disordered carbon structures(21, 22). A very strong signal of the G band is observed after 10 minutes of CO exposure, and new bands at 193, 261, 284, and 300 cm^{-1} develop. The presence of these new bands together with the G and D bands indicates the formation of SWNT over the catalyst surface [23].

Figure 7.2 also shows the SEM and TEM images obtained for the model catalyst at different reaction times. First, after contact with CO for 1 minute, SEM and TEM images indicate that the catalyst particles start changing their morphology; indeed it is clear that the surface of the particles became rougher compared to the ones observed before exposure to carbon monoxide (Fig. 7.1). After 3 minute exposure to CO, a few

short SWNTs are clearly observed, while after 10 minutes a high density of long bundles of SWNTs is evident, which is in agreement with the Raman results.

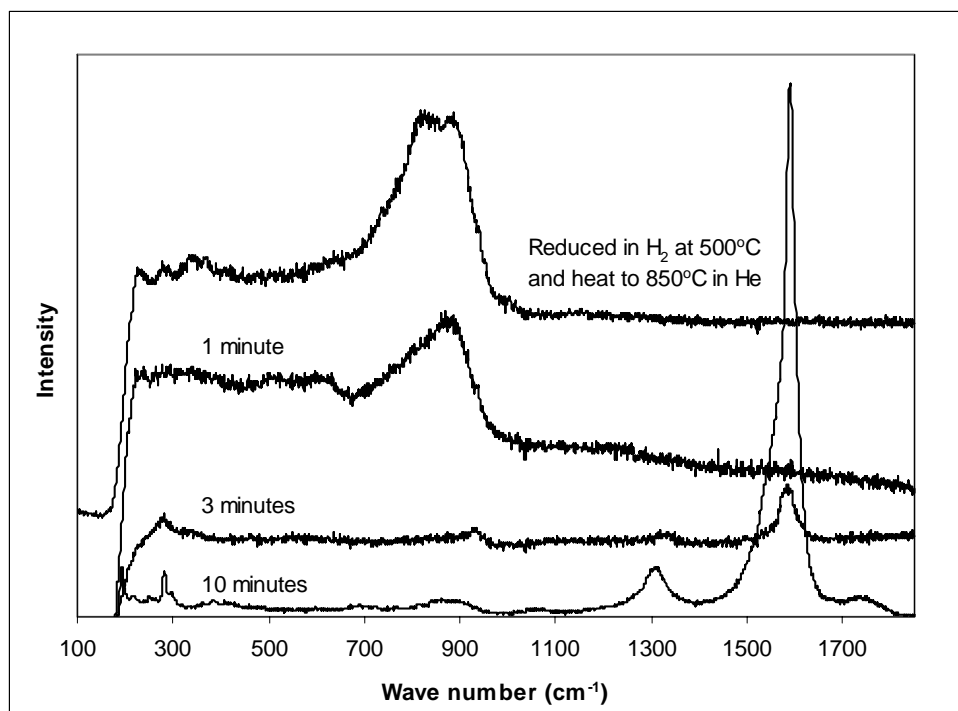
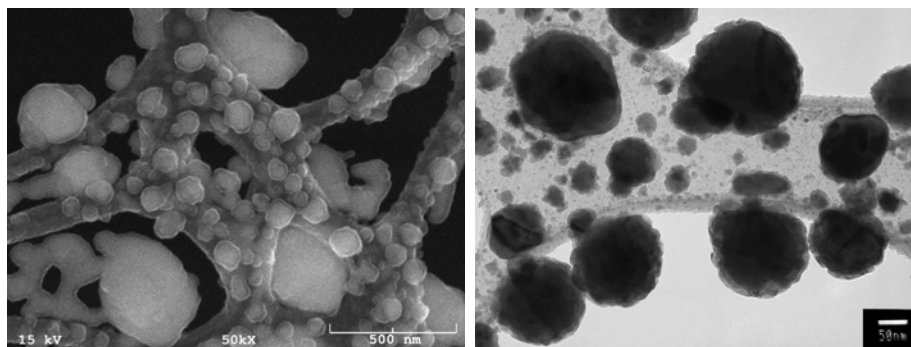
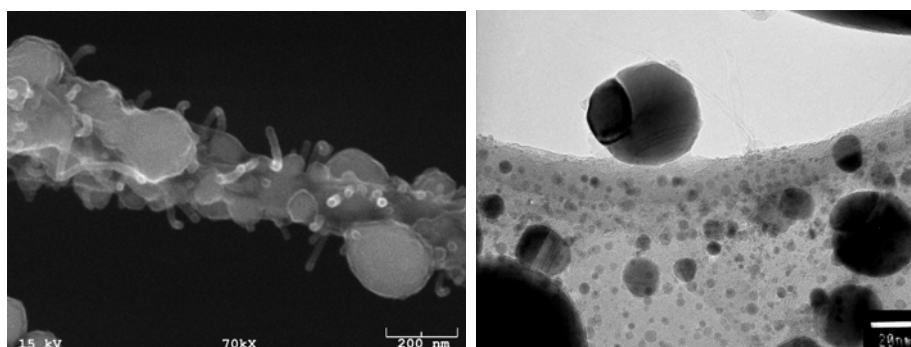


Figure 7.2 Raman spectra, SEM and TEM images obtained on a CoMo catalyst prepared over a silicon monoxide coated grid after reaction with CO for 1, 3, and 10 minutes.

1 minute CO



3 minutes CO



10 minutes CO

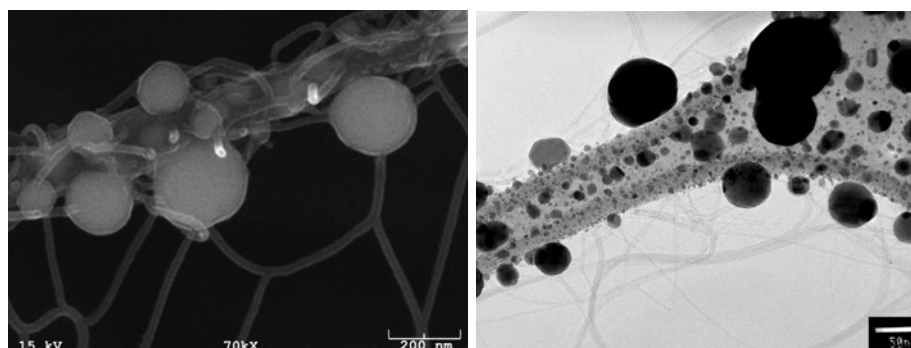


Figure 7.2 (Cont'd) Raman spectra, SEM and TEM images obtained on a CoMo catalyst prepared over a silicon monoxide coated grid after reaction with CO for 1, 3, and 10 minutes.

In previous work, our group has reported (9, 10), that the strong interaction between cobalt and molybdenum in this catalytic system plays a very important role in the production of SWNTs. Indeed, cobalt is stabilized by molybdenum in an oxidized form in a chemical environment similar to the one of cobalt in CoMoO_4 . EXAFS and XANES analysis of the real powder catalyst showed that even under the H_2 environment at high temperature Co and Mo species are still in the oxidized state, however; in the Co-Mo suboxide form instead of CoMoO_4 species. When CO is in contact with the catalyst, these pre-reduced cobalt molybdate species are converted to an unstable CoMo carbide; Co is no longer stabilized in this new matrix and starts migrating towards the surface where it gets reduced in the form of very small Co metallic clusters which trigger SWNT growth. This explanation is in agreement with what we observed in this study. The presence of these pre-reduced cobalt molybdate species together with some MoO_2 species is observed right before the reaction starts. This MoO_2 species should be generated from the decomposition of some cobalt molybdate during thermal pretreatment. The segregation of this free oxidic molybdenum phase might be linked to the formation of additional free cobalt. However we did not observed any Raman signal related to carbon deposition after 1 minute reaction with CO. It is possible that at the early stages of the reaction CO reacts with the cobalt molybdate and MoO_2 species first so these species began to transform into the unstable Co-Mo carbide and Mo_2C as previously reported (10). Then simultaneous formation of additional small Co metallic occurs and the growth of SWNTs begins after exposure to CO for less than 10 minutes. As mentioned above, carbon deposits were not observed after exposure to CO for 1 min, indicating that the

remaining amount of carbon dissolved into the cobalt nanoparticles after formation of carbidic species is not enough for the nucleation of SWNT during this early reaction stages.

Figure 7.3 shows a large catalyst particle of about 200 nm observed after 10 minutes reaction with CO at two different magnifications. It can be clearly seen that the particle is composed of three main regions labeled in the figure as (a), (b), and (c). This large particle is not representative of the powder catalyst, on which all the particles are smaller than 2 nm. However, this relatively large particle has allowed us to identify the transformation that take place in the bimetallic moieties. Using electron dispersive X-ray analysis (EDX), we found that region (a) is composed of Co and Mo; however the amount of Co in that region is significantly higher than the amount of Mo. Region (b) consists only of cobalt and region (c) also has both Co and Mo but in contrast to region (a) in this case the amount of Mo is significantly larger than Co. Figure 7.3B shows the interface between regions (a), (b), and (c). It is easy to observe in the outer surface of region (b) (composed of only Co) a thick layer of graphitized carbon. In contrast, a very thin layer of graphitized carbon was detected on regions (a) and (c). Moreover, a SWNT is observed and it seems to emerge from the interface between regions (a) and (b). Based on these observations, we can hypothesize that this phase separation is critical for SWNT growth. Indeed, as observed by Raman spectroscopy, the formation of a Mo-rich phase starts during catalyst pretreatment of catalyst prior to reaction. During CO

disproportionation, this phase separation keeps taking place as CO react with the pre-reduced cobalt molybdate species.

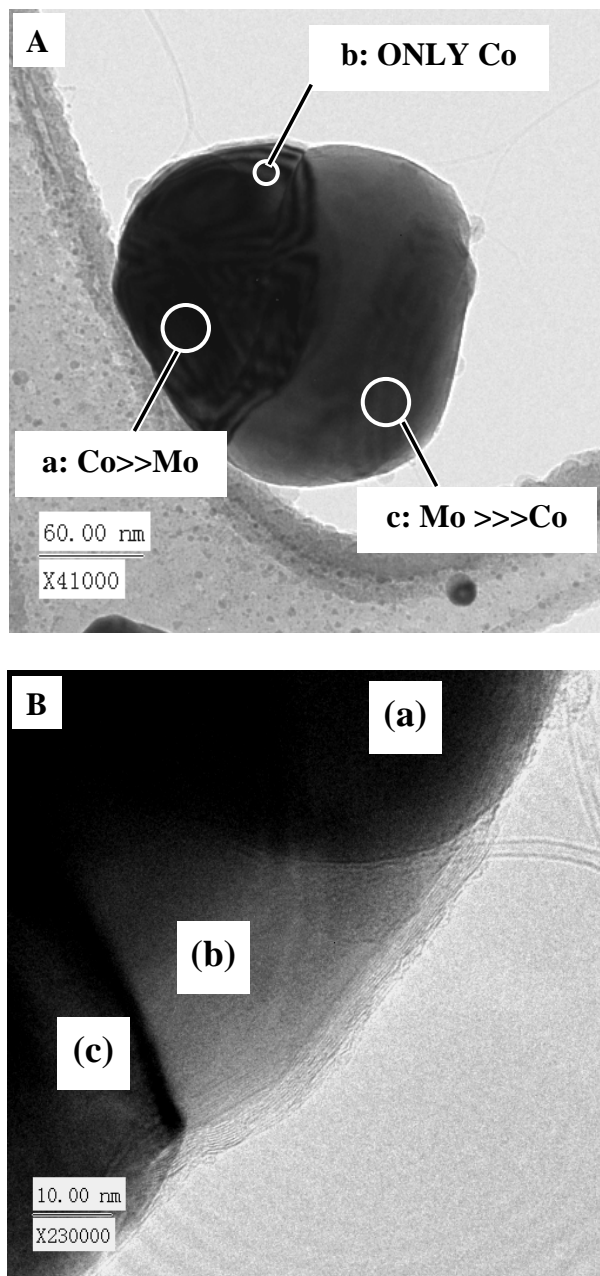


Figure 7.3 TEM images of a metal particle of a CoMo 2:1 catalyst obtained over a silicon monoxide grid after expose to CO for 10 minutes at 850°C.

As described above, we have previously proposed a growth mechanism in which pre-reduced cobalt molybdate species are converted into unstable CoMo carbide when CO is in contact with the catalyst, leading to the formation of very small metallic Co clusters which are responsible for the SWNT growth. From the phase separation observed in Figure 7.3 it is possible that region (a), (Co \gg Mo) is close to the original of the cluster composition (fresh catalyst), since the original material was prepared keeping a Co to Mo molar ratio of two. In the case of small particles, we can speculate that as CO is fed into the system and phase separation takes place, the pre-reduced cobalt molybdate phase begins to transform into Co and Mo carbide; as a result, the original pre-reduced cobalt molybdate phase splits into two additional phases. When very small metallic Co region are formed during this phase separation a carbon nucleation cap is formed, triggering the growth of SWNT. By contrast in the case of the observed large particle, as the one labeled (b) in Figure 7.3, we believe that as phase separation proceeds, the Co clusters are initially formed at the interface between region (a) and region (b), leading to the growth of the observed SWNTs. After longer reaction time, region (b) composed of mostly Co became larger; as a consequence a thick layer of graphitized carbon was formed over this metallic region.

To compare with the growth from CO, a similar electron microscopy study of SWNTs growth from CH₄ decomposition was performed using CH₄ as a feed; the results are shown in Figure 7.4. Contrary to the long induction period seen with CO, in this case, SWNTs were detected right after the grid containing the pretreated model catalyst

was exposed to CH_4 . However, after 1 minute exposure the length of the observed nanotubes was very short and the overall yield very low. As the grid remained in contact with CH_4 for longer times, i.e. 3 minutes; the length and yield of the obtained SWNT significantly increased. And after 10 minute reaction, an even higher yield of long SWNTs is observed. Nevertheless, it is clear that the amount of SWNTs produced from CH_4 is much smaller than that obtained from CO disproportionation (Fig. 7.2). As mentioned above for the Co-Mo bimetallic system, Co is stabilized in an oxidized form and small metallic Co clusters are released under reaction conditions before SWNT start to grow. As a consequence, the ability of the carbon feedstock to react with the cobalt molybdate species is critical in the growth process and the reducibility of the catalyst under the particular feed seems to play a central role.

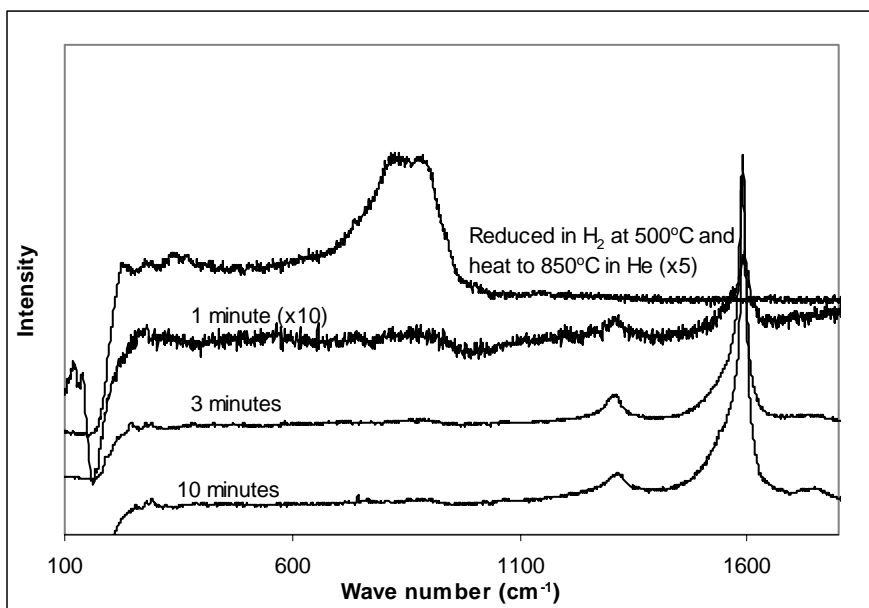


Figure 7.4 Raman spectra, SEM and TEM images obtained on a CoMo catalyst prepared over a silicon monoxide coated grid after reaction with CH_4 for 1, 3, and 10 minutes.

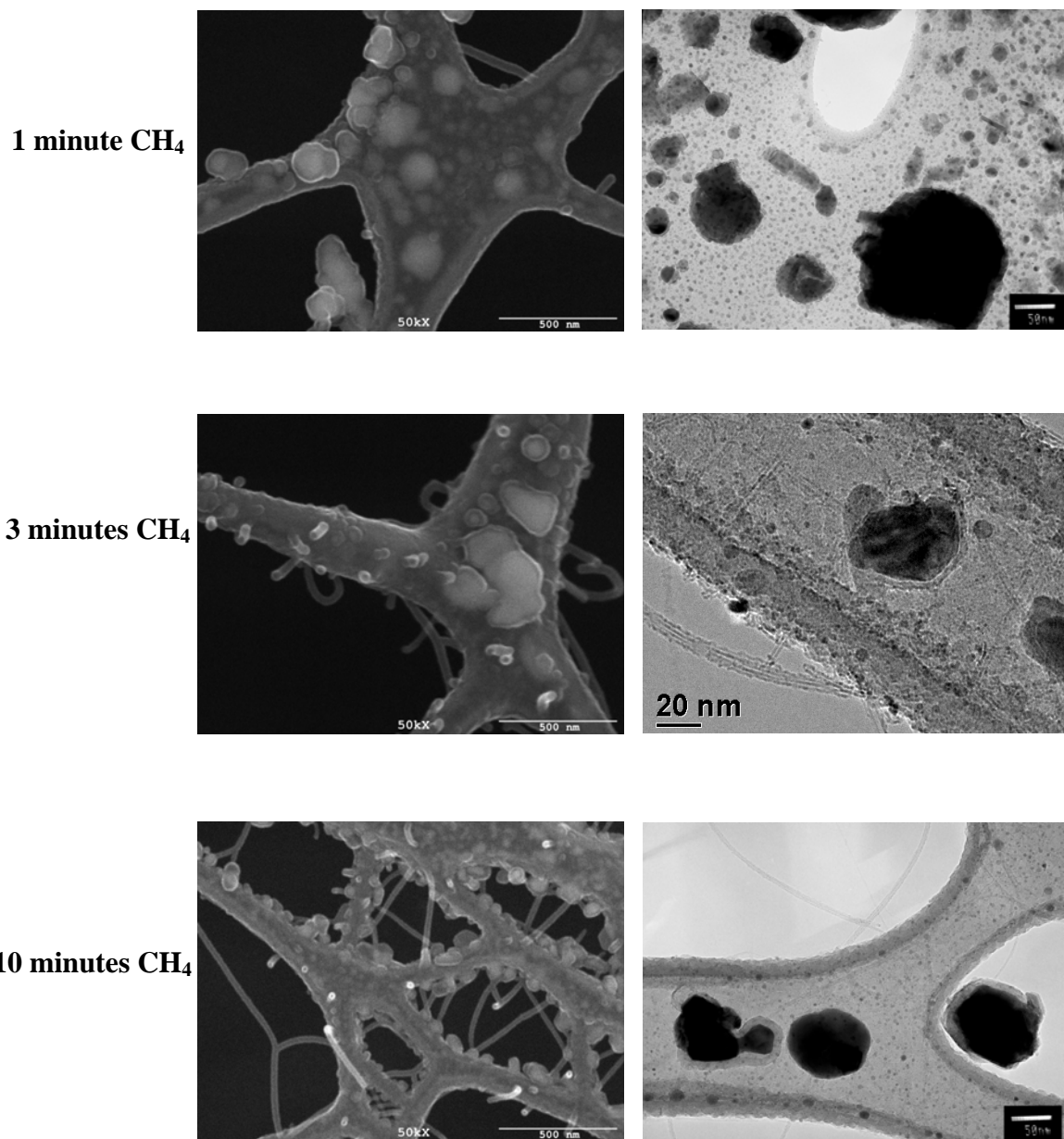


Figure 7.4 (Cont'd) Raman spectra, SEM and TEM images obtained on a CoMo catalyst prepared over a silicon monoxide coated grid after reaction with CH₄ for 1, 3, and 10 minutes.

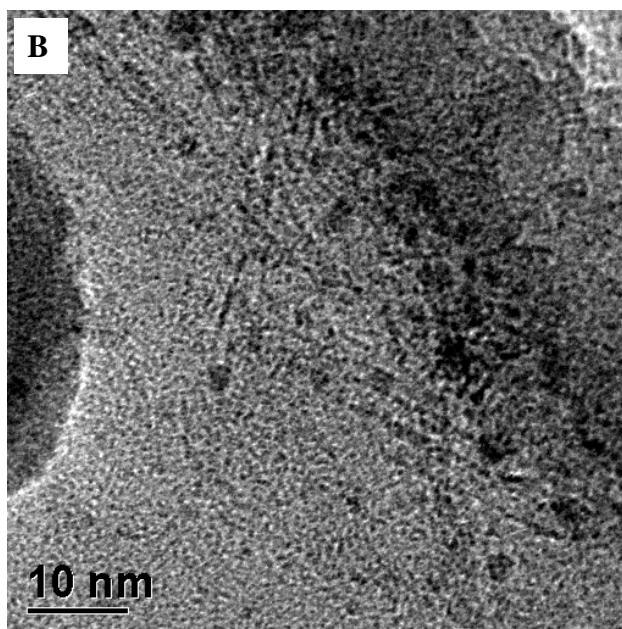
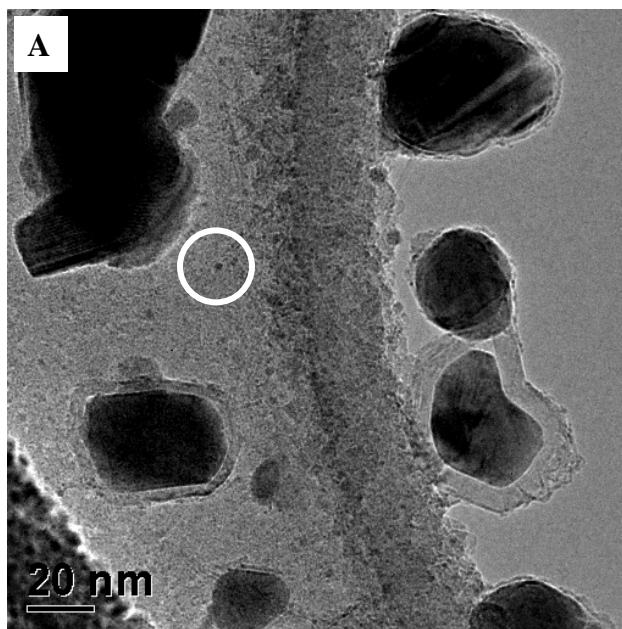


Figure 7.5 TEM images of (A) metal particles obtained on a CoMo 2:1 catalyst prepared over a silicon monoxide coated grid after reaction with CH_4 for 3 minutes and (B) the high magnification image of the circle area in (A).

Figure 7.5 shows the TEM images of the model catalyst contact with CH₄ for 3 minutes. It can be seen in Figure 7.5a that some of the big particles have been encapsulated; these particles are composed of Co and Mo as determined by EDX analysis. By contrast, SWNT seem to emerge from the small particles in the same area, as shown in Figure 7.5b. This is a general trend as Figure 7.4 and 5, in the case of CH₄ feed, metallic particles are encapsulated by graphite and SWNTs seem to grow in the area that contain small particles. However in the case of the material grown using CO, metal particle encapsulation was not observed. At longer reaction times, nanotubes still grow only from the small metal particles in case of CH₄, while the larger metal particles become encapsulated by graphite; by contrast, it was observed that SWNTs grow also from the large particles in case of CO which do not encapsulate (Fig. 7.2 and 7.3).

Moreover, the TEM and Raman results indicate that when CH₄ is used SWNTs grow immediately after exposure to the gas phase, while with the CO feed SWNT only grow after a longer period of time.

The reason for these differences can ascribe to either different reactivity of CH₄ and CO towards the cobalt molybdate species or to the differences of these two feeds in the rate of carbon deposition. As described above phase separation occurs after the thermal pretreatment prior to starting of the reaction. It is likely that the segregation of MoO₂ from cobalt molybdate is related to a simultaneous formation of a cobalt-rich phase or small cobalt particles. After CH₄ is fed into the system, it could react on these

metallic Co particles and dissociated leading to incipient carbon deposits which dissolve into the metal to initiate SWNTs growth. During this stage the difference in reactivity between methane and CO becomes critical. If phase separation did occur after pretreatment prior to reaction, CH₄ molecules might prefer to adsorb and react on the Co rich region instead of the Mo rich phase, as a consequence SWNT growth initiates from the Co-rich phase. In contrast, in case of carbon monoxide, the gas feedstock might prefer to react with the Mo rich phase, leading to transformation of the cobalt molybdate and molybdenum oxide into carbides before the SWNT growth triggered, accounting for the “induction time” observed for SWNT grow from CO. Another scenario could be that both CH₄ and CO react with cobalt molybdate and molybdenum oxide in the same way as CO does, i.e. forming a carbidic phase; however the rate of CH₄ decomposition compared to CO is faster, as a consequence the amount of carbon deposited on the surface is larger in the case of methane. This leads to a higher amount of carbon dissolving into metallic Co and nucleation of SWNTs could start right after contact with CH₄ for 1 minute.

According to the growth process we proposed for the case of CO feedstock (10), pre-reduced cobalt molybdate species began to transform into Co and Mo carbide, leading to phase separation after exposure to CO prior to SWNT growth. In the case of CH₄, it might be possible that the cobalt molybdate species do not react with CH₄ in the same way as CO does, therefore there is either a slower rate of separation or no phase separation at all after CH₄ was fed. We need to emphasize that the present study was performed using a Co/Mo molar ratio larger than one, contrasting with previous studies,

in which a Co/Mo ratio of 1:3 was used. This excess in cobalt in the cobalt molybdate matrix could result in a weaker interaction between Co and Mo. Once the catalyst is exposed to methane, carbon deposition occurs in the cobalt molybdate particles with excess in Co, carbon begins depositing in these cobalt rich- areas and nucleation of SWNTs occurs. As a result, SWNT growth appears from within the whole cobalt molybdate phase which seems to spit out the small metallic cobalt particle that is actually responsible for nucleation and growth of the nanotube.

The case of larger particles requires further consideration. As observed from Fig. 7.5a, for the case of CH₄ feed, the large particles are encapsulated by carbon deposits, while in the case of CO this encapsulation was not observed. It is well known that rate of CH₄ decomposition is greater than the rate of CO disproportionation (24), consequently the amount of carbon deposition on the metal cluster is higher for the case of CH₄ decomposition. This could result in a higher rate of metal encapsulation which will finally lead to a lower yield of SWNTs. In fact, Zhang *et. al.* (25) have reported that during CH₄ decomposition over Co/SiO₂, CH_x species are formed over the metal surface. They observed formation of carbon monoxide and explained it by proposing that CH_x species present on the catalyst surface would migrate from the metal to the support and this mechanism would help cleaning the catalyst surface. Moreover, their observations lead them to conclude that this cleaning of the catalyst surface by migration of CH_x species to the support is only significant in the first 2-3 minutes of reaction, while at longer time, it was not efficient to keep the catalyst surface clean. This result is in

agreement with our TEM observation, indeed our observations clearly indicate that metal encapsulation of large particle was observed just after 3 minutes of reaction.

The TEM study on the model catalyst clearly indicates that CO and CH₄ have different ability to react with the Co-Mo bimetallic system. CO seems to react with the pre-reduced cobalt molybdate species and be able to transform these species into a dual Co-Mo carbide through a phase separation process, generating small Co-rich areas within the particle matrix or fully releasing metallic Co particles. By contrast, CH₄ appears to follow one of two reaction paths. It either reacts with the excess amount of Co present in the catalyst before reaction or forms a carbon-containing complex alloy with the pre-reduced cobalt molybdate before the growth of SWNTs, without involving a phase segregation step. Moreover, the rate of CH₄ decomposition is faster than the rate of CO disproportionation, leading to a larger amount of carbon deposition and metal encapsulation when CH₄ is used as carbon source.

7.3.2 CoMo/SiO₂ powder catalyst

We can link the behavior of the model catalyst to that of high surface area powder catalysts if we take into consideration the differences in particle size. We have used two different Co/Mo molar ratios: 1:3 and 2:1, SWNT synthesis was carried using CO and CH₄. Figure 7.6a shows the Raman spectra of the products obtained from either CO disproportionation or CH₄ decomposition over a CoMo (1:3)/SiO₂ catalyst. It is

observed that in the case of the material grown using CO, the G band has a very high intensity while the intensity of D band is very low. Also, the radial breathing mode bands of SWNT are clearly observed and show a relatively high intensity indicating the presence of high quality SWNTs in the product. A contrasting behavior is observed in the case of the material grown using CH₄ feed. In this case the intensity of the D band is quite high, whereas the radial breathing mode bands are not observed. This result indicates that either there are not SWNTs in the product obtained from CH₄ decomposition or that their amount is very small compared to other forms of carbon such as amorphous carbon, graphite or nanofibers. The result clearly indicates that CO has a better performance than CH₄ for production of SWNTs when a bimetallic CoMo (1:3) supported on SiO₂ catalyst is used. These results might seem to contradict the result obtained on the model system in which both CO and CH₄ showed a similarly good performance. However, we must note that in the case of the model system, a catalyst rich in Co was employed. As mentioned above, the interaction between Co and Mo plays an important role in the production of SWNTs and this interaction is altered when Co/Mo molar ratio varies. Therefore, it is interesting to compare the performance of SWNTs production using CO and CH₄ as feeds over a catalyst with a similar Co to Mo molar ratio as the one used in the model system, i.e. Co/Mo > 1.

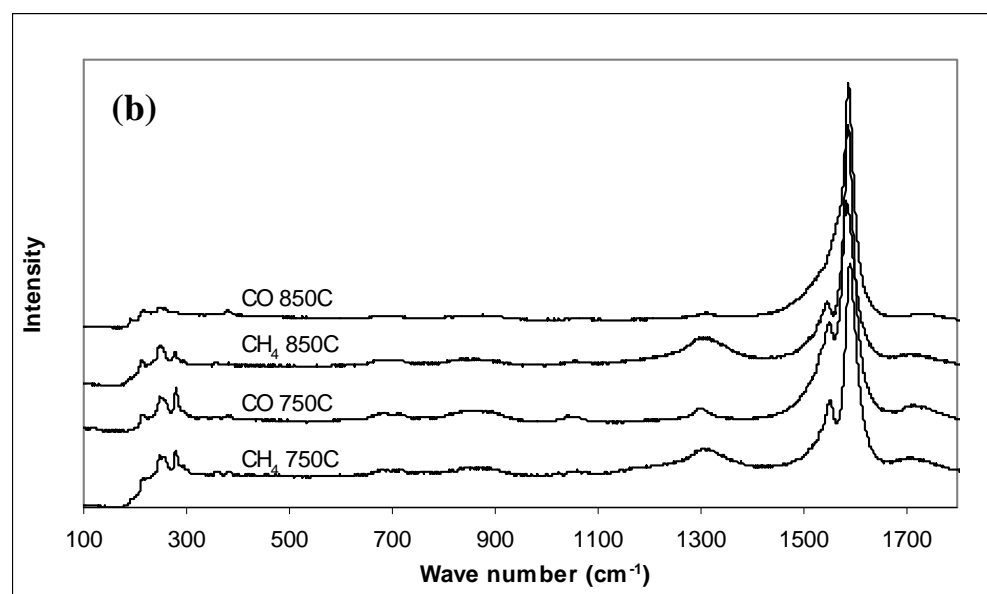
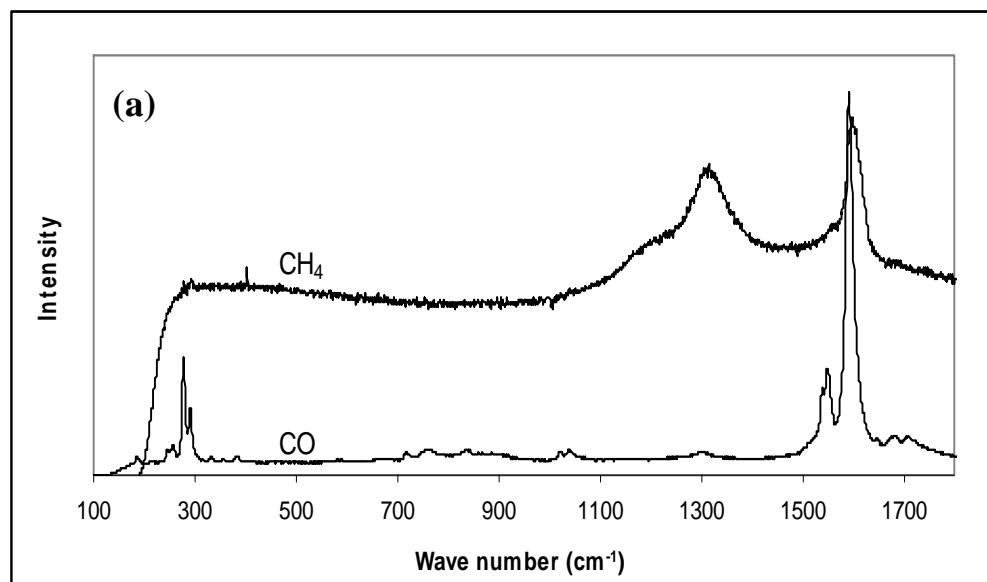


Figure 7.6 Raman spectra of the products obtained over (a) CoMo (1:3)/SiO₂ powder catalyst using CO and CH₄ at 750°C and (b) CoMo (2:1)/SiO₂ powder catalyst using CO and CH₄ at 750°C and 850°C

Figure 7.6b shows the Raman spectra of the product obtained over a CoMo (2:1)/SiO₂ catalyst at 750°C and 850°C using either CO or CH₄ as feed. In contrast to the results obtained for the CoMo (1:3)/SiO₂ catalyst, both CO and CH₄ generate a carbon deposit that shows the characteristic Raman signature of SWNTs, i.e. a split G band with high intensity, a small D band, and radial breathing mode bands. Figure 7.7a illustrates a quality parameter calculated from the Raman spectra, as $(G/(D+G))$; where, D and G are the integrated areas of the D (disorder) and G Raman bands, respectively. This term is a good indication of the quality of the SWNT sample, since it qualitatively measures the amount of ordered SWNT compared to defects and other disordered sp³ carbon species. As we have reported before a $(G/(D+G))$ parameter approaching unity is representative of a high-quality product. (26). Using this quality parameter to evaluate the Raman spectra shown in Fig.7.6b, it becomes evident that at both reaction temperatures (750 and 850°C) CO yields a product of better quality compared to that obtained from CH₄. Indeed, in the case of CO, the $(G/(D+G))$ parameter is nearly unity which indicates a product of extremely high quality, and this value does not seem to be affected by the reaction temperature. However, with CH₄ the reaction temperature does have an effect on the quality of the material; it deteriorates as temperature increases to 850°C. The amount of carbon present in the samples was quantified by temperature-programmed oxidation (TPO). Figure 7.7b shows the carbon yields on each sample. It can be seen that the amount of carbon deposited on the catalysts using CO is around 4% and this amount does not seem to vary much with reaction temperature in parallel with the constant quality observed with this feed. By contrast, the carbon yield in the product

obtained from CH₄ accompanied by a drop in quality changes dramatically with reaction temperature. At 750°C the carbon yield is 2% and it increased to 8% at 850°C. This result is not surprising; indeed, it has been observed before that the amount of carbon deposits obtained from CH₄ decomposition increases with temperature (27). On the other hand, the value of the quality parameter for the product obtained from CH₄ at 850°C shows the lowest value when compared to all others.

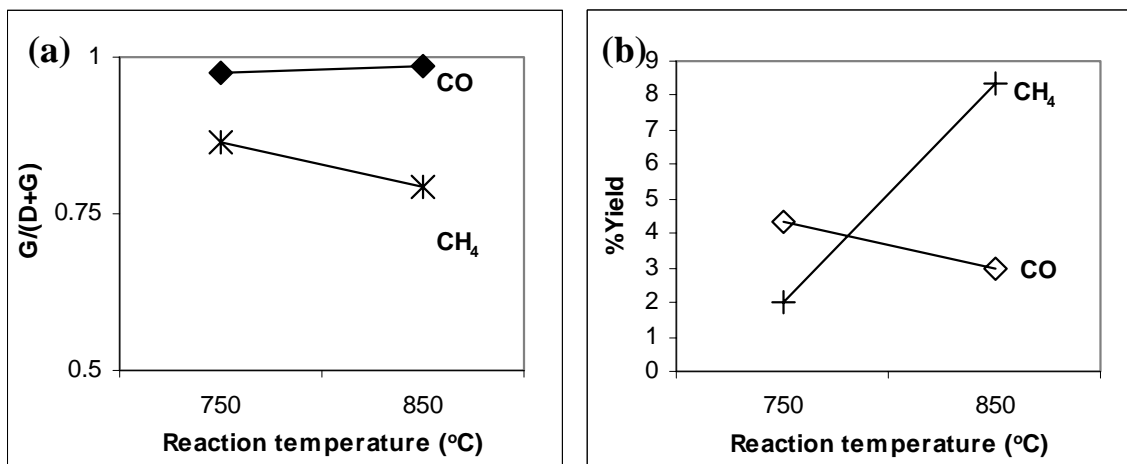


Figure 7.7 (a) contribution of the D band to the Raman spectra and (b) amount of carbon deposited from products obtained using CO and CH₄ as feed at 750 and 850°C.

TEM analysis on each of the samples described above was obtained to compare with the Raman spectra. Figure 7.8 shows SWNTs were observed in all samples. Interestingly, no significant amounts of graphitic species or nanofibers are observed for the sample produced with CH₄, despite exhibiting a large D band. Therefore, it is possible that this increased D band is due to defects in the SWNT themselves or to

amorphous carbon undetected by TEM. It is noteworthy to mention that in case of CO reaction at 850°C; many small particles were observed, while lesser amounts of small particles were noticed in other samples, particularly in the case of CH₄ reaction at 750°C.

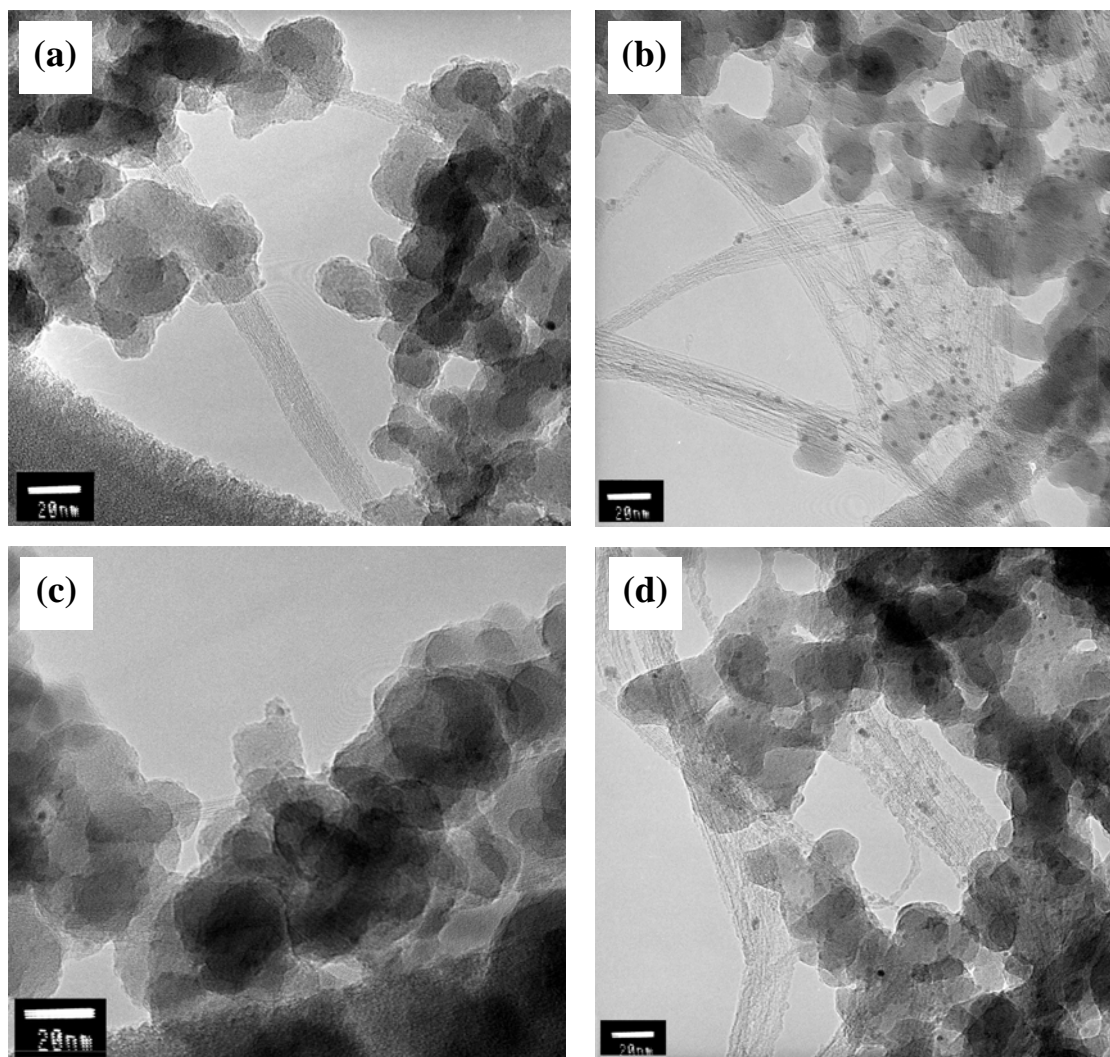


Figure 7.8 TEM images of SWNTs obtained over CoMo (2:1)/SiO₂ powder catalysts using (a) CH₄ at 850°C, (b) CO at 850°C, (c) CH₄ at 750°C, and (d) CO at 750°C.

As reported in our previous work, SWNTs produced using the CoMoCAT process (CoMo (1:3)/SiO₂) have very narrow (n,m) distribution (28). The two dominant structures obtained in this case are (6,5) and to a lesser extent (7,5). In order to compare the chirality of the materials obtained using methane and a different catalyst composition; we performed optical absorption experiments on the dispersed SWNTs produced. The results are shown in Figure 7.9. In contrast to nanotubes obtained using the CoMo (1:3)/SiO₂ catalyst, which show a narrow distribution of nanotube structures, the material obtained either from CO or from CH₄ over a CoMo (2:1)/SiO₂ catalyst exhibit a variety of nanotube structures. In order to perform a more quantitative comparison, we fitted the optical absorption spectra with Gaussians. The results of the fittings are summarized in Table 7.1. The main structures observed in all samples are (8,7), (7,6), and (8,6). Interestingly, for the case of CH₄, the nanotube structures do not seem to depend strongly on reaction temperature as the relative amount of the most abundant structures is similar at 750 and 850°C, i. e. about 40% for (8,7), 30% for (7,6), and 10% for (8,6). In the case of CO, the reaction temperature has some effect on the nanotube structure although much less pronounced than the one we have previously shown for CoMo (1:3)/SiO₂. As seen in Figure 7.9, absorption spectra of the sample obtained from CO at 850°C looked similar to the one obtained on sample produced from CH₄ at the same temperature, however, the contribution of the (8,7) nanotube in the spectra of the sample obtained with CO at 850°C slightly decreases. At the same time, the small peak corresponding to the (7,5) nanotube increases to some extent. In the case of CO at 750°C, the peaks corresponding to (7,5) and (6,5) structures are clearly observed while the contribution of the (8,7) and (8,6)

structures change to about 25% and 20%, respectively. For comparison, the product distribution obtained at 750°C on a CoMo (1:3) catalyst is included in Table 1; the differences are noteworthy.

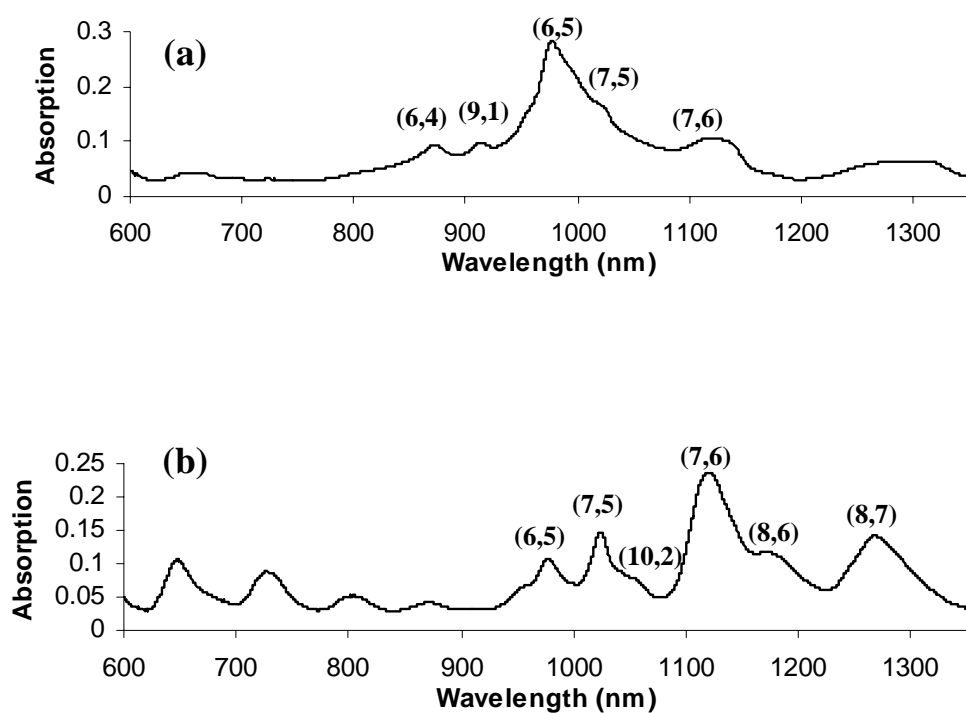


Figure 7.9 Optical absorption spectra of nanotubes produced various conditions; (a) CoMo (1:3)/SiO₂, CO 750°C, (b) CoMo (2:1)/SiO₂, CO 750°C, (c) CoMo (2:1)/SiO₂, CO 850°C, (d) CoMo (2:1)/SiO₂, CH₄ 750°C, and (e) CoMo (2:1)/SiO₂, CH₄ 850°C

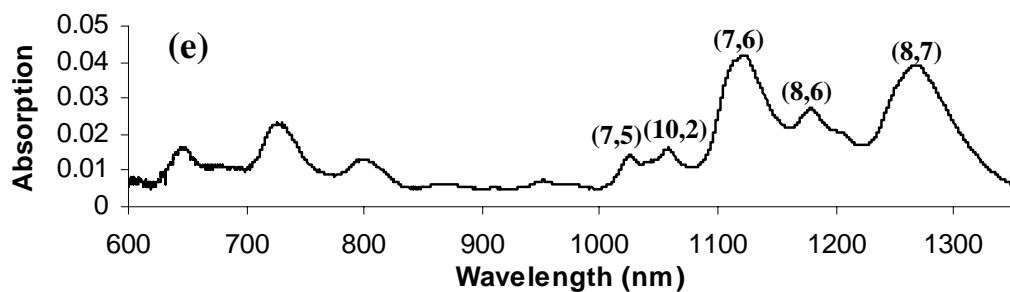
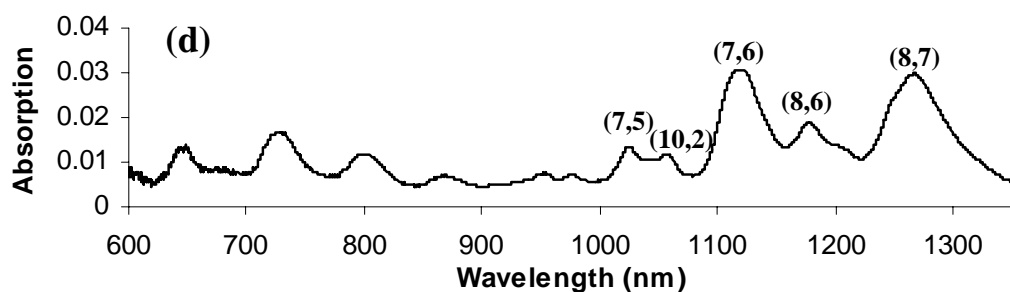
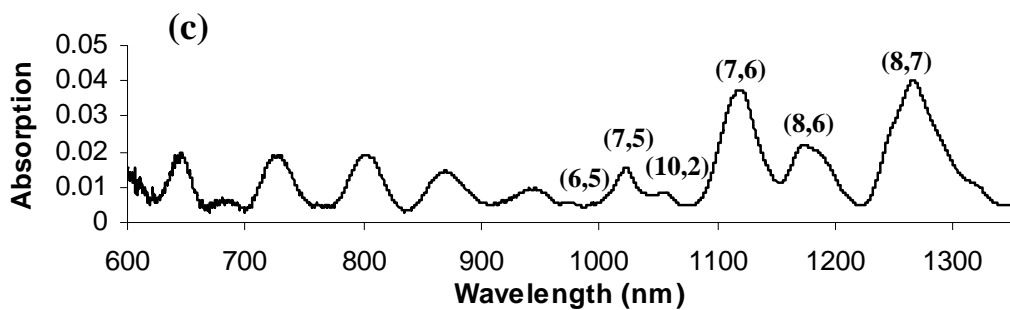


Figure 7.9 (Cont'd) Optical absorption spectra of nanotubes produced various conditions; (a) CoMo (1:3)/SiO₂, CO 750°C, (b) CoMo (2:1)/SiO₂, CO 750°C, (c) CoMo (2:1)/SiO₂, CO 850°C, (d) CoMo (2:1)/SiO₂, CH₄ 750°C, and (e) CoMo (2:1)/SiO₂, CH₄ 850°C

Table 7.1 Gaussian–Lorentzian fitting obtained on the optical absorption spectra of the carbon deposit obtained over CoMo (2:1)/SiO₂ using CO and CH₄ as feed at 750 and 850°C.

(n,m)	Diameter (nm)	CH ₄ (CoMo 2:1)		CO (CoMo 2:1)		CO(CoMo 2:1)
		750 (°C)	850 (°C)	750 (°C)	850 (°C)	750 (°C)
8,7	1.032	40.90	40.77	25.61	33.5	-
7,6	0.895	31.77	32.47	30.11	29	4.36
8,6	0.966	11.09	10.98	19.49	9.98	-
7,5	0.829	4.65	2.08	9.79	5.8	10.85
6,5	0.757	1.15	0.08	9.46	0.34	75.93
8,3	0.782	1.66	0.63	1.19	4.26	1.23
8,1	0.678	1.58	1.26	1.31	0.86	-
10,2	0.884	2.70	3.8	3.05	1.28	-
9,7	1.103	1.83	1.99	-	3.12	-
9,1	0.757	-	-	-	-	0.86
6,4	0.692	-	-	-	-	1.74
11,3	1.014	2.63	4.4	-	6.26	-
10,0	0.794	-	1.5	-	-	-
14,0	1.111	-	-	-	5.59	-
9,2	-	-	-	-	-	5.03

The results above clearly indicate that the quality, structure, and yield of SWNTs strongly depend on the catalyst formulation, reaction feedstock and reaction temperature. Using two different Co:Mo molar ratios we have observed variations in performance when different carbon-containing molecules were used as feedstock. The catalyst with a Co:Mo molar ratio of 1:3 gave good performance only when CO was used as feed, while in the case of the CoMo (2:1)/SiO₂ catalyst both CO and CH₄ are able to grow high quality SWNTs (Fig.7.6b). These results can be rationalized in terms of the interaction between Co and Mo. By using a low ratio of Co to Mo molar ratio (1:3), the interaction between Co and Mo seems to be different than when a catalyst with higher Co to Mo ratio is used. XRD analysis of CoMo (1:3)/SiO₂ and CoMo (2:1)/SiO₂ powder catalyst is shown in Figure 7.10. After calcination at 500°C, CoMoO₄ phase were observed in both catalysts, however, in the case of CoMo (2:1)/SiO₂ Co₃O₄ phase was also detected. This difference is expected because of an excess amount of Co in the CoMo (2:1)/SiO₂ catalyst is not interact with Mo. The significant change in phase detected was observed after treatment in H₂ at 500°C. In the case of CoMo (1:3)/SiO₂, CoMoO₄ phase was no longer exists, while MoO₂ phase was visible. In contrast, only Co₃O₄ species was still visible in the case of CoMo (2:1)/SiO₂ catalyst, nevertheless, it is possible in this case that MoO₂ species are very small because the amount of Mo is less than in the case of CoMo (1:3) catalyst so it cannot be detected by XRD. Therefore, it can be implied that CoMoO₄ species may decompose or reduce under H₂ atmosphere at high temperature into other form of Co-Mo oxide. These observations are in agreement

with the model catalyst mentioned above and the EXAFS and XANES studies in our previous report.

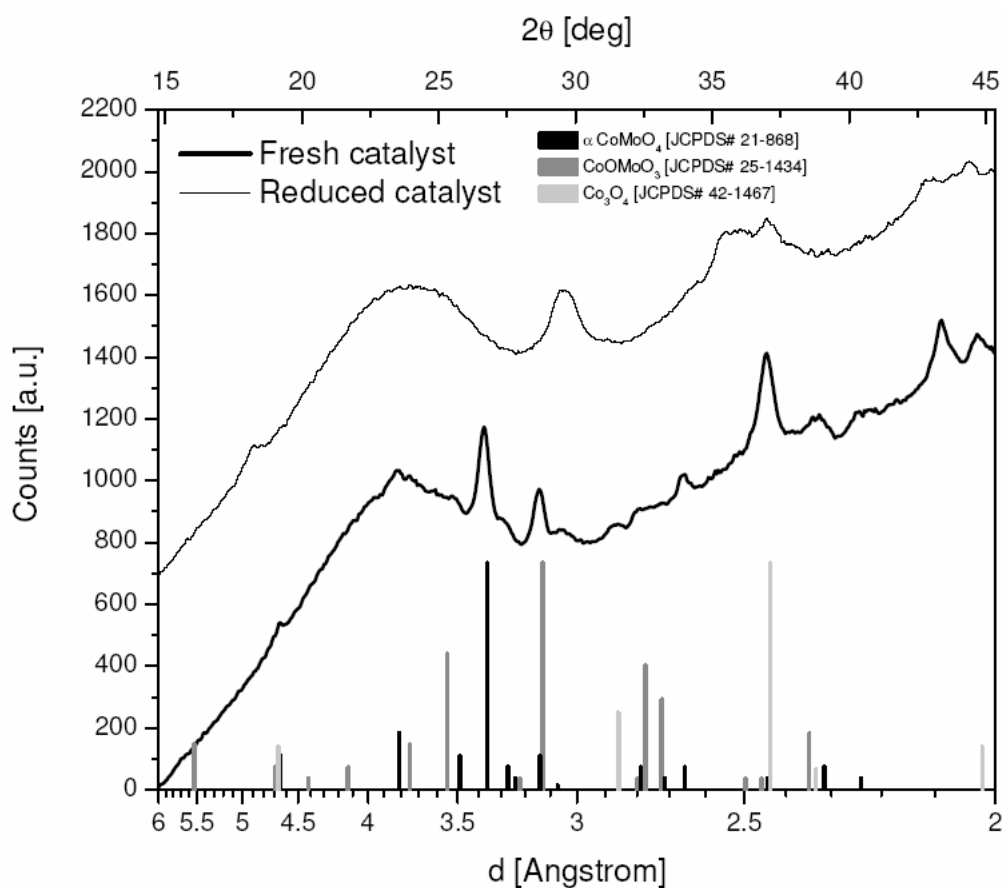


Figure 7.10 XRD analysis of CoMo (1:3)/SiO₂ and CoMo (2:1)/SiO₂ powder catalyst after calcination and reduction in H₂ at 500°C

As explained in the model catalyst study, CO and CH₄ react differently with the pre-reduced cobalt molybdate. While CO seems to transform the pre-reduced cobalt molybdate species into Mo carbide and small metallic cobalt, CH₄ appears to decompose either by forming a complex carbon containing alloy with the whole matrix or react with

the excess of Co released during the thermal pretreatment of the catalyst prior to reaction. Therefore, if the interaction between Co and Mo is very strong or Co atoms were surrounded by Mo atoms, like in case of the CoMo (1:3)/SiO₂ catalyst there would be a lower amount of segregated Co produced after the pretreatment of the catalyst, resulting in a lower extent of catalytic CH₄ decomposition. By contrast, in the case of CO, the gas feedstock is able to transform the pre-reduced cobalt molybdate species into Mo carbide, thus releasing at the same time small metallic Co, which initiate SWNTs growth.

The effects of reaction temperature observed for the catalyst with 2:1 molar ratio can be rationalized following a similar line of reasoning. As shown above the reaction temperature has almost a negligible effect on the nanotube structure for CH₄ feed. By contrast, when CO feed is used the distribution of chiralities changes with reaction temperature. CO transforms the pre-reduced cobalt molybdate species into Mo carbide through a phase separation process, but in the case of CH₄ decomposition, a phase separation is not involved and instead carbon incorporation into the cobalt molybdenum matrix seems to occur. It is likely that at 850°C, CO is able to release more small metallic Co than when the reaction is run at 750°C. In fact, this is in agreement with the TEM observations (Fig. 7.8b), which indicate that larger amounts of small metal particles can be detected at 850°C when the reaction is run with CO.

7.4. CONCLUSIONS

The mechanistic steps of SWNT growth over a bimetallic CoMo catalyst was directly observed using a model system built on a TEM grid. Methane and CO were compared as reaction feedstock. It was found that CO and CH₄ react with the cobalt molybdate phase present in the CoMo/SiO₂ catalysts in different fashion. CO tends to transform cobalt molybdate species into Mo carbide and metallic Co throughout metallic Co throughout a phase separation. On the other hand CH₄ seems to have less ability to convert cobalt molybdate but instead decomposed incorporating carbon into the cobalt molybdate matrix for SWNT growth. In the real catalyst, reaction conditions and catalyst formulations play an important role in the performance of the catalyst for SWNTs production. The quality, carbon yield and the distribution of chiralities of the nanotubes produced are affected by the reaction conditions.

REFERENCES

- 1 M.A. Ermakova, D.Yu. Ermakov, L.M. Plyasova, G.G. Kuvshinov, *Catal. Lett.* 62, 93 (1999)
- 2 P.E. Anderson, N.M. Rodriguez, *J. Mater. Res.* 14, 2912 (1999)
- 3 A.S. Johansson, J.O. Carlsson, *Thin Solid Films* 261, 52 (1995)
- 4 K. Hernadi, A. Fonseca, J.B. Nagy, D. Bernaerts, J. Riga, A. Lucas, *Synth. Metals* 77, 31 (1996)

- 5 C. Gautier, E. Frackowiak, B. Bonnamy, F. Beguin, *Electrochem.Soc. Proc.* 8, 1291 (1998)
- 6 Y.H. Mo, A.K.M.F. Kibria, K.S. Nahm, *Synthetic Metals* 122, 443 (2001)
- 7 Y. Murakami, Y. Miyauchi, S. Chiashi, S. Maruyama, *Chem. Phys. Lett.* 374, 53 (2003)
- 8 P. Nikolaev, M.J. Bronikowski, R.K. Bradley, F. Rohmund, D.T. Colbert, K.A. Smith, *Chem. Phys. Lett.* 313, 91 (1999)
- 9 W. E. Alvarez, B. Kitiyanan, A. Borgna, and D. E. Resasco, *Carbon* 39, 547 (2001)
- 10 J. E. Herrera, L. Balzano, A. Borgna, W. E. Alvarez, D. E. Resasco, *J. Catal.* 204, 129 (2001)
- 11 S. Amelinckx, X.B. Zhang, D. Bernaerts, X.F. Zhang, V. Ivanov, J.B. Nagy, *Science* 265, 635 (1994)
- 12 S. Fan, M. G. Chapline, N. R. Franklin, T. W. Tomblor, A. M. Cassell, H. Dai, *Science*, 283, 512 (1999)
- 13 Y. M. Li, W. Kim, Y.G. Zhang, M. Rolandi, D.W. Wang, H.J. Dai, *J. Phys. Chem. B* 105, 11424 (2001)
- 14 Y. Zhang, Y. Li, W. Kim, D. Wang, H. Dai, *Appl. Phys. A* 74, 325 (2002)
- 15 J. Gavillet, A. Loiseau, C. Journet, F. Willaime, F. Ducastelle, J.-C. Charlier, *Phys. Rev. Lett.* 87, 275504 (2001)
- 16 J. Gavillet, J. Thibault, O. Stephan, H. Amara, A. Louseau, Ch. Bichara, J.-P. Gaspard, F. Ducastelle, *J. Nanosci. Nanotech.*, 4, 346 (2004)
- 17 A. Loiseau, J. Gavillet, F. Ducastelle, J. Thibault, O. Stephan, P. Bernier, S. Thair, *C.R. Physique* 4, 975 (2003)
- 18 R. S. Wagner and W. C. Ellis, *Appl. Phys. Lett.* 4, 89, (1964)

- 19 L. Alvarez, T. Guillard, J.L. Sauvajol, G. Flamant, D. Laplaze, Chem. Phys. Lett. 342, 7 (2001)
- 20 B. Kitiyanan, W.E. Alvarez, J.H. Harwell, D.E. Resasco, Chem. Phys. Lett. 317, 497 (2000)
- 21 S. Rols, A. Righi, L. Alvarez, E. Anglaret, R. Almairac, C. Journet, P. Bernier, J.L. Sauvajol, A.M. Benito, W.K. Maser, E. Munoz, M.T. Martinez, G.F. de la Fuente, A. Girard, J.C. Ameline, Eur. Phys. J. B 18, 201 (2000)
- 22 S. Bandow, S. Asaka, Y. Saito, A.M. Rao, L. Grigorian, E. Richter, P.C. Eklund, Phys. Rev. Lett. 80, 3779 (1998)
- 23 A. M. Rao, E. Richter, S. Bandow, B. Chase, P.C. Eklund, K.A. Williams, S. Fang, K. Subbaswamy, M. Menon, A. Thess, R.E. Smalley, G. Dresselhaus, M.S. Dresselhaus, Science 275, 187 (1997)
- 24 A. Shamsi, C.D. Johnson, Effect of pressure on the carbon deposition route in CO₂ reforming of ¹³CH₄.
- 25 Y. Zhang, K. Smith, Catal. Today 77, 257 (2002)
- 26 J. E. Herrera, D. E. Resasco, Chem. Phys. Lett., 376 302 (2003)
- 27 A. Shamsi, C. D. Johnson, "Effect of pressure on catalyst activity and carbon deposition during CO₂ reforming of methane over noble-metal catalysts"
- 28 S. M. Bachilo, L. Balzano, J.E. Herrera, F. Pompeo, D.E. Resasco, R. B. Weisman, J. Am. Chem. Soc. 125, 11186 (2003)